



**HAL**  
open science

# Subsurface-intensified oceanic vortices: impact on the sea-surface and mutual interactions

Daniele Ciani

► **To cite this version:**

Daniele Ciani. Subsurface-intensified oceanic vortices: impact on the sea-surface and mutual interactions. Earth Sciences. Université de Bretagne occidentale - Brest, 2016. English. NNT: 2016BRES0069 . tel-01481211

**HAL Id: tel-01481211**

**<https://theses.hal.science/tel-01481211>**

Submitted on 2 Mar 2017

**HAL** is a multi-disciplinary open access archive for the deposit and dissemination of scientific research documents, whether they are published or not. The documents may come from teaching and research institutions in France or abroad, or from public or private research centers.

L'archive ouverte pluridisciplinaire **HAL**, est destinée au dépôt et à la diffusion de documents scientifiques de niveau recherche, publiés ou non, émanant des établissements d'enseignement et de recherche français ou étrangers, des laboratoires publics ou privés.



université de bretagne  
occidentale

UNIVERSITE  
BRETAGNE  
LOIRE

THÈSE / UNIVERSITÉ DE BRETAGNE OCCIDENTALE

*sous le sceau de l'Université Bretagne Loire*

pour obtenir le titre de

DOCTEUR DE L'UNIVERSITÉ DE BRETAGNE OCCIDENTALE

*Mention : Océanographie Physique et Environnement*

École Doctorale : EDSM

présentée par

**Daniele Ciani**

Préparée au Laboratoire d'Océanographie  
Physique et Spatiale

## **Tourbillons océaniques intensifiés en subsurface: signature en surface et interactions mutuelles**

Thèse soutenue le 26 octobre 2016

devant le jury composé de :

**M Igor Bashmachnikov**

*Professeur Associé - St. Petersburg State University, St. Petersburg, Russie / Examineur*

**M Xavier Carton**

*Professeur des Universités - Université de Bretagne Occidentale, Brest, France / Encadrant*

**M Bertrand Chapron**

*Chercheur - Ifremer, Brest, France / Encadrant*

**M Alain Colin de Verdière**

*Professeur des Universités - Université de Bretagne Occidentale, Brest, France / Président du Jury*

**M Yves Morel**

*Directeur de Recherche - Observatoire Midi-Pyrénées, Toulouse, France / Rapporteur*

**M Álvaro Júdice Peliz**

*Professeur Associé - Universidade de Lisboa, Lisbonne, Portugal / Examineur*

**M Gilles Reverdin**

*Directeur de Recherche - Université Pierre et Marie Curie, Paris, France / Rapporteur*

**M Jacques Verron**

*Directeur de Recherche - LEGI, Grenoble, France / Examineur*

Laboratoire d'Océanographie Physique et Spatiale  
Université de Brest, CNRS, IRD, Ifremer, IUEM, Brest, France

**PhD Manuscript:**  
**Subsurface-Intensified Oceanic Vortices:**  
**Impact on the Sea-Surface and Mutual Interactions**

**PhD Candidate:**  
Daniele Ciani

**Supervisors:**

Xavier Carton

Laboratoire d'Océanographie Physique et Spatiale, Univ. Brest/IUEM, Brest, France

Bertrand Chapron

Laboratoire d'Océanographie Physique et Spatiale, Ifremer, Brest, France



*Ce manuscrit est dédié aux gens qui doutent...*

# Contents

<b>1</b>	<b>General Introduction</b>	<b>1</b>
1.1	Theoretical Background . . . . .	4
1.2	Review of subsurface-intensified vortices . . . . .	9
1.2.1	Meddies and Smeddies . . . . .	9
1.2.2	Thermocline Eddies in the Atlantic Ocean . . . . .	10
1.2.3	Cuddies . . . . .	11
1.2.4	Peddies and Reddies . . . . .	11
1.2.5	Swoddies . . . . .	13
1.2.6	Leddies . . . . .	13
1.2.7	Mode Water Eddies . . . . .	14
1.2.8	Japan Intrathermocline Eddies (ITE) . . . . .	15
1.3	Surface signature of oceanic eddies . . . . .	16
1.3.1	Surface signature of surface-intensified vortices . . . . .	16
1.3.2	Surface signature of subsurface-intensified vortices . . . . .	20
1.4	Summary . . . . .	25
<b>2</b>	<b>Main objectives and structure of the manuscript</b>	<b>27</b>
<b>3</b>	<b>Influence of deep vortices on the ocean surface</b>	<b>30</b>
3.1	Introduction . . . . .	31
3.2	Materials and Methods . . . . .	34
3.2.1	Quasi-Geostrophic framework . . . . .	34
3.2.2	QG numerical model . . . . .	36
3.2.3	Primitive equation model . . . . .	38
3.3	Theoretical Analysis . . . . .	41
3.3.1	Surface influence of steady vortices . . . . .	41

3.3.2	Surface expression of translating vortices . . . . .	48
3.4	Numerical results . . . . .	53
3.4.1	Surface signature of deep anticyclones: steady case . . . . .	53
3.4.2	Comparison with the point vortex model . . . . .	56
3.4.3	Surface signature of deep anticyclones: dynamic case, CLAM-3DQG model . . . . .	58
3.4.4	Surface signature of deep anticyclones: dynamic case, ROMS model . . . . .	60
3.4.5	Parametric study of the dipolar signatures . . . . .	62
3.4.6	Surface signature of deep anticyclones: the case of a vortex advected by a surface-intensified shear flow . . . . .	69
3.5	Discussion, Conclusions and Openings . . . . .	74
<b>4</b>	<b>On the merger of subsurface isolated vortices</b>	<b>79</b>
4.1	Introduction . . . . .	79
4.2	Materials and Methods . . . . .	82
4.3	Results . . . . .	87
4.3.1	Merger sensitivity to vortex parameters . . . . .	87
4.4	Merger related effects . . . . .	98
4.4.1	Evolution of PVa volume integral . . . . .	98
4.4.2	Vortex deformation . . . . .	102
4.4.3	Final PVa structure of the merged vortex . . . . .	106
4.5	Conclusions and Perspectives . . . . .	110
4.6	Further Studies (A): the merger of intrathermocline eddies: the cyclonic case . . . . .	112
4.6.1	The case of Large-scale cyclones . . . . .	112
4.6.2	Small-scale cyclones . . . . .	115
4.6.3	Discussion . . . . .	117
4.7	Further Studies (B): The role of relative vorticity and of the divergence in the merger experiments . . . . .	119
4.8	The Ertel Potential Vorticity Anomaly in isopycnal coordinates . .	121
<b>5</b>	<b>Surface Signature of Mediterranean Water Eddies in a long-term high resolution simulation</b>	<b>123</b>

---

5.1	Introduction . . . . .	124
5.2	Methods . . . . .	128
5.2.1	The model . . . . .	128
5.2.2	Definition of the Meddy surface signature . . . . .	128
5.2.3	Meddy metrics and oceanic background parameters . . . . .	129
5.3	Results . . . . .	134
5.3.1	Along-trajectory Meddy surface signature . . . . .	134
5.4	SSH response to i-EPVa changes . . . . .	157
5.5	Statistics of SSH anomalies over modelled meddies . . . . .	158
5.6	Discussion and Conclusions . . . . .	160
5.7	Further Studies: Meddies' aspect ratio in the numerical simulation .	164
<b>6</b>	<b>Conclusions and Perspectives</b>	<b>167</b>
6.1	Main results . . . . .	168
6.1.1	Surface signatures of subsurface anticyclones in idealized oceanic basins . . . . .	168
6.1.2	Merger of subsurface anticyclones . . . . .	170
6.1.3	Surface signature of Mediterranean Water Eddies (Meddies) in a realistic simulation . . . . .	171
6.2	The main perspectives . . . . .	173

Subsurface-Intensified Oceanic Vortices:  
Impact on the Sea-Surface and Mutual  
Interactions

Daniele Ciani

December 7, 2016

# Chapter 1

## General Introduction

The oceanic motions, at mesoscale, are characterized by horizontal scales ranging from 20 to 200 km and time scales ranging from a few days to a few weeks. The expression of this dynamics is mostly given by vortices (eddies) and meanders of unstable currents. These structures can be described by the quasi-geostrophic approximation, except when strong density fronts or large accelerations are present. Mesoscale motions contain more than 80% of the ocean eddy kinetic energy and are globally more energetic than the general circulation. Mesoscale motions can also be long lived, and thus contribute efficiently to the heat and salt transport in the ocean. For example, vortices are mesoscale recirculating features which trap water masses from their origination areas and carry them over large distances across the ocean (up to several thousands of miles).

Observations of the ocean show that mesoscale features do not exhaustively describe the ocean dynamics. This is also suggested by modeling experiments, in which the modeled eddy kinetic energy increases for an increasing model spatial resolution. Indeed, a fine spatial resolution allows one to take into account submesoscale features and to see that they significantly contribute to the ocean energy budget and circulation. Submesoscale structures have horizontal scales between 0.5 and 20 km and time scales from a few hours to a few days. Physically, they are given by small eddies, filaments or turbulent patches, and they can result from frontal, mixed layer instabilities and from the straining and shearing of mesoscale structures. Motion at submesoscale is also instrumental in the energy cascade to small scales, where dissipation takes place.

---

Most of the comprehensive studies of mesoscale and submesoscale dynamics rely on surface (satellite) data and on high resolution models. For an observational approach, only surface data from satellite sensors are able to provide high space-time resolution and synopticity at planetary scale. High resolution and synopticity can be achieved locally by dedicated oceanic cruises, though they can only concentrate on one or a few eddies. Synopticity and medium resolution can be achieved regionally by ARGO float data (nowadays, ARGO floats are distributed over the global ocean at an average 3-degree spacing). The context illustrated here is a source of two main questions:

- how do surface and subsurface motions (e.g. motions near the thermocline) interact at mesoscale, and can lead to submesoscale structures?
- what is the measurement resolution and accuracy, especially at the surface, necessary to capture subsurface mesoscale or submesoscale eddies?

The purpose of this work is to contribute to these questions via the following studies:

- the surface signature of subsurface eddies;
- the life cycle and interaction of some subsurface mesoscale and submesoscale structures (mainly eddies).

These studies were also motivated by recent observations of surface mesoscale eddies south and east of the Arabian Peninsula (during the PHYSINDIEN 2011 experiment) and of subsurface submesoscale features in the same region [L'Hégaret (2015)]. Colocated satellite and *in-situ* measurements were used to characterize the observed structures. Preliminary analyses indicated that the shear and strain created by the surface eddies may be held responsible for the formation of the deeper submesoscale features and, recently, this was confirmed by Vic et al. (2015). Occurrences of subsurface mesoscale eddies in the Arabian Sea have also been documented by past works. In particular, a mesoscale eddy of Persian Gulf Water was identified and measured near the Straits of Hormuz by Senjyu et al. (1998). It laid at a depth of 250 m, was about 50 km in diameter and 300 m thick. Mesoscale eddies of Red Sea Water were also measured and described by Shapiro and Meschanov (1991) and Meschanov and Shapiro (1998). They can lie at depths

between 600-800 m, they can be 30 to 100 km wide and can extend vertically for about 300 m.

Nevertheless, our work will not be limited to this region. Indeed, varying the characteristics of the eddies, one can account for several types of subsurface structures which can be found in the ocean. Beyond the ones already introduced, one can cite Meddies (Mediterranean Water eddies in the Atlantic ocean [Richardson et al. (2000a)]), generated by the Mediterranean Sea outflow as well as Leddies (Levantine intermediate water eddies [Testor and Gascard (2003)]), Swoddies (Slope Water Oceanic eddies [Pingree and Le Cann (1992)]) and Mode water eddies [Sweeney et al. (2003a)], resulting from slope currents instability or deep convection. Before we address the questions listed above, we review previous studies on the oceanic mesoscale and on its surface signatures. Furthermore, we will provide a short overview of the variety of subsurface eddies which can be found in the ocean.

## 1.1 Theoretical Background

In recent years, several works have attempted to infer ocean dynamics at depth taking advantage of surface informations. This effort is justified by the fact that, unlike for the internal ocean, observations of the sea surface are available at global scale with high repetitiveness, and up to submesoscale resolutions (nowadays in the thermal band and, in the future, also in altimetry, with the SWOT mission [Fu et al. (2009)]). It is essential to review these works in order to understand the advantages and limits of such an approach.

The totality of the reviewed studies relies on the theoretical knowledge provided by the quasi-geostrophic framework. In this context, the physical variable "potential vorticity", generally referred to as PV, is a conserved quantity and represents the key for describing the entire fluid motion. In a quasi-geostrophic continuously-stratified flow and in a Cartesian frame, the expression for PV is given by equation 1.1 [Vallis (2006)]:

$$PV = f + \frac{\partial^2 \psi}{\partial x^2} + \frac{\partial^2 \psi}{\partial y^2} + \frac{\partial}{\partial z} \left( \frac{f^2}{N^2} \frac{\partial \psi}{\partial z} \right) \quad (1.1)$$

where  $f$  is the Coriolis parameter,  $\psi$  is the stream function and  $N$  is the Brunt-Väisälä frequency. The stream function,  $\psi$ , is related to the geostrophic velocities by means of its spatial derivatives, as indicated in equation 1.2,

$$(u_g, v_g) = (-\partial_y \psi, \partial_x \psi) \quad (1.2)$$

where the subscript  $g$  stands for geostrophic. Inversion of equation 1.1 for determination of the stream function then becomes the main task in this framework [Bishop and Thorpe (1994), Hoskins et al. (1985)]. In order to do this, provided a positive value for the quantity  $N^2$  (assuring ellipticity for equation 1.1), the inversion is possible if two vertical boundary conditions are known, and they are often expressed as density fluctuations at the ocean surface and at depth via the following relations

$$-\frac{\rho_0 f_0}{g} \frac{\partial \psi}{\partial z} \Big|_{z=0} = \rho|_{z=0} \quad (1.3)$$

and

$$\left. \frac{\partial \psi}{\partial z} \right|_{z=-H} = 0 \quad (1.4)$$

in which the second condition is the assumption of absence of density fluctuations at the ocean bottom. For lateral conditions, one can choose double periodicity (if the  $f$ -plane approximation is used) or other conditions imposed by the geometry of the particular problem. Lapeyre and Klein (2006), taking advantage of the Surface Quasi-Geostrophic (SQG) dynamics introduced by Bretherton (1966), investigated the effects of splitting the inversion in two different problems. A first problem (interior), in which one considers a non-zero internal PV and no surface density fluctuations, and another in which one considers zero internal PV anomalies forced by non-zero surface density (buoyancy) fluctuations. Mathematically, the interior and surface problems take the following form

$$\frac{\partial^2 \psi_{int}}{\partial x^2} + \frac{\partial^2 \psi_{int}}{\partial y^2} + \frac{\partial}{\partial z} \left( \frac{f_0^2}{N^2} \frac{\partial \psi_{int}}{\partial z} \right) = PV \quad (1.5)$$

with

$$\left. \frac{\partial \psi_{int}}{\partial z} \right|_{z=0} = 0 \quad (1.6)$$

and

$$\frac{\partial^2 \psi_s}{\partial x^2} + \frac{\partial^2 \psi_s}{\partial y^2} + \frac{\partial}{\partial z} \left( \frac{f_0^2}{N^2} \frac{\partial \psi_s}{\partial z} \right) = 0 \quad (1.7)$$

with

$$-\left. \frac{\rho_0 f_0}{g} \frac{\partial \psi_s}{\partial z} \right|_{z=0} = \rho|_{z=0} \quad (1.8)$$

where  $g$  is the acceleration imposed by gravity,  $\rho$  is the density of sea water and  $\rho_0$  a reference density value. In this case, the total stream function can be reconstructed after the inversion of equations 1.5-1.8, simply saying that  $\psi_{tot} = \psi_{int} + \psi_s$ . If one assumes a basin with a constant stratification ( $N = N_0$ ) the surface-forced solution, in spectral space, takes the following form:

$$\hat{\psi}_s(\bar{k}, z) \propto \frac{\hat{b}_s(\bar{k})}{N_0 \mathbf{k}} \exp\left(\frac{N_0 \mathbf{k} z}{f_0}\right) \quad (1.9)$$

where  $(\hat{\cdot})$  stands for horizontal Fourier transform,  $\bar{k} = (k_x, k_y)$  is the wave vector in spectral space,  $\mathbf{k} = |\bar{k}|$  its modulus and  $b = -g\rho/\rho_0$  is the surface buoyancy. The surface-forced solution is proportional to the surface buoyancy and its projection along the vertical coordinate decays exponentially with depth.

The last equation is generally referred to as Surface Quasi-Geostrophic equation [Held et al. (1995)] and, in the particular case of Brunt-Väisälä frequency chosen empirically from independent observations ( $N = N_0$ ), it becomes effectiveSQG equation (eSQG). It describes a motion which is regulated by the sea surface density fluctuations, i.e., temperature fluctuations (whenever salinity fluctuations can be neglected).

In general, a complete description of the ocean motion cannot neglect internal PV anomalies. Despite this, Lapeyre and Klein (2006), showed that, for a baroclinically unstable jet forced by large scale density gradients, the surface solution  $\psi_s$  well approximates the total one in the first 500 m of the water column (for scales from 50 to 150 km). In fact, the authors could relate the three-dimensional PV anomalies to the surface buoyancy as in equation 1.10,

$$PV'(x, y, z) = \frac{1}{f_0} \alpha(z) b'_s(x, y) \quad (1.10)$$

where  $\alpha(z)$  can be derived from the large scale potential vorticity distribution and from surface buoyancy. This implies that, in spectral space, one can express the internal solution as the product of a function of depth and wavenumber ( $\hat{\phi}(\mathbf{k}, z)$ ) and of the surface buoyancy, like in equation 1.11,

$$\hat{\psi}_{int}(\bar{k}, z) = \hat{\phi}(\mathbf{k}, z) \hat{b}_s(\bar{k}) \quad (1.11)$$

This result is essential. In fact, Equations 1.9 and 1.11 are both proportional to  $\hat{b}_s(k)$ , assuring that surface and internal solutions are spatially correlated and will only vary in the vertical. Furthermore, for surface-intensified motions it is the surface solution that dominates.

Still remaining in this context, Isern-Fontanet et al. (2008a), tested the eSQG approach on a realistic global circulation model (POP). They used sea surface

temperature as a proxy of sea surface buoyancy and could find that:

- the eSQG method is able to reconstruct the horizontal structure of ocean currents from SST and from the knowledge of the vertical average of the Brunt-Väisälä frequency, resolving scales from 10 to 400 km and down to 500 m depth;
- the use of SST for estimation of surface density anomaly is only valid in regions where temperature fluctuations are larger than salinity fluctuations;
- the modeled and eSQG-derived fields show increasing correlations for increasing values of surface wind stress, indicating that eSQG validity is higher for cases of deepened Mixed Layer;

Klein et al. (2009), using a primitive equations model and SQG theory, reconstructed vertical velocities for an idealized turbulent field in presence of surface wind stress (inducing a surface Mixed Layer (ML)). Their work showed that:

- SQG reconstruction is efficient in reconstructing vertical fields in the range 100 to 1000 m depth, for large-scale motions up to 400 km;
- the reconstruction fails to retrieve vertical motions in the first meters of the water column (where the ML is present). In fact, it is in this region that ageostrophic effects are more intense (as Ekman Pumping), making QG balance no more valid;

Beyond the problems related to the presence of a surface Mixed Layer, Isern-Fontanet et al. (2008a) also point out that SQG theory fails to predict subsurface intensified motions (which are the main interest of the present work). In fact, in these cases, surface density anomalies will be weak or even absent. Ponte et al. (2013a) and Ponte and Klein (2013) proposed solutions to make SQG theory more robust and could show that:

- introducing information on vertical mixing in the SQG theory significantly improves the estimation of horizontal and vertical circulation in the ocean;
- it is possible to reconstruct the ocean 3D circulation even in case of weak surface density anomalies. In this case, the reconstruction is operated using

a modified version of Equation 1.10, taking into account SSH observations instead of surface density ones. The results show that horizontal mesoscale reconstruction is efficient up to a 500 m depth, while the submesoscale cannot be described by this technique. For what concerns vertical velocities, the complete reconstruction is only possible at large scale, while, progressively descending towards submesoscale, the information is reliable only in the first tens of meters of the water column. Very recently, Qiu et al. (2016) found similar results the specific case of the Kuroshio Extension region.

These considerations point out that observations of the sea surface are a powerful instrument for inferring ocean circulation at depth. Despite this, there is a class of oceanic motions that cannot be investigated by pure SQG approach. Among these motions we can have subsurface-intensified vortices, whose presence in the world ocean is abundant. That is why, one of the purposes of this work will be to better characterize surface signatures of *a-priori* known subsurface structures. This will help understanding whether or not it is possible to detect them in a systematic way, via observation of the sea-surface.

## 1.2 Review of subsurface-intensified vortices

Subsurface-intensified oceanic motions have been extensively studied via observational and modeling studies. They often result from sinking of denser water masses towards subthermocline depths or from deep convection [Lee et al. (2000), Johns et al. (1999)]. They can exist in different forms, such as subsurface currents, or lens-shaped warm and salty anomalies. The latter are often subsurface-intensified anticyclonic vortices and they can range from submesoscale to mesoscale. Among them, we can find Meddies (Mediterranean Water Eddies), Thermocline eddies in the Atlantic Ocean, Cuddies (Californian Undercurrent Eddies), Peddies (Persian Water Eddies), Reddies (Red Sea Water Eddies), Swoddies (Slope Water Ocean Eddies), Leddies (Levantine Water Eddies), Mode Water Eddies and Japan Intrathermocline Eddies.

### 1.2.1 Meddies and Smeddies

Meddies (Mediterranean Water Eddies) are generated by the Mediterranean Sea outflow into the north-eastern Atlantic Ocean, through the Strait of Gibraltar [Armi and Zenk (1984), Pingree and Le Cann (1993b), Bower et al. (1997), Richardson et al. (2000a), Carton (2001), Barbosa Aguiar et al. (2013)].

Figure 1.1 shows a snapshot of salinity at typical depths of the Mediterranean outflow (in a numerical simulation). The generation and propagation of some Meddies is indicated by the high salinity circular patches in the domain. Indeed, the Mediterranean outflow can undergo instability and generate fragments in the shape of anomalously warm and salty lenses (compared to the surrounding ocean) of 20-180 km in diameter. Their thicknesses range from some hundred meters up to 1200 m. Meddies usually form and stabilize at depths of about 800-1200 m. Beyond their thermohaline structure, they are given by anomalies in the velocity field with respect to the background ocean, reaching swirl velocities that can exceed 0.3 m/s in some cases. Meddies' pathways have been largely investigated by means of hydrological surveys, analytical and numerical approaches. Their displacement is essentially westward-southwestward, and, the main causes of this are the Meddy interaction with ambient currents or the development of  $\beta$ -gyres [Morel (1995)]. Meddies are long-lived structures (lifetime exceeding 1 year) and, since every single eddy can carry up to  $10^{11}$  tons of salt of Mediterranean origin [Bashmachnikov

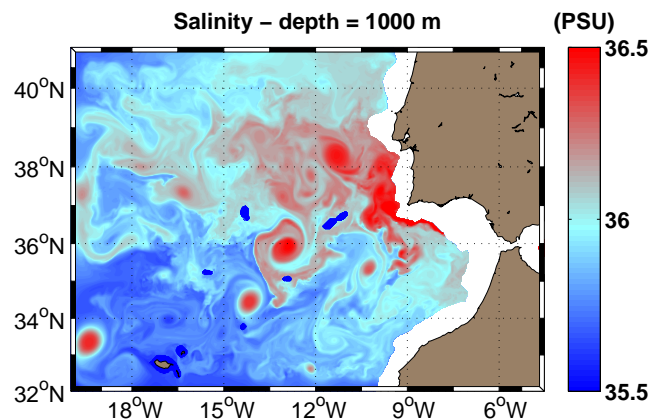


**Figure 1.1:** *Salinity snapshot of the Mediterranean Outflow with Meddies detachment (numerically modeled), adapted after Barbosa Aguiar et al. (2013). Meddies are given by the submesoscale and mesoscale high salinity circular patches in the domain.*

et al. (2015)], they have a relevant impact on the three-dimensional distribution of tracers in the Atlantic Ocean.

Moreover, the exchanges between the Mediterranean Sea and the Atlantic Ocean take place at different levels. Ambar (1983) and Pingree and Morrison (1973) showed that three main branches can be observed and that they are distributed within the first 1000 m of the water column. Each of these branches can become unstable and eventually eject eddies. Pingree and Le Cann (1993a) found evidence of a Shallow-Meddy (Smeddy) at a depth of about 700 m, swirling at about 0.2 m/s. The thickness of its main core, as shown by vertical sections of the density field, did not exceed 400 m and its radius was estimated to be between 30 and 40 km.

### 1.2.2 Thermocline Eddies in the Atlantic Ocean

During the *Tourbillon Experiment* [Arhan et al. (1983), Arhan and De Verdière (1985)], whose aim was to characterize typical mesoscale eddies in the Atlantic, an anticyclonic eddy was detected at approximately 14.5°W and 47°N by means of *in-situ* observations. The data revealed an anticyclonic eddy of radius 50 to 70

km, spinning at a maximum speed of 30 cm/s and intensified at 500 m depth. Its velocity field decreased rapidly through the main thermocline and more gradually up to the surface but its signatures were evident at all depths between the surface and 4000 m. The eddy was also able to trap fragments of Mediterranean Water that were found to circulate anticyclonically around it, acting like a passive tracer.

### 1.2.3 Cuddies

In the Eastern Pacific, the Californian Undercurrent generates subsurface vortices with characteristics similar to Meddies. Such vortices, named Cuddies (Californian Undercurrent Eddies), are mainly formed along the Californian continental shelf (between approximately 123°W to 124°W and 33°N to 42°N) and are involved in the transport of nearshore waters from the coastal zone into the interior of the Northeastern Pacific. Recently, they have been observed and characterized using RAFOS floats deployed at depths between 300 and 1000 m [Collins et al. (2013)]. These subsurface eddies can swirl at velocities between 5 to 20 cm/s, have mean radii of 10 to 100 km and are intensified at depths that range from 100 to 1000 m. Like Meddies, they are long-lived structures, with observed lifetimes that can exceed 1 year.

### 1.2.4 Peddies and Reddies

Peddies and Reddies (respectively, Persian and Red Sea Water eddies) are other examples of subsurface vortices generated by the interaction between marginal seas and the open ocean, in particular from water masses exchanges between the Northern Indian Ocean and both the Persian Gulf and Red Sea [Shapiro and Meschanov (1991), Senjyu et al. (1998), Meschanov and Shapiro (1998)]. Such hydrological features have mostly been studied via *in-situ* measurements, and are given by lens-shaped warm and salty anomalies (compared to the background ocean) in the Arabian Sea.

Reddies result from the instability of the Red Sea outflow, which exits through Bab el Mandeb. The Red Sea Water outflow into the Indian Ocean has been studied by Shapiro and Meschanov (1991), who, using about 40 years of hydrographic data from the National Oceanographic Data Center, determined the main branches of the outflow and the position of some associated subsurface lenses (see figure 1.2).

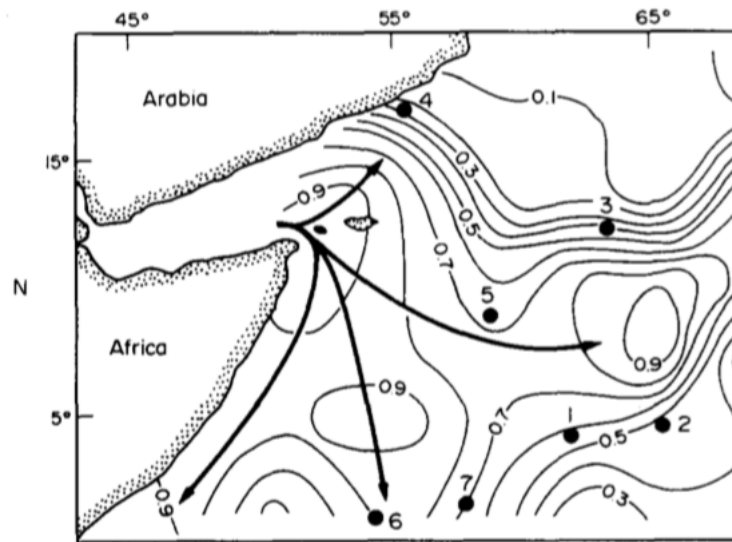


**Figure 1.2:** *Branches of the Red Sea water outflow (solid lines) and positions of some REDDIES in the Indian Ocean (black circles), after Shapiro and Meschanov (1991).*

In the figure, solid lines indicate the branches of the Red Sea water outflow, while the black dots indicate the positions of some observed Reddies. Such eddies are mostly found at depths of 400 to 800 m, their radii range from 20 to 50 km and their thicknesses are around 400-500 m. Occurrences of submesoscale Reddies are also possible. Fedorov and Meschanov (1988), found a 10 km wide and 80 m thick Red Sea water lens at a depth of about 300 m in the Gulf of Aden.

Peddies are salty and warm lens-shaped anomalies resulting from the instability of Persian Gulf Water outflow in the Gulf of Oman. The precise instability mechanism is not well known, but Carton et al. (2012) have shown that remotely formed surface eddies were able to tear fragments from the Persian Gulf outflow. Similarly, Vic et al. (2015) pointed out that the surface eddies can participate to the generation of Peddies via interactions with topography. Senjyu et al. (1998) observed a lens at a depth of about 300 m, with a 25 km radius and a vertical scale of 150 m. Persian Gulf water can also generate subsurface small-scale eddies (observed during PHYSINDIEN-2011 experiment), as previously mentioned.

### 1.2.5 Swoddies

These subsurface-intensified vortices originate from the poleward Iberian slope current. This current flows along the Iberian Peninsula and enters the Bay of Biscay at depths between 100 and 200 m [Pingree and Le Cann (1992), Carton (2001), Le Cann and Serpette (2009)]. This current extends northward mostly in winter, and, due to interaction with several capes and canyons, can become unstable. The result of this process is the formation of subsurface eddies called Slope Water

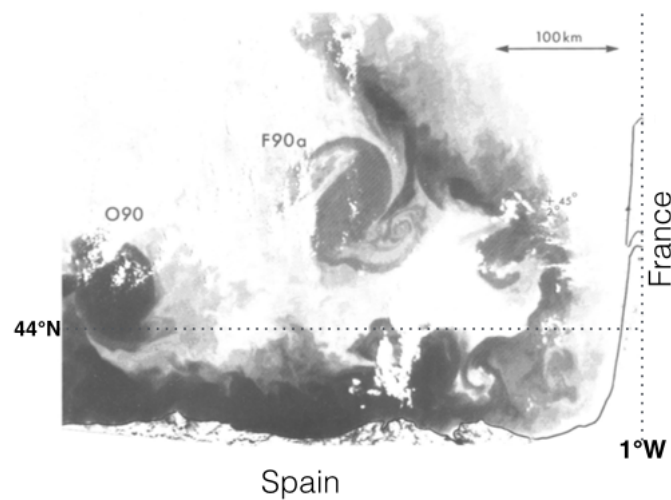


**Figure 1.3:** Thermal band satellite image of a Swoddy (F90a) in the Bay of Biscay, adapted after Pingree and Le Cann (1992).

oceanic eddies. They have lifetimes of about one year, and can drift southwestward at velocities larger than 1 cm/s. They are lenticular warm water anomalies of 35 to 50 km in radius, swirl velocities up to 0.3 m/s and they are generally intensified at depths between 70 and 300 m. Using sea-surface temperature observations from the NOAA-10 and 11 satellites, Pingree and Le Cann (1992) found evidence of a Swoddy in the Bay of Biscay, in the form of an anticyclonically rotating tripole, as shown in figure 1.3.

### 1.2.6 Leddies

Leddies (Levantine intermediate water eddies) are observed in the Mediterranean Sea; they are fragments of detached Levantine Intermediate Water (LIW), which

is generated in the eastern Mediterranean Sea and flows across the whole basin up to the Strait of Gibraltar. In the western Mediterranean, this current is generally characterized by a positive temperature and salinity anomaly found between 200 and 1000 m below the sea-surface [Millot (1999)]. A cartoon showing the LIW circulation and some associated eddy-like features in the western Mediterranean is provided by Millot (1999), (see Figure 1.4). Subsurface vortices detaching from the LIW can have radii between 25-50 km. Testor and Gascard (2003) found evidence of a Ledy off southern Sardinia, in 1997. Its radius was about 25 km, its orbital velocity was around 0.15 m/s, the estimated lifetime was of about half a year. Recently, Bosse et al. (2015), combining CTD, Argo floats and Gliders observations, identified several Leddies off the Corsica western coasts. They had mean radii around 5 km and swirl velocities rarely exceeding 0.1 m/s. Such eddies were mostly intensified at depths around 500 m and extended vertically several hundred meters.

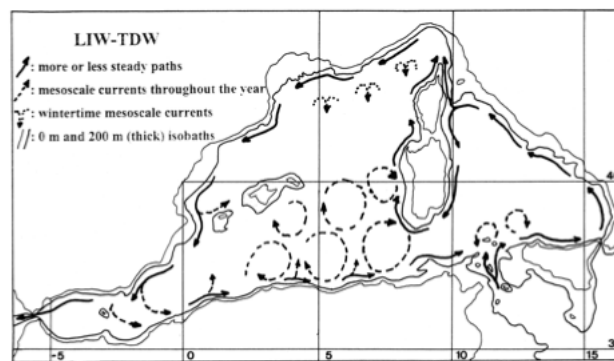


**Figure 1.4:** *Circulation of Levantine Intermediate Water in the western Mediterranean [Millot (1999)].*

### 1.2.7 Mode Water Eddies

Mode Waters in the Sargasso Sea, resulting from deep convection during winter, are also sources of subsurface anticyclones for the Atlantic Ocean. Such eddies are generally referred to as Mode water eddies [Brundage and Dugan (1986), Sweeney et al. (2003a)]. They can carry water masses of the Sargasso Sea towards the south, hence, towards more stratified environments, if compared to their origination areas.

This dynamics makes them long-lived structures (lifetimes exceeding 1 year), and it favors their anticyclonic rotation. These eddies can span from submesoscale to mesoscale. In the first case, they have been defined as Submesoscale Coherent Vortices [McWilliams (1985)], and their radii can go down to 5 km. At mesoscale, they are characterized by radii around 75 to 100 km (see e.g. figure 1.5), and they are mostly found at depths of 1000 m below the sea-surface.

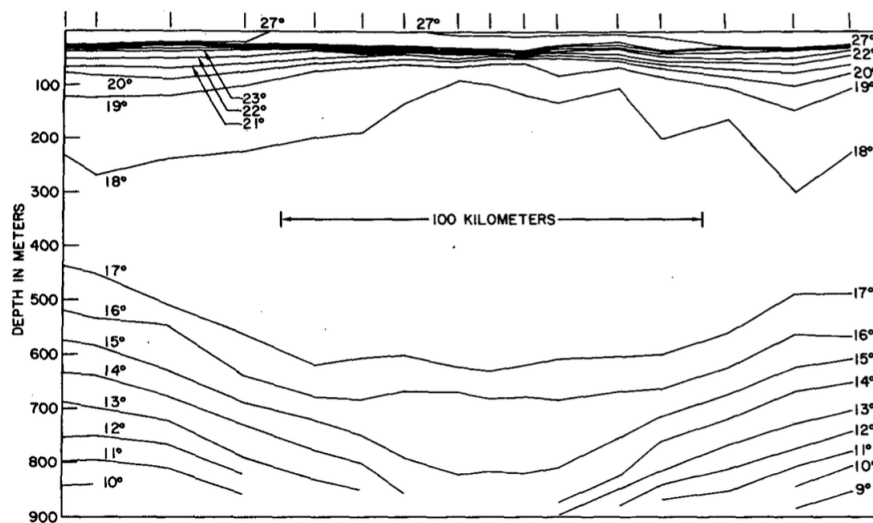


**Figure 1.5:** Isotherm section across a mesoscale Mode Water Eddy, after Brundage and Dugan (1986).

### 1.2.8 Japan Intrathermocline Eddies (ITE)

In the East Japan Sea, subsurface eddies can be generated by mixing in the upper thermocline during winter. Hydrological surveys evidenced the existence of subsurface mesoscale lenses off the western Honshu coast [Gordon et al. (2002)]. They are mostly intensified at depths around 100 m and they are characterized by doming isopycnals in the upper thermocline, while an isopycnal depression is observed below the main core. Such eddies can have radii around 50 km and vertical extents up to 500 m. Inside the ITE cores, the observed geostrophic swirl velocities are around 0.3 to 0.4 m/s.

## 1.3 Surface signature of oceanic eddies

Oceanic vortices can generally be recognized by means of their signature at the sea-surface, superimposed on that of the mean circulation. Their recirculating character often generates monopolar, dipolar or sinusoidal patches in altimetric, visible and thermal-band satellite imagery; this is mainly due to the advection of temperature, salt and nutrients. The surface expression of eddies can derive from both surface-intensified and subsurface-intensified recirculating structures. In the following section we review some of the past and recent studies on the surface expression of oceanic eddies.

### 1.3.1 Surface signature of surface-intensified vortices

Sweeney et al. (2003a) state that, on average, surface-intensified cyclones can be identified as cold and ring-shaped sea-surface temperature anomalies. Indeed, surface cyclones rise isopycnals and lower the sea-surface elevation, due to the higher density of the water circulating within them. For surface-intensified anticyclones, the behavior is the opposite, see also figure 1.6.

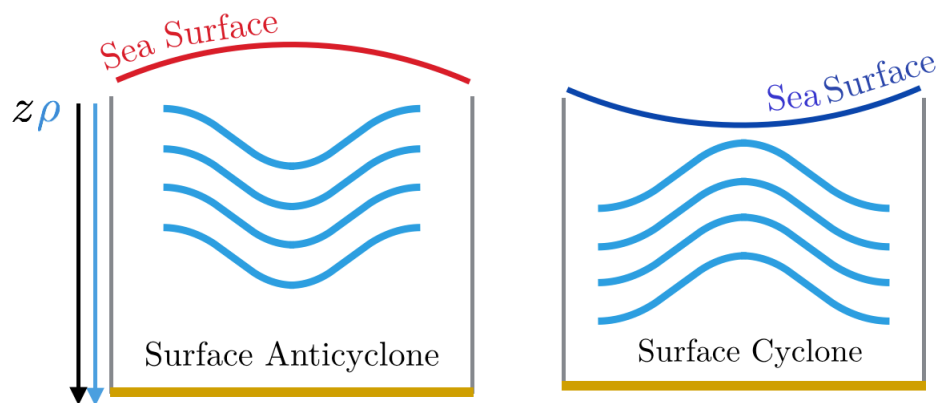


**Figure 1.6:** *Isopycnal structure of surface-intensified cyclones and anticyclones, adapted after Sweeney et al. (2003a). The red and blue colors stand for positive and negative sea-surface temperature anomalies.*

Among surface-intensified vortices, those associated to the major oceanic currents (Gulf-Stream, the North Brazil Current, the Agulhas current, the Kuroshio Current, the East Australian Current and the Antarctic Circumpolar Current) have

been thoroughly characterized. In general, they are long-lived structures with radii in the mesoscale range, i.e., compatible with present-day satellite and *in-situ* observations resolutions. In what follows, we present a brief review of the surface-intensified eddies associated to the major currents, also giving some elements about their signature at the sea-surface:

- the Gulf-Stream is a western boundary current generated at subtropical latitudes (Mexican Gulf) and flowing northeastward along North-American continental slope, and then detaching from it. North of this current, warm-core anticyclonic eddies with radii between 50-100 km are generally found. Their vertical extent can reach 1500 m. South of the Gulf-Stream's main path, occurrences of cyclonic cold-core eddies are also possible. Such eddies can have larger radii and vertical extent, if compared to the warm ones [Carton (2001)];
- the North-Brazil Current, originated at approximately 10°S and 31°W by the splitting of the South Equatorial Current, experiences a northeastward retroflection (near 7°N). Anticyclones can be formed as consequent detachment of the retroflection meander. Richardson et al. (1994) found evidence of several recirculating features with surface radii up to 200 km, vertical extents of about 1000 m and swirling at speeds up to 0.8 m/s;
- another major retroflecting current is the Agulhas Current. It is a western boundary current of the south-western Indian Ocean and it flows down the east coast of Africa from 27°S to 40°S. The interaction with the Antarctic Circumpolar Current causes retroflection (between 20°E and 16°E ), making its propagation mainly eastward. The retroflection area, as for the Brazilian Current, is a source of eddies. Colton and Chase (1983) and Lutjeharms and Ballegooyen (1988) could find evidence of such eddies (also known as Agulhas Rings) in the retroflection area. They are warm-core anticyclonic structures, their radii can reach 300 km and the swirl velocities can reach 1 m/s. The lifetime of the Agulhas rings can exceed two years in some cases;
- the Kuroshio Extension (KE) is a western boundary current generated from an extension of the subtropical gyre in the North Pacific Ocean. According to Niiler et al. (2003), warm-core eddies are mostly found to the north of the

KE jet, while the cold-core ones are found to the south, both of them being generated by meanders of the KE jet. Ebuchi and Hanawa (2001) assert that these eddies can have swirl velocities around 0.2 m/s and are mostly in the mesoscale range (around 100 km in diameter);

- the East Australian Current is a western boundary system flowing southward in the south-western Pacific, off eastern Australia. Nilsson and Cresswell (1980) showed that, poleward meanders of this current, can generate warm-core anticyclonic eddies. Their radii can be around 200 km and the swirl velocities can reach 1 m/s;
- Frenger et al. (2013), investigating the mesoscale eddy activity in the Antarctic Circumpolar Current, related the presence of mesoscale surface oceanic vortices to the behavior of the atmospheric boundary layer. They used around 600000 snapshots of mesoscale eddies detected by means of satellite measurements. On average, anticyclonic eddies were associated to positive sea surface temperature (SST) anomalies, and vice versa for the cyclonic case. These anomalies are in the form of sinusoidal distortions of the pre-existing temperature gradient field and, on average, they can reach values of  $\pm 0.5^{\circ}\text{C}$  for the anticyclonic and cyclonic case, respectively (see e.g. figure 1.7-a). Furthermore, the presence of such surface eddies influences the lower atmosphere, triggering monopolar surface wind-speed anomalies of the order of  $\pm 0.1\text{-}0.2$  m/s (averaged value, figure 1.7-b) and anomalies in the cloud fraction of  $\pm 2\%$  in the anticyclonic and cyclonic case, respectively (figure 1.7-c).

Moreover, Chelton et al. (2011), using sixteen years of satellite altimetric observations, pointed out that mesoscale surface-intensified eddies are not only generated in the aforementioned areas. According to their study, the whole ocean, via baroclinic instability, can be a source of eddies, except for two areas classified as "eddy-deserts" (centered at about  $27^{\circ}\text{N}$  to  $40^{\circ}\text{W}$  and  $50^{\circ}\text{S}$  to  $95^{\circ}\text{W}$ ). The main features of surface mesoscale eddies, at global scale, are listed below:

- 60% of the mesoscale eddies induce monopolar positive anomalies in the elevation of the sea-surface. Such anomalies can be higher than 5 cm, and 25% of them have values between 10 and 30 cm. In particular, the cross

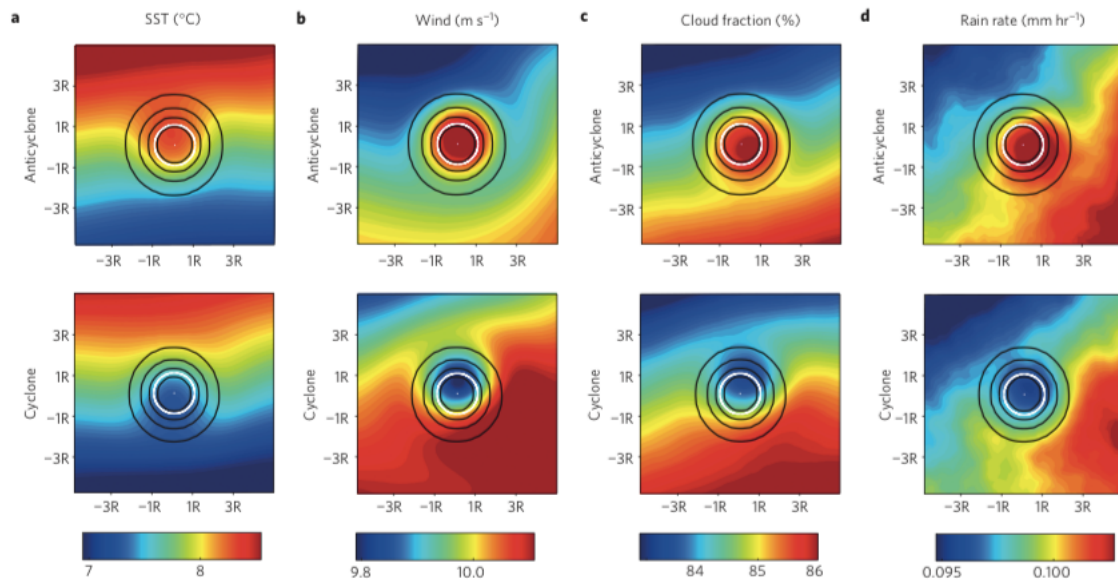


**Figure 1.7:** *Surface signature of mesoscale surface-intensified vortices, after Frenger et al. (2013).*

section of the monopolar signatures can be approximated by a Gaussian function for  $2/3$  of the eddy radius;

- the preferential polarity for mesoscale eddies is cyclonic, even though the longest-lived ones are anticyclones;
- more than 90% of the eddies have horizontal scales between 100 and 300 km;
- 50% of the eddies are characterized by swirl velocities between 0.1 and 0.2 m/s, while only 5% were found to swirl at 0.4 m/s or more;
- the estimated Rossby number for global eddies is around 0.05 in 82% of the observed cases, making quasi-geostrophic approximation a proper tool of investigation;
- almost the totality of the eddies is non linear, i.e., the ratio between their rotational and translational speed is larger than 1. A consequence of this behavior is a non-negligible impact on horizontal distribution of active and passive tracers;

To reinforce the last point, we cite the work of McGillicuddy et al. (1999). The authors, using both models and observations, could conclude that mesoscale eddy dynamics can influence the upper ocean biogeochemistry. In fact, the vertical isopycnal displacement induced by cyclonic eddies causes injection of nutrients in the near-surface waters. The upward nutrient injection was also confirmed by the distribution of phytoplankton biomass, spatially correlated with the nutrient enhancement areas. The authors, in attempting to characterize SSH and chlorophyll (CHL) anomalies in the south-eastern Pacific Ocean, could find that the CHL westward transport, generally attributed to propagation of Rossby Waves, is indeed operated by mesoscale eddies. Ten years of observations of SSH and CHL fields made it possible to track mesoscale eddies between  $130^{\circ}\text{W}$ - $80^{\circ}\text{W}$  and  $22^{\circ}\text{S}$ - $18^{\circ}\text{S}$ , leading to the following conclusions:

- the eddy-induced anomaly on the CHL tracer is dipolar;
- this structure is due to the redistribution of chlorophyll due to the eddy velocity field;

On average, a clockwise rotating eddy living in a northward CHL gradient, will generate a dipolar anomaly in which the positive pole is located in the trailing half of the eddy itself. For clockwise eddies tracked in the  $130^{\circ}\text{W}$ - $80^{\circ}\text{W}$  and  $22^{\circ}\text{S}$ - $18^{\circ}\text{S}$  (using ten years of observations), the eddy velocity field was found to bring high concentrations of CHL southward (taking advantage of the southward velocity component of its trailing half) and vice versa.

### 1.3.2 Surface signature of subsurface-intensified vortices

Subsurface-intensified vortices can also affect the ocean surface. Sweeney et al. (2003a) proposed an idealized model for interpreting the surface signature of Mode Water Eddies in the Sargasso Sea (see section 1.2.7). For these eddies, the density structure is given by a double concave lens locally rising the near-surface isopycnals and pushing down the lower ones. In the upper ocean, the isopycnal displacement will then be the same given by surface-intensified cyclones (see figure 1.6 and figure 1.8). This structure will cause upwelling and would most likely generate a negative temperature anomaly at the sea-surface.

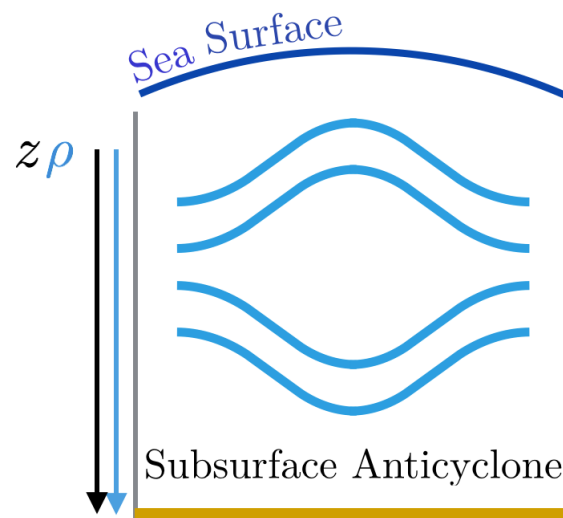


**Figure 1.8:** *Isopycnal structure of subsurface-intensified anticyclones, adapted after Sweeney et al. (2003a). The blue colors at the sea-surface indicates a negative temperature anomaly.*

Pingree and Le Cann (1992), using both satellite and *in-situ* observations, showed that subsurface-intensified anticyclones in the Bay of Biscay (Swoddies) can have a signature in thermal-band satellite imagery, which one can recognize as cold spots in sea-surface temperature.

Stammer et al. (1991), combining altimetric observations (Geosat) and *in-situ* data, proved that Meddies can be detected and tracked by satellite altimetry. Encouraged by previous results, stating that Meddies can bias the surface circulation up to 5 cm/s (see e.g. Kase et al. (1989)), they compared two years of Geosat altimetric observations with an hydrographic-derived altimetry map. Hydrographic data consisted of dynamic topography obtained via CTD measurements in the area 20°W-10°W and 30°N-50°N. In this area, using satellite altimetry, four positive sea-surface height (SSH) anomalies were found in correspondence of salinity and temperature anomalies at depth (Meddies). The study showed that satellite-derived anomalies were in agreement with the ones obtained via *in-situ* measurements, confirming that the surface signatures of subsurface anticyclones (i.e., Meddies) are given by positive anomalies in SSH fields.

Bashmachnikov and Carton (2012), taking advantage of the quasi-geostrophic theory, combining *in-situ* and altimetric observations, characterized the surface signature of Meddies in the Atlantic Ocean. The theoretical approach consisted in modeling the Meddies as step-like potential vorticity anomalies, successively reduced to point vortex potential vorticity distributions. This technique lead to an analytical determination of the sea-surface elevation above an underlying Meddy. Its expression is given by equation 1.12,

$$SSH_{anom} \propto \frac{|q|R^3}{NH} \quad (1.12)$$

where  $q$  is the potential vorticity of the eddy,  $R$  is its radius,  $N$  is the Brunt-Väisälä frequency in the upper ocean and  $H$  is the depth of the eddy core (along the water column). Equation 1.12 shows that the SSH anomaly above the Meddy is proportional to the eddy potential vorticity, to its cubic radius, inversely proportional to its depth and to the upper ocean stratification. The Meddy's signature consists of a positive monopolar anomaly (whose intensity can go up to 15 cm for larger Meddies) and it is associated to a surface anticyclonic circulation.

We recall that AVISO maps allow identification of a mesoscale feature only if it is larger than 4 cm and if it does not entirely lie between the satellite ground-tracks. The detection threshold can go down to 2 cm for altimetric features laying on the ground track [Fu and Cazenave (2000)]. Bashmachnikov and Carton (2012) state that, for climatological stratifications in the Eastern North Atlantic, Meddies with radii of 10 km could never be detectable in AVISO gridded products. This is illustrated by Figure 1.9-a-b, showing the latitude under which Meddy detection (by means of AVISO maps) is not achievable. In particular, the information is shown in a  $[H, R]$  diagram, where  $H$  is the Meddy depth and  $R$  its radius. The diagrams in (a) and (b) correspond to a threshold of 4 cm and 2 cm, respectively.

Bashmachnikov et al. (2013) further investigated the Meddies' surface signature, looking for signals in both altimetry and the thermal band satellite observations. Their work suggested that the surface signature of a Meddy is given by a positive SSH anomaly (corresponding to a negative anomaly in surface relative vorticity) and by a cold-core anticyclonic rotating anomaly (opposite to typical SST anomalies of surface-intensified anticyclones [Sweeney et al. (2003a), Chelton et al. (2011)]). The cold-core associated to the anticyclonic rotation results from

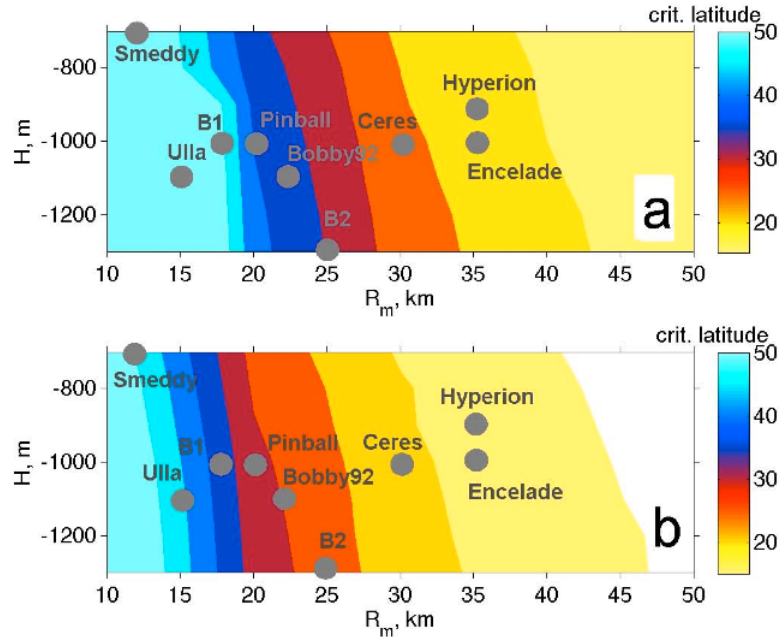


**Figure 1.9:** Critical latitudes for Meddy detection with AVISO products in a  $[H, R]$  diagram ( $H$ =Meddy Depth and  $R$ =Meddy Radius). (a) Altimetric threshold of 4 cm, (b) altimetric threshold of 2 cm, after Bashmachnikov and Carton (2012).

two main effects:

1. uplifting of isopycnal levels induced by the vertical density structure of the Meddy, given by a double-convex lens superimposed on the local rest stratification;
2. entrainment of cold water in the surroundings of the Meddy surface signature. This effect can induce intensification of anticyclonic circulation, with consequent intensification of surface water convergence and positive feedback on the original SST anomaly.

This is summarized by Figure 1.10 and Figure 1.11.

Very recently, Assassi et al. (2016) investigated the surface-signature of both surface and subsurface-intensified vortices in the proximity of the Peru-Chile upwelling system. Taking advantage of a realistic numerical simulation they found that, focusing on mesoscale eddies generating sea-level anomalies larger than  $\pm 2$  cm, it

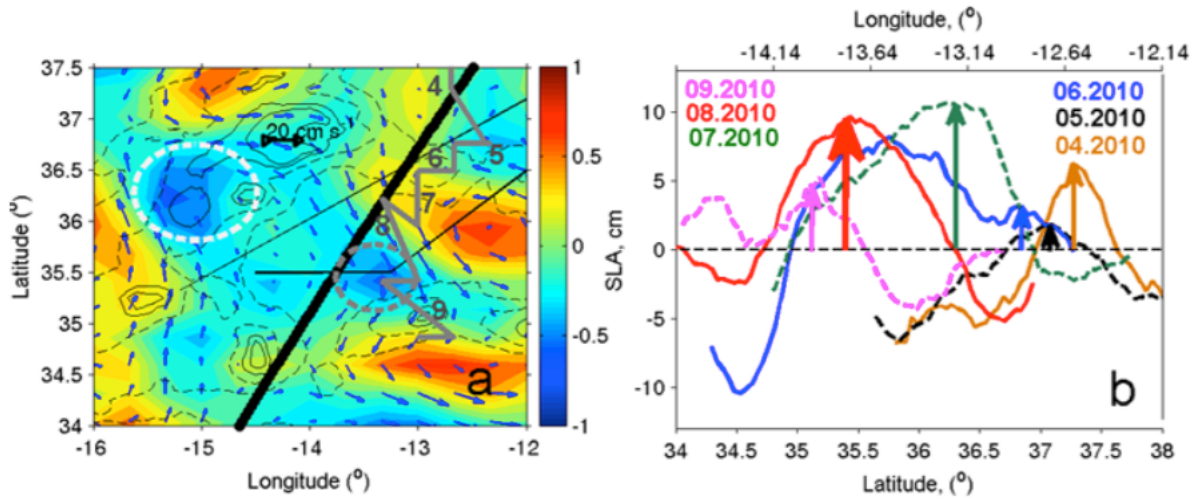


**Figure 1.10:** a) Relative vorticity ( $10^{-5}s^{-1}$ ) and geostrophic currents in presence of a Meddy (dashed grey circle). The thick grey line marks the Meddy trajectory. b) Satellite-derived sea level anomaly (from satellite Jason-1). The arrows indicate the Meddy position at depth, after Bashmachnikov et al. (2013).

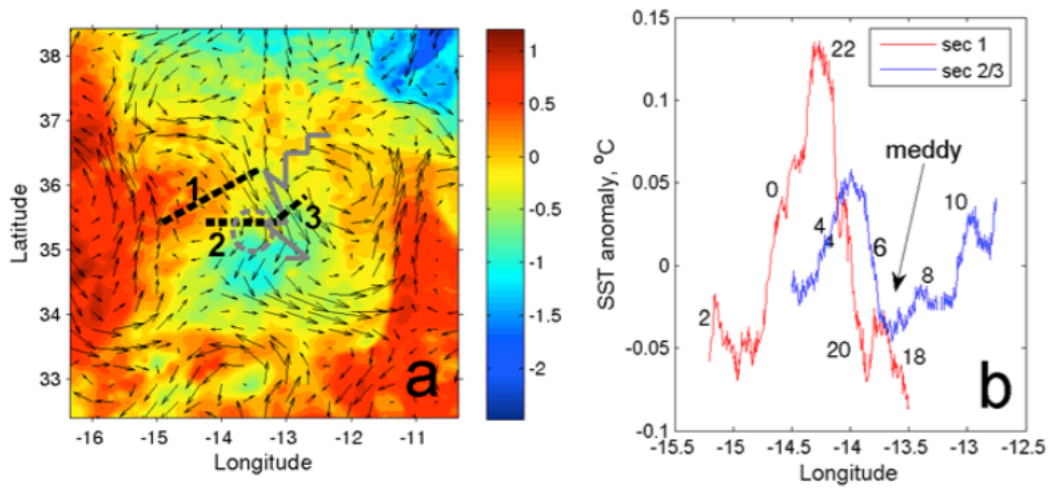


**Figure 1.11:** a), Snapshot of AVHRR-derived SST anomalies ( $^{\circ}C$ ) in presence of a Meddy, (dashed grey circle). The thick grey line marks the Meddy trajectory; (b) in-situ-derived temperature anomalies (ADCP) along the transects 1 and 2-3, shown in (a), after Bashmachnikov et al. (2013).

is possible to detect subsurface vortices from observation of the sea-surface (combining sea-surface density and sea-surface height). Indeed, most of the subsurface vortices (intensified at depths seldom exceeding some hundred meters) were found to generate surface signatures in agreement with the models illustrated in figures 1.6 and 1.8.

Despite the review presented in this section, further comments on the sea-surface temperature anomalies in presence of subsurface anticyclones are necessary.

Anticyclones living at intrathermocline depths, in the north-eastern Atlantic, often contain anomalously warm and salty water. In the early stages of their life-cycle, their surface thermal signature can be given by warm anomalies (see e.g. the case of Swoddies in figure 1.3). The generation of a cold anomaly can be a result of the vortex evolution, as also shown by Pingree and Le Cann (1992) and can strongly depend on the local temperature gradients at the sea-surface. This means that occurrences of warm sea-surface temperature anomalies in presence of an underlying anticyclone are possible (as also shown by Oliveira et al. (2000) for the case of Meddies). With this comment, we just wish to point out that the physical considerations about the surface signature of subsurface anticyclones, summarized by figure 1.8, describe a scenario that can change in presence of intense surface turbulence or even atmospheric forcings. Further analyses on this topic have been carried out and will be presented in chapter 5.

## 1.4 Summary

The geophysical context presented in this chapter can be summarized by the following highlights:

- oceanic vortices are carriers of heat, salt and nutrients, hence, they influence the three-dimensional distribution of tracers in the ocean. A synoptic knowledge of their positions and mean pathways can help evaluating the oceanic tracer budgets at global scale;
- surface and subsurface-intensified eddies can locally modify the sea-surface properties generating monopolar, sinusoidal and dipolar anomalies in SSH-SST and surface-nutrients distributions. We wonder to which extent these

signatures can be used as a proof of the existence of subsurface-intensified eddies, with the aim to track them via satellite observations;

- present-day theoretical studies on three-dimensional reconstruction of ocean dynamics (based on the SQG theory) state that there is a class of motions that cannot yet be captured by observations of the sea-surface. In particular, all the motions intensified at depths around 1000 m cannot be correctly reconstructed;
- a future satellite mission (SWOT [Fu et al. (2009)]) will provide two-dimensional and high precision altimetric observations of the sea-surface. The measurement precision of the SWOT observations will be around 2 cm at global scale, which is only achieved for along-track data by present-day altimetry. This encouraged us to further investigate the surface expression of subsurface anticyclones, mainly in the elevation of the oceanic free-surface;
- the tracking of subsurface eddies could possibly rely on a synergy between sea-surface height, temperature and salinity observations. Despite this, for structures intensified at depths of 1000 m or more, SST signatures can be significantly affected by atmospheric forcing or by surface turbulence (if compared to the ones associated to mesoscale surface-intensified vortices).

## Chapter 2

# Main objectives and structure of the manuscript

In this chapter, we give an overall description of the main topics treated throughout the manuscript. In addition, we will briefly introduce some elements on the materials and methods used in our studies. In all the chapters that follow, a thorough description of the methods will be given in more details, in relation to the specific matter of investigation.

This manuscript is organized as follows. In **chapter 3**, the surface signature of subsurface anticyclonic eddies will be investigated in the perspective of a purely altimetric detection. The SSH anomalies induced by *a-priori* known subsurface eddies will be studied by means of analytical and numerical models. The analytical models will be developed in the context of the quasi-geostrophic (QG) theory and will deal with eddies reduced to point-vortex structures embedded in an oceanic basin at rest. Such an approach, provided the approximation of dealing with infinite oceanic basins, will allow us to derive analytically the vortex-induced three-dimensional stream function. Its value at the sea-surface, in a QG context, will be proportional to the surface signature of the eddy in the SSH fields. On the other hand, the numerical experiments will be based on both QG and primitive equations (PE) models. The QG model is the Combined Lagrangian Advection Method, CLAM-3DQG [<http://www-vortex.mcs.st-and.ac.uk/~dgd/FIBOSI>]. The model solves the coupled QG-SQG equations (where SQG stands for surface quasi-geostrophy [Lapeyre and Klein (2006)]) in the spectral space and allows

---

the retrieval of the three-dimensional stream function via Fourier's transform on the horizontal and via 4th-order compact-difference solution in the vertical. The PE model is the Regional Oceanic Modeling System, ROMS [Shchepetkin and McWilliams (2005)]. ROMS is a free-surface, split-explicit and terrain-following model that solves the full set of Navier-Stokes equations in the hydrostatic and Boussinesq approximation. For the specific studies illustrated in chapter 3, ROMS will be used in idealized configuration, in the absence of bottom topography and in both the  $f$ -plane and  $\beta$ -plane approximations.

The experiments based on the QG and the PE models, will consist in the introduction of subsurface anticyclones (of predefined structure) in an oceanic basin at rest and to observe the response of the surface oceanic layer (in SSH) to the evolution of the subsurface eddy. The intensities and shapes of the eddy-induced SSH anomalies will be studied as a function of the vortex characteristics, like its radius, swirl velocity, vertical extent and depth. The possibility of varying the vortex structure will also allow to study a large variety of subsurface anticyclones, like the ones we have reviewed throughout chapter 1.

We go on studying the life cycle of subsurface anticyclonic eddies, focusing on a particular aspect: the merger with nearby subsurface anticyclones. This phenomenon is very common in the global ocean and, for the specific case of Meddies, proved to be the main mechanism through which such eddies grow in radius as they drift off the Iberian Coast [Bashmachnikov et al. (2015)]. In our case, the study will be conducted in a numerical and idealized context, taking advantage of the ROMS model. The simulations will be run in a flat-bottomed oceanic basin and in the  $f$ -plane approximation.

This study will focus on both mesoscale eddies with characteristics similar to Meddies and smaller-scale Peddies, like the one described in L'Hégaret (2015). In particular, we will determine the critical conditions for the merging process to take place as well as the consequences of merger on the structure of the vortex. Indeed, merger, modifying the eddy's initial structure, is among the factors that can positively influence the surface expression of subsurface anticyclones. The results of this study are described in **chapter 4**.

**Chapter 5** will bring the investigations of chapter 3 and 4 towards a more realistic context. Indeed, the surface signature of Meddies will be studied in a long term ( $\simeq 20$  years) realistic numerical simulation. Such simulation, initially

---

built to determine a census of Meddies' characteristics in the Atlantic Ocean [Barbosa Aguiar et al. (2013)], is based on the PE model ROMS, in a realistic configuration. The modeled oceanic region is the north-eastern Atlantic Ocean, off the Iberian Coasts ( $4.5^{\circ}\text{W}$  to  $20^{\circ}\text{W}$  and  $32^{\circ}\text{N}$  to  $41^{\circ}\text{N}$ ), where Meddies are abundant (see e.g. Bower et al. (1997) and Richardson et al. (2000a)). The model was run for 24 years (with a four years spin-up time) and a climatological atmospheric forcing was applied (COADS monthly climatologies [Da Silva et al. (1994)]). The use of this model will allow the simultaneous in-depth analysis of the Meddies characteristics, the ones of the background ocean and of the sea-surface. The occurrences of Meddy merger, as well as the eddy interactions with bottom oceanic topography and surface intensified structures (like eddies and fronts), will be observed and will be related to the evolution of the eddy surface signature. In this context, the Meddies' surface expression will be studied in SSH, SST and SSS fields. This will allow to evaluate the contribution of a synergy between different satellite observations for the detection of subsurface eddies in the Atlantic Ocean.

Finally, the main conclusions and perspectives of the studies presented in this manuscript will be illustrated in **chapter 6**.

# Chapter 3

## Influence of deep vortices on the ocean surface

This chapter is inspired by the paper

*Influence of deep vortices on the ocean surface*, by

Daniele Ciani<sup>1</sup>, Xavier Carton<sup>1</sup>, Igor Bashmachnikov<sup>2</sup>, Bertrand Chapron<sup>3</sup> & Xavier Perrot<sup>4</sup>

1: Laboratoire de Physique des Océans, UMR6523, Université de Bretagne Occidentale, Brest, France

2: Marine and Environmental Sciences Center (MARE), Faculdade de Ciências, Universidade de Lisboa, Lisbon, Portugal

3: Laboratoire d'Océanographie Spatiale, Ifremer, Centre de Brest, Plouzané, France

4: Laboratoire de Météorologie Dynamique, Ecole Normale Supérieure, Paris, France

published in the Journal of Discontinuity, Non-Linearity, and Complexity

2015 - 4(3) 281-311

[Most of section 3.4.6 was not in the original paper]

## 3.1 Introduction

The oceanic motions at mesoscale are characterized by horizontal scales ranging from 20 to 200 km and time scales ranging from a few days to a few weeks. The expression of this dynamics is mostly given by gyres, vortices (eddies), meanders of unstable currents and other turbulent features. Mesoscale motions are long-lived, contain more than 80% of the ocean eddy kinetic energy and are globally more energetic than the general circulation. Hence, their impact on transport of heat and salt in the global ocean is relevant. For example, vortices are recirculating features which trap water masses from their origination areas and carry them over large distances across the ocean [Quadfasel and Baudner (1993), Drillet et al. (2005)].

Observations of the ocean show that mesoscale features do not exhaustively describe the ocean dynamics. This is also suggested by modeling experiments, in which the modeled eddy kinetic energy increases as the model horizontal spatial resolution increases [Capet et al. (2008)]. Indeed, a finer spatial resolution allows one to take into account submesoscale features and to see that they significantly contribute to the ocean energy budget and circulation. Submesoscale structures have horizontal scales between 0.5 and 20 km and time scales from a few hours to a few days. Physically, they are given by small vortices, filaments or turbulent patches, and they can result from hydrodynamic instabilities and from the straining and shearing of pre-existing mesoscale structures.

The ocean is highly populated by mesoscale and submesoscale vortices at depths ranging from 0 to 1000 m. For instance, *deep vortices* are the ones living at depths between 100 and 1000 m. Occurrences of these structures have been documented by observations and numerical models and show that deep vortices can be observed in the Atlantic, Indian Ocean as well as the Mediterranean Sea. They can result from mixing processes, or from the exchanges between semi-closed highly evaporative basins and the open ocean, which can take place at different levels [Pingree and Morrison (1973)]. The first mechanism explains the existence of subsurface EDDIES in the North-Western Atlantic Ocean [Sweeney et al. (2003b), McWilliams (1985), Carton (2001)], while the second one generates Mediterranean Water Eddies (MEDDIES) off of Gibraltar Strait [Richardson et al. (2000a), Bower et al. (1997), Pingree and Le Cann (1993b)], REDDIES from the Red Sea outflow and PEDDIES from the Persian Gulf outflow (REDDIES=Red Sea Water EDDIES, PEDDIES=Persian Gulf Water EDDIES). These last two types of eddies evolve in the NW Indian Ocean, [Senjyu et al. (1998), Shapiro and Meschanov (1991)]. Ocean currents can also generate vortices while flowing down a sloping topography, or by sinking processes due to their density anomaly with respect to the background

environment. These last two mechanisms constitute the generation processes for Slope Water Eddies (SWODDIES) in the Bay of Biscay and for Levantine Intermediate Water Eddies (LEDDIES) in the western Mediterranean Sea [Milot (1999)], respectively.

In general, vortices living in proximity of the sea-surface and characterized by mesoscale horizontal scales, have a recognizable and largely investigated signature on remotely sensed oceanic fields, [Frenger et al. (2013), Chelton et al. (2011)]. Such fields are given by satellite-derived Sea-Surface Temperature (SST) and Sea-Surface Height (SSH), the latter expressing the sea-surface elevation induced by dynamical structures. Vortices signature on the ocean surface is the key for their detection and tracking, which is essential to estimate the eddy influence on oceanic energy, heat and salinity budgets.

The smaller the vortex horizontal scale and the larger its depth, the harder becomes its detection. In fact, the surface-induced signal increasingly weakens and it is difficult to isolate it from the background surface dynamics. In recent years, several works have attempted to infer subsurface dynamics from observations of the sea-surface. Lapeyre and Klein (2006) and Ponte and Klein (2013), using Surface Quasi-Geostrophic (SQG) theory, showed that this task can be successful if one restricts this method to study the ocean in the first 500 m of the water column and for features of horizontal lengths in the mesoscale range. These results, considering typical scales of deep vortices shown in Table 3.1, point out a limit of the SQG theory, which would not be suitable for identifying features as deep vortices, whose radii can go down to the submesoscale range and depths can be way beyond 500 m.

**Table 3.1:** Most common deep vortices in the world ocean (Anticyclones: clockwise rotation in the Northern Hemisphere). In the table MS = Mediterranean Sea, NEA = north-eastern Atlantic Ocean, NWA = north-western Atlantic Ocean, NWI = north-western Indian Ocean.

	Basin	Depth (m)	Thick. (m)	Radius (km)	Rotation (m/s)
LEDDIES	MS	200 – 1000	300-1000	25-50	0.2
MEDDIES	NEA	600 – 1200	300-1000	20-50	0.3-0.4
NWA-EDDIES	NWA	700 – 1500	100-1000	15-100	0.2-0.5
PEDDIES	NWI	250 – 400	100	20-30	0.3
REDDIES	NWI	400 – 800	400-500	20-50	0.15
SWODDIES	NEA	70 – 300	200	30-50	0.3

Alternative approaches at inferring subsurface dynamics from sea-surface observations are provided by the combined use of satellite-derived and *in-situ* observations. Separately, the two kinds of measurements cannot give an exhaustive description of the subsurface dynamics. Satellites provide synoptic though sometimes noisy informations, since the sea-surface dynamics can be comparable to or can dominate the surface expression of the deeper oceanic motions. On the other hand, *in-situ* measurements can give a precise information on the ocean properties at different depths, but they remain very limited in space and time. In the last fifteen years, many studies have attempted at combining satellite-derived observations and *in-situ* data to detect vortices living at depth. Stammer et al. (1991), stated that Meddies can be detected using the combination of *in-situ* and altimetric observations (namely, measurements of the sea-surface elevation). Meddies, as other subsurface anticyclones, are in fact associated to positive, monopolar anomalies in altimetric fields [Sweeney et al. (2003b)]. Recently, Bashmachnikov and Carton (2012) and Ienna et al. (2014) confirmed this behavior. Other hints for Meddy detection can come from combining *in-situ*, altimetric and satellite-derived surface temperature fields. In fact, subsurface anticyclones, beyond their effect on SSH may lower SST due to their three-dimensional density structure [Sweeney et al. (2003b)]. Taking advantage of these characteristics, Bashmachnikov et al. (2013) showed that Meddies can be associated to SST cold anomalies in clockwise rotation. Even in this last case, the use of colocated *in-situ* observations was fundamental to strengthen informations coming from remotely-sensed fields.

Since one is interested in studying deep vortices to evaluate their impact on the global ocean, an automatic and synoptic detection would constitute the ideal scenario for such an investigation. The perspective of a future satellite altimetric mission (Surface Water and Ocean Topography, SWOT [Fu et al. (2009)]) which will improve present-day satellite altimetry performances, encouraged us in further investigating the impact of deep vortices on the ocean surface (mostly in SSH fields). The SWOT mission will provide global altimetric observations of the ocean at submesoscale horizontal resolutions and with precision measurements in the 2 cm range. Today, such horizontal resolutions are not achievable and the 2 cm measurement precision characterizes only a fraction of the global altimetric observations [Fu and Cazenave (2000)].

The study of the impact of deep vortices on the ocean surface will be carried out in an idealized context. Even though occurrence of both cyclonic and anticyclonic deep vortices is possible, we chose to focus on anticyclones, which represent a large amount of subsurface recirculating motions [Sweeney et al. (2003b), McWilliams (1985), Carton (2001), Pingree and Le Cann (1993b), Senjyu et al. (1998), Shapiro and Meschanov

(1991), Millot (1999)]. Supposing the existence of isolated deep vortices living in a background dynamics at rest, we will try to derive their signature at the sea surface using both analytical models in the frame of the Quasi-Geostrophic theory (QG hereafter) and numerical models. The numerical models will be the 3D Combined Lagrangian Advection Method with buoyancy surface boundary conditions (CLAM-3DQG hereafter, [<http://www-vortex.mcs.st-and.ac.uk/~dgd/FIBOSI>]), which simulates the ocean dynamics in a QG context, and the Regional Oceanic Modeling System (ROMS, Shchepetkin and McWilliams (2005)) which solves numerically the whole set of prognostic equations for the three components of oceanic motions, as well as temperature and salinity.

In section 3.2, the Materials and Methods used for the investigation will be illustrated. In particular, we will recall some elements of the Quasi-Geostrophic framework as well as the main principles of the CLAM-3DQG and ROMS numerical models. In sections 3.3 and 3.4, we will show the results issued from the analytical and numerical studies, respectively. Finally, section 3.5 will provide a discussion of the results and of possible future investigations.

## 3.2 Materials and Methods

### 3.2.1 Quasi-Geostrophic framework

In the QG theory, which is a suitable framework for mesoscale coherent vortices [Carton (2001)], a vortex can be represented by its potential vorticity, a quantity taking into account its rotation and the conjugated effects of Coriolis acceleration (imposed by Earth's rotation) and of buoyancy. Assuming a uniformly stratified ocean, the potential vorticity  $Q$  is expressed by equation 3.1:

$$\nabla_H^2 \psi + \frac{f_0^2}{N_0^2} \frac{\partial^2 \psi}{\partial z^2} = Q(x, y, z) \quad (3.1)$$

where  $\nabla_H^2 = \frac{\partial^2}{\partial x^2} + \frac{\partial^2}{\partial y^2}$ ,  $f_0$  is the Coriolis parameter,  $N_0$  is the Brunt-Väisälä frequency and  $\psi = \psi(x, y, z)$  is the stream function [Vallis (2006)]. Generally, the first term on the left-hand side of Equation 3.1 is referred to as relative vorticity of a QG fluid, while the second one is called stretching. In a Cartesian frame, the stream function is related to the fluid horizontal motion and satisfies  $\vec{u} = \vec{k} \times \nabla \psi$ , where  $\vec{k} = (0, 0, 1)$  [Vallis (2006)]. In a QG context, the determination of  $\psi(x, y, z)$  is then crucial for evaluation of geostrophic currents. Furthermore, this quantity allows one to estimate the sea-surface elevation and sea-surface temperature, the first being proportional to  $\psi(x, y, 0)$  and the latter to

$\partial_z \psi|_{z=0}$ . Looking at equation 3.1, it is evident that the determination of the stream function will depend on the inversion of the potential vorticity  $Q$ . If one manipulates equation 3.1, rescaling the vertical coordinate as  $Z = (N_0/f_0)z$ , the following expression for  $Q$  is obtained:

$$\nabla^2 \psi = Q \quad (3.2)$$

where the Laplacian operator is now given by  $\frac{\partial^2}{\partial x^2} + \frac{\partial^2}{\partial y^2} + \frac{\partial^2}{\partial Z^2}$ . In this case, the analytical inversion of equation 3.2 is possible and the stream function  $\psi$  can be evaluated via the Green's functions [Bashmachnikov and Carton (2012)]. Normally, this technique is suitable for vortices mathematically represented as point vortices, in which the vortex potential vorticity loses its spatial extent and is concentrated in a geometrical point of a three-dimensional ocean (see section 3.3.1 for further details).

Since our aim is to evaluate the sea-surface expression of deep vortices, such structures will be thought as potential vorticity anomalies living in a background dynamics at rest. Such anomalies will be placed at a finite distance from the sea-surface and will be characterized by various rotation rates, thicknesses and radii in order to account for the whole class of oceanic deep vortices listed in table 3.1. The associated stream function  $\psi$  will be obtained using the aforementioned method and will be evaluated at the sea surface for inferring the associated anomaly in the SSH field.

### 3.2.2 QG numerical model

The CLAM-3DQG model simulates the following system of equations:

$$\left\{ \begin{array}{l} \frac{DQ_{int}}{Dt} = 0 \\ \frac{D_s b_s}{Dt} = 0 \\ \frac{\partial^2 \psi_{int}}{\partial x^2} + \frac{\partial^2 \psi_{int}}{\partial y^2} + \frac{\partial}{\partial z} \left( \frac{f_0^2}{N^2} \frac{\partial \psi_{int}}{\partial z} \right) = Q_{int} \\ \frac{\partial \psi_{int}}{\partial z} \Big|_{z=0} = 0 \\ \frac{\partial^2 \psi_s}{\partial x^2} + \frac{\partial^2 \psi_s}{\partial y^2} + \frac{\partial}{\partial z} \left( \frac{f_0^2}{N^2} \frac{\partial \psi_s}{\partial z} \right) = 0 \\ f_0 \frac{\partial \psi_s}{\partial z} \Big|_{z=0} = b|_{z=0} \end{array} \right. \quad (3.3)$$

where  $\frac{D}{Dt} = \partial_t + \vec{u} \cdot \vec{\nabla}()$  and the subscript  $s$  indicates sea-surface related quantities. The system of equations 3.3 is actually known as coupled QG-SQG (Quasi Geostrophic and Surface Quasi Geostrophic) dynamics [Lapeyre and Klein (2006)] and it allows one to take into account the contribution of surface buoyancy (notice that  $b = f_0 \partial_z \psi$ ) and internal sources of potential vorticity  $Q_{int}$  for the determination of the three-dimensional motion. The total stream function resulting from equation 3.3 will be  $\psi = \psi_{int} + \psi_s$ . Numerically, the stream function derivation is achieved through Fourier's transform in the horizontal. Along the vertical coordinate, a 4th-order compact-difference solution is used. Its expression in Fourier's space is:

$$\left[ \frac{\partial^2}{\partial z^2} - (k^2 + l^2) \right] \hat{\psi}(k, l, z) = \hat{q}(k, l, z) \quad (3.4)$$

for each horizontal wavevector  $(k, l)$ . The assumption of a constant Brunt-Väisälä frequency  $N_0$ , and Coriolis parameter  $f_0$ , leads to the scaling of vertical coordinate  $z$  by the ratio  $N_0/f_0$ . The physical initialization consists of a three-dimensional isolated sub-surface potential vorticity anomaly  $q(r, z)$  representing a deep isolated anticyclone:

$$q(r, z) = -q_0 J_0(\alpha_R r) \left\{ 1 + \cos \left( \frac{\pi(z - z_0)}{H} \right) \left[ \left( \frac{\pi}{\alpha_R H} \right)^2 + 1 \right] \right\} \quad (3.5)$$

where  $J_0$  is the zero order Bessel function,  $z_0$  indicates the position of the isolated vortex

along the vertical,  $q_0$  is the intensity of the potential vorticity,  $H$  is the vortex thickness and  $\alpha_R$  is the parameter through which the horizontal size of the vortex can be controlled. Note that, in order to get a bounded structure,  $q(r, z)$  is set to zero for all  $r$  verifying  $\alpha_R r > \lambda_{01}$ , with  $\lambda_{01}$  the first root of the zero order Bessel function. The resulting structure has the shape shown in figure 3.1. The motivation for choosing this profile is to study how the surface signature of the vortex will develop with time. In fact, if the quantity  $z_0 + H/2$  is smaller than the total depth of the considered oceanic basin, equation 3.5 will assure the absence of any initial sea-surface elevations.

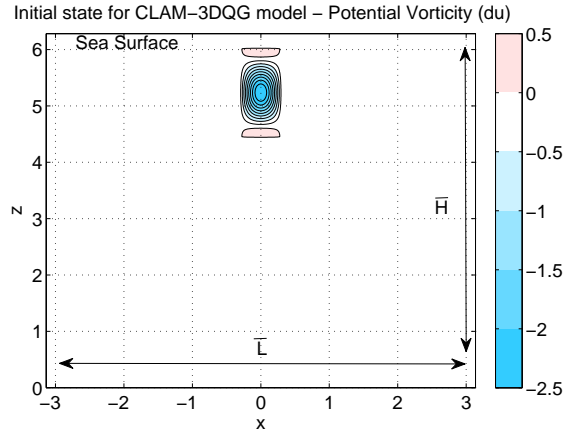


**Figure 3.1:** *Potential Vorticity (dimensionless units) of a subsurface vortex for numerical simulation with CLAM-3DQG model (Vertical Section).*

The runs are performed in a flat-bottomed ocean in a  $f$ -plane configuration. The three-dimensional volume in which the simulations are run measures  $\bar{H} \bar{L}^2$  (as shown in figure 3.1) and is adimensionalized and taken to be equal to  $(2\pi)^3$ .  $\bar{H}$  depends on the chosen aspect ratio, which in our case is equal to 0.7 (considering the  $N_0/f_0$  stretch along the vertical). The domain is doubly periodic. Simulations with the CLAM-3DQG model required the introduction of a deep current in order to observe the sea-surface response in a dynamic context (see section 3.3.2 for further details) and a cartoon of this configuration is given in figure 3.2. The current consists of a single cosine-like vertical variation and has maximum intensity at the depth of the vortex core  $z_0$  (i.e. where the minimum PV is located). Its analytical expression is given by:

$$U(z) = U_0 \cos \left[ \frac{\pi}{2} (z - z_0) \right] \text{Heav}(z - z_0 + 1) \text{Heav}(z_0 - z + 1) \quad (3.6)$$

where  $U_0$  has been arbitrarily chosen as 20% of the vortex rotational speed, which is initially  $\sqrt{u^2 + v^2}$  and  $Heav$  is the Heaviside function.

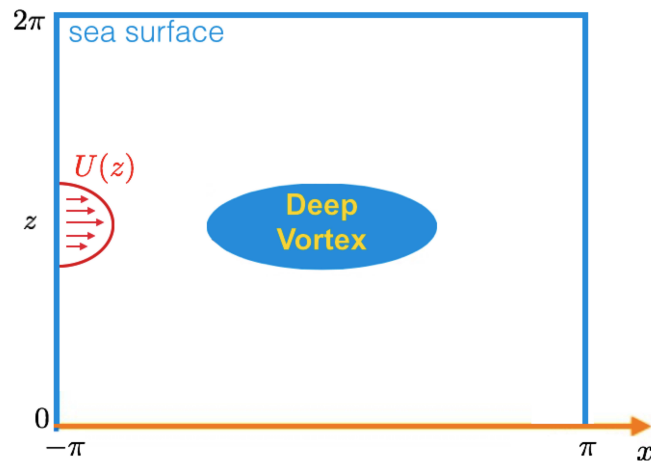


**Figure 3.2:** A translating subsurface vortex for numerical simulations with the CLAM-3DQG model. Translation is operated by means of the analytical function  $U(z)$ .

Integration in time has been performed for several configurations. For each run, the parameters characterizing the subsurface vortex ( $q_0$ ,  $\alpha_R$ ,  $H$  and  $z_0$ ) have been changed in order to test the sea-surface response to their variation. In particular, surface stream function fields (directly proportional to sea-surface elevation in the QG context) have been extracted and observed.

### 3.2.3 Primitive equation model

The ROMS model [Shchepetkin and McWilliams (2005)] is a primitive equation ocean model simulating the Reynolds-averaged Navier-Stokes equations with the assumptions of hydrostatic and Boussinesq approximation. The model has been used in idealized configuration. Simulations have been run in a flat-bottomed east-west periodic oceanic basin, in the  $\beta$ -plane approximation and in absence of atmospheric forcing. This choice is justified by the interest in isolating the dynamics of the system given by the vortex plus the sea-surface. The oceanic basin under consideration can have two sizes: a basin measuring  $600 \text{ km} \times 600 \text{ km} \times 4 \text{ km}$  (respectively in the zonal, meridional and vertical directions) is used to study deep anticyclones in the submesoscale range and with swirl velocities around 0.2 m/s. On the other hand, when faster rotating mesoscale anticyclones are studied, we choose a horizontally larger basin ( $600 \text{ km} \times 1000 \text{ km}$ ). Indeed,

larger vortices undergo a more efficient south-western drift [Cushman-Roisin and Beckers (2011)], and need a meridionally larger basin in order to study their evolution far from the southern boundary of the domain. The domain resolution is 2 km in the horizontal and the vertical discretization is given by 80 non-uniformly spaced levels. A finer resolution has been chosen for levels closer to the sea-surface. The model is initialized by means of a background density stratification described by an analytical function, exponentially decaying with depth, whose parameters can account for the geography of the Rossby radius of deformation [Chelton et al. (1998)]. In our case, the Rossby radius is around 40 km, corresponding to vortices living at latitudes of about  $20^\circ N$ . The analytical expression for mean density profiles is given by equation 3.7,

$$\rho(z) = \rho_0 \exp[-\alpha_\rho z / \bar{H}] \quad (3.7)$$

with  $\alpha_\rho = 0.24$ ,  $\bar{H} = 4$  km (the vertical extent of the basin) and  $\rho_0 = 1027.5$  kg·m<sup>-3</sup>. Deep anticyclones are introduced in such a rest stratification making use of cyclogeostrophic balance. This approach allows one to take into account the combined effects of Earth's rotation, pressure gradient field and the spinning of the vortex (a non-negligible feature if anticyclones with  $Ro \simeq 1$  are dealt with [Carton (2001)]). The density anomalies associated to the deep anticyclones have been derived from the general form of the cyclogeostrophic balance, which, in polar coordinates, takes the form of equation 3.8,

$$\frac{v_\theta^2}{r} + f_0 v_\theta = \frac{1}{\rho_0} \frac{dp(r, z)}{dr} \quad (3.8)$$

with  $r$  the distance from the center of the vortex,  $v_\theta$  the azimuthal velocity,  $f_0$  the Coriolis parameter and  $dp/dr$  the pressure gradient field. This relation, once chosen the velocity field, contains the information on the density structure associated to the vortex. The velocity field has been chosen in the form prescribed by equation 3.9 and it represents an analytical approximation of a deep anticyclone:

$$v_\theta = \frac{-v_0 r}{R} e^{-\frac{r^2}{R^2}} e^{-\frac{(z-z_0)^2}{H^2}} \quad (3.9)$$

where,  $v_0$  is the intensity of the field,  $R$  its Radius,  $z_0$  its position along the vertical and  $H$  the thickness. Integrating equation 3.8 between  $r$  and  $\infty$ , and, considering that only coherent vortices are treated in this work, the pressure field can be assumed to be zero far from the vortex center (namely at  $r = \infty$ ) and one can write that:

CHOSEN PARAMETERS				DERIVED QUANTITIES	
$v_\theta$	$R$	$H$	$z_0$	$p'(r, z)$	$\rho'(r, z)$
Initial Speed	Radius	Thickness	Depth	Pressure Anomaly	Density Anomaly

**Table 3.2:** Table of parameters and derived quantities for initialization of ROMS experiments

$$\int_r^\infty \frac{dp'(r', z)}{dr'} dr' = p'(\infty) - p'(r, z) = -p'(r, z) \quad (3.10)$$

finally getting the equation 3.11 for the pressure field:

$$p'(r, z) = \beta e^{-\frac{2(z-z_0)^2}{H^2}} e^{-\frac{2r^2}{R^2}} - \gamma e^{-\frac{(z-z_0)^2}{H^2}} e^{-\frac{r^2}{R^2}} \quad (3.11)$$

with:

$$\beta = \frac{\rho_0 v_0^2}{4}$$

$$\gamma = \frac{\rho_0 f_0 v_0 R}{2}$$

The derivative of equation 3.11 with respect to the  $z$  variable yields the density anomaly associated to the vortex and the latter is superimposed to the rest stratification to get the final three-dimensional density field. In other words, the hydrostatic equilibrium is imposed and it prescribes density anomalies directly from the pressure anomaly  $p'(r, z)$ :

$$\frac{dp'(r, z)}{gdz} = -\rho'(r, z) \quad (3.12)$$

where  $g$  is the gravity acceleration. Table 3.2 summarizes the possible choices of parameters and all the derived quantities. A panel showing typical initial configurations for a ROMS experiment is presented in figure 3.3. In particular, we show the initial state relative to a submesoscale anticyclone rotating at 0.2 m/s (maximum tangential speed). The initial states for other configurations will all resemble the one in figure 3.3, with different characteristics dependent on the choice of the parameters. We recall that the varying vortex parameters are the key to account for different types of oceanic deep anticyclones (see Table 3.1). As in the previous case, integration in time has been performed for several configurations. For each run, the parameters characterizing the deep anticyclone, shown in Table 3.2, have been varied. Differently from the CLAM-3DQG model, ROMS

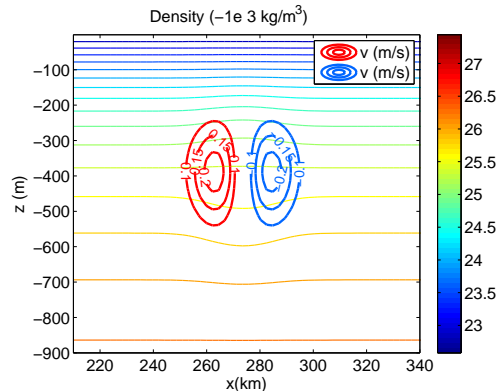


**Figure 3.3:** Schematic of the Initial State for a ROMS experiment. Submesoscale anticyclone rotating at a maximum tangential speed of 0.2 m/s. Here, the sea surface is at  $z=0$ .

provides a direct physical information on the elevation of the sea-surface. Results will be shown in section 3.4.

### 3.3 Theoretical Analysis

The determination of the surface effects induced by deep vortices is analytically evaluated in the QG framework. We will distinguish the case of *steady* and *translating* anticyclones. Though the second ones represent a more frequent geophysical feature, steady anticyclones are convenient for the analytical inversion of equation 3.2. Despite this, qualitative analytical evaluations are possible in the dynamic case as well.

#### 3.3.1 Surface influence of steady vortices

In recent years, Meddies have been studied with the point vortex model [Bashmachnikov and Carton (2012)]. This model is useful and provides analytical solutions if the ocean is considered as infinite in all directions. Otherwise, boundary conditions have to be implemented in order to invert equation 3.1. In particular, the ocean-atmosphere interface is a physical boundary, as is the ocean bottom (the lateral boundaries of the ocean are often remote enough to be neglected). For intrathermocline baroclinic vortices (as in our case), the influence of the oceanic bottom can be overlooked, except if special boundary conditions are imposed there. Therefore, we mostly consider the effect of the ocean-atmosphere interface. This interface can be neglected if continuity of the

stream function, of its vertical derivative and of the Brunt Väisälä frequency are assured. Since Brunt-Väisälä frequencies in the upper ocean and in the lower atmosphere are comparable [Vallis (2006)]<sup>1</sup>, the main consequence of this constraint is the existence of an atmospheric circulation induced by the subsurface vortex. This problem can be overcome noticing that the intensity of winds in the lower atmosphere ( $\simeq \mathcal{O}$  (m/s)) is much more intense than typical ocean surface circulations induced by interior vortices ( $\simeq \mathcal{O}$  (cm/s)) [Pingree and Le Cann (1993b), Bashmachnikov et al. (2013)]. Hence, the eventuality of such a circulation would be negligible compared to atmospheric motion and the approximation of an infinite ocean is reasonable. Taking inspiration from Bashmachnikov and Carton (2012), we will derive the three-dimensional stream function for two specific cases of subsurface potential vorticity anomalies (described in Morel and McWilliams (1997)).

### Point Vortices

The description of interior QG anticyclones by Morel and McWilliams (1997) states that, if equation 3.13 is valid and equation 3.1 is taken into account, deep anticyclones can be classified as rotational (R) or stretching (S) vortices. These vortices satisfy a condition of null potential vorticity integral over the domain volume  $v_T$ ,

$$\int \int \int_{v_T} Q(x, y, z) dv_T = 0 : \quad (3.13)$$

If rotational effects dominate on stretching, the resulting structure will be called R-vortex and the potential vorticity (PV) anomaly will be in the form of an internal core surrounded by an opposite sign PV ring. The S-vortex will be the reference model for the opposite case, and the potential vorticity anomaly will exhibit a tripolar vertical structure given by an inner core and opposite sign anomalies at the bottom and on top of it, as shown by figure 3.4. We now idealize these R and S configurations into equivalent point vortex distributions. Given a potential vorticity distribution,

$$Q(x, y, z) = \Gamma \delta(x) \delta(y) \delta(z) \quad (3.14)$$

indicating a point vortex located in the origin of a reference frame, the corresponding

---

<sup>1</sup>It is worth pointing out that this assumption might not be completely rigorous. Although the Brunt-Väisälä frequency exhibits comparable values in the upper ocean and the lower atmosphere, its mathematical derivation is not possible at the real ocean-air interface (the density vertical derivative cannot be defined there)

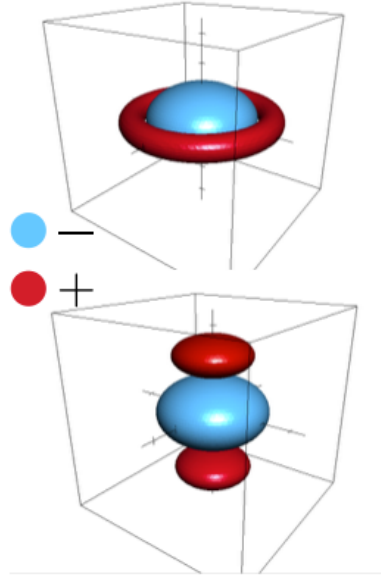


**Figure 3.4:** *Top:R-Vortex, bottom:S-Vortex, adapted after Morel and McWilliams (1997).*

stream function (in polar coordinates and in an infinite domain) is:

$$\psi_{PV}(r) = \int \int \int_V G(r - r') * \Gamma \delta(r') d^3 r' \quad (3.15)$$

which, for  $r' = 0$  and  $G(r) = -1/(4\pi r)$ , yields:

$$\psi_{PV}(r) = -\frac{\Gamma}{4\pi r} \quad (3.16)$$

where  $\Gamma = \int \int \int_v Q dv$ , and  $v$  corresponds to the volume of a realistic vortex.

### R-Vortices

A schematic point R-vortex is given in Figure 3.5. A potential vorticity ring surrounds the central point vortex. We specify that:

- the Cartesian to spherical coordinate transformation yields  $x = r \cos \phi \cos \lambda$ ,  $y = r \cos \phi \sin \lambda$  and  $Z = r \sin \phi$ , where  $\lambda$  and  $\phi$  are the azimuthal and zenithal coordinates;

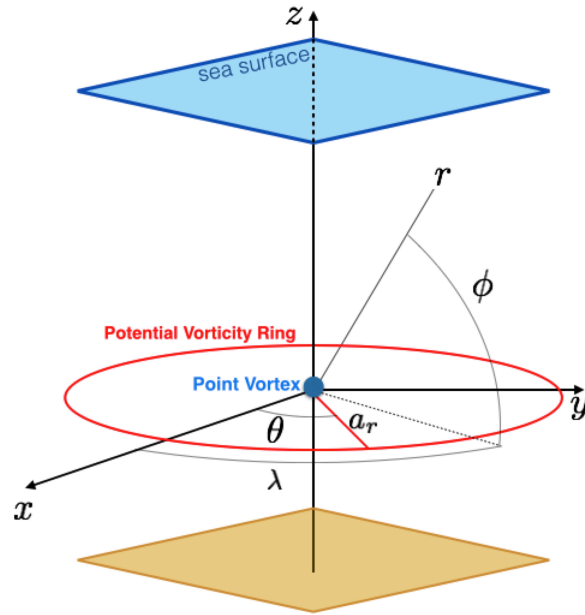


**Figure 3.5:** Schematics of the potential vorticity distribution given by a point vortex and a potential vorticity ring.

- the radius  $r$ , considering the scaling of the vertical coordinate will be given by  $r = \sqrt{x^2 + y^2 + Z^2}$ , and it gives the distance from the center of the reference frame;
- the radius  $r_\theta$  indicates the distance from the center of the reference to the potential vorticity ring (whose radius is  $a_r$ ) and it is given by  $r_\theta = \sqrt{(x - a_r \cos\theta)^2 + (y - a_r \sin\theta)^2 + Z^2}$  and using the spheric coordinates one yields  $r_\theta = r^2 + a_r^2 - 2a_r r \cos\phi \cos\theta'$ , with  $\theta' = \theta - \lambda$ ;

Using equation 3.16 and computing a line integration, the stream function associated to the potential vorticity ring becomes:

$$\psi_{RING}(r, \phi, \lambda) = \int_{-\lambda}^{-\lambda+2\pi} \frac{\Gamma}{8\pi^2 r_{\theta'}} d\theta' = \frac{\Gamma}{8\pi^2 \sigma} \int_{-\lambda}^{-\lambda+2\pi} (1 - \zeta \cos\theta')^{-1/2} d\theta' \quad (3.17)$$

with  $\sigma = \sqrt{r^2 + a_r^2}$  and  $\zeta = 2ra_r \cos\phi / (r^2 + a_r^2)$ . Since solutions for  $r > a_r$  are searched, the expression of  $\zeta$  justifies a Taylor expansion for the integrand.

Furthermore, without loss of generality, the dependence on the azimuthal variable can be eliminated, as the integral is evaluated over a  $2\pi$  interval. These considerations lead

to the following expression for the RING stream function:

$$\psi_{RING}(r, \phi) = \frac{\Gamma}{8\pi^2\sigma} \int_0^{2\pi} \left( 1 + \frac{3}{16}\zeta^2 + \frac{\zeta}{2}\cos\theta' + \frac{3}{16}\cos 2\theta' \right) d\theta' \quad (3.18)$$

Considering that the integrand contains periodic functions and that the integral extrema are between 0 and  $2\pi$ , all the terms multiplied by the cosine function do not give any contribution. Using the explicit expression for the  $\zeta$  parameter, integrating over the angle  $\phi$  and adding the contribution of the point vortex stream function one can get the stream function for the total configuration shown in Figure 3.5, which is given by the following expression <sup>2</sup>:

$$\psi_{TOT} = \psi_{PV} + \psi_{RING} = -\frac{\Gamma}{4\pi r} + \frac{\Gamma}{4(r^2 + a_r^2)^{1/2}} \left[ 1 + \frac{3a_r^2 r^2}{8(r^2 + a_r^2)^2} \right] \quad (3.19)$$

Thus, the sea-surface elevation above the subsurface vortex can be expressed by:

$$\eta = \frac{f_0}{g} \psi_{TOT}(x, y, z = z^*) \quad (3.20)$$

where  $z^*$  indicates the distance between the vortex and the sea surface and  $f_0$  and  $g$  are the Coriolis parameter and gravity acceleration, respectively.

### S-Vortices

In order to model the S-vortex-like structure, a vertical tripole of potential vorticity is used. We first compute  $\psi$  for a vertical dipole (figure 3.6), which consists of two point vortices of integrated potential vorticity  $\pm\Gamma$  separated by a distance  $\delta$ . In general, for anticyclonic vortices  $\Gamma$  is negative. In what follows, the vortex positive and negative poles will be thus indicated by  $-\Gamma$  and  $\Gamma$ , respectively.

We will compute the stream function at the sea surface, at a point  $P(x, y, z)$ . We define

- $\alpha$ , the angle between the vertical coordinate and the line connecting a point vortex to the point  $P$ ;
- $r_{+/-}$ , the distance between the two point vortices and the point  $P$ ;

---

<sup>2</sup>In the case of R-vortices (and S-vortices, in the following section) we neglect the contribution to the surface stream-function given by the vortex-induced temperature anomaly, the latest being proportional to the quantity  $\left. \frac{\partial\psi}{\partial z} \right|_{z=z^*}$

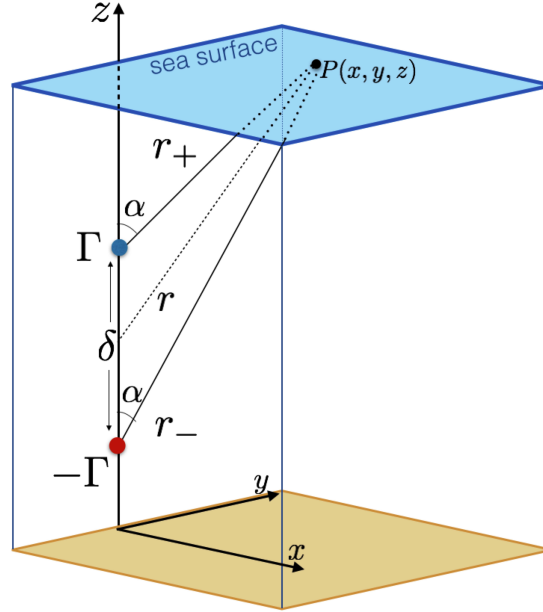


**Figure 3.6:** Schematics of the potential vorticity distribution given by a vertical dipole of point vortices.

- $r$ , which for the chosen configuration (i.e.  $r \gg \delta$ ) will satisfy  $r \simeq r_{+/-}$

The total stream function will be the superposition of the solutions for the two point vortices:

$$\psi_{Dipole} = \psi_{\Gamma_+} + \psi_{\Gamma_-} = \frac{\Gamma}{4\pi} \left( \frac{1}{r_-} - \frac{1}{r_+} \right) = \frac{\Gamma}{4\pi} \left( \frac{r_+ - r_-}{r_+ r_-} \right) = \frac{\Gamma}{4\pi} \left( \frac{\delta r \cos \alpha}{r^3} \right) \quad (3.21)$$

which, in a cartesian frame yields:

$$\psi_{Dipole} = \psi_{\Gamma_+} + \psi_{\Gamma_-} = \frac{\Gamma \delta}{4\pi} \left( \frac{Z}{(x^2 + y^2 + Z^2)^{3/2}} \right) \quad (3.22)$$

This framework makes the computation for the vertical tripole completely analogous. We can consider the tripole as the combination of two poles plus an opposite sign central one, thus:

$$\psi_{Tripole} = \frac{\Gamma/2}{4\pi} \left( \frac{1}{r_d} \right) - \frac{\Gamma}{4\pi r} + \frac{\Gamma/2}{4\pi} \left( \frac{1}{r_u} \right) \quad (3.23)$$

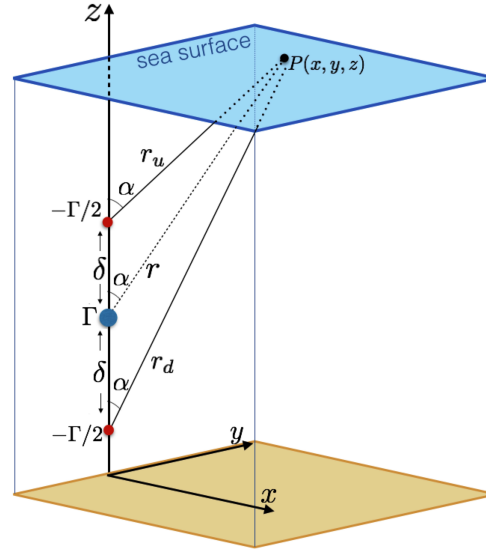


**Figure 3.7:** Schematics of the potential vorticity distribution given by a vertical tripole of point vortices.

with:

$$\begin{cases} r - r_u = \delta \cos \alpha \\ r_d - r = r - r_u \\ r_d - r_u = 2\delta \cos \alpha \end{cases} \quad (3.24)$$

The total stream function, can be written as:

$$\psi_{Tripole} = \frac{\Gamma}{4\pi} \left( \frac{rr_u - 2r_dr_u + rrd}{r_dr_r_u} \right) \quad (3.25)$$

and, after some manipulations, one can get:

$$\psi_{Tripole} = \frac{\Gamma}{4\pi} \left( \frac{\delta^2 r^2 \cos^2 \alpha}{r^5 - \delta^2 r (r \cos \alpha)^2} \right) \quad (3.26)$$

which, in cartesian coordinates becomes:

$$\psi_{Tripole} = \frac{\Gamma}{4\pi} \left( \frac{\delta^2 Z^2}{(x^2 + y^2 + Z^2)^{5/2} - \delta^2 (x^2 + y^2 + Z^2)^{1/2} Z^2} \right) \quad (3.27)$$

In analogy with the R-vortex case, the QG expression for the induced sea-surface elevation will be:

$$\eta = \frac{f_0}{g} \psi_{Tripole}(x, y, z = z^*) \quad (3.28)$$

where  $g$ ,  $f_0$  and  $z^*$  are the same as for equation 3.20.

Summarizing, the models proposed in this section lead to analytical predictions of the stream function generated by deep vortices (provided the knowledge of their potential vorticity distributions). The knowledge of the stream function allows one to determine the vortices sea-surface expression. In fact, in the quasi-geostrophic framework, the sea-surface elevation is related to the surface stream function of the considered oceanic basin. As we will also show in section 3.4.1, the sea-surface elevation induced by a steady isolated deep anticyclone (living in an oceanic basin at rest) is always positive and monopolar.

Equations 3.19 and 3.27 (for R and S-Vortices respectively) show that the stream function can have a decay up to  $1/r^3$  from the vortex center and it depends linearly on  $\Gamma = \int \int \int_v Q dv$  (the vortex integrated potential vorticity). For a finite-volume vortex of uniform potential vorticity, the quantity  $\Gamma$  could also be approximated by  $\Gamma \simeq QHR^2$ , allowing one to say that the vortex-induced stream function (hence, its surface signature) depends quadratically on the vortex radius  $R$  and linearly on its thickness  $H$ .

To avoid the divergence of  $\psi$  (at  $r=0$ ) and of the vortex integrated kinetic energy, expressed by equation 3.29, the results of this section are to be used in the  $r > 0$  region.

$$E = \frac{1}{2} \int \int \int_V (\nabla \psi(x, y, z))^2 dx dy dz \quad (3.29)$$

### 3.3.2 Surface expression of translating vortices

The development of the surface signature of a deep vortex can also be predicted in a dynamical framework, i.e., when a vortex is drifting in an oceanic basin. One of the main mechanisms responsible of vortex drift is known as self-advection and it results from the variation of the Coriolis parameter with latitude [Bashmachnikov and Carton (2012), Cushman-Roisin and Beckers (2011)]. Advection currents are also responsible of vortex displacement. In general, a drifting vortex is a more realistic schematization of oceanic vortices, if compared to the steady case [Chelton et al. (2011)]. The theoretical estimates of the dynamical signature will rely on QG theory and on the conservation of potential vorticity, which is a realistic assumption during the early stages of the vortex evolution. Notice that any interaction with the oceanic bottom will be neglected here. In the case

of a layered ocean (as in figure 3.8 and 3.9), if the layer above the eddy (considered as a localized volume of potential vorticity anomaly) is homogeneous, its potential vorticity (PV hereafter) can be given by its shallow-water expression [Vallis (2006)]:

$$Q = \frac{\zeta + f_0}{h} \quad (3.30)$$

The Shallow-water PV anomaly is:

$$\delta Q = \frac{\zeta + f_0}{h} - \frac{f_0}{H^*} \quad (3.31)$$

where  $h$  is the height of a local column and  $H^*$  the height of the unperturbed one. Then two cases can occur:

1. There is initially a signature above the drifting eddy (a steady signature in terms of sea-surface elevation for instance). The upper layer fluid can have zero potential vorticity anomaly (everywhere horizontally) and in that case, the column above the eddy will have a smaller height ( $h \simeq H_1 - \Delta H$ , since  $\eta_s \ll \Delta H$ ) and negative relative vorticity ( $\zeta_0 < 0$ ). The resulting PV at the stage labelled as "1" (see Figure 3.8) will be:

$$Q_1 = \frac{\zeta_0 + f_0}{H^* - \Delta H} \quad (3.32)$$

Since we make the assumption of zero PV anomaly,

$$Q_1 = \frac{f_0}{H^*} \quad (3.33)$$

When this fluid column moves away (climbs down) from the eddy, it experiences stretching, i.e, it increases its height (to  $h = H^*$ ). Therefore its relative vorticity will go back to zero (following the condition of zero potential vorticity anomaly above). This column will therefore finally have zero stretching and zero relative vorticity. On the other hand, the column initially in front of the eddy (labelled with "2"), which will climb up the eddy due to eddy drifting, has initially zero stretching and zero relative vorticity.

$$Q_2 = \frac{f_0}{H^*} \quad (3.34)$$

Climbing up the eddy, it will diminish its height (to  $h = H^* - \Delta H$ ) and therefore it will develop negative relative vorticity ( $\zeta_0 < 0$ ). Since it has zero PV anomaly,

$$Q_2 = \frac{\zeta_0 + f_0}{H^* - \Delta H} = \frac{f_0}{H^*} \quad (3.35)$$

The two columns have replaced each other. The initial monopolar steady signature remains monopolar. A cartoon of this dynamics is presented in figure 3.8. In the figure  $\eta_s$  indicates the sea-surface elevation.

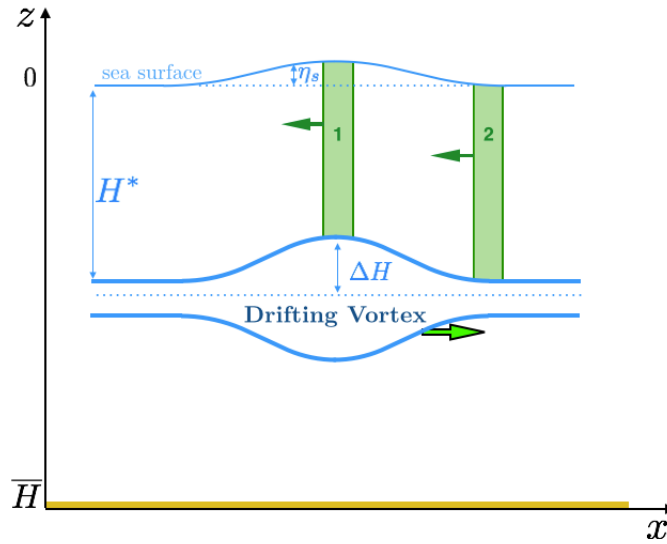


**Figure 3.8:** *Dynamics of a monopolar signature. Case of a preexisting steady signature.*

2. There is initially no (steady) signature above the eddy. The upper layer fluid cannot have zero PV anomaly everywhere, because the fluid column above the eddy has negative vortex stretching and zero relative vorticity. The corresponding shallow-water PV will be:

$$Q_1 = \frac{f_0}{H^* - \Delta H} \quad (3.36)$$

Let's assume nevertheless that the upper fluid out of the eddy has zero PV anomaly

and therefore zero relative vorticity, then:

$$Q_2 = \frac{f_0}{H^*} \quad (3.37)$$

When the fluid column above the eddy climbs down, it will gain height and therefore positive relative vorticity, so:

$$Q'_1 = \frac{\zeta_1 + f_0}{H^*} = \frac{f_0}{H^* - \Delta H} \quad (3.38)$$

with  $\zeta_1 > 0$ . The fluid column which climbs up the eddy will have negative stretching and therefore negative vorticity, leading to:

$$Q_2 = \frac{f_0}{H^*} = \frac{f_0 + \zeta_0}{H^* - \Delta H} \quad (3.39)$$

with  $\zeta_0 < 0$ .

Therefore, from zero steady signature, a dipolar dynamical signature develops. A bump in sea-surface elevation will appear in the leading half of the eddy and a hollow will appear in the trailing one. Note nevertheless that this depends strongly on the initial potential vorticity distribution. Figure 3.9 shows schematically the explained dynamics and the resulting (final) signature, which, hereafter will be referred to as dipolar signature.

In this section, the surface signature of deep vortices has been investigated taking advantage of analytical models relying on the QG framework. The characterization has been presented in both a steady and dynamic case, referred to a steady and drifting deep vortex respectively. Considering a vortex three-dimensional potential vorticity distribution, the stream function (a quantity related to sea-surface elevation and sea surface temperature in the ocean) can be obtained in idealized configurations.

Steady deep anticyclones, and vortices in general, can be modeled by means of point vortices, a schematization allowing one to consider their realistic potential vorticity structure and to translate it in equivalent idealized distributions. Such point vortex distribution allows the use of Green's functions for the determination of the associated stream function. Hence, an analytical form of the surface effects related to a deep anticyclone has been obtained for realistic R-vortices and S-vortices [Morel and McWilliams (1997)] and it is shown by equations 3.19 and 3.27. In both cases, the sea-surface elevation depends linearly on the vortex potential vorticity  $q$  and the thickness  $H$ , quadratically



## 3.4 Numerical results

### 3.4.1 Surface signature of deep anticyclones: steady case

In this section, we will determine the surface signature of deep anticyclones in an oceanic basin at rest via a numerical approach (ROMS, [Shchepetkin and McWilliams (2005)]). We choose the analytical velocity field shown in equation 3.9 and, using the cyclo-geostrophic balance (equation 3.8), we obtain the vortex three-dimensional density distribution. Furthermore, we require the velocity field to be identically null at the ocean bottom, which is a realistic assumption for intrathermocline eddies (as the one shown in figure 3.3). The estimation of the sea-surface elevation induced by the deep anticyclone can be related to its density structure and is expressed by equation 3.40.

$$\eta(r) = \int_{\bar{H}}^0 \frac{\rho_d}{\rho_s} dz \quad (3.40)$$

where  $\rho_d$  is the density anomaly associated to the deep anticyclone,  $\rho_s$  is the background density structure and  $\bar{H}$  indicates the ocean depth (Figure 3.10). The steady signature

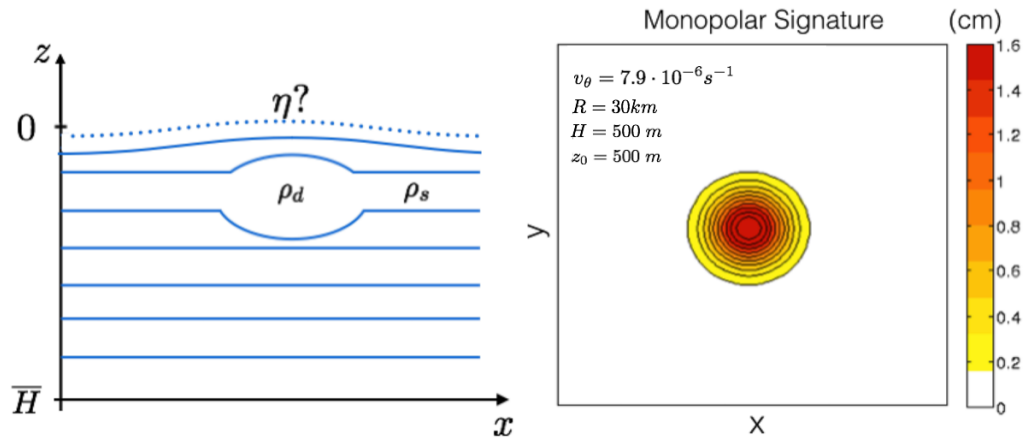


**Figure 3.10:** Steady monopolar signature of a subsurface anticyclone in the mesoscale range. The vortex parameters are illustrated in table 3.2

of a deep anticyclone in SSH fields, in absence of bottom velocities, has always the form of a monopolar positive anomaly superimposed on the flat sea surface (justifying, in this context, the equivalence between sea-surface elevation and sea-level anomaly, which will be used hereafter). In an idealized  $f$ -plane configuration and in the absence of external

forcing, a coherent isolated vortex will remain invariant, so will its surface signature. A parametric investigation of the sea-level anomaly induced by a subsurface vortex is achieved. The maximum intensity of this surface signature behaves like summarized in figure 3.11, indicating:

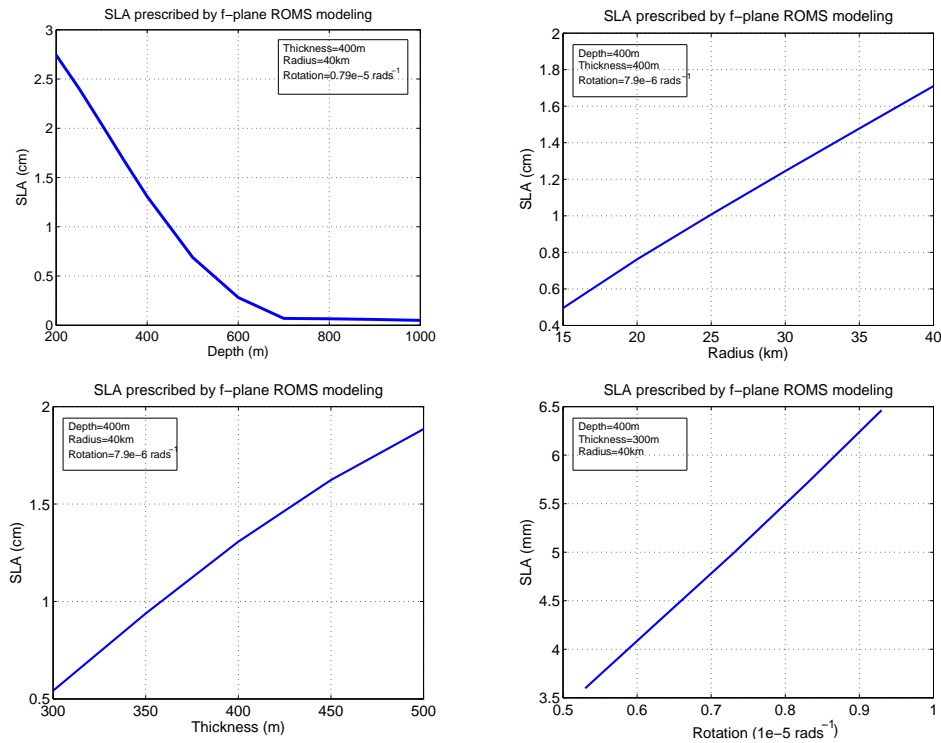


**Figure 3.11:** Parametric study of the maximum sea-level anomaly (SLA) induced by a deep anticyclone. Dependences are studied as a function of the vortex depth (upper-left), thickness (upper-right), radius (lower-left) and initial angular velocity (lower-right).

- inversely quadratic dependence with respect to the vortex depth  $z_0$  (checked fitting the experimental data with a  $z^{-2}$  function);
- linear dependence with respect to the vortex radius, as shown by the upper-right panel of figure 3.11);
- linear dependence with respect to the vortex thickness;
- linear dependence with respect to the vortex initial angular velocity, which, according to equation 3.1 can be related to the vortex potential vorticity;

Considering the vortex structure in terms of its potential vorticity anomaly (shown in figure 3.12-a), we compare the results of the numerical experiments with the theoretical predictions of equation 3.19, discussed in section 3.3.1. The dependence of the maximum SLA on the vortex depth, thickness and angular velocity are qualitatively in agreement with the analytical estimations. In particular, the validity of the dependence on the vortex depth was checked fitting equation 3.19 with a  $z^{-2}$  function (with  $z$  the depth). The fit yielded an  $R^2 = 0.95$ .

Finally, the experimental dependence of the maximum SLA on the vortex radius was only linear, while theory mostly predicted a quadratic relation. Indeed, in the model, the effects of a varying Brunt-Väisälä frequency (which is not taken into account in the theoretical approach) as well as the fact that the modeled vortex is not perfectly isolated ( $\int \int \int Q \, dV \neq 0$ <sup>3</sup>, with  $V$  the volume of the oceanic basin) may generate deviations from theory.

Moreover, if anticyclones with velocity fields around 0.2 m/s are studied (this is a typical velocity for deep anticyclones, as suggested by Table 3.1) the minimum requirements for the sea-level anomaly to be  $\mathcal{O}(\text{cm})$  are:

1. a mesoscale range for the deep anticyclone, i.e., when the vortex diameter is slightly larger than the Rossby radius of deformation (40 km at a latitude of 20°N) ;
2. provided condition 1, the ratio between the vortex depth and thickness has to be around 0.9;

A threshold in the centimeter range is appropriate for present-day and future satellite altimetry (in the future, the measurement precision of satellite-derived altimetric maps will go down to 2 cm on a global scale [Fu et al. (2009)], presently, this is achieved only for a fraction of the world ocean [Fu and Cazenave (2000)]); this could allow the detection of an oceanic vortex from space, assuming, nevertheless, the idealized requirement of a surrounding ocean at rest.

---

<sup>3</sup>The integrated potential vorticity anomaly of the core (in absolute value) exceeds the one of the surrounding ring by about 15%

### 3.4.2 Comparison with the point vortex model

A quantitative comparison between the point vortex theory and a realistic vortex is presented here. The PV structure (Ertel PV anomaly [Vallis (2006)]) of the analytically modeled vortex (in the static case), is similar to the one shown in figure 3.12-a. The comparison is then operated by means of equation 3.19, that models a deep vortex as a point-vortex surrounded by a potential vorticity ring. In reality, for a different choice of the vortex parameters (mainly varying the depth), opposite sign PV patches can vertically bound the vortex core. Nevertheless, the horizontal patches are often more intense, justifying the choice of equation 3.19 for the comparison.

A preliminary analysis suggests a scaling of the quantities in use, i.e., the Ertel PV anomaly (EPVa) and the stream function  $\psi$ . The EPVa has dimensions of  $\text{m}^{-1}\text{s}^{-1}$ , while the one appearing in equation 3.19 (via the  $\Gamma$  quantity) relies on quasi-geostrophic theory, in which the PV (PVQG in this context) has dimensions of  $\text{s}^{-1}$ . The scale factor between the two quantities is  $N^2/g$ , leading to the following relation:

$$PVQG \simeq EPVa \frac{g}{N^2} \quad (3.41)$$

We also recall that, in the QG framework, the sea-surface elevation is related to the surface stream function  $\psi_s$  via equation 3.20. In particular, the maximum sea-level anomalies induced by the point-vortex structure (figure 3.5) have been observed as a function of vortex depth and initial potential vorticity. In fact, parameters such as thickness and radius cannot be used in a point-vortex context, where the key quantity is the integral of the PV anomaly over the volume occupied by the vortex motion. We study the case of a vortex with the following parameters: radius = 40 km, thickness = 300 m (and 400 m), depths between 200 and 1000 m and angular velocities between  $0.5 \cdot 10^{-5}$  and  $1.06 \cdot 10^{-5}$  rad/s (about 0.2 to 0.4 m/s), shown in figure 3.12. The analysis confirms that the sea-level anomaly maintains a monopolar structure and that its maximum intensities, provided some restrictions, respect the values observed for realistic vortices. Figure 3.12-c-d indicate that the restrictions for the theory to be used are the following:

- Velocity restriction: the point-vortex-like structure has to be considered valid in all cases in which the corresponding real vortex is well described by the quasi-geostrophic (QG) theory, i.e., the Rossby number  $Ro$  has to be significantly lower than unity. This will assure applicability of equation 3.19, that relies on QG framework and that has been used for validation. Figure 3.12-c clearly shows how, for a fixed radius and thickness, an increase in initial angular velocity (i.e., relative

vorticity) corresponds to an increase in Rossby number, taking the vortex far from geostrophy [Carton (2001)] and making the theoretical description divergent from the realistic case;

- Depth restriction: the point-vortex-like structure is an appropriate approximation of a vortex when the corresponding realistic structure is fully immersed in the ocean. (i.e. PV anomaly isosurfaces do not intersect the sea surface). If this condition is not verified, the point vortex theory underestimates the sea-level anomalies above a deep vortex;

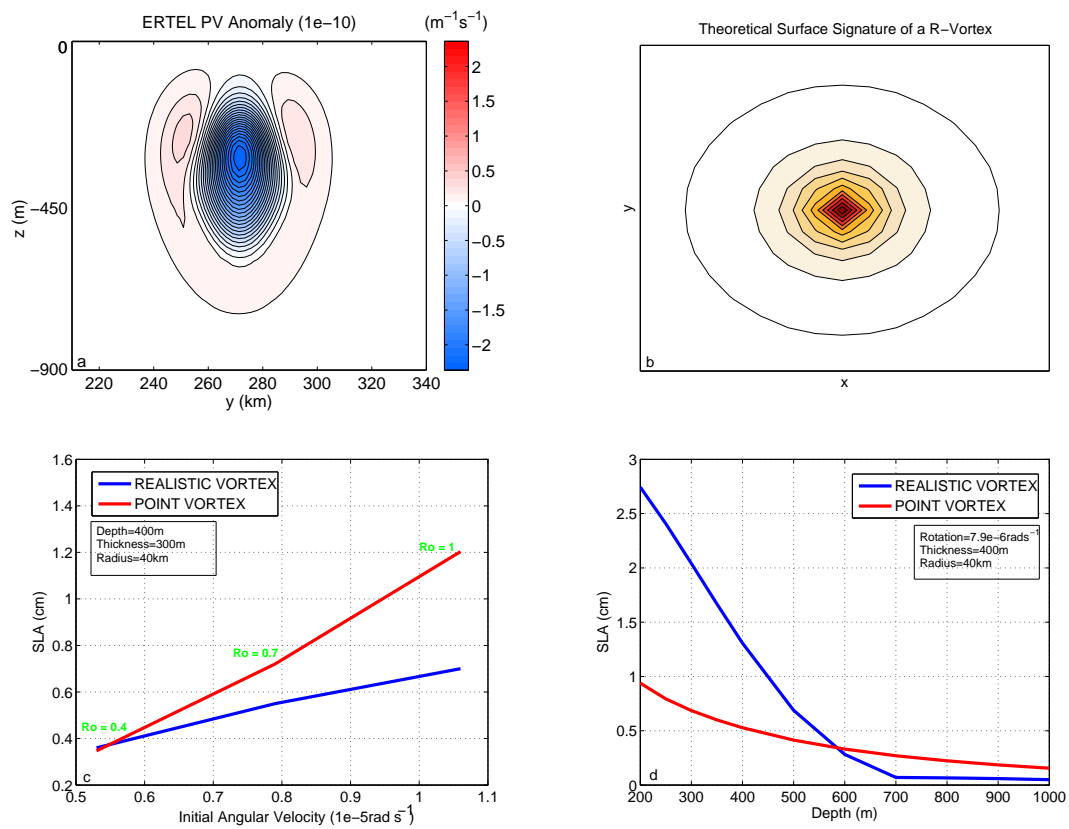


**Figure 3.12:** Parametric study of the sea-level anomaly (SLA) induced by a deep anticyclone. Dependence is studied as a function of the vortex initial angular velocity (c) and depth (d). The monopolar sea-level anomaly is shown in b.

### 3.4.3 Surface signature of deep anticyclones: dynamic case, CLAM-3DQG model

Here we show the development of a dipolar signature generated by a deep anticyclone drifting by means of the subsurface current expressed by equation 3.6. The QG simulations are run in a doubly periodic oceanic basin. We work in rescaled coordinates, considering to deal with a basin measuring  $600 \text{ km} \times 600 \text{ km} \times 2 \text{ km}$  in the zonal, meridional and vertical directions respectively and in a  $f$ -plane configuration. We choose to initialize the deep anticyclone using equation 3.5, assuring that the vortex has a null initial surface signature. The response of the sea-surface to the vortex displacement will be studied in a parametric way, for instance, varying the anticyclone characteristics introduced in section 3.2.2 ( $q_0, \alpha_R, H, z_0$ ). The reference simulation studies a deep anticyclone in the submesoscale range, having radius  $R = 15 \text{ km}$ , thickness  $H = 100 \text{ m}$  and depth  $z_0 = 300 \text{ m}$ . Every parameter of the vortex is then incremented of a varying amount (from 10 to 100% of the original value and up to 160% for the radius) and the maximum stream function at the sea-surface (a proxy of sea-level anomaly in this context) is extracted and observed.

The case of a mesoscale vortex (whose radius  $R'$  is  $R' = R + 0.7R$ ) is presented in figure 3.13; it shows four snapshots of the surface stream function exhibiting the sea-level bumps and hollows induced by the drifting anticyclone at depth.

The pattern of the surface signature, in agreement with theoretical predictions, is dipolar and grows in intensity and extent for increasing times of integration. The positive sea-level anomaly, considering an eastward drift (green arrow in figure 3.13), lays in the leading half of the vortex, whose projection at the sea surface is indicated by the green point.

The parametric study shows that the surface stream function exhibits:

- quadratic dependence with respect to the vortex radius (checked fitting the experimental data with a quadratic function);
- linear dependence with respect to the vortex initial potential vorticity;
- inversely quadratic dependence with respect to the vortex depth  $z_0$  (checked fitting the experimental data with a  $z^{-2}$  function);
- linear dependence with respect to the vortex thickness.

These results are shown in figure 3.14 and, for every run, refer to the maximum value of the surface stream function observed in the late stages of the simulation ( $t > 70$ ,

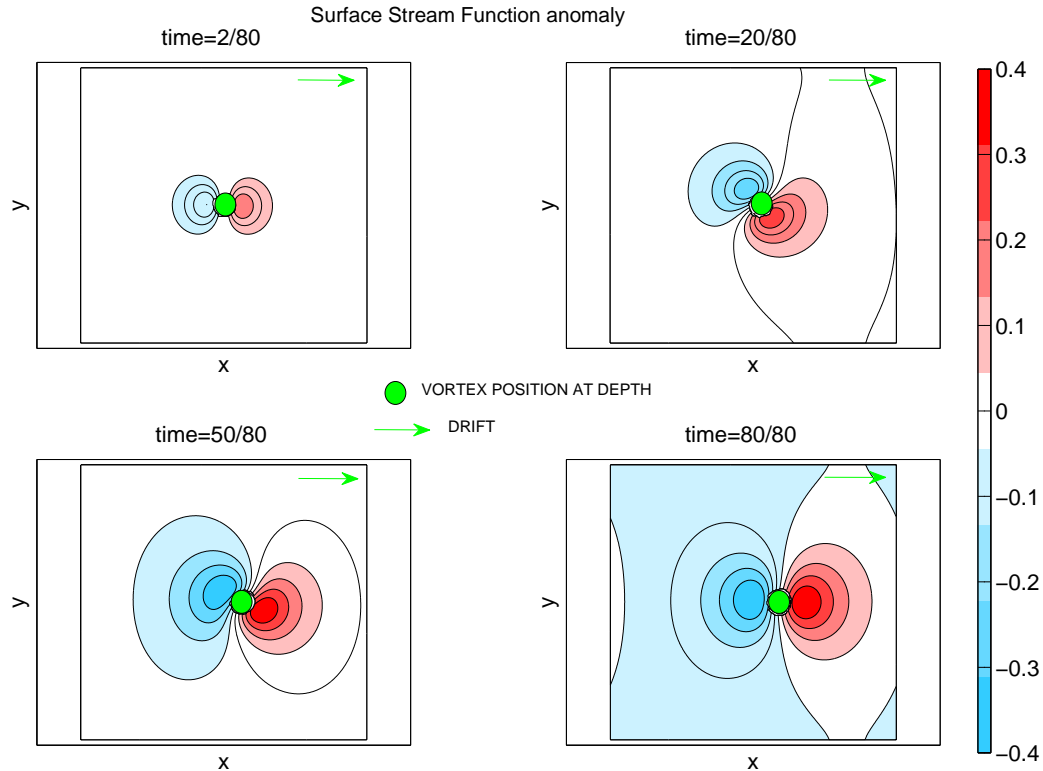


**Figure 3.13:** *Dynamics of a dipolar signature for a mesoscale deep anticyclone (CLAM-3DQG model).  $X$  and  $Y$  are the zonal and meridional boundaries of the domain. All the quantities are expressed in dimensionless units ( $du$ ).*

over 80 time steps). Given the potential vorticity structure of the vortex, shown by figure 3.1, we qualitatively compare the results of the numerical experiments with the theoretical predictions obtained for S-vortices, expressed by equation 3.27 and discussed in section 3.3.1. According to this equation, the surface stream function induced by a deep anticyclone depends linearly on the vortex potential vorticity and thickness, quadratically on its radius and has a cubic dependence on the inverse of the vortex depth. In the modeled case, the dependence of the surface signature on the vortex potential vorticity, radius and thickness are in agreement with theory (and it was confirmed fitting the experimental data with different polynomial functions, like in section 3.4.1). On the other hand, the modeled dependence on the inverse of the vortex depth, mostly turned out to be quadratic. Again, this deviation with respect to theory could mostly be due

to the structure of the modeled vortex. Like for the case discussed in section 3.4.1, the integrated potential vorticity is not null in these experiments, and deviations from theory, that dealt with perfectly isolated vortices, may occur.

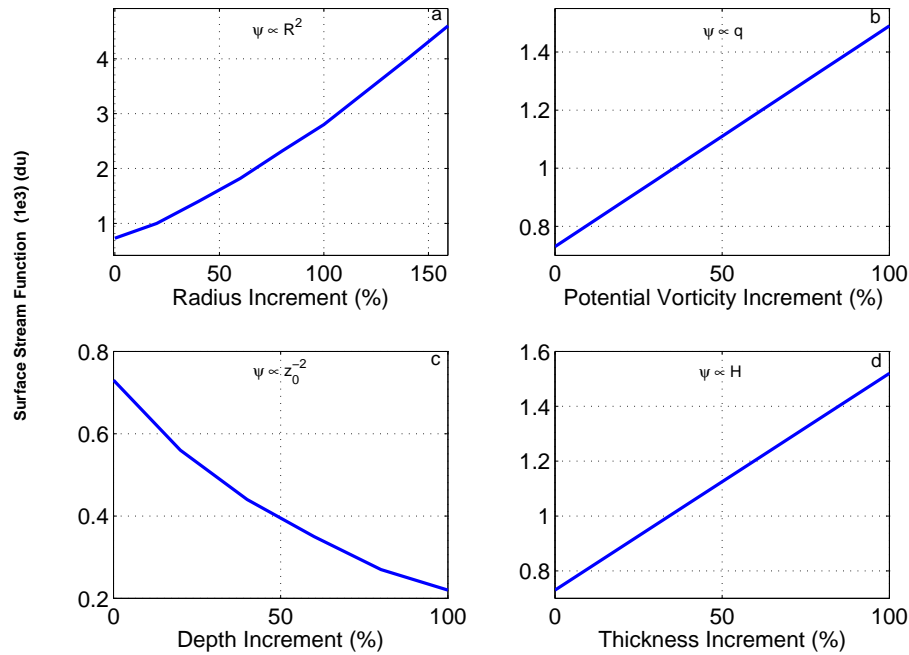


**Figure 3.14:** *Parametric study on the surface stream function induced by a deep anticyclone (CLAM-3DQG model). a) Dependence on the vortex Radius, b) Dependence on initial potential vorticity, c) Dependence on vortex Depth and d) Dependence on vortex thickness. The Stream Function is in dimensionless units and is presented as a function of the parameter increment with respect to the reference simulation.*

### 3.4.4 Surface signature of deep anticyclones: dynamic case, ROMS model

In order to characterize the surface signature of deep anticyclones in a more realistic context, the experiments with the ROMS model have been run in the  $\beta$ -plane. Similarly to section 3.4.3, the surface expression of the deep anticyclones is studied in a parametric way, varying the vortex characteristics in order to account for different oceanic eddies (see table 3.1). All the simulations have been initialized in absence of any initial sea-

level anomalies. The reference experiment consists in the evolution of a deep anticyclone with characteristics similar to a submesoscale Peddy recently observed in the Arabian Sea [L'Hégaret (2015)]. Its characteristics have been reproduced in an idealized context and are shown in figure 3.3. During its evolution, the vortex moves southwestward in the basin, in agreement with Morel and McWilliams (1997) (figure 3.15 shows the vortex displacement over 200 days). Introduction of planetary  $\beta$ -effect makes the ROMS simulations substantially different from the QG case (CLAM-3DQG model). Here, the displacement of the vortex is not due to a deep current but to self-advection. In this case, the vortex is characterized by a radius of 15 km, a thickness of 100 m, an initial angular velocity field of 0.53 rad/s (corresponding to a maximum tangential velocity of 0.2 m/s) and a depth of 300 m. The evolution of the sea-level anomaly is shown in figure 3.16. The maximum signal is reached after about 200 days and, considering the

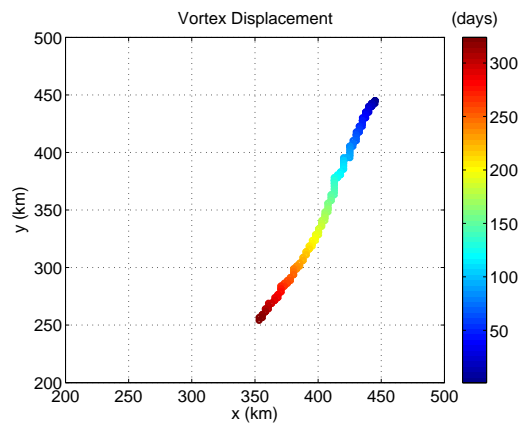


**Figure 3.15:** *Displacement of a submesoscale deep anticyclone under planetary  $\beta$  effect ( $v=0.2$  m/s,  $R=15$  km,  $H=100$  m,  $z_0=300$  m).*

dipolar structure (bottom-right snapshot), the difference between positive and negative anomalies ( $\Delta$ SSH hereinafter) does not exceed 3 mm. The maximum horizontal extent of the dipolar signature (after the vortex has been drifting for about one month) is almost 6 times the vortex diameter. Furthermore, in the early stages of the vortex evolution, one can recognize the structure predicted by the idealized model illustrated in Section 3.3.2. After one month, the initial dipolar signal triggers a Rossby wave (allowed in  $\beta$ -plane approximation) visible in the trailing half of the anticyclone, whose projection at the sea surface is given by the green dot in figure 3.16

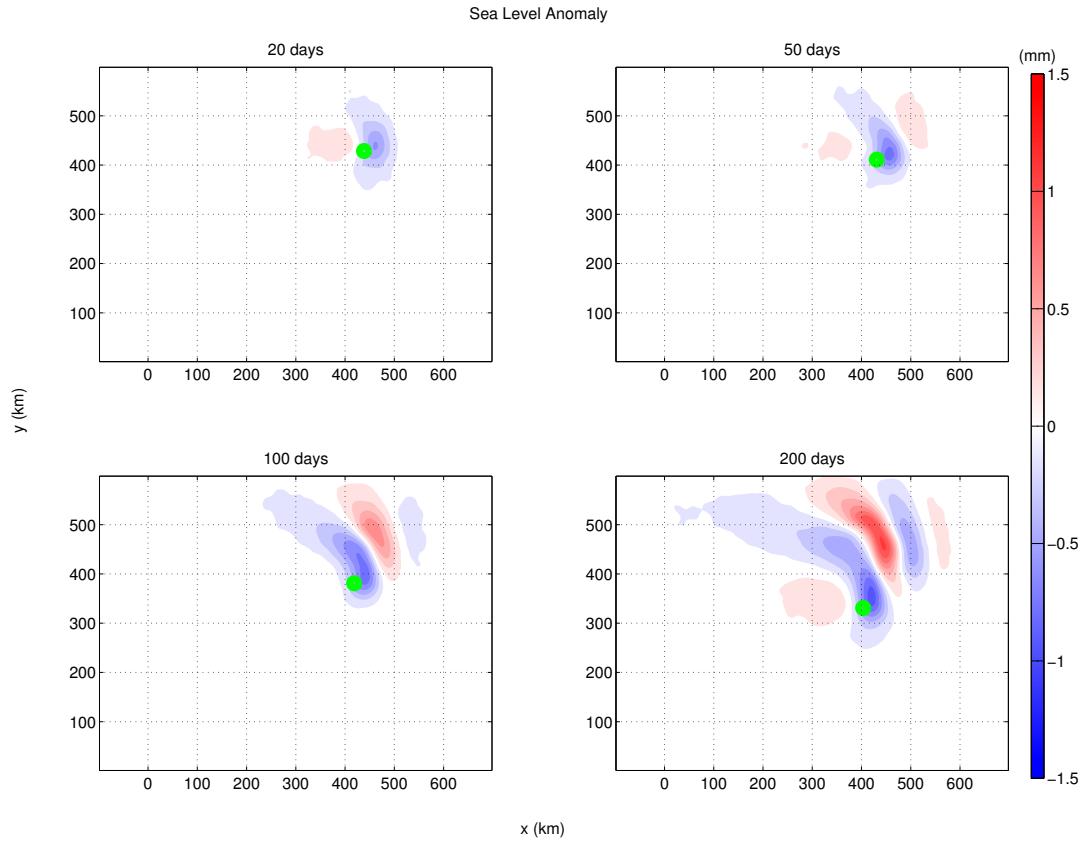


**Figure 3.16:** Sea-level anomaly induced by the displacement of a deep anticyclone in the submesoscale range ( $v=0.2$  m/s,  $R=15$  km,  $H=100$  m,  $z_0=300$  m). The green spot represents the surface projection of the vortex position at depth.

### 3.4.5 Parametric study of the dipolar signatures

The variety of deep anticyclones summarized by table 3.2 justifies a parametric study for the dipolar signature, similarly to sections 3.4.1 and 3.4.3. Simulations have been run with the prescription of null sea level anomaly at time  $t = 0$ . In order to provide a representative study, the sea-surface response is analyzed with respect to vortex radius, thickness and depth for three different angular velocity regimes. The chosen velocities are  $0.53$ ,  $0.79$  and  $1.06 \cdot 10^{-5}$  rad/s ( $0.2$ ,  $0.3$  and  $0.4$  m/s in terms of maximum tangential speed). In particular, we were interested in determining the maximum intensity of the dipolar signature as well as the time needed for the maximum intensity to be attained.

### Dependence on the vortex radius

Figure 3.17 shows the dependence of the dipolar signature on the vortex radius. The panels in the first row contain the  $\Delta SSH$  evolution computed as the difference between the maximum positive and negative sea-level anomalies in the whole basin and for every time step; note that the spatial distribution of the signal is similar to the one shown in figure 3.16. The vertical lines in the plots indicate the time step after which the simulation

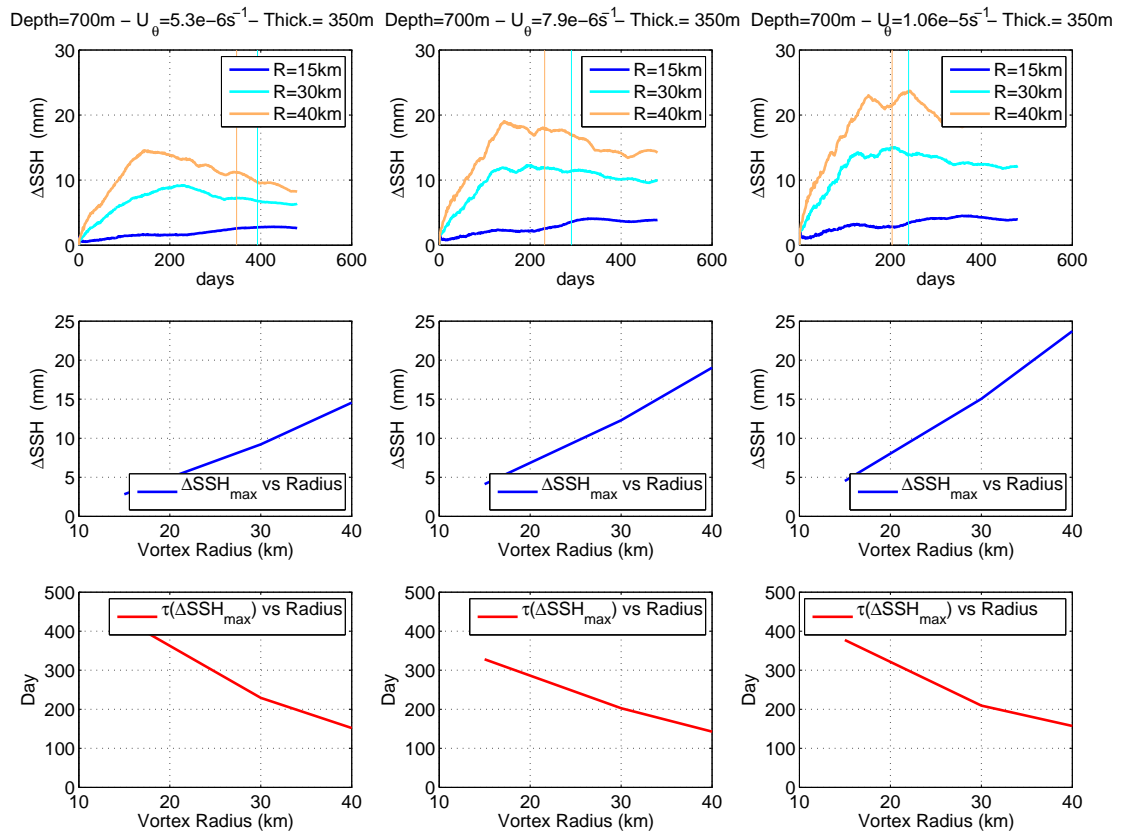


**Figure 3.17:** Dependence of the dipolar signature on vortex radius for three different angular velocity regimes. Line 1:  $\Delta SSH$  vs time, Line 2:  $\Delta SSH_{max}$  vs radius, Line 3:  $\tau(\Delta SSH_{max})$  vs radius.

is not physically acceptable, as the vortex crashes against the southern boundary of the domain. The interpretation of the results is though possible, because the maximum sea level anomaly always occurs before the vortex reaches the boundary. In figure 3.17, the

---

second and third rows show the dependence of the maximum surface signature on vortex radius and the time necessary for the maximum signature to be attained. The intensity of the dipolar signature is clearly proportional to the vortex radius, growing from a few millimeters up to more than 2 cm for a radius in the 15 to 40 km range; the time necessary for the development of the signature reduces by about 4 times from the submesoscale up to the mesoscale range (considering the 15 – 40 km radii range in our case), namely, from 400 down to 100 days.

Another effect to note is the impact of the vortex radius on the efficiency of the drift. Larger radii cause a more rapid southwestward vortex displacement, yielding a shorter time for the vortex to reach the southern boundary.

### Dependence on the vortex thickness

The dependence of the dipolar signature on thickness shows similarities with respect to the previous case. Though the signal variation looks very slight, an increase of the signature intensity with the vortex thickness is observed. Moreover, the times required for the development of the maximum signature decrease for an increase of the parameter. The only exception to this behavior is shown by the bottom-left panel of figure 3.18. The

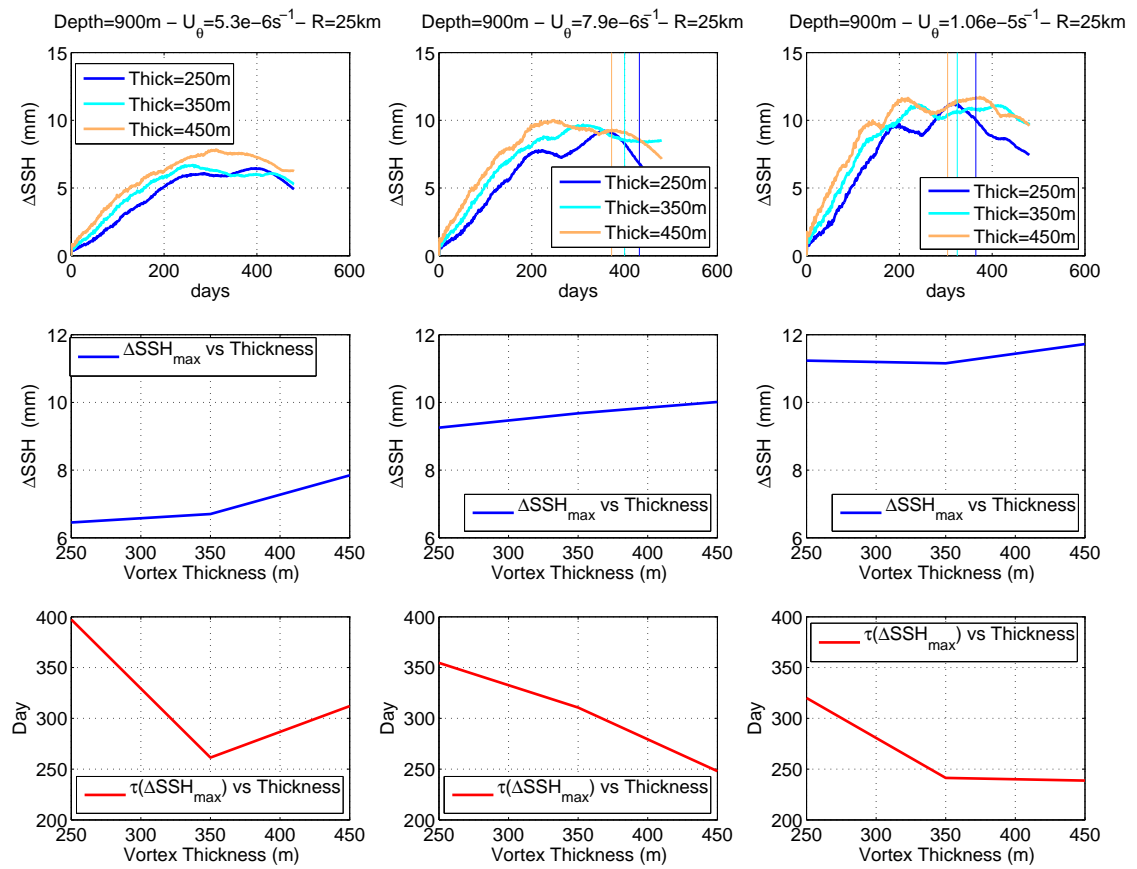


**Figure 3.18:** Dependence of the dipolar signature on vortex thickness for three different angular velocity regimes. Line 1:  $\Delta SSH$  vs time, Line 2:  $\Delta SSH_{max}$  vs thickness, Line 3:  $\tau(\Delta SSH_{max})$  vs thickness.

very slight differences between the signals (considering one velocity range at a time) can be principally due to two factors: the limited choice for the vortex parameters and the development of the Rossby wave train. The second factor is actually imposed by physical

---

reasons, while the first is a consequence of the requirements for the initial state of the simulations. In fact, not only initialization requires initial sea-level anomalies to be null, but it needs vortices to be statically stable as well (i.e., the vertical density profile across them must be a monotonic function of the  $z$  coordinate). This imposes a restriction on the parameters' choice.

In this series of experiments, the maximum intensity of the dipolar signature (defined as  $\Delta\text{SSH}$ ) never crossed the 1.5 cm threshold.

### Dependence on the vortex depth

The dependence of the dipolar signature on the vortex depth exhibits a less clear behavior in terms of the signature intensity.

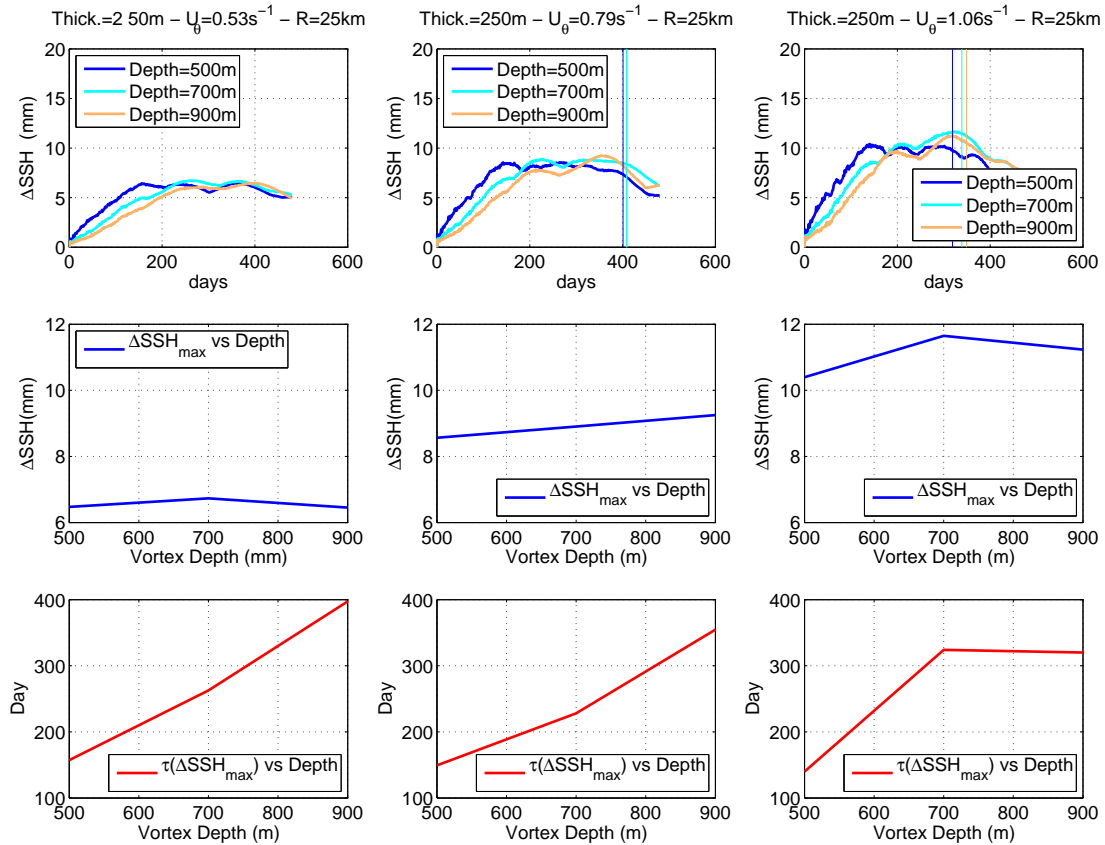


**Figure 3.19:** Dependence of the dipolar signature on vortex depth for three different angular velocity regimes. Line 1:  $\Delta SSH$  vs time, Line 2:  $\Delta SSH_{\max}$  vs depth, Line 3:  $\tau(\Delta SSH_{\max})$  vs depth.

The results seem to be in contrast with theory, as, for increasing vortex depths, the dipolar signature maximum intensity does not show a significant trend. This happened even if we let vary the depth by about 100% with respect to its initial value (from 500 to 900 m). Effects of the stratification are probably to investigate, as for example a non substantial change in Brunt-Väisälä frequency in this depth range.

The time of development of the signature grows up significantly with depth, exhibiting

an increase around 100% in the chosen depth range.

### Dependence on Vortex Rotational Velocity

Among the whole set of simulations, we chose the ones exhibiting the maximum values in terms of  $\Delta\text{SSH}$  and we characterized the dependence of the dipolar signature on the vortex swirl velocity. Figure 3.20 shows that the altimetric signature exhibits a linear dependence on the vortex swirl velocity. Furthermore, for increasing velocities (i.e., relative and potential vorticities), a decreasing time for the onset of maximum surface signature is observed.

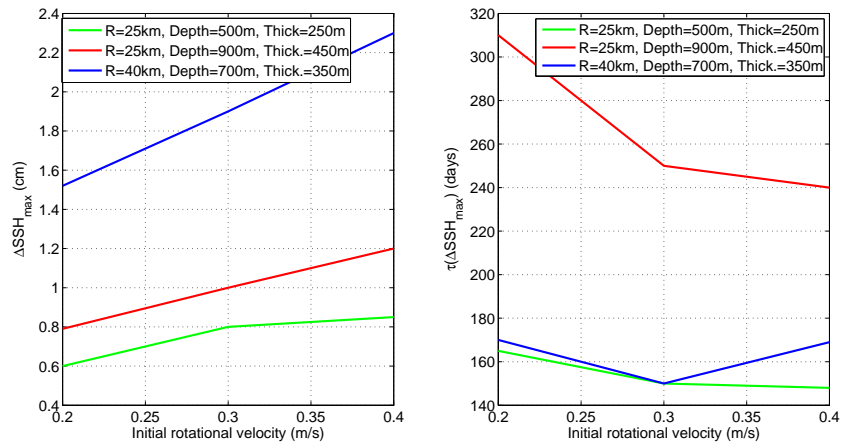


**Figure 3.20:** *Dependence of the altimetric signature on vortex angular velocity (left). Time for onset of maximum  $\Delta\text{SSH}$  signal (right).*

### 3.4.6 Surface signature of deep anticyclones: the case of a vortex advected by a surface-intensified shear flow

Here we study the development of the dipolar sea-level anomaly for an eddy drifting under the effect of a surface-intensified shear flow. The simulation was run in a east-west periodic oceanic basin measuring  $600 \text{ km} \times 600 \text{ km} \times 4 \text{ km}$  (respectively in the zonal, meridional and vertical directions) and in a  $f$ -plane approximation. The velocity profile of the zonal flow  $U_f$ , in a Cartesian reference frame with an upward pointing  $z$  axis, is expressed by equation 3.42,

$$U_f \propto yz \quad (3.42)$$

indicating that the velocity profile is characterized by a vertical and meridional shear. A computation based on equation 3.1 indicates that the zonal flow does not satisfy the Charney-Stern-Pedlosky conditions for the onset of baroclinic instability, since the potential vorticity associated to the velocity profile in (3.42) does not exhibit any sign inversions in the oceanic basin [Vallis (2006)]. This was also confirmed by simulating the long-term evolution ( $\simeq 400$  days) of the zonal flow taken separately (using the aforementioned numerical framework), that showed a mostly eastward and laminar motion. The vertical profile of  $U_f$  (centered at the position where the deep anticyclone was subsequently initialized, i.e.,  $x = y = 300 \text{ km}$ ) is shown in figure 3.21.

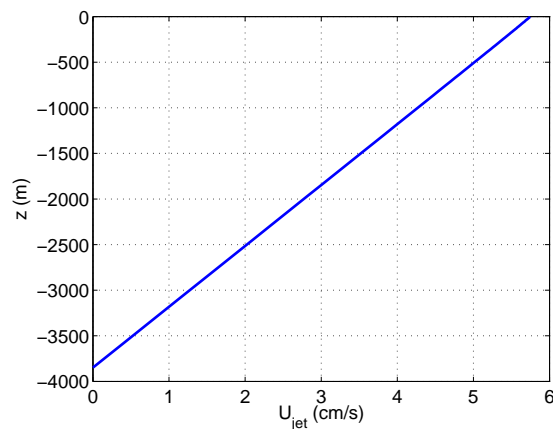


**Figure 3.21:** Vertical profile of the zonal flow of equation 3.42.

We study the case of a mesoscale subsurface anticyclone with the following characteristics: swirl velocity =  $0.4 \text{ m/s}$ , radius =  $40 \text{ km}$ , depth =  $700 \text{ m}$ , thickness =  $400 \text{ m}$ . Given the

depth of the deep anticyclone, its main core will interact with a mean eastward current of 5 cm/s, i.e. only 12% of its maximum swirl velocity.

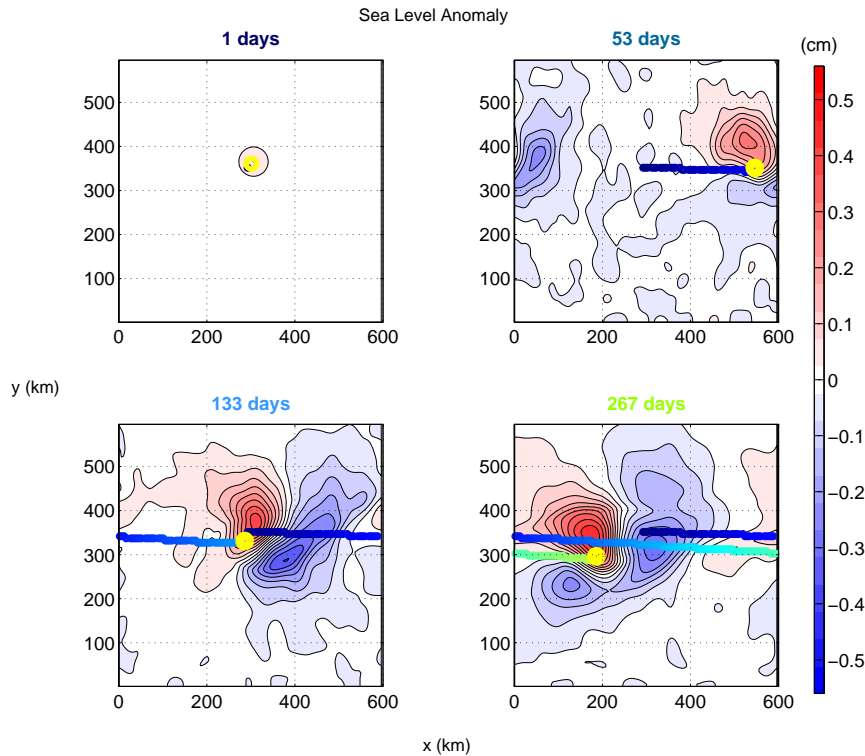


**Figure 3.22:** Onset of the altimetric signature of a subsurface anticyclone advected by a surface-intensified eastward shear flow (see also equation 3.42). The anomalies are evaluated filtering out the contribution of the large scale sea-level anomaly due to the shear flow. The eastward trajectory of the vortex is indicated by the horizontal line in the domain (blue is for the early stages of the evolution, light green is around day 270).

As figure 3.21 shows, during the 400 days of run, the vortex exhibits a mostly eastward trajectory, except for a southward displacement of its main core (figure 3.22 suggests a net southward drift of around 60 km in 270 days). The southward displacement is possibly due to the mechanism described in Colin de Verdière (1992), that relates the southward motion of Meddies to their vertical shrinking. In our case, the subsurface eddy lost 19% in thickness during 390 days, as confirmed by the evolution of the eddy isopycnal structure shown in figure 3.23 (for this particular analysis, the eddy thickness was defined as the distance between the isopycnals showing maximum deflection). The corresponding mean southward velocity was around 0.3 cm/s. These results actually underestimate the

observations of Meddy Sharon, that, during 365 days, lost 20% in thickness and moved southward at a mean velocity of 1.8 cm/s. These differences can have several reasons, like the inviscid and non diffusive conditions of the simulation (although the model advection scheme introduces numerical viscosity), as well as the nature of the background potential vorticity. Indeed, in this case, the  $f$ -plane approximation was used and the only source of a large scale PV gradient is the isopycnal structure associated to the baroclinic flow.

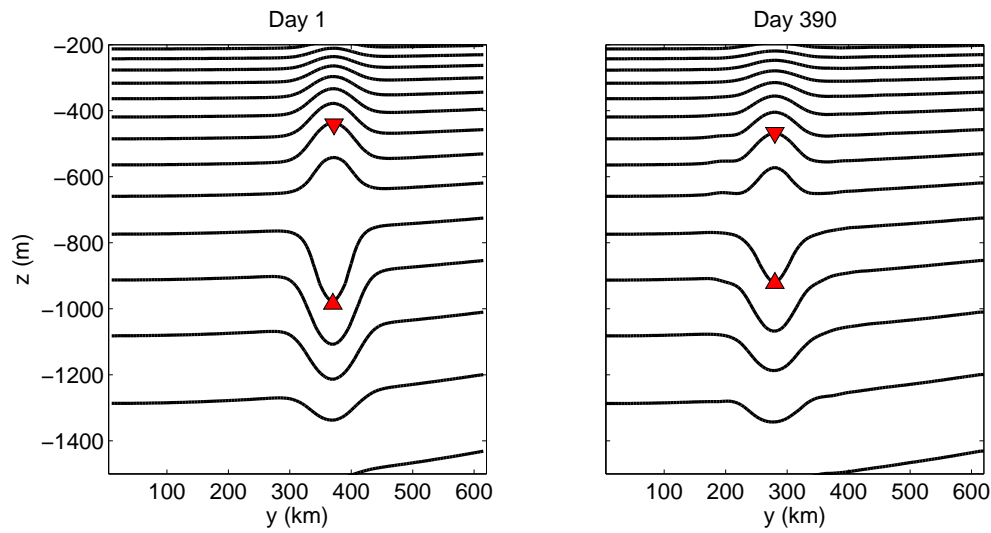


**Figure 3.23:** *Isopycnal structure across the subsurface eddy (meridional section). Left: Day 1, Right: Day 390. The red triangles indicate the positions where the maximum isopycnal deflection is observed.*

The surface signature of the subsurface anticyclone is still dipolar (note that, in this case, the sea-level anomaly is obtained subtracting the large-scale contribution of the surface-intensified shear flow). Differently from the case described in section 3.4.4, the vortex lives in an environment where the Coriolis parameter is constant, hence, no Rossby waves were excited during the vortex evolution. As a result, the vortex surface signature, once set up, was not dispersed by the propagation of a Rossby wave train and kept its original pattern unvaried for around 400 days. The maximum  $\Delta$ SSH kept a fairly constant value of approximately 1 cm, and the positive pole of the signature was spatially correlated with the position of the eddy at depth (indicated by the yellow dot in figure 3.22). Furthermore, considering an eastward displacement of the vortex, the dipolar signature exhibits an inverse polarity with respect to the case described in sections 3.3.2 (dynamic case), 3.4.3 and 3.4.4. Indeed, introducing a surface-intensified shear flow, one modifies the dynamics of the upper oceanic layers. In fact, considering

the flow vertical profile, the water columns above the deep anticyclone (e.g.  $U_1(z)$  in figure 3.24) initially move faster than the deep vortex (e.g.  $U_2(z)$  in figure 3.24). As a result, the relative motion of the vortex (at depth) plus the water columns, would correspond to an eddy moving in the opposite direction with respect to the upper oceanic layers (see also figure 3.24). This mechanisms can explain the polarity inversion of the vortex surface signature.

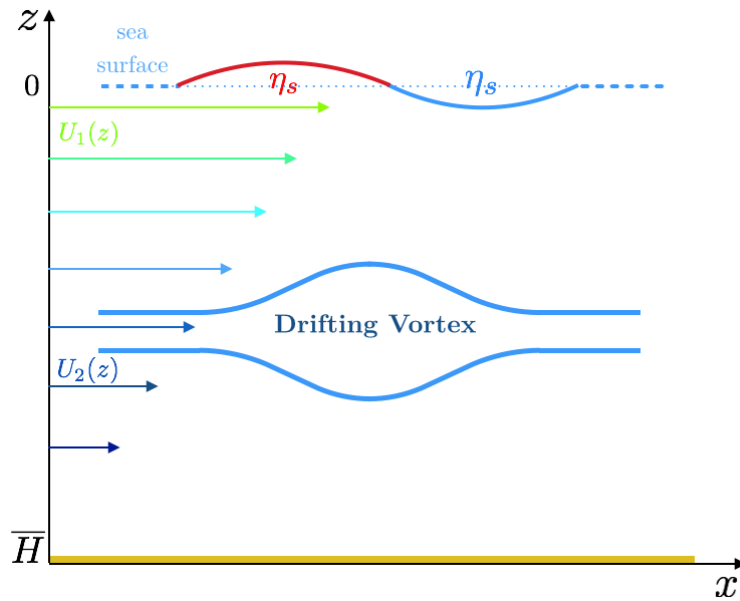


**Figure 3.24:** *Cartoon of the onset of the altimetric signature for a subsurface anticyclone advected by a surface-intensified eastward shear flow.*

Summarizing, in sections 3.3 and 3.4, the steady signature of deep anticyclones has been investigated numerically by means of a QG model (CLAM-3DQG) and of a primitive equations model (ROMS) in a steady and a dynamic case. In the steady case, we could confirm that the surface signature is a monopolar positive anomaly in sea-surface elevation. Furthermore, a parametric study on the vortex parameters suggested that this feature depends linearly on the vortex radius, thickness and rotational velocity, while it decreases with the vortex square depth.

This behavior can also be compared with the predictions of analytical point vortices, if structures with low Rossby numbers are dealt with and if their potential vorticity isosurfaces do not intersect the ocean surface.

The mechanism of development of a dipolar surface signature for a deep anticyclone has been confirmed by both the CLAM-3DQG and the ROMS model. For the simulations

with ROMS, in  $\beta$ -plane approximation, the limit of short times has to be considered. In fact, the vortex displacement allows the generation of a Rossby wave train at the sea surface that strongly affects the vortex signature. When the  $f$ -plane approximation is used, and the vortex interacts with a surface intensified jet, the signature maintains a dipolar structure for times that can exceed one year and its positive pole is mostly located above the center of the deep anticyclone.

The parametric dependence of the dipolar signature on the vortex parameters is different in a QG (CLAM-3DQG) and Primitive Equations (ROMS) context. In the first case, the modeled anticyclone, living in a  $f$ -plane configuration and advected by a deep current, maintains a dipolar signature all along the simulation and its intensity depends linearly on the vortex potential vorticity and thickness, quadratically on the vortex radius and it diminishes with the vortex square depth. In the second case, the dependence is linear on the vortex radius, thickness and rotational velocity while no significant trend can be observed as a function of the vortex depth. We believe that the formation of the Rossby wave train and effects of the ocean background stratification can be responsible of this different behavior, but further analyses may be necessary to confirm this.

### 3.5 Discussion, Conclusions and Openings

In this chapter, we have investigated the surface signature of deep anticyclones by means of analytical and numerical models. The impact of such deep structures on the sea-surface is a key element for their detection by means of satellite altimetry, which provides global and synoptic information on the world ocean. The capabilities of satellite altimetry will improve in years to come with the SWOT mission [Fu et al. (2009)]. This satellite mission will provide global altimetric measurements of the sea-surface at submesoscale horizontal resolutions and with precisions higher than 2 cm (which is presently achieved only for along-track observations [Fu and Cazenave (2000)]). The detection of deep vortices is an important task in oceanography. In fact deep vortices, together with surface-intensified cyclones and anticyclones, contribute to the global three-dimensional distribution of oceanic tracers.

In recent years, many studies have investigated the surface signature of subsurface anticyclones in realistic and idealized contexts [Stammer et al. (1991), Bashmachnikov and Carton (2012), Ienna et al. (2014), Assassi et al. (2016)] and concluded that, if deep anticyclones are dealt with, the expected influence on the sea surface results in a positive altimetric anomaly, mostly due to their three-dimensional density structure. A recent theoretical approach, based on QG theory and point vortex model, stated that the surface altimetric signature of a Meddy (a subsurface anticyclone) depends linearly on the vortex thickness and potential vorticity, quadratically on its radius and linearly on the inverse of the vortex depth [Bashmachnikov and Carton (2012)].

In this work, analytical models based on the QG framework, as well as numerical experiments in the QG and Primitive Equation context, have allowed us to characterize the surface signature of deep anticyclones, leading to the following main results:

- If analytical point vortex models are used in a more realistic context, i.e., structures like the R-vortices or S-vortices [Morel and McWilliams (1997)] are taken into account, the sea-level anomaly above deep steady anticyclones still depends linearly on the vortex potential vorticity  $q$ , the thickness  $H$  and quadratically on the vortex radius  $R$ . In fact, these parameters are included in the quantity  $\Gamma = qHR^2$  of equations 3.19 and 3.27. Despite this, contrarily to recent theoretical results [Bashmachnikov and Carton (2012)], we found that the surface signature can depend on the inverse of the cubic depth (according to theory). This is due to a screening effect of the opposite sign potential vorticity anomalies surrounding the central point vortex, which cannot be taken into account if a single point vortex is used. Furthermore, section 3.4.2 showed that the point vortex models we proposed

are in agreement with the results obtained using realistic vortices. This is true if the anticyclone potential vorticity isosurfaces do not intersect the sea-surface (i.e., if the vortex motion is fully immersed in the ocean) and if the vortex can be described by the QG approximation (Rossby number  $\ll 1$ ). The surface steady signature is always characterized by a positive monopolar anomaly (if an ocean at rest is considered). For realistic deep anticyclones spinning at about 0.2 m/s, this anomaly reaches  $\mathcal{O}(\text{cm})$  if mesoscale structures are considered and if the ratio between the vortex depth and thickness is around 0.9. We recall that a signature in the range of the centimeters can assure detection by satellite altimetry (provided the idealized condition of an ocean at rest). This is also summarized by figure 3.25, in which the numerically derived steady signature (sea-level anomaly, see also section 3.4) for anticyclonic vortices is shown in a Thickness - Depth diagram and for an average stratification (typical of  $30^\circ\text{N}$ ). Results are presented in both a submesoscale (Radius=15 km, left panel) and a mesoscale range (Radius=50 km, right panel) and for rotational velocities of 0.2 m/s. The green line (right panel) indicates the 2 cm threshold, representing the measurement precision for along-track satellite altimetric products (for instance, a fraction of the global AVISO maps [Fu and Cazenave (2000)] and future global SWOT measurements [Fu et al. (2009)]). Hence, all signals below the green line (right panel) represent a detectable sea-level anomaly. It is evident that no deep vortex in the submesoscale range has a chance to be detected by present-day and future satellite altimetry (no signal crosses the 2 cm threshold, left-panel) while, according to table 3.1, for larger MEDDIES, LEDDIES and REDDIES, detection is possible;

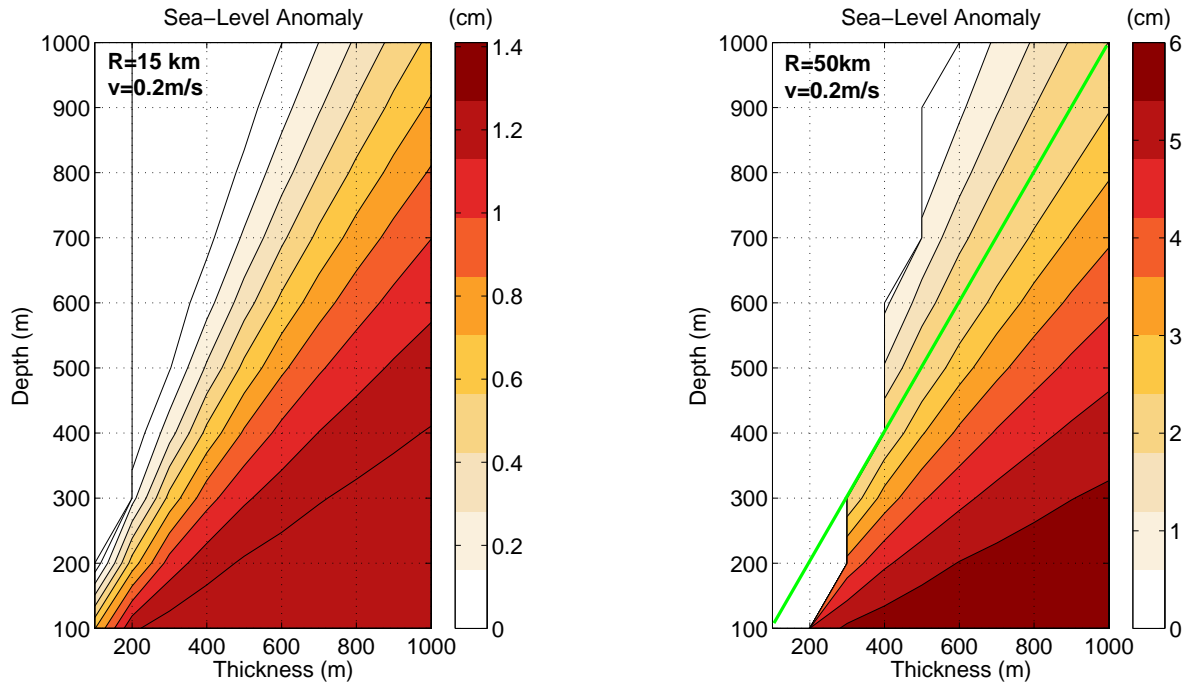


**Figure 3.25:** Sea-level anomaly in a Thickness-Depth diagram for anticyclonic vortices in the submesoscale range (left) and in the mesoscale range (right). The green line (right panel) indicates a sea-level anomaly of 2 cm.

- The nature of the surface signature depends on the dynamical context in which the vortex lives in. If drifting effects are taken into account and the initial steady signature is absent, both a theoretical and a numerical framework predict that a dipolar, rather than a monopolar signature will develop. This is clearly shown by simulations in a QG framework using the CLAM-3DQG model. Furthermore, if the vortex drift is obtained by means of a linearly sheared current in a  $f$ -plane context, the dipolar structure remains stable for long times. A parametric study on the intensity of the surface signature shows that this feature increases linearly with the vortex potential vorticity and thickness, quadratically on the vortex radius, and that it decreases with the square depth of the anticyclone;
- Using the ROMS model in idealized configuration and in a  $\beta$ -plane approximation, we could determine that the surface signature of deep anticyclones is still dipolar. This is true for short times only, in fact, as the vortex drifts southwestward because of planetary  $\beta$ -effect, the development of a Rossby wave train is observed behind

the main initial signature. The parametric study on the surface signature stated that this feature depends linearly on the vortex radius, thickness and swirl velocity, while results have a more complicated interpretation for what concerns the vortex depth. The oceanic stratification and the excitation of the Rossby waves may degrade the vortex surface signature, but further investigations are necessary to explain this behavior. Finally, provided the idealized condition of an ocean at rest, the detection of subsurface vortices by means of satellite altimetry is assured in the mesoscale range only, i.e., for structures generating anomalies of the order of some centimeters in the sea-surface elevation;

- The simulation with the primitive equations model ROMS, in a  $f$ -plane approximation and in presence of a shear flow, pointed out that a subsurface anticyclone generates a dipolar signature in the long-time limits (more than one year). Moreover, in this case, the positive pole of the signature was spatially correlated with the eddy position at depth, which is more in agreement with observations [Bashmachnikov and Carton (2012), Bashmachnikov et al. (2013)]. This result indicates that, most likely,  $\beta$ -effect alone cannot explain the surface expression of subsurface anticyclones and that the role of surface-intensified advection currents has to be taken into account.

We believe that possible perspective for this work can be summarized by the following main lines:

- characterization of the spatial and temporal correlation for the surface signatures of deep vortices (still in a numerical context). Determining the typical space and time scales over which the signatures vary is crucial for their automatic detection by means of satellite sensors. In particular, the life-cycle of the subsurface structures can be sampled at a rate related with the measurement repetitiveness of present and future generation satellite sensors. Our point is that even signatures with critical signal-to-noise ratios can be good candidates for detection of subsurface structures. In particular, this will happen when their imprints in oceanic fields are persistent and preserve a recognizable pattern;
- take into account the possibility of interaction between subsurface vortices, e.g., merger (already documented by hydrological surveys [Schultz Tokos et al. (1994), Richardson et al. (2000a)]). This would require the analysis of two main mechanisms: first, the conditions under which merger is possible and, second, to which extent merger is able to feed a subsurface eddy with potential vorticity or to modify its three-dimensional structure. Indeed, recalling that the crucial parameters

driving the surface expression of deep anticyclones are the potential vorticity, the radius and the vertical extent, any variation of these parameters could certainly affect the vortex signature at the sea-surface (this problem will be studied in detail in chapter 4);

- improve the characterization of the surface signatures of deep vortices via analyses of the sea-surface temperature (SST) and/or sea-surface salinity (SSS) fields. The results could determine the validity of the synergy between Sea-surface height, temperature and salinity for the detection of deep vortices via satellite observations. Actually, both the numerical and the observational approach are possible. An example of observational approach is given by Bashmachnikov et al. (2013), who studied the manifestation of Mediterranean Water Eddies in both altimetry and SST. In chapter 5 we will present a study based on a realistic numerical simulation [Barbosa Aguiar et al. (2013)], on the surface expression of Mediterranean Water Eddies in SSH, SST and SSS fields. The advantage of using a realistic model consists in the simultaneous availability of informations on the full three-dimensional Meddies structure and on the ocean surface dynamics. Furthermore, the realistic context has the additional advantage to account for the effects of oceanic bottom topography, a non-negligible feature for the study of Meddies (as also pointed out in Richardson et al. (2000a)).

# Chapter 4

## On the merger of subsurface isolated vortices

This chapter is inspired by the paper

*On the merger of subsurface isolated vortices*, by

Daniele Ciani<sup>1</sup>, Xavier Carton<sup>1</sup> & Jacques Verron<sup>2</sup>

1: Laboratoire de Physique des Océans, UMR6523, Université de Bretagne Occidentale, Brest, France

2: Laboratoire de Glaciologie et Géophysique de l'Environnement, UMR5183, CNRS-UJFR, Grenoble, France

published in the Journal of Geophysical and Astrophysical Fluid Dynamics  
2016 - 110 (1) 23-49

### 4.1 Introduction

The global ocean is highly populated by vortical structures. Such features are recirculating motions at both mesoscale and submesoscale; they can be found at different depths in the water column [Ebbesmeyer et al. (1986); Carton (2001); Chelton et al. (2011); Shapiro and Meschanov (1991); Richardson et al. (2000a); Rubino et al. (2012); Ciani et al. (2015)]. The mechanisms generating such structures range from the instability

of large scale currents to small scale turbulence or deep convection. Due to planetary rotation and to the oceanic stable stratification, mesoscale vortex motions are mostly confined in the horizontal plane. Thus, vortices have a major impact on the evolution of water masses across the oceans, regulating the three-dimensional distribution of active and passive oceanic tracers.

Oceanic vortices often interact with currents, topography or other vortices [Masina and Pinardi (1991); Schultz Tokos et al. (1994); Cenedese et al. (2005); Filyushkin et al. (2011); Barbosa Aguiar et al. (2013); Sokolovskiy et al. (2013); L'Hégaret et al. (2014); Molemaker et al. (2014)]. Among these interactions, vortex merger gives rise to larger structures; it has been shown in geophysical turbulence studies to explain the inverse energy cascade (i.e., energy transfer from small to larger spatial scales). Merger happens when two like-signed vortices get in contact, start exchanging fluid masses, collapse towards each other and eventually generate a single coherent structure. The merger of vortical structures was also considered in atmospheric studies and engineering applications, since it plays a role in the evolution of air masses [Kieu and Zhang (2008)] and in the dynamics of propeller wakes or wind turbines [Delbende et al. (2015)].

In an oceanographic context, vortex merger has been mostly investigated and observed by means of *in-situ* measurements [Schultz Tokos et al. (1994), L'Hégaret et al. (2014)], realistic modeling [Barbosa Aguiar et al. (2013), Molemaker et al. (2014)], and analytical and idealized numerical modeling in a quasi-geostrophic context [Carton (1992), Masina and Pinardi (1991), Verron et al. (1990), Reinaud and Dritschel (2005), Bambrey et al. (2007)]. Potential Vorticity (PV) or its anomaly with respect to rest, is a key quantity to study the problem, since it is conserved for all fluid elements in absence of dissipation.

In past studies, it has been pointed out that critical conditions have to be verified for merger to occur. For instance, the distance between the two vortices has to reach a threshold which depends on the vortex potential vorticity structure.

When barotropic vortices are studied, provided a uniform PV structure (unshielded vortex), this distance (evaluated between the centers) is about 3.2 to 3.3  $R$ , where  $R$  is the vortex radius [Overman et al. (1981), Dritschel (1985), Dritschel and Legras (1991), Dritschel (1995)]. If more realistic vortices are studied (e.g. Gulf-Stream rings) the critical distance can be smaller than 2.5  $R$ , as stated by Masina and Pinardi (1991) and Valcke and Verron (1997). For realistic vortices, the PV structure changes in sign in the horizontal or in the vertical (Olson, 1980; Paillet et al., 2002). In the first case, the horizontal PV will be composed of a negative core surrounded by an opposite sign annulus. This annulus can reduce the critical merging distance due to shielding effect of

the vorticity annulus [Carton (1992)].

On the other hand, Reinaud and Dritschel (2005) pointed out that, in three dimensional contexts, the merging process is also influenced by the vortex shape. Prolate and tilted structures can in fact become unstable and eventually merge at higher distances than predicted by classical merger. Moreover, Filyushkin and Sokolovskiy (2011) have shown that the critical distance for the merging lenses (which are supposed to be vortex patches in the middle layer in the three-layer quasi-geostrophic model) is a non-monotonous function of the Froude number.

In this work, we investigate the merger of two identical subsurface anticyclones in the framework of the full primitive equations, for idealized vortices representing several types of oceanic subsurface eddies, e.g., Meddies, Peddies and Reddies, respectively subsurface eddies generated by the Mediterranean water, Persian Gulf water and Red Sea water outflows [Richardson et al. (2000a), Senjyu et al. (1998), Shapiro and Meschanov (1991)]. This study is carried out by means of the Regional Oceanic Modeling System [Shchepetkin and McWilliams (2005)]. The study has been motivated by occurrence of Meddy collisions off of Gibraltar strait [Schultz Tokos et al. (1994), Barbosa Aguiar et al. (2013), L'Hégaret et al. (2014)] as well as the detection of small lens-like vortices (radius  $\simeq 15$  km), the so called Peddies, generated by the Persian Gulf water outflow in the Arabian Sea [L'Hégaret (2015)]. We will summarize the family of subsurface eddies using two types of idealized structures, that will be labelled with M and P, to indicate larger Meddy-like vortices and the smaller Peddy-like structures.

Here, the study will be carried out in an idealized context, which is the ideal framework for a parametric investigation. The subsurface anticyclones are here horizontally and vertically shielded. We will determine the critical conditions for merger of subsurface anticyclones to occur, also accounting for the sensitivity to vortex rotational velocity and to background stratification.

This chapter is organized as follows. Section 4.2 focuses on the description of the model and the determination of the initial states for the merger experiments. We go on illustrating the results of the simulations in section 4.3, defining the critical conditions for merger to take place. In section 4.4, we describe the effects of merger on the structure of the final vortex and in particular on its deformation. Finally, the conclusions are presented in section 4.5.

## 4.2 Materials and Methods

We study the interaction of subsurface anticyclones in an idealized flat-bottomed, doubly-periodic oceanic basin and in  $f$ -plane approximation. Our tool of investigation is the primitive equation ROMS model [Shchepetkin and McWilliams (2005)]. The oceanic basins under consideration are of three types, and they are chosen in order to fit the idealized structures investigated here. If larger Meddy-like vortices are dealt with (radius  $\simeq 30$  km), the basin measures  $500 \text{ km} \times 500 \text{ km} \times 3 \text{ km}$  for the zonal, meridional and vertical coordinate, respectively. In this case, the horizontal resolution is 2 km. For the study of Peddy-like structures (radius  $\simeq 15$  km) we reduce the horizontal extent of the basin to  $300 \text{ km} \times 300 \text{ km}$  but we increase the horizontal resolution to 1 km. In a final study, in order to describe smaller features generated after the merger, we keep the horizontal extent of the basin to  $300 \text{ km} \times 300 \text{ km}$  and we choose a horizontal resolution of 500 m. For all the cases, the vertical discretization is given by 80 non-uniformly spaced levels (a lower resolution is set for bottom levels). All the experiments are characterized by a free decaying dynamics. Each of the analyzed simulations is initialized by means of a background density stratification  $\bar{\rho}(z)$ :

$$\bar{\rho}(z) = \rho_0 \exp(-\alpha z/\bar{H}) \quad (4.1)$$

with  $\alpha = 0.18$ ,  $\bar{H} = 3$  km (the vertical extent of the basin) and  $\rho_0 = 1027.5 \text{ kg}\cdot\text{m}^{-3}$ . The parameters have been chosen in order to respect the geography of the Rossby radius of deformation ( $R_d$  hereinafter) [Chelton et al. (1998)]. We initially set this parameter to about 36 km, which is a typical value of  $R_d$  in the north-eastern Atlantic. Furthermore, such a  $R_d$  is a good approximation of the internal radius of deformation in the northern Arabian Sea (about 40 km), making it suitable for both Meddies and Peddies/Reddies applications. This choice is justified by occurrences of Meddy collisions described by numerical models and observations [Schultz Tokos et al. (1994), Barbosa Aguiar et al. (2013), L'Hégaret et al. (2014)]. Note that  $R_d$  is computed via determination of the baroclinic modes associated to our analytic stratification and it is the internal radius of deformation related to the first baroclinic mode.

Cyclogeostrophic balance is used in order to derive the density anomaly associated to the subsurface anticyclones at the beginning of the simulation. In this way, the Coriolis acceleration, pressure gradient field and the centrifugal acceleration can be taken into account, which is an advisable choice if structures with  $Ro \simeq 1$  are studied (Carton, 2001).

In cylindrical coordinates, the cyclogeostrophic balance is expressed by

$$\frac{v_\theta^2}{r} + f_0 v_\theta = \frac{1}{\rho_0} \frac{dp}{dr}(r, z) \quad (4.2)$$

with  $r$  representing the distance from the center of a generic vortex,  $v_\theta$  its azimuthal velocity,  $f_0$  the Coriolis parameter and  $dp/dr$  the pressure gradient field. This relation, provided knowledge of the velocity field, contains the information on the density structure associated to the vortex. This balance is only an approximation of the gradient-wind balance, which should be used for multiple vortices, but which is more complex to implement. The initial velocity field is an analytical approximation of a subsurface anticyclonic vortex:

$$v_\theta = -\frac{v_0 r}{R} \exp\left(-\frac{r^2}{R^2}\right) \exp\left(-\frac{(z-z_0)^2}{H^2}\right), \quad (4.3)$$

where  $v_0$  is the intensity of the field (in  $\text{rad}\cdot\text{s}^{-1}$ ),  $R$  its Radius,  $z_0$  its position along the vertical and  $H$  the thickness. Integrating (4.2) between  $r$  and  $\infty$ , and, recalling that only coherent vortices are treated in this work, the pressure field can be assumed to be zero far from the vortex center (namely at  $r = \infty$ ) so that one can write

$$\int_r^\infty \frac{dp'}{dr'}(r', z) dr' = p'(\infty) - p'(r, z) = -p'(r, z) \quad (4.4)$$

which finally provides the pressure field

$$p'(r, z) = \beta \exp\left(-\frac{2(z-z_0)^2}{H^2}\right) \exp\left(-\frac{2r^2}{R^2}\right) - \gamma \exp\left(-\frac{(z-z_0)^2}{H^2}\right) \exp\left(-\frac{r^2}{R^2}\right) \quad (4.5)$$

with

$$\beta = \frac{\rho_0 v_0^2}{4}, \quad \gamma = \frac{\rho_0 f_0 v_0 R}{2}.$$

The  $z$ -derivative of (4.5) yields the density anomaly associated with the vortex and this anomaly is then superimposed on the rest stratification to obtain the total three-dimensional field. The hydrostatic equilibrium is imposed and it prescribes density anomalies directly from pressure anomaly  $p'(r, z)$ :

$$\frac{1}{g} \frac{dp'}{dz}(r, z) = -\rho'(r, z), \quad (4.6)$$

where  $g$  is the gravity acceleration. A snapshot of a typical initial state for subsurface anticyclones' merger experiments is shown in figure 4.1. The vertical sections of density,

velocity field and Ertel potential vorticity anomaly (PVa hereinafter) are given for Meddy-like (M) and Peddy-like (P) vortices (hereinafter, the M and P label will be used for simplicity). Note that the expression for the Ertel potential vorticity is given by:

$$PV = \frac{1}{\rho} [(\partial_x v - \partial_y u + f) \partial_z \rho - \partial_z v \partial_x \rho + \partial_z u \partial_y \rho] \quad (4.7)$$

with  $(u, v)$  the zonal and meridional components of the velocity field, respectively (Vallis, 2006). The PVa is computed from (4.7) as

$$PVa(\bar{x}, t) = PV(\bar{x}, t) - PV_{rest}(\bar{x}, t) \quad (4.8)$$

where  $\bar{x} = (x, y, z)$  and the subscript *rest* indicates a region which is not affected by the eddies' dynamics.

These initial states represent our reference configuration, as they fit most of the observed subsurface vortices in the world ocean [Pingree and Le Cann (1993b), Carton (2001), Bashmachnikov and Carton (2012)].

The PVa vertical structure at time  $t = 0$ , figure 4.1 (M and P case), suggests that we are dealing with a hybrid structure containing features of both *S*-vortices and *R*-vortices. *S* and *R*-vortices are idealized quasi-geostrophic interior eddies whose potential vorticity structure (QGPV) is determined by the relative dominance of stretching and rotation, respectively [Morel and McWilliams (1997)]. In the *R* case, the eddy exhibits a negative QGPV core surrounded by an opposite sign QGPV annulus, while *S* structures consist of a QGPV negative core vertically bounded by opposite sign QGPV lobes (see also figure 1 in Morel and McWilliams, 1997). In our case, a negative PVa core is horizontally and vertically shielded by means of a positive PVa annulus and a pair of positive lobes, respectively. If the relative distance between the two anticyclones decreases, the positive PVa annuli, surrounding the vortex internal cores can interact, thus generating a series of alternating positive and negative PVa poles, as shown in the bottom-right panel of figure 4.1. In the same panel, we show that the PVa upper lobes are absent. This is due to the steepness of the chosen density profile (exponentially decaying with depth, as shown in equation 4.1) close to the sea-surface. For shallower and deeper eddies (top-right panel of figure 4.1) both the horizontal and vertical shields are present.

As also illustrated by earlier works [Carton (1992), Valcke and Verron (1997)], we will show the role played by the PVa annuli in the merger: in some cases they will prevent the merging process via dipolar effects.

In the P case, the pair of anticyclones is initially placed at a depth of 1000 m, the vortex radii are of 15 km, their thickness is around 200 m and the initial swirl velocity is of 0.2 m/s. For the M pair, depth and swirl velocity remain the same, and we choose a

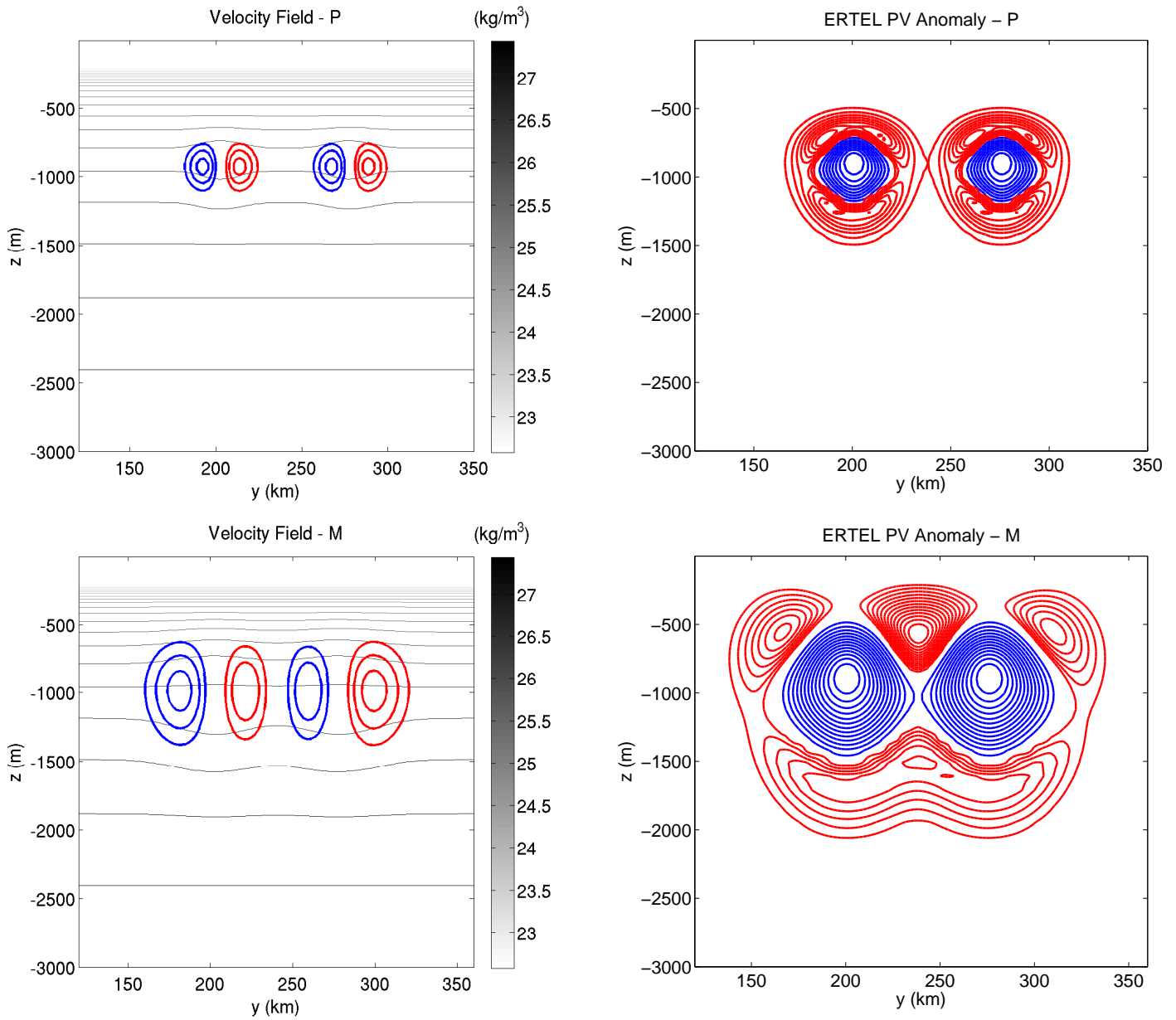


**Figure 4.1:** Initial state for subsurface vortex merger experiments with the ROMS model. Top-left and bottom-left: Vertical sections of density and swirl velocity field for P and M-vortices. The bold contours indicate the zonal component of the swirl velocity and go from 0.1 m/s to 0.2 m/s at intervals of 0.05 m/s. Red and blue lines indicate a flow directed towards or going out of the y-z plane, respectively. Top-right and bottom-right: Vertical section of PVA for P and M-vortices. The PVA shields are given by red contours.

radius of 30 km and a thickness around 500 m. This can be justified by observations of subsurface anticyclones in the mid-latitude ocean [Pingree and Le Cann (1993b), Carton (2001), Bashmachnikov and Carton (2012)]. The dimensionless parameters describing our problem are the Rossby number  $R_0$ , the Burger number  $Bu$ , the Reynolds number  $Re$  and the stretching factor  $S$ . They are all summarized in table 4.1 and, hereinafter, they will also be used for the characterization of subsurface vortices. Note that in table 4.1, we introduce three quantities:

- $\nu$ , the fluid kinematic viscosity;
- $\Delta h$ , the vortex induced isopycnal deformation, evaluated along the vertical axis, at the level where  $\partial_y \rho(y, z)$  exhibits its maximum value (solid arrow in figure 4.2).
- $\bar{h}$ , the thickness of the unperturbed isopycnal layer bounding the subsurface vortex (evaluated at  $r = \infty$  from the vortex center, dashed arrow in figure 4.2);

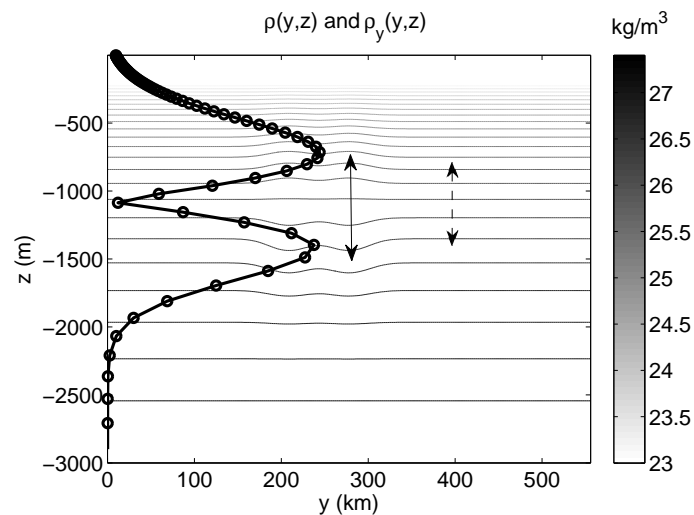


**Figure 4.2:** Meridional section of density field  $\rho(y, z)$  and its meridional gradient (bold line), in a  $M$  case. The solid and dashed arrows indicate the isopycnal deformation induced by the subsurface vortex and the corresponding unperturbed isopycnal layer, respectively.

Summarizing, the subsurface vortex merger experiments take place in a high  $Re$  regime. Though explicit kinematic viscosity is set to zero in our experiments,  $Re$  is not infinite. Indeed, the model advection scheme introduces an intrinsic (numerical) viscosity. Furthermore, if rotational velocities are set to their reference value, geostrophy is best

**Table 4.1:** *Characteristics of the modelled subsurface vortices in terms of dimensionless hydrodynamical numbers.*

	Definition	Value (M)	Value (P)
BURGER NUMBER	$Bu = (R_d/R)^2$	1.36	5.42
REYNOLDS NUMBER	$Re = v_\theta R/\nu$	$\gg 1$	$\gg 1$
ROSSBY NUMBER	$R_0 = v_\theta/(f_0 R)$	0.13	0.26
STRETCHING FACTOR	$\Delta h/\bar{h}$	0.35	0.41

verified for M vortices ( $Ro \ll 1$ ). The stretching factor indicates that in both M and P cases, the relative isopycnal deformation is around 30%. In the end, the Burger numbers suggest that, for the M case, stratification and rotation will influence the motion to a similar degree ( $Bu \simeq 1$ ). In the P case ( $Bu > 1$ ), the effects of rotation will dominate and the dynamics will tend to a two-dimensional-like behavior [Cushman-Roisin and Beckers (2011)].

## 4.3 Results

We test the subsurface vortex merger sensitivity to the choice of the initial parameters. This will allow us to determine the conditions under which this phenomenon can take place in an idealized primitive equations context. Our tool of investigation is the Regional Oceanic Modeling System (ROMS) [Shchepetkin and McWilliams (2005)]. In particular, the occurrence of merger is studied as a function of the vortices' relative distance, initial swirl velocity and background stratification for both M and P structures. Such a parametric investigation will be achieved modifying the initial state parameters.

### 4.3.1 Merger sensitivity to vortex parameters

#### Relative Distance

We define the initial relative distance between the subsurface anticyclones (i.e., the distance between their centers, at a depth of 1000 m) as a function of the vortex radius  $R$ . In the M case, and for our potential vorticity distribution, the critical distance for merging occurrence  $d_{cM}$  was found to be

$$d_{cM} = 2.5R.$$

An increase of this parameter of only about  $0.1 R$  prevents the merging process from occurring. This is shown by figures 4.3 and 4.4, both illustrating the time evolution of a horizontal section of PVa at a depth of 1000 m.

At the critical distance, the positive annuli interact, but are torn apart by the strong shear created by the cores. These two cores can collapse at the center, thus initializing the merging process (figure 4.3). The annuli are strongly deformed and advected around the central core. The filamentation of the strongly elongated core (at 12-14 days) leads to the injection of negative PVa into the annulus, which further weakens its influence. Finally, the central core has gathered the PVa of the two initial cores. For initially more distant vortices (figure 4.4) the annulus influence on the cores becomes stronger than the cores mutual interaction. The latter are advected radially outwards by their annulus via a dipolar effect and merger is prevented. This behavior is in agreement with the results of Valcke and Verron (1997), who, studying the merger of baroclinic shielded quasi-geostrophic vortices (with a potential vorticity structure comparable to that of an R-vortex), could determine two particular regimes of interaction: the Diverging and the Diverging Interaction case. In both cases, the merging process was not observed. This was due to a redistribution of the annuli's opposite-sign potential vorticity. Such a mechanism generates a repulsive effect on the two cores, thereby preventing their merger into a single core structure.

For P vortices, the critical initial distance for merger occurrence is of the same order of magnitude than in the M case, being

$$d_{cP} = 2.6R.$$

Furthermore, similarly to the previous case, an increase of this parameter of about  $0.1 R$  prevents the merging process from taking place. This is shown by figure 4.5 and 4.6. These results show that the merger critical distance is smaller than the predictions of classical two-dimensional merger or of barotropic unshielded quasi-geostrophic vortices. This is in agreement with the results of Masina and Pinardi (1991) and Valcke and Verron (1997), who also found critical distances around  $2.4 R$  for shielded baroclinic vortices by means of numerical experiments in the quasi-geostrophic context.

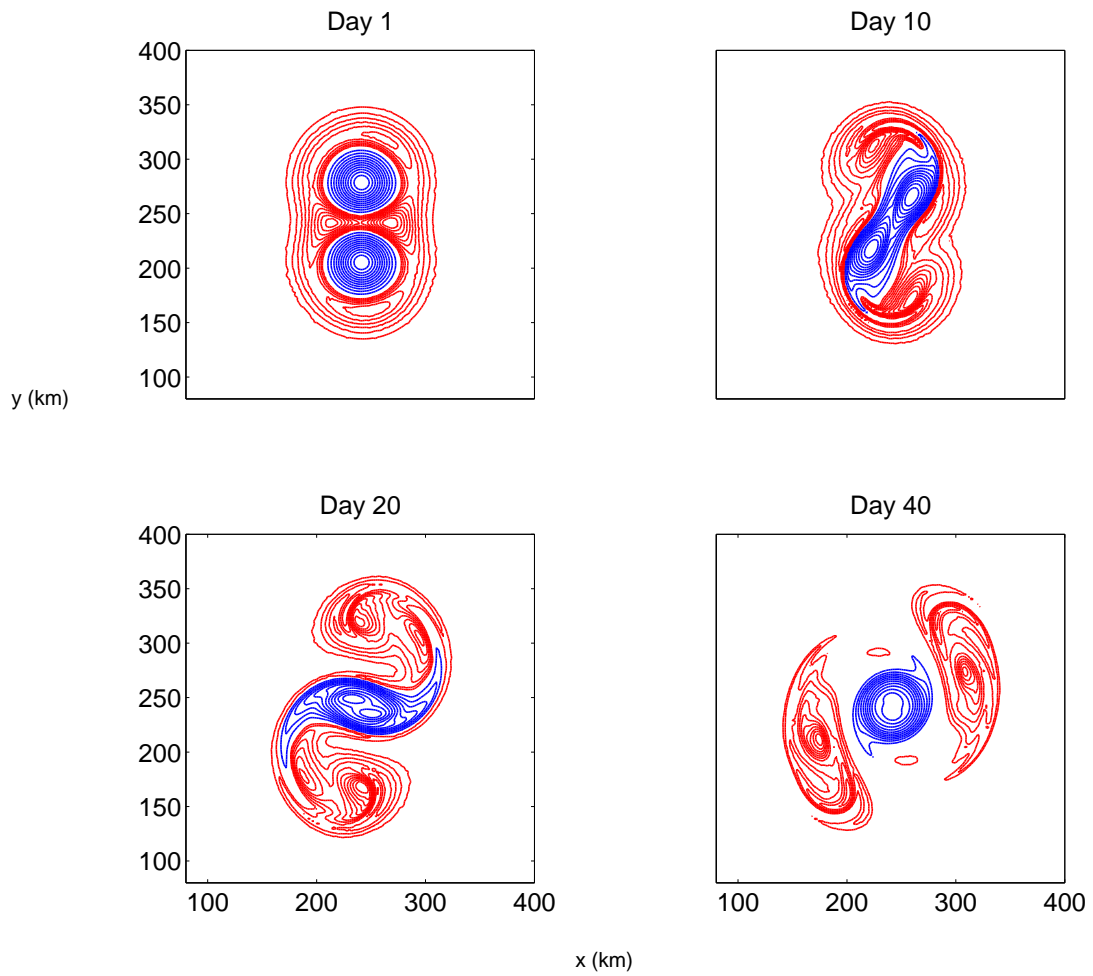


**Figure 4.3:** Horizontal sections of  $PV_a$  at the vortex core. The relative initial distance between the subsurface anticyclones is  $d_{cM} = 2.5R$  ( $M$ -vortices)

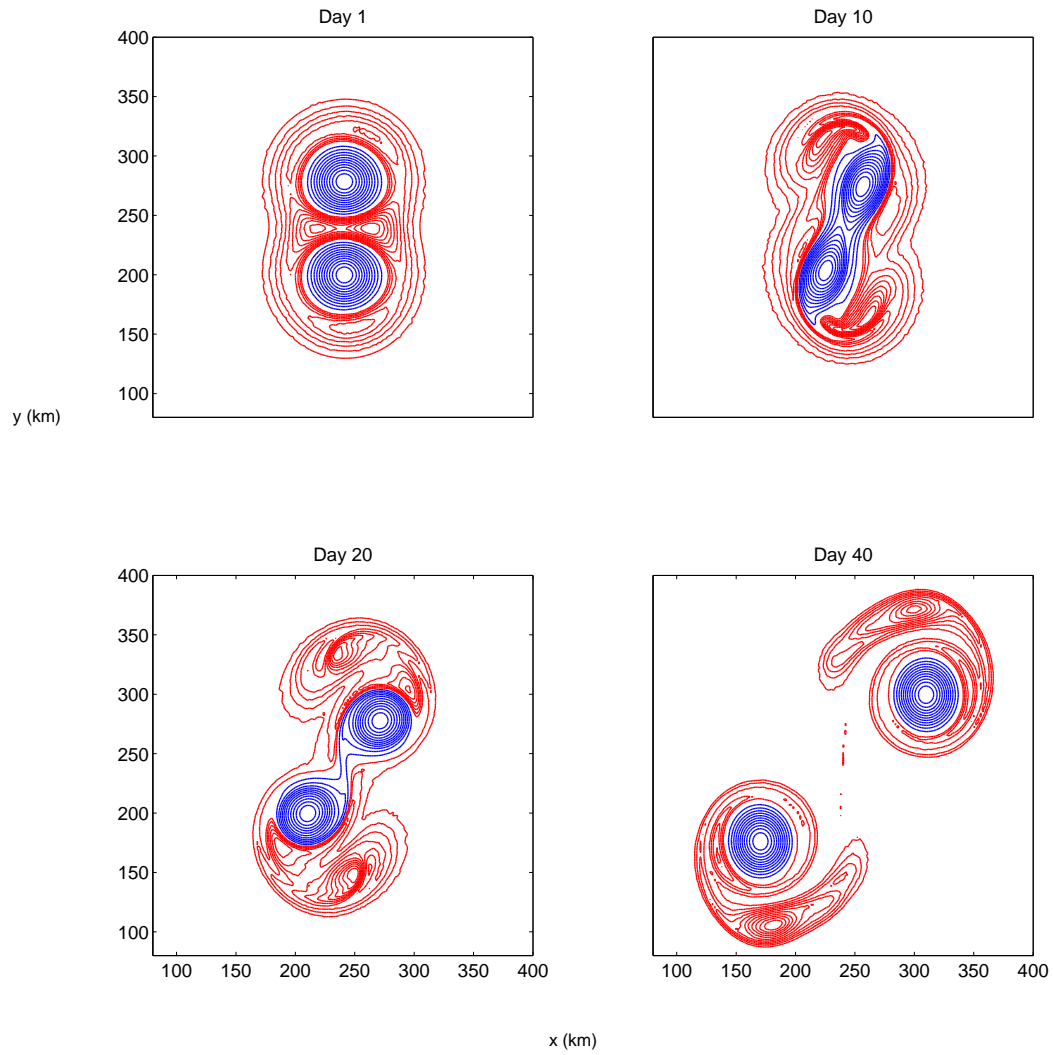


**Figure 4.4:** *Horizontal sections of PVa at the vortex core. The relative initial distance between the subsurface anticyclones is  $d = 2.6 R$  ( $M$ -vortices)*

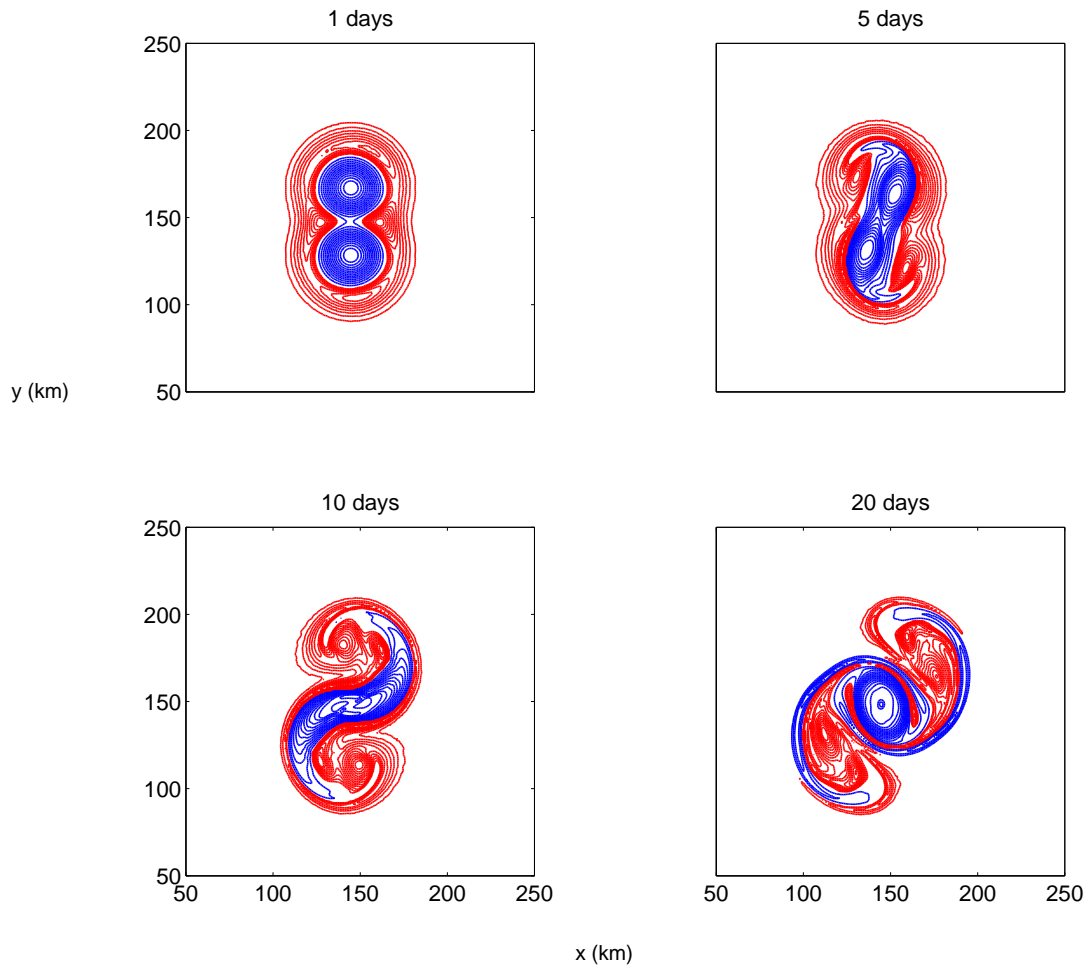


**Figure 4.5:** *Horizontal sections of PVa at the vortex core. The relative initial distance between the subsurface anticyclones is  $d_{cP} = 2.6 R$  ( $P$ -vortices)*

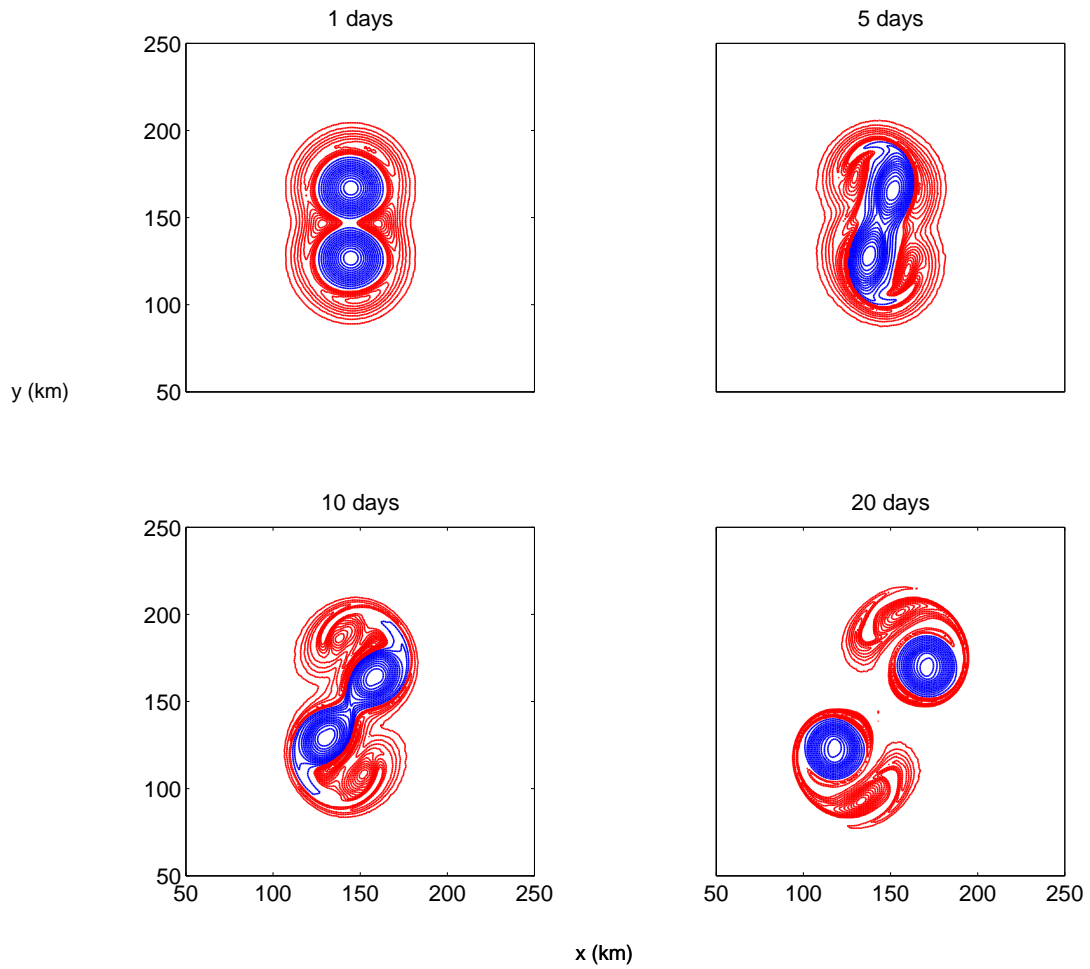


**Figure 4.6:** *Horizontal sections of PVa at the vortex core. The relative initial distance between the subsurface anticyclones is  $d = 2.7 R$  (P-vortices)*

### Influence of initial swirl velocity

The effects of initial swirl velocity are investigated here. Choosing initial states already illustrated in figure 4.1 and Table 4.1, we let the initial swirl velocity vary from 0.1 m/s to 0.4 m/s and we observe the corresponding merging behavior. The dimensionless numbers affected by the changing swirl velocities, in the non-viscous limit, will be the Rossby number and the Stretching factor. The corresponding values for different experiments are summarized in Table 4.2. Such values indicate that increasing the intensity of the velocity field one gets less geostrophic vortices, as expressed by the increase of Rossby number. Moreover, equation 4.3 states that the velocity field determines the density anomaly associated to the vortex. Hence, the Stretching factor also varies when faster rotating vortices are dealt with. Indeed, if we increase the intensity of the velocity field without varying its horizontal extent, the vortex core isopycnal layers will be more stretched in the vertical, and the corresponding stretching factor will be larger.

**Table 4.2:** *Rossby numbers ( $Ro$ ) and Stretching Factor ( $S$ ) for vortex merger experiments with changing rotational velocity EXP 1= slowest rotation,...,EXP 5=fastest rotation.*

M-vortices					
	EXP 1	EXP 2	EXP 3	EXP 4	EXP 5
$Ro$	0.06	0.09	0.13	0.20	0.27
$S$	0.24	0.32	0.35	0.44	0.50

P-vortices				
	EXP 1	EXP 2	EXP 3	EXP 4
$Ro$	0.20	0.26	0.40	0.53
$S$	0.35	0.41	0.92	0.92

In order to give a quantitative description of this process, we define the merging time as the time when the core of the final vortex (generated by the merger of the two initial subsurface anticyclones) is constituted by a single contour of PVa (where PVa contours are drawn from the minimum up the maximum PVa value, whose order of magnitude is  $10^{-11}$  m/s, at intervals of  $10^{-12}$  m/s). Note that this merging time definition will also be used for studying the effects of the background stratification on merger.

If a critical initial distance is chosen, then the merger does not occur for swirl velocities lower than 0.15 m/s, for the M case. In this particular case, the two vortices interact for about one month and, afterwards, their cores separate giving rise to two coherent structures. This regime is then called Slight Interaction. On the other hand, for faster swirl velocities (0.15 m/s to 0.4 m/s), the merging process is achieved for progressively shorter times, inversely proportional to the vortex initial rotation rate. In the P case, the Slight Interaction regime is overcome at rotational speeds around 0.2 m/s, with a similar dependence of merger with respect to time. As for the M case, an increase in vortex swirl velocity results in an accelerated merging process. This is schematically summarized by figure 4.7, where the yellow and cyan areas indicate the slight interaction and merger regimes, respectively. In particular, the "No Merger" label stands for a regime in which the merger is possible over a longer time but was not achieved yet.

### Influence of the background stratification

Here are studied the effects of the background stratification on the merger of subsurface anticyclones. As we did for the case of initial swirl velocity, the study is carried out in a parametric way. We vary the background stratification in order to get associated Rossby deformation radii comprised between about 30 and 50 km. In the real northern ocean, such values correspond to typical stratifications in the latitude range between 20°N and 30°N [Chelton et al. (1998)], where subsurface anticyclones are abundant [Meschanov and Shapiro (1998), Shapiro and Meschanov (1991), Pingree and Le Cann (1993b), Armi and Zenk (1984), Richardson et al. (2000a)]. In both the M and P case, we investigate the effects of stratification on vortices whose initial relative distance is the critical one, for instance,  $d_{cM} = 2.5 R$  and  $d_{cP} = 2.6 R$ , respectively. The choice of the other initial parameters has already been discussed in section 4.2 and is schematically shown by figure 4.1. Note that the choice of  $R_d$  range, of geographical interest, has also technical reasons. Considering the analytical structure of the subsurface anticyclones (specified in section 4.2) some values of  $R_d$ , for instance the smaller ones, can lead to statically unstable anticyclones, which are not of interest in this study.

The dimensionless numbers affected by this parametric study are the Burger number ( $Bu$ ) and the Stretching Factor ( $S$ ). Their values for the corresponding experiments are listed in table 4.3. Here, the variation of  $Bu$  and  $S$  is due to the varying background stratification. For instance, higher values of  $R_d$  are obtained by choosing steeper background stratifications (i.e., higher values of  $|\partial_z \rho(x, y, z)|$ ).  $Bu$  is a monotonic increasing function of  $R_d$  (see also table 4.1) and its effects on the flow have already been discussed at the end of section 4.2. Moreover, as  $R_d$  is incremented, the vortex core isopycnal

layers will extend less in the vertical, as the vortex will be embedded in an increasingly stratified environment. Hence, larger values of  $R_d$  yield smaller stretching factors.

**Table 4.3:** Burger number ( $Bu$ ) and Stretching factors ( $S$ ) for vortex merger experiments with changing stratification. EXP 1=lowest  $R_d$ ,..., EXP 4=highest  $R_d$

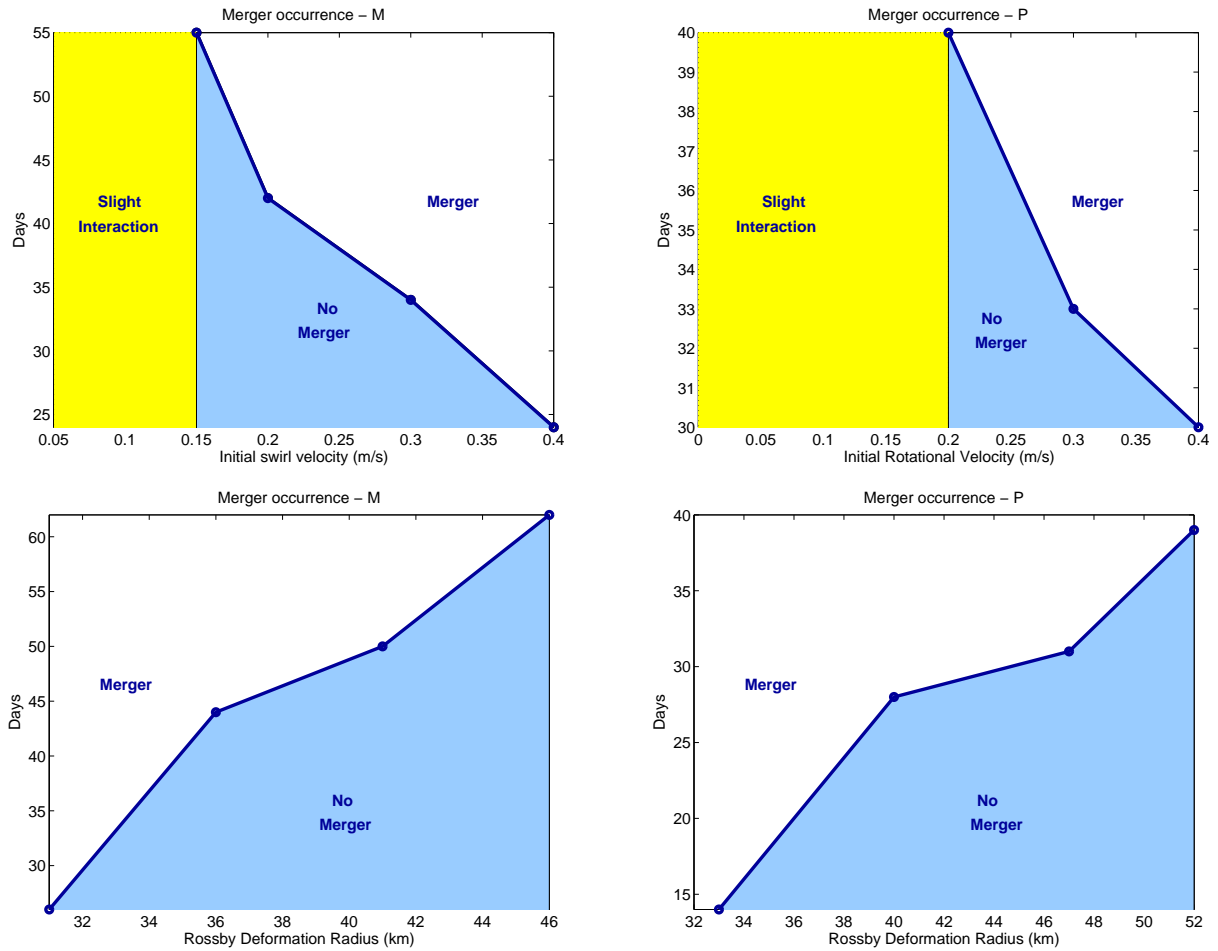
M-vortices				
	EXP 1	EXP 2	EXP 3	EXP 4
$Bu$	1.06	1.44	1.86	2.35
$S$	0.36	0.35	0.26	0.19

P-vortices				
	EXP 1	EXP 2	EXP 3	EXP 4
$Bu$	4.84	5.76	7.11	9.81
$S$	0.89	0.58	0.56	0.48

In the M case, and in the observed stratification range, the merging time increases with increasing  $R_d$ . In particular, if  $R_d$  varies from 30 km to approximately 50 km, the time required for the merger to be completed will increase from 1 month to 2 months. In the P case, the merger behavior is analogous to the M case. In fact, changing  $R_d$  from 30 km to 50 km, the time needed for merger is 2.7 times larger. Once again, this is schematically shown by figure 4.7.

In past works, the background stratification was also found to influence the critical merging distance. Waugh (1992) showed that this quantity monotonically increases with  $R_d$ , while Filyushkin and Sokolovskiy (2011) found that it is a non-monotonic function of the Froude number (the Froude number being also a function of  $R_d$ ). In our experiments, when  $R_d$  is incremented, P-vortices merge at increasingly larger distances. If  $R_d$  varies from 36 km to 52 km,  $d_{cP}$  goes from  $2.6 R$  to  $2.7 R$ , and does not vary significantly for larger  $R_d$ . For M-vortices, considering a realistic range of  $R_d$  values for typical Meddy latitudes ( $20^\circ\text{N}$  to  $40^\circ\text{N}$ ), no substantial variations of the critical merging distance were evidenced.



**Figure 4.7:** Time required for subsurface vortex merger. Top-left and top-right images show the dependence on initial rotational velocity in a M and P case, respectively. Analogously, bottom-left and bottom-right images show the dependence on the Rossby deformation radius. In the figure, the dots correspond to the experiments actually run in our study.

### Further considerations on the dimensionless hydrodynamical numbers

Here we discuss the influence of the hydrodynamical numbers (listed in tables 4.2 and 4.3) on the vortex merger. These numbers characterize the hydrodynamical regime in which the merger experiments take place. At the end of section 4.2, the hydrodynamical context was discussed for M and P-vortices in their "reference-shape", i.e., with characteristics typical of Meddies and Peddies observed in the ocean. Here we study the impact of

varying the vortex swirl velocity and environmental stratification on the merger.

When the vortex swirl velocity increases from 0.15 m/s to 0.4 m/s, and the vortex radius is kept constant, the Rossby number monotonically increases (as shown in table 4.2). In our case  $Ro$  reaches its maximum value ( $Ro = 0.53$ ) for P-vortices spinning at 0.4 m/s.

When  $Ro$  approaches unity, the flow switches from geostrophic to unbalanced dynamics, and in the limit of  $Ro = 1$  anticyclonic eddies can undergo centrifugal instability (see also Molemaker et al., 2014). In our study, even the less geostrophic anticyclones (i.e.,  $Ro = 0.53$ ) are far from this threshold. These conditions assure that the anticyclonic eddies we deal with, are keen to maintain their coherent structure.

Furthermore, increasing  $Ro$  will affect merger. If the critical conditions for merger are satisfied, the shear of vortex swirl velocity determines the rate at which the two vortex cores will exchange water masses. Hence, larger swirl velocities will accelerate the merging process. This is confirmed by comparing the stream function of two couples of merging M-vortices spinning at 0.15 m/s and 0.4 m/s, respectively (evaluated at 1000 m depth and in the rotating framework of the two co-rotating vortices). In the second case, larger stream function and velocity gradients bound the area around the centers of the two initial anticyclones; i.e., the area involved in the merging process (not shown). The larger shear of the vortex velocity field (compared to the 0.15 m/s case) will favor destabilization and will lead to a more efficient water exchange between the cores of the anticyclones.

As stated in the previous section, when one increases the vortex swirl velocity without changing the vortex radius, the subsurface anticyclones are characterized by an increasing Stretching factor  $S$ , indicating that the isopycnal layers associated to the anticyclones core will be more stretched in the vertical.

In table 4.3, the tendencies of both the Burger number  $Bu$  (increasing) and the Stretching factor  $S$  (decreasing), indicate that when  $R_d$  is increased, the motion progressively switches to a two-dimensional fashion.

Except for M-vortices in their "reference shape", where  $Bu$  is of order unity, all the other configurations indicate a predominance of relative vorticity over stretching.  $Bu$  reaches its maximum value (around 10) for P-vortices embedded in the most stratified environment, i.e., when  $R_d \simeq 52$  km (Cushman-Roisin and Beckers, 2011). In addition, the vertical structure of the vortex cores will extend less in the vertical as  $R_d$  is incremented (as expressed by the decaying  $S$  values).

In our experiments, the increase in  $R_d$  also resulted in a progressively larger merging-time for both the couples of M and P-vortices. This behavior can be explained observing

equation 4.7. When  $R_d$  is incremented, the quantity  $|\partial_z \rho(x, y, z)|$  becomes larger. Hence, the PVa gradients across the two vortex cores will increase. As a result, merger will need more time to balance such gradients and eventually yield the single contour core (which is the condition that we defined as merging-time).

## 4.4 Merger related effects

### 4.4.1 Evolution of PVa volume integral

Here we quantify how merger modifies the structure of subsurface anticyclones. In particular, we determine the vortex evolution as a function of time, making use of its three-dimensional PVa integral. This quantity is directly related to the vortex stream function, hence, to its velocity field. A simple way to look at this problem is to consider three-dimensional quasi-geostrophic vortices [Carton (2001)]. For idealized oceanic vortices, the stream function of a vortex is the convolution of the PVa with the Green's function. Hence, higher PVa volume integrals will yield faster rotating vortices. The PVa analysis will be carried out for both M and P-Vortices. At first, we determine the time evolution of the PVa volume integral in a case of merger and in another in which vortices only slightly interact. The merger case results from an initial state in which two subsurface anticyclones (as the ones illustrated in figure 4.1) are separated by distances  $d_{cM}$  and  $d_{cP}$  and spin at approximately 0.2 m/s. The slight interaction is instead obtained increasing  $d_{cM}$  and  $d_{cP}$  by  $0.1 R$ . Four experiments are then performed. The set of dimensionless numbers for the M and P cases are given in table 4.4. The dimensionless hydrodynamical numbers have already been discussed in sections 4.2 and 4.3.

**Table 4.4:** *Characteristics of the modelled subsurface vortices for determination of the PVa volume integral.*

	$Bu$	$Re$	$Ro$	$S$	$d_{cMERG.}$	$d_{cSLIGHT INT.}$
M-vortices	1.36	$\gg 1$	0.13	0.35	$2.5 R$	$2.6 R$
P-vortices	5.42	$\gg 1$	0.26	0.41	$2.6 R$	$2.7 R$

In both the merger and slight interaction cases, the PVa volume integral has been evaluated taking into account the contribution of the negative PVa core only. This is justified by the fact that the annuli, as well as the positive lobes, are not coherent structures

throughout the merging (or slight-interaction) process, but they undergo strong deformation and filamentation (see for example figure 4.14).

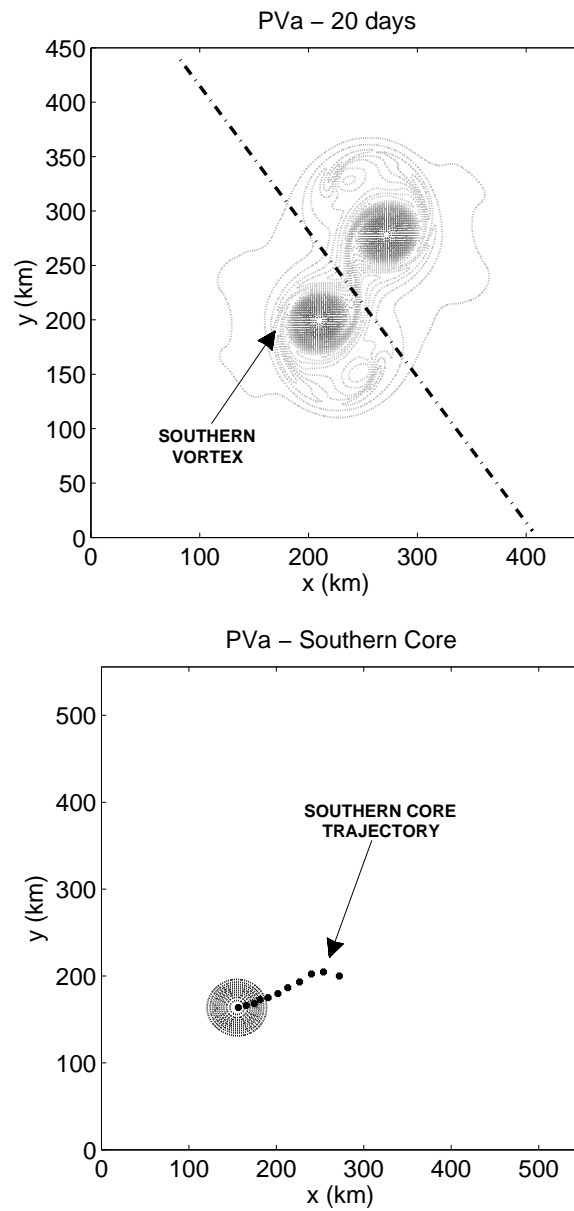


**Figure 4.8:** Tracking of a single subsurface vortex for evaluation of the PVa volume integral in the slight interaction case. Top: separation line between the two vortices (dash-dotted line), Bottom: trajectory of the PVa negative core.

In particular, in the slight interaction case, the contribution of a single vortex is consid-

ered to establish PVa budgets. Given the symmetry of our configuration, the "southern-vortex" has been arbitrarily selected, putting to zero all the PVa values located northeast of the separation line (dash-dotted line in figure 4.8). Its displacement has been automatically tracked in the oceanic basin, and the PVa integral has been evaluated in a moving cylinder, centered at the vortex core and whose radii are around 60 km and 40 km in the M and P case, respectively. The evaluation of the PVa volume integral becomes much easier when merger occurs, as the vortex becomes nearly steady after about 20 days, making its tracking a trivial task. The cylinder in which the integral is evaluated has the same characteristics as in the slight-interaction case.

Performing the computation in such cylinders, allows one to evaluate the PVa integral on the main coherent structure of the vortex, neglecting filaments and production of smaller eddies.

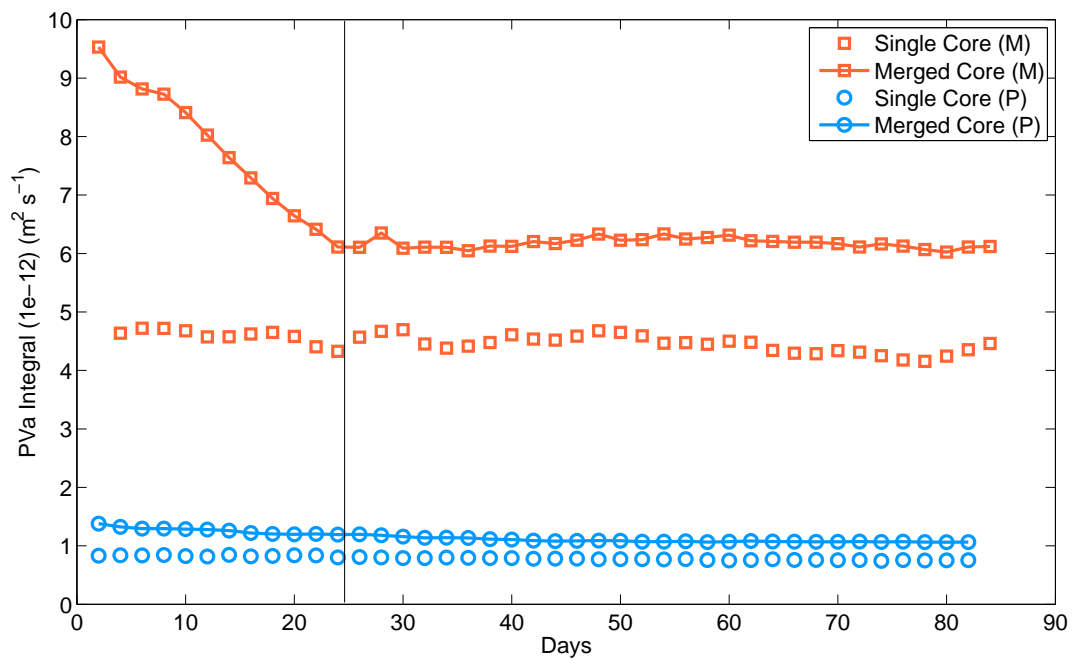


**Figure 4.9:** PVa integral for the core of the subsurface vortex. Squares and circles refer to the PVa integral for M and P-vortices, respectively, with unfilled symbols corresponding to the "Slight Interaction" case (single vortex) and filled symbols corresponding to the "Merger" case (two vortices). The thin vertical line indicates the time when a single coherent structure is generated by the merger of the two initial vortices.

The results for M and P cases are shown in figure 4.9. When vortices slightly interact, the core PVa integral is fairly constant throughout the simulation.

On the other hand, when merger occurs, the two vortex cores have to be taken into account and the PVa integral is initially doubled compared to the slight interaction case. As the system evolves, the PVa integral monotonically decreases until merger is completed (around day 25, vertical line of figure 4.9). Afterwards, the PVa integral of the merged core becomes constant with time; yet its value is larger than in the slight interaction case. The monotonic decrease of PVa integral (for merging vortices) indicates that part of the total PVa, initially stored in the two vortex cores, is lost due to filaments (in addition to the filamentation of the PVa annuli).

The filamentation processes occurring during merger, associated to a migration of PVa from the core of the vortex towards its periphery, can be quantified by means of the Merger Efficiency (ME hereinafter), similarly to Waugh (1992). In our case, this quantity is expressed by the ratio of PVa integral at the end of the simulation (around day 80) over its value computed at time  $t = 0$ , as shown by (4.9),

$$ME = \frac{\int_V PVa_f(x, y, z) dV}{\int_V PVa_i(x, y, z) dV}, \quad (4.9)$$

where  $V$  indicates the volume of integration (the cylinder) and the subscript  $i$  and  $f$  stand for initial and final state of the simulation, respectively. The computed ME values are 0.64 and 0.67 in the M and P-case, respectively. Earlier works on the merger of two-dimensional Rankine and Gaussian vortices suggest that the ME can be higher than the one obtained in this context, with values generally exceeding 0.8 [Waugh (1992), Trieling et al. (2005)]. Our experiments indicate that for both M and P-vortices, the merger induces a non negligible filamentation, causing a partial loss (around 35%) of the PVa associated to the vortex cores. This different behavior is due to the unlike-signed PVa of the three-dimensional anticyclones we dealt with. During merger, the filamentation of the vortex cores (as shown by the continuous contours in figure 4.3, 4.5 and 4.14) is particularly enhanced across the areas where the relative vorticity (hence the PVa) changes in sign, i.e., at the cores peripheries. In these regions, the strain increases and reaches its maximum values, favoring the vortex deformation with the consequent migration of water masses away from the centers of the vortices (see e.g. figure 4.10).

Nevertheless, the merging process yields a single vortex whose PVa integral is larger than that of the initial vortex core. Indeed, averaging the values of the PVa integral from day 25 onward, we can estimate that the PVa gain due to merger is around 39%

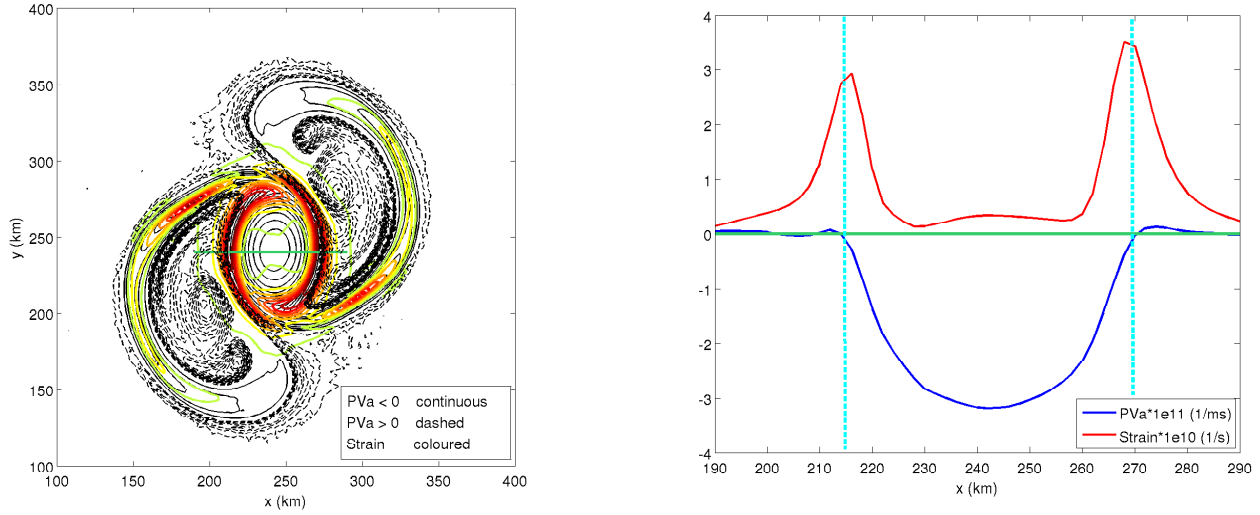


**Figure 4.10:** *Left: strain (colored contours) and PVa (black contours). The negative and positive PVa values are indicated by continuous and dashed contours, respectively. Right: strain (red) and PVa (blue) evaluated along the green radial indicated in the left panel.*

and 42% in the M and P case, respectively. This has been computed using (4.10):

$$PVa_{\text{GAIN}} = \frac{\left\langle \int_V PVa_{\text{Merge}}(t > 25) dV \right\rangle_{[M/P]}}{\left\langle \int_V PVa_{\text{Single Core}}(t > 25) dV \right\rangle_{[M/P]}} - 1, \quad (4.10)$$

where  $t$  is the time in days and the subscript [M/P] indicates M and P-vortices, respectively.

#### 4.4.2 Vortex deformation

Another merger-induced effect, which was evident in all the simulations, is the deformation of the two vortices before and after the merging process has taken place.

The subsurface anticyclones initially have a circular shape. If their relative distance is the critical one, they start exchanging potential vorticity, and exhibit an elliptic shape. This deformation is evident up to the latest stages of the simulations, as shown by figures 4.11 and 4.15. In order to quantify this phenomenon, we compute the geometrical moment for one of the two subsurface vortices before the merging process and on the merged structure afterwards; for both M and P vortices. The geometrical moments,

expressed by (4.11), allow us to define which are the preferential deformation modes (see (4.12)) of our three-dimensional structure all along the simulation. In particular, in (4.11), the following quantities have been introduced:

- $(x_c, y_c, z_c)$  the coordinates of the vortex center in the oceanic basin;
- $R$  the vortex radius;
- $H$  the vortex thickness;
- $pva$ , the normalized PVa:

$$M_{mnp}(t) = \iiint \left( \frac{x - x_c}{R} \right)^n \left( \frac{y - y_c}{R} \right)^m \left( \frac{z - z_c}{H} \right)^p pva(x, y, z, t) dx dy dz, \quad (4.11)$$

$$Mode_i(t) = \sqrt{(M_{i00})^2 + (M_{0i0})^2 + (M_{00i})^2}. \quad (4.12)$$

Before the merging process, the computation of the deformation modes is performed isolating the core of one of the two subsurface anticyclones (the southern one, as explained in section 4.4.1). The isolation consists in neglecting one of the two vortices and its PVa shields, as schematically shown in figure 4.11. After the merger, the only required operation is the elimination of the PVa shield. Note that in this particular analysis, we define the "after-merger" by visual inspection, observing when a single coherent core is formed.

The results of this analysis are shown in figure 4.12. In both the M and P case, a clear dominance of the mode 2 is evident all along the simulation, confirming our prediction. Note that, in the initial stages, mode 3 grows as the vortices come close to each other. This mode corresponds to the "pear-shaped" equilibria for two close two-dimensional vortices [Overman et al. (1981)].

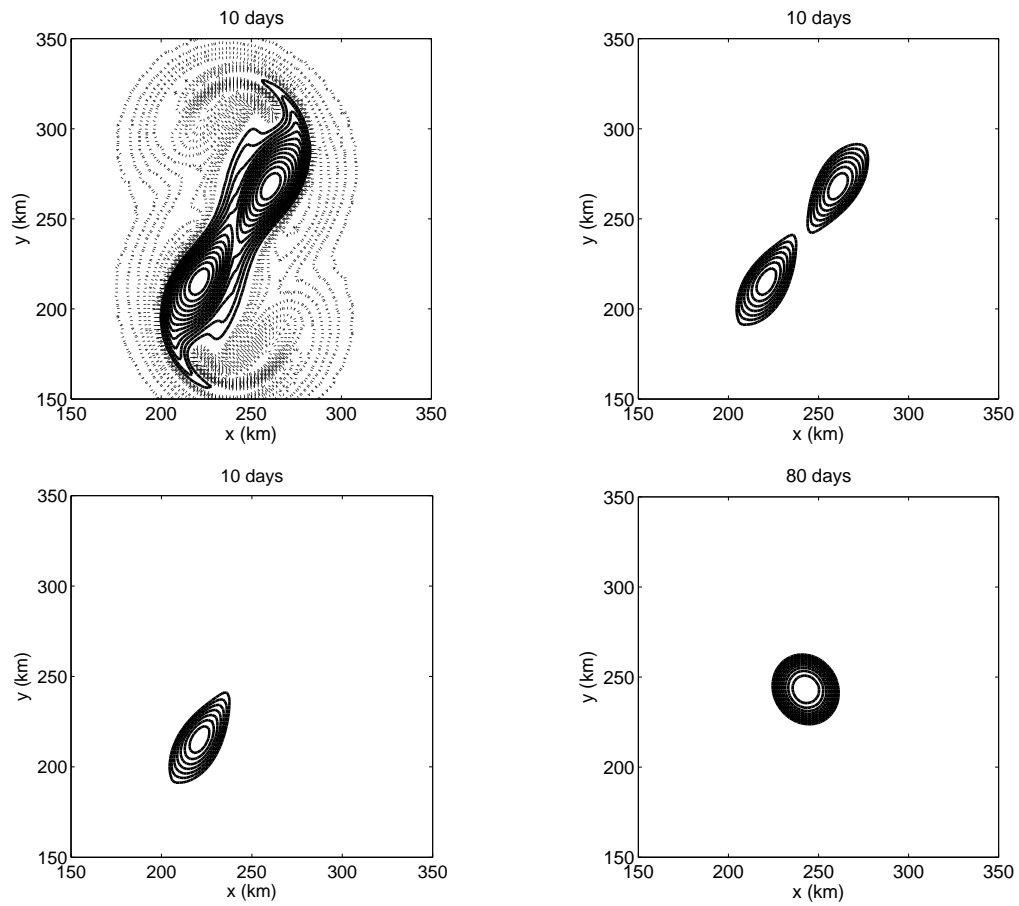


**Figure 4.11:** Isolation of a single subsurface vortex for evaluation of the geometric moment. The images show a snapshot of  $PV_a$  for two  $M$  anticyclones during merger (10 days) and after merger (80 days)

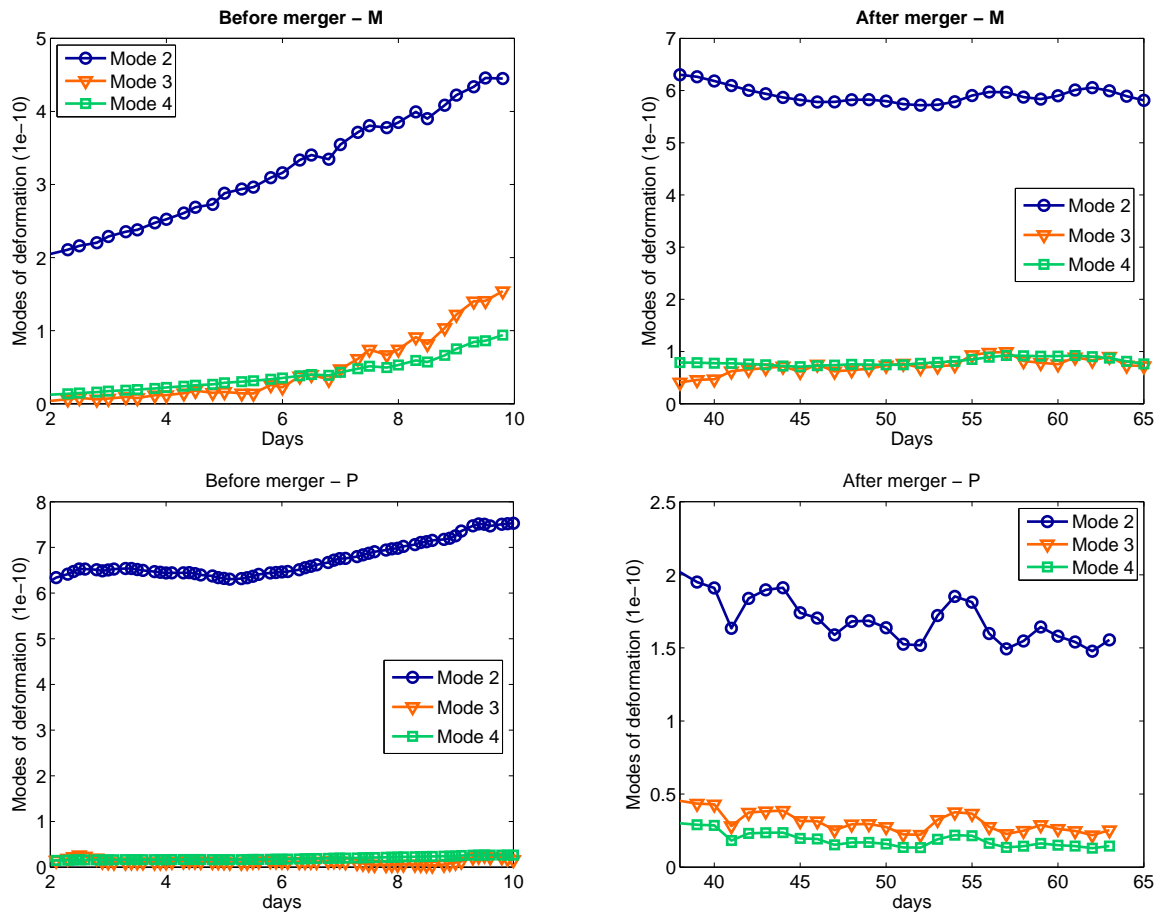


**Figure 4.12:** Deformation modes for the subsurface vortex merger. Top-left and top-right figures are related to M-vortices, before and after the merger, respectively. Results for P-vortices are shown in the bottom-left and bottom-right figures.

### 4.4.3 Final PVa structure of the merged vortex

One remarkable feature is the PVa structure after the merging process has taken place. For both M and P-vortices, horizontal sections of PVa indicate the generation of multipoles. Visual inspection suggests that this feature becomes evident after approximately 50 days in the P case and 100 days in the M case (note that in this section simulations have run for 200 days at a horizontal resolution of 500 m). The main PVa core is surrounded by two satellite small vortices (labelled as E1 and E2) whose radii can be as small as 10 km (see figure 4.15) and are generated by the instability of peripheral filaments (as shown by figure 4.14 for M-vortices; not shown for P-vortices). Vertical profiles of kinetic energy evaluated through the center of these eddies indicate that their vertical extent can reach several hundred meters (figure 4.13). In the end, the lifetime of these small-scale features can reach or exceed five months, as indicated by the latest stage of the simulations.

The vertical section of PVa shows that the merged vortex maintains some of the features of the initial state. As stated in section 4.2, the initial PVa structure couples the effect of both R-vortices and S-Vortices (Morel and McWilliams, 1997), and this is still the case for the final vortex. In fact, patches of opposite sign PVa still surround and vertically bound the merged vortex. However, the horizontal structure exhibits a tripole-like configuration, though many small vortices and filaments orbit the main vortex core. Vertically, the PVa shield is fragmented into upper and lower lobes. The merged structure has radii and thicknesses comparable to those of the initial vortices. In the M case, the merged vortex increases its radius by about 30% and decreases its thickness by 20%, while, in the P case, the percentages are around 18% and 9%, respectively. These values have been estimated focusing on the variations of the negative core, neglecting the noisier area given by the positive PVa shields.

These results are also in agreement with the work of Bashmachnikov et al. (2015). The authors, using *in-situ* data, found that Meddies progressively increase in radius as they drift west of the Iberian Peninsula; within distances of 600 km from the Portuguese coasts. They pointed out that merger is the main mechanism responsible for this behavior. Moreover, they observed that Meddy thicknesses only slightly decrease as merger events take place. Hence, in the real ocean, the Meddy aspect ratio is a decreasing function of the distance from the Iberian peninsula, i.e., as merging events are produced, as also shown by our idealized experiments.

In summary, the set of dimensionless numbers describing the effects of merger on subsurface anticyclones are illustrated in table 4.5. The Rossby and Burger numbers will slightly decrease because of the increasing radii. Moreover, the merging process does not

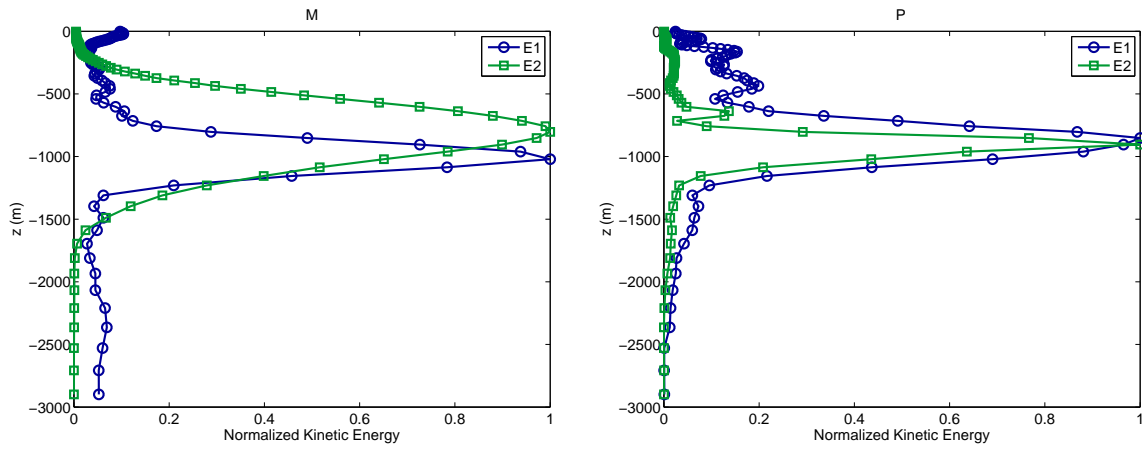


**Figure 4.13:** Vertical profiles of kinetic energy through the centers of the eddies *E1* and *E2* (see also figure 4.15). Results are presented for *M* and *P*-Vortices.

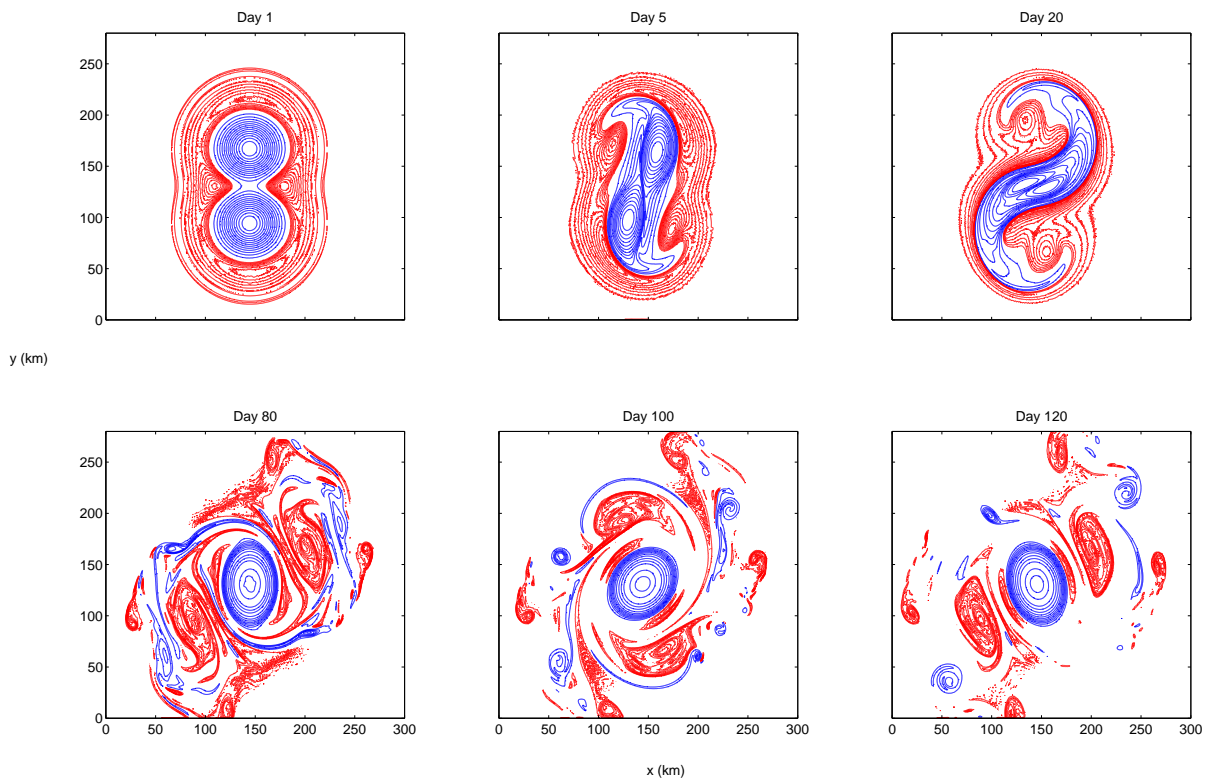


**Figure 4.14:** Generation of peripheral eddies via filament instability (*M*-vortices).

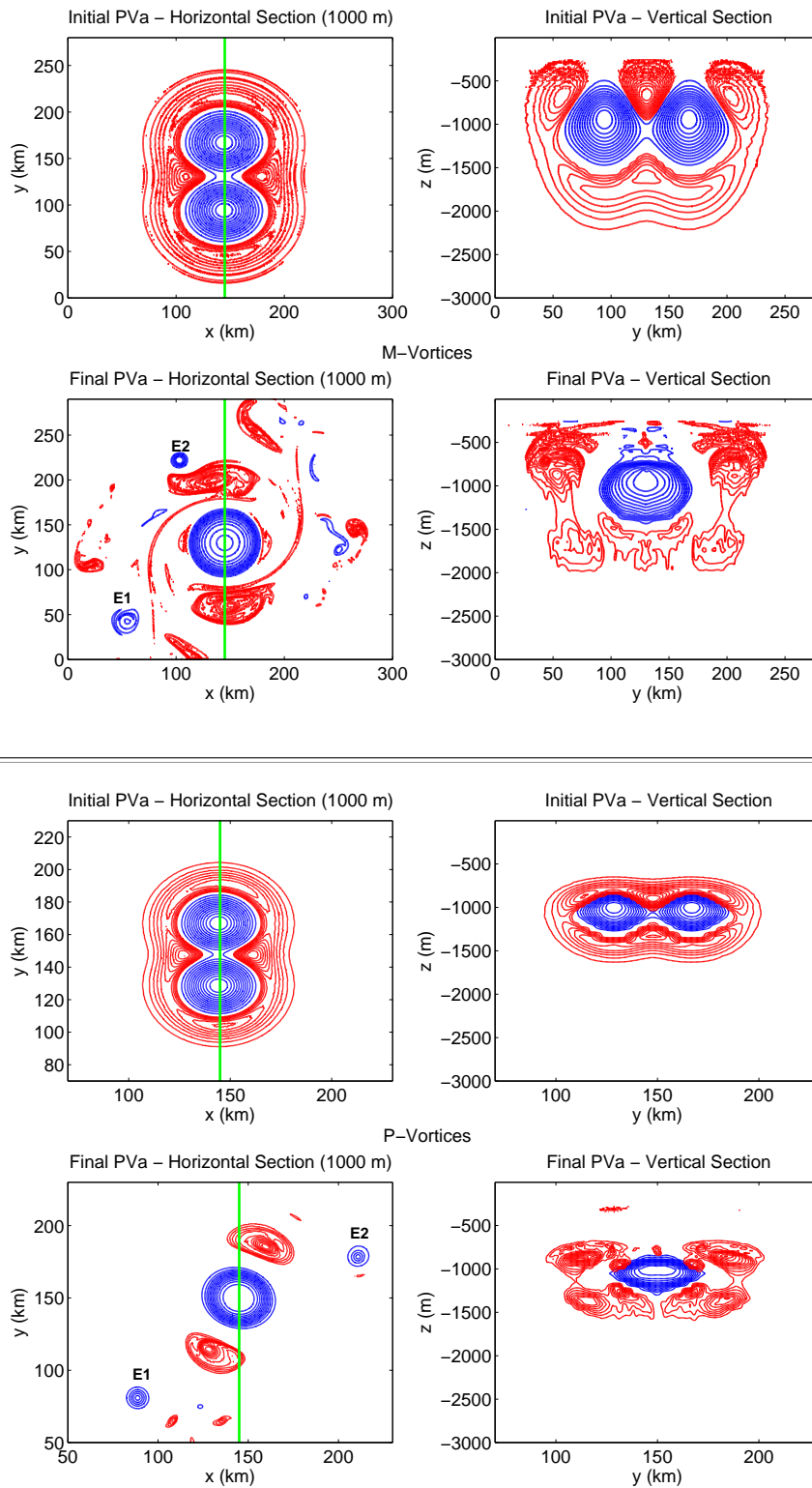


**Figure 4.15:** Initial and final sections of PVa for merger of subsurface anticyclones (*M* and *P*-Vortices). The vertical sections are estimated along the radial indicated by the bold vertical line. The peripheral eddies are labelled as *E1* and *E2* in both cases.

significantly change the isopycnal structure of the vortex. The stretching factors are in fact comparable before and after the merger.

The implications of the vortex characteristics on merger have already been discussed in the previous sections. Nevertheless, the different Burger numbers characterizing the M and P-vortices ( $Bu_M = 0.9$ ,  $Bu_P = 4.25$ ) are worth commenting. As pointed out at the end of section 4.2, when  $Bu > 1$  the flow is predominantly two-dimensional [Cushman-Roisin and Beckers (2011)], as relative vorticity mostly drives the motion. On the other hand, a Burger number of order unity indicates a regime in which rotation and stratification equally contribute to determine the flow; giving the PVa-distribution a more three-dimensional character. Indeed, maps of vertical velocity evaluated at the final stage of the simulations in correspondence of the vortex core (not shown) confirm this behavior. In the M case, upward velocities at 1000 m depth are larger than in the P case, as we observe upward motions up to 4 m/day against the value of 2 m/day observed for P-vortices. Moreover, such vertical displacements are spatially correlated with the main filaments located around the merged core (see lower-left panel of figure 4.15 for M-Vortices); and filaments are known to be regions of enhanced vertical motions [Ponte et al. (2013b)]. However, such vertical velocities still allow the motion to be predominantly two-dimensional, as the core of the merged M-vortex swirls at a maximum speed of 0.28 m/s.

**Table 4.5:** *Hydrodynamical numbers for the modelled subsurface vortices before and after the merger.*

M-vortices				
	$Bu$	$Re$	$Ro$	$S$
BEFORE Merger	1.36	$\gg 1$	0.13	0.36
AFTER Merger	0.90	$\gg 1$	0.10	0.40

P-vortices				
	$Bu$	$Re$	$Ro$	$S$
BEFORE Merger	5.42	$\gg 1$	0.26	0.41
AFTER Merger	4.25	$\gg 1$	0.20	0.37

## 4.5 Conclusions and Perspectives

In this chapter we have investigated the merger of subsurface lens-like anticyclones in the context of the full primitive equations. The study has been carried out by means of the Regional Oceanic Modeling System (ROMS) in academic configuration and neglecting any atmospheric forcing or interaction with topographic features. This choice is justified by the evidence of colliding lens-like isolated anticyclones off of Gibraltar Strait (referred to as Meddies) confirmed by past and recent studies based on observations and realistic modeling [Schultz Tokos et al. (1994); Barbosa Aguiar et al. (2013); L'Hégaret et al. (2014)]. Furthermore, this study also provides an idealized description for the merger of smaller subsurface eddies, as the ones recently observed in the north-western Indian Ocean (Peddies) by means of *in-situ* measurements [L'Hégaret (2015)]. Meddies and Peddies (respectively, Mediterranean and Persian-water eddies) are both subsurface eddies generated by the sinking of salty and warm water masses in semi-closed basins and their subsequent outflow into the open ocean. The first are characterized by radii comprised between 20 and 50 km and they can extend vertically from some hundred meters up to 1 km while the second have smaller radii and vertical extent. Both of such structures spin at velocities around 0.2 m/s. In our study, these oceanic eddies are studied by means of analytical three-dimensional fields, i.e., the density and the velocity field.

The critical parameters for merger occurrence have been determined. If a reference state is chosen, in which two subsurface anticyclones spin at about 0.2 m/s, the critical merger distances are  $d_{cM} = 2.5 R$  and  $d_{cP} = 2.6 R$  for M and P-Vortices, respectively (with  $R$  the vortex radius and M/P indicating Meddy-like and Peddy-like lenses). This parameter can also be affected by background oceanic stratification and vortex rotational velocity. In particular, we found that faster rotating lenses living in less stratified environments, provided the conditions for merger, require smaller times to complete the merging process. Slower rotating lenses merge with increasing times and may need smaller critical distances than  $d_{cM}$  and  $d_{cP}$  for merger to take place.

The results presented here are in agreement with past studies on the merger of both barotropic and baroclinic idealized vortices (Masina and Pinardi, 1991; Carton, 1992; Valcke and Verron, 1997) and are mostly due to the chosen vortex structure in terms of potential vorticity. The novelty of our approach is given by the choice of the high-resolution primitive equations context. This allowed us to investigate the merger of realistic three-dimensional subsurface-intensified lenses and the consequent deformation of their structure; as well as the production of small-scale features.

In particular, we studied the merger of baroclinic, shielded subsurface anticyclones [Morel and McWilliams (1997)]. The assumption of isolated (shielded) vortex is in general more realistic compared to like-signed-PV vortices [Olson (1980); Paillet et al. (2002)].

Merger related effects have also been investigated. We could determine the structure of the final merged vortex for M and P-Vortices. During and after the merging process, the initial circular-section vortices switch to an elliptic shape as a result of the vortex-vortex interaction. The initial, shielded PV is maintained for several months. Furthermore, the merging process reinforces the vortex, mainly increasing its horizontal extent. These results are also corroborated by observations of merging events in the real ocean. Meddies (corresponding to our idealized M-vortices), as they drift away from the Iberian coasts, go through several merging processes and their aspect ratio progressively decreases, as pointed out in Bashmachnikov et al. (2015).

Besides this, production of long-lived, small-scale features has also been observed. Subsurface, lens-like anticyclones can in fact be generated by the instability of peripheral filaments. Their radii can go down to 10 km and they can live for several months, in the absence of other larger-scale structures than the merged vortex.

The numerical framework presented here also constitutes a basis for future investigations on the merger of vortical structures. Firstly, the results of this chapter could be enriched considering different initial configurations for the subsurface vortices, still in the context of a primitive equations model. For instance, one could introduce a vertical offset between the couple of shielded subsurface anticyclones, or a tilt in the vortex rotational axis (like in Reinaud and Dritschel (2005)). We expect this to have an impact on the critical merger distance as well as on the possibility of a merger mechanism to take place. Indeed, modifying the geometry of the initial state, the mutual eddy core-eddy shield interaction will be different compared to the cases studied here. Moreover, the introduction of a bottom topography in the oceanic basin represents another step towards a more realistic study of subsurface vortex merger. A proof of this is given in Bashmachnikov et al. (2015), who stated that Meddies mostly merge in the first 600 km off the Iberian Coast. In this distance range, the presence of the Iberian continental slope and of seamounts cannot be neglected and certainly modifies the Meddies pathways and behavior. Most likely, the merger mechanisms will also be affected by the topographic features and it is worth studying this with a series of controlled experiments.

In the following chapter, whose main scope is to investigate the signature of Meddies at the sea-surface, the merger of subsurface anticyclones will be observed in a full realistic simulation. In particular, we will show that merger allows Meddies to enhance their signature at the ocean surface, principally because of the increase in the Meddy integrated

potential vorticity anomaly.

## 4.6 Further Studies (A): the merger of intrathermocline eddies: the cyclonic case

In this manuscript we have been focusing on the study of subsurface-intensified anticyclones. Nevertheless, occurrences of oceanic intrathermocline cyclones are also possible. This is corroborated by observations and numerical simulations, as shown by Chérubin et al. (2007), Serra et al. (2010) and Barbosa Aguiar et al. (2013) for the north-eastern Atlantic Ocean. Motivated by these results and taking advantage of the same numerical framework developed to study the merger of M and P vortices, we investigated the possibility of merger between subsurface-intensified cyclones. The initial states for the experiments are analogous to the ones discussed in section 4.2 and shown in figure 4.1. The main difference is given by the choice of an opposite sign  $v_\theta$  with respect to equation 4.3.

In what follows, we present some preliminary results on the sensitivity of merger to the eddies' relative distance. Similarly to the anticyclonic case, the vortices we dealt with have a potential vorticity structure that changes in sign vertically and horizontally. In this case, the horizontal and vertical sections of PVa indicate that the positive anomaly is given by the eddy core, while the negative anomalies are located at the eddies' peripheries (see for example figure 4.16). We will limit the sensitivity studies to eddies swirling at 0.2 m/s, hence (neglecting the stretching factor) the set of hydrodynamical numbers for the following experiments, as well as their implication on the eddy dynamics, will be the same showed and commented in table 4.1.

### 4.6.1 The case of Large-scale cyclones

Differently from the anticyclonic case, larger scale cyclones ( $R = 30$  km) merge when they swirls at a relative critical distance of  $\mathbf{d}_{cL} = 2.1 \mathbf{R}$  (where the subscript L stands for large-scale), while this value was 2.5 R for M-vortices. After 15 days of interaction, the cores, as well as the peripheries of the two cyclones, are highly deformed and start generating a single structure which will eventually constitute the core of the new merged vortex. Fine-scale structures (e.g. filaments) are ejected from both peripheral and central areas of the eddies, similarly to what occurred during the merger of subsurface shielded anticyclones (see also section 4.4).

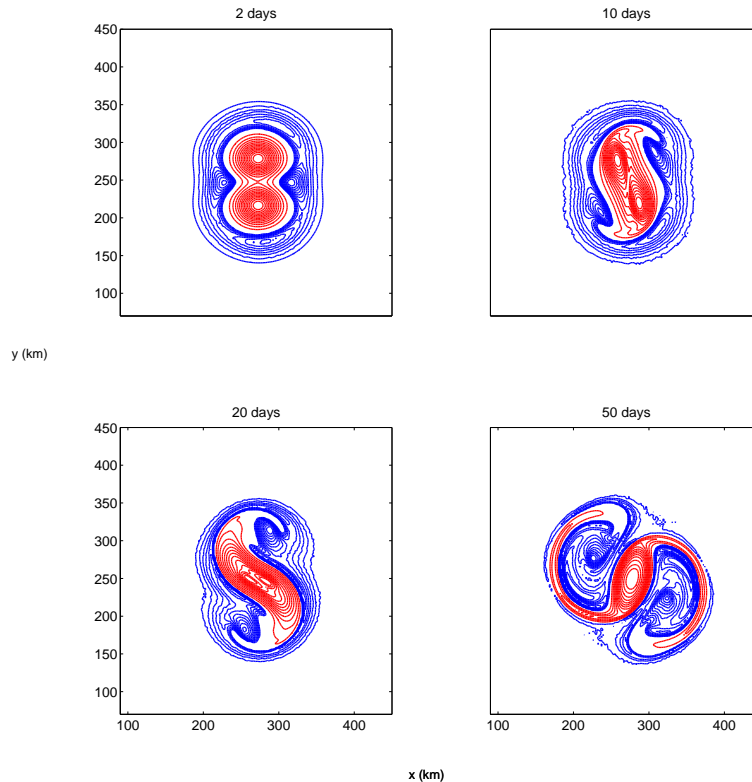


**Figure 4.16:** Horizontal sections of  $PV_a$  at the core of the subsurface cyclones ( $z = -1000$  m). The relative initial distance between the eddies is  $2.3 R$ .

Furthermore, the simulations evidenced that, in the cyclonic case, the merger behavior seems to be richer than for anticyclones. Indeed, increasing the critical distance between the two vortices to  $2.2 R$ , the horizontal sections of  $PV_a$  suggest a partial merger regime, see e.g. figure 4.17 (bottom panel, snapshot at  $t = 50$  days). The partial merger, though not quantified via evaluation of the integrated  $PV_a$ , is evidenced by the larger radius of the easternmost cyclone in the domain. We recall that in the anticyclonic case, increasing the relative distance by about  $0.1 R$  (from  $2.5 R$  to  $2.6 R$ ) made the interaction regime switch directly from merger to slight-interaction. Finally, if the relative distance between the cores of the two cyclones is further increased, up to  $2.3 R$ , the two vortices slightly interact during 20 days and separate afterwards due to the action of the peripheral opposite sign  $PV_a$  (dipolar effect).

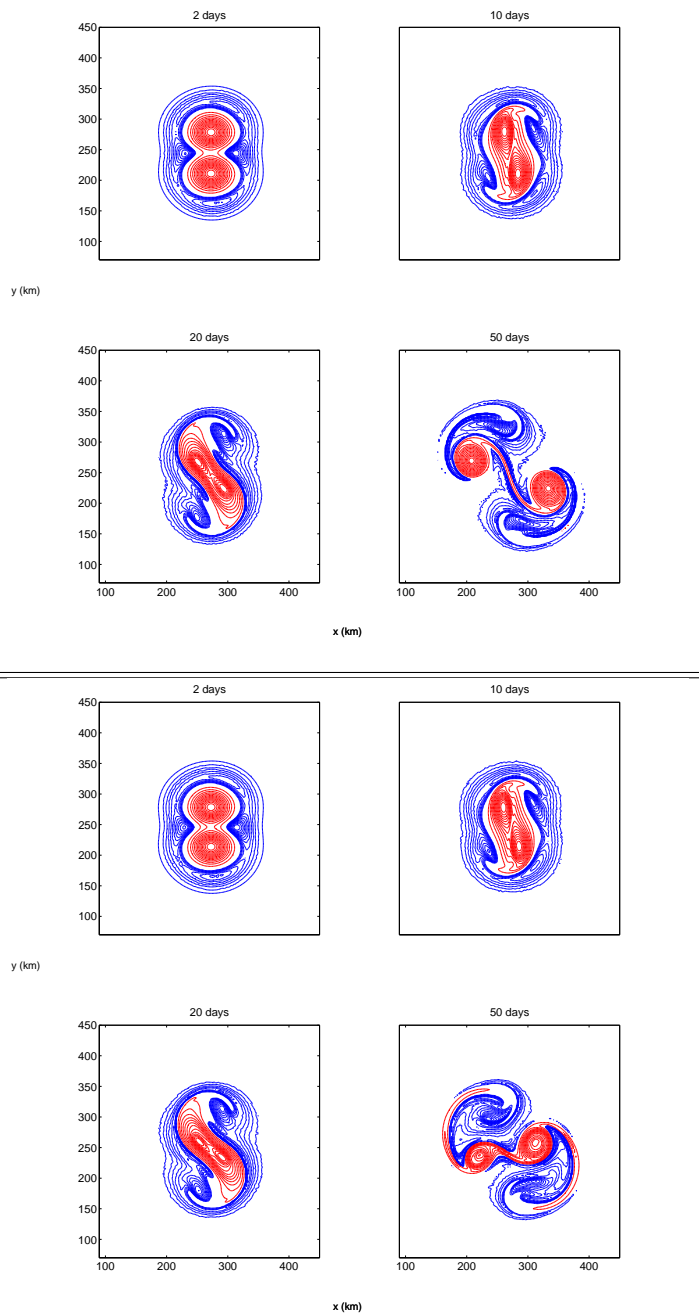


**Figure 4.17:** Horizontal sections of  $PVa$  at the core of the subsurface cyclones ( $z = -1000$  m). Top: the relative initial distance between the eddies is  $2.3 R$  (dipolar effect). Bottom: the relative initial distance between the eddies is  $2.2 R$  (partial merger).

### 4.6.2 Small-scale cyclones

The merger dynamics for small-scale subsurface cyclones ( $R = 15$  km) is similar to the one discussed in the previous section; even though the critical merger distance is even smaller,  $\mathbf{d}_c \mathbf{S} = 1.9 \mathbf{R}$  (where the subscript S stands for small-scale). These results are shown by figure 4.18.

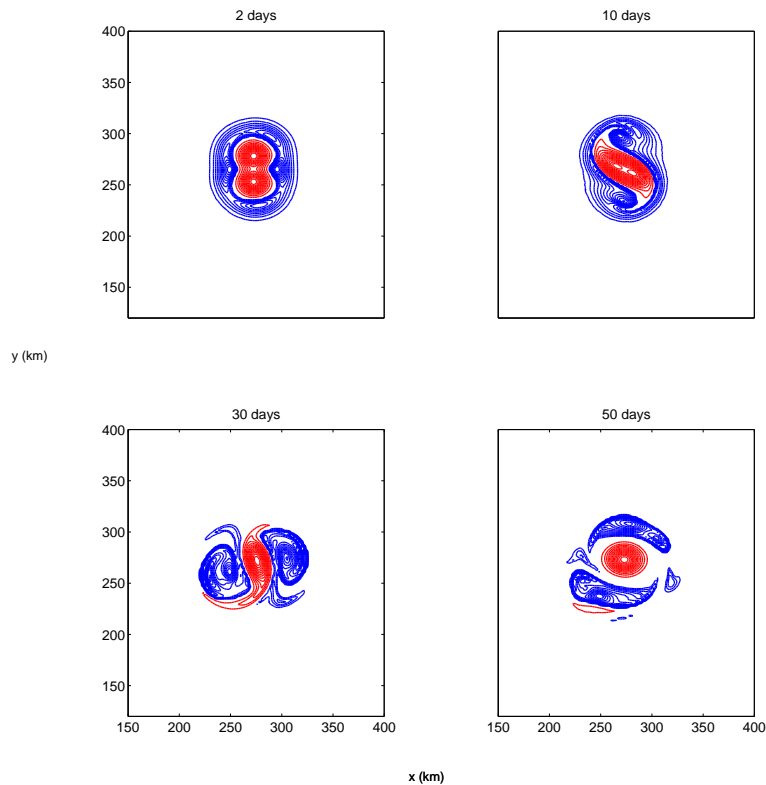


**Figure 4.18:** *Horizontal sections of PVa at the core of the subsurface cyclones ( $z = -1000$  m). The relative initial distance between the eddies is  $1.9 R$ .*

On the other hand, the partial merger and the slight-interaction regimes (still due to the dipolar effect) are obtained for relative distances of  $2.0 R$  and  $2.1 R$  respectively (see e.g. figure 4.19).

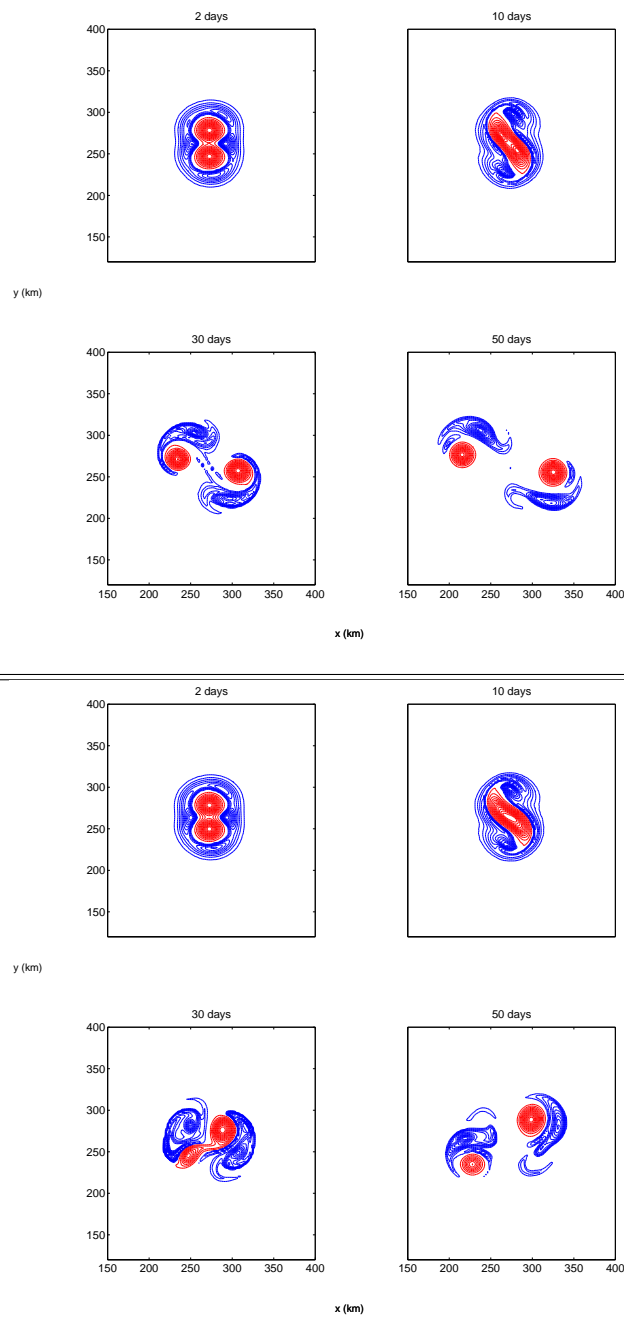


**Figure 4.19:** Horizontal sections of  $PV_a$  at the core of the subsurface cyclones ( $z = -1000$  m). Top: the relative initial distance between the eddies is  $2.1 R$  (dipolar effect). Bottom: the relative initial distance between the eddies is  $2.0 R$  (partial merger).

### 4.6.3 Discussion

Inspired by the results on the Merger of Meddy-like and Peddy-like vortices (M and P-vortices), shown throughout chapter 4, we ran simulations on the merger of intrathermocline cyclones. The aim of these experiments is to highlight similarities and differences between intrathermocline cyclones and anticyclones with respect to the merger, in an idealized numerical simulation. The main similarity between the two classes of subsurface eddies consists in the high sensitiveness of the eddies' behavior with respect to their relative distance. At the critical merger distance, the two eddies interact and eventually generate a single-core structure. In both the cyclonic and the anticyclonic case, the single-core structure is obtained over timescales that never exceed one month. If the eddies' relative distance is increased by about  $0.1 R$  (with  $R$  the eddy radius), they initially co-rotate and eventually separate moving away from each other. This is due to the redistribution of the opposite-sign peripheral PVa during the co-rotation phase, with consequent generation of peripheral vortices that trigger a dipolar drift of the initial eddies. Another similarity is given by the production of fine-scale structures during the merging process (mainly filaments).

The main differences in the behavior of subsurface cyclones and anticyclones are given by the value of the critical merging distance, as well as the existence of a partial merger regime, which was not observed for the anticyclonic case. While M and P-vortices merge at respective critical distances of  $2.5 R$  and  $2.6 R$ , their cyclonic counterparts (Large scale and Small-scale cyclones) need to be closer for the merging process to occur. Indeed, in the cyclonic case, the critical merger distances reduce to  $2.1 R$  and  $1.9 R$  (for Large and Small-scale cyclones, respectively). Also note that, in the cyclonic case, the smaller the eddy radius and vertical extent, the smaller the critical merger distance, which is in contrast with the results for M and P-vortices. One of the main reasons for the smaller critical merger distance of the cyclonic case is due to the initialization of the subsurface eddies. Indeed, as equation 4.2 indicates, the radial pressure gradient  $dp/dr$  is larger in a cyclonic case, if compared to the anticyclonic one (being  $v_\theta > 0$ ). Hence, choosing an opposite signed  $v_\theta$ , equation 4.2 yields an asymmetric pressure field (hence density field), if compared to the anticyclonic case. This is also evidenced by the PVa gradients across the eddies' cores, shown in figure 4.20. In the cyclonic case, larger PVa gradients are observed at the eddy periphery, indicating that the peripheral PVa shielding effect will be higher. Thus, merger will occur at a smaller critical distance than for anticyclones.

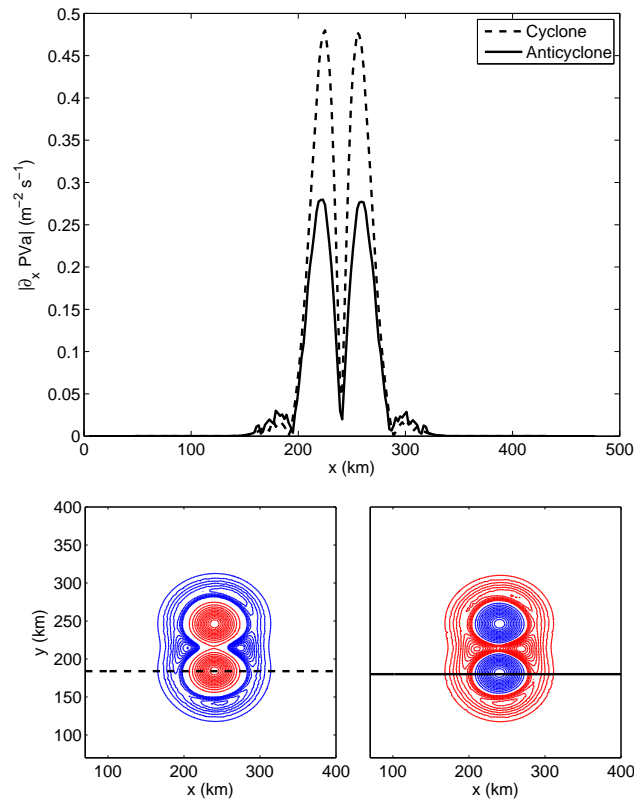


**Figure 4.20:** Horizontal gradient (absolute value) of  $PVa$  ( $\cdot 10^{10} m^{-1} s^{-1}$ ) across the cores of cyclonic and anticyclonic subsurface eddies, at  $z = -1000$  m. The gradients are evaluated along the black radials indicated in the two bottom panels.

This may indicate that, in general, the inverse energy cascade is not favored for subsurface cyclones, if compared to their anticyclonic counterparts swirling at an equal rotation rate (at least in the context of the cyclogeostrophic approximation). All these preliminary results certainly need to be further investigated. Indeed, if the intuition on the inverse energy cascade was confirmed by further analyses, it might help understanding the net asymmetry between subsurface cyclones and anticyclones generated by the Mediterranean Outflow, evidenced by recent numerical studies. [Barbosa Aguiar et al. (2013)].

## 4.7 Further Studies (B): The role of relative vorticity and of the divergence in the merger experiments

In this paragraph, we evaluate the contributions of relative vorticity ( $\xi$ ) and of the velocity field's divergence ( $\zeta$ ) during the merger of subsurface anticyclones. In order to do this, we choose the experiment on the merger of M-vortices, whose initial state is shown in figure 4.1 and whose results have been described in section 4.3.1. The expression for  $\xi$  and  $\zeta$  are given below:

$$\xi = \partial_x v - \partial_y u \tag{4.13}$$

$$\zeta = \partial_x u + \partial_y v \tag{4.14}$$

where  $u$  and  $v$  are the zonal and meridional components of the velocity field, respectively. As indicated by the bottom panel of figure 4.21, in the early stages of the simulation, the divergence field exhibits a double quadrupolar structure (one quadrupole for each anticyclone). This is mainly due to the elliptic deformation of the two anticyclones. Later on (around day 20), the divergence snapshot shows the existence of a wave field, mainly located in the areas where peripheral filaments are found.

On the other hand, the relative vorticity field exhibits a structure similar to the PVa sections of figure 4.3, where a central vorticity core is surrounded by an opposite sign vorticity shield. Furthermore, figure 4.21 indicates that the relative vorticity is larger than the divergence field throughout the whole merging process. In particular, the ratio  $|\xi/\zeta|$  goes from 30 (in the early stages of the simulation) up to around 150 for times exceeding one month. This indicates that, during the merger of mesoscale subsurface anticyclones, the effects of rotation dominate on the divergence of the velocity field. Despite this, the emission of gravity waves (associated to the diverging component of the velocity field) was evidenced in correspondence of the merger (around day 20) and it is associated to the production of filaments from the instability of the vortex peripheral and central areas.

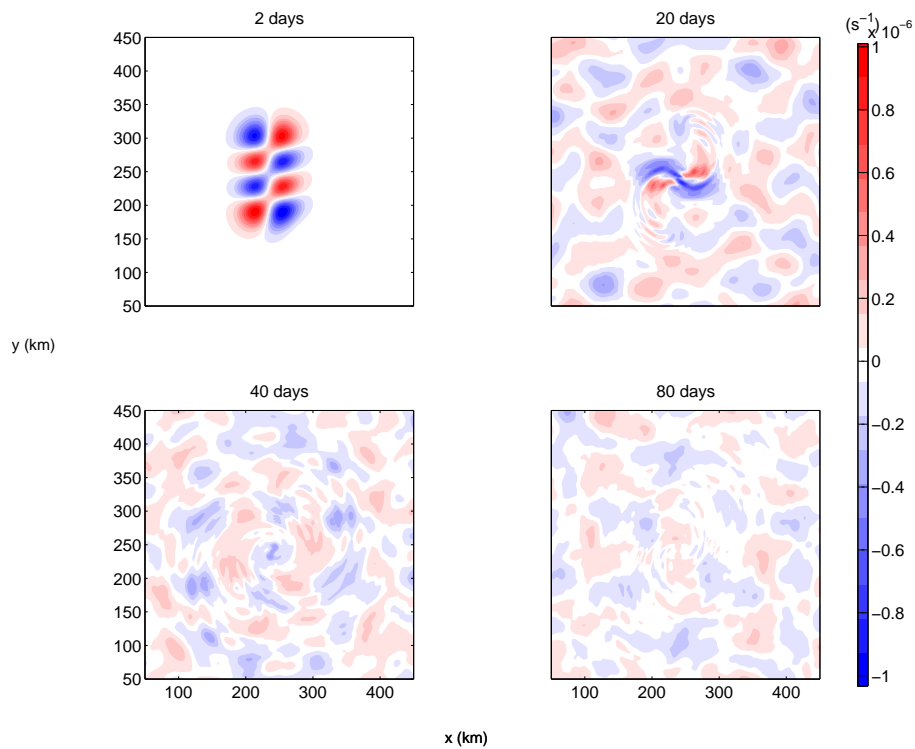
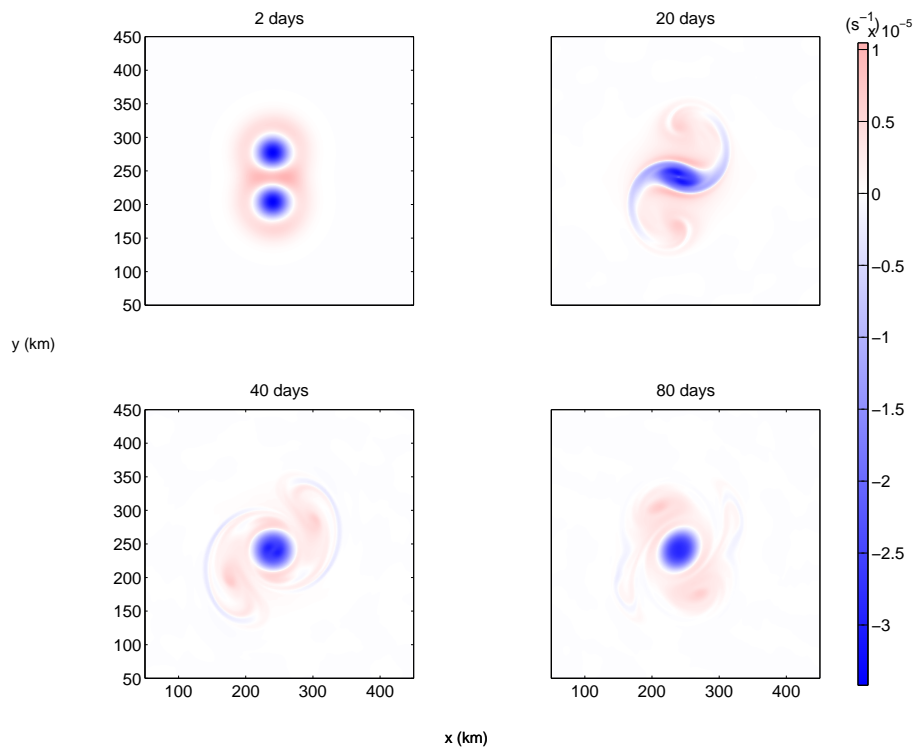


**Figure 4.21:** Horizontal sections of relative vorticity (top) and velocity field divergence (bottom) for the merger of  $M$ -vortices : Radius=30 km, Thickness= 500 m, Depth = 1000 m, Swirl velocity = 0.2 m/s (see also figure 4.1). The horizontal sections are evaluated at  $z \simeq -1000$  m.

## 4.8 The Ertel Potential Vorticity Anomaly in isopycnal coordinates

In this work, we have mostly represented vertical and horizontal maps of Ertel potential vorticity (PVa) in a cartesian framework. This representation, though possible [Vallis (2006)], only allows to have a diagnostic and instantaneous view of our system. If one wishes to predict the evolution of a system based on the conservation of the Ertel potential vorticity, this quantity should rather be represented along isopycnal surfaces. For this reason we want to compare maps of PVa in the cartesian and isopycnal framework. This will help understanding to which extent our representation can also be used in a prognostic context. In order to do this, we arbitrarily chose an initial state of a numerical simulation used to study the merger of subsurface-intensified anticyclones. We show the case of a couple anticyclones with the following characteristics (see also equation 4.3):

- Swirl velocity,  $v_0 = 30$  cm/s;
- Thickness,  $H = 500$  m;
- Radius,  $R = 30$  km;
- Depth,  $z_0 = 1000$  m.

Figure 4.22 shows the vertical sections of PVa through the cores of the anticyclonic couple. In the right panel, we show its representation in an isopycnal framework. Here, the PVa has been interpolated over fifty isopycnal surfaces " $\rho_{iso}$ " ( with  $\rho_{iso}$  going from 1022.4 to 1027.3  $\text{kg}\cdot\text{m}^{-3}$  at steps of 0.1  $\text{kg}\cdot\text{m}^{-3}$ ) and has been plotted as a function of their depth along the water column ( $z(\rho_{iso})$ ).

Comparing the two PVa representations of Figure 4.22, we could confirm that they are highly resemblant. The structures associated to the anticyclonic cores and peripheral shields (discussed earlier in this chapter) exist in both the cartesian and isopycnal framework and have similar shapes.

Hence, the PVa representation used in our work, which had a major diagnostic purpose, can also be seen as a proxy of a diagnostic PVa, i.e., the one evaluated along isopycnal layers.

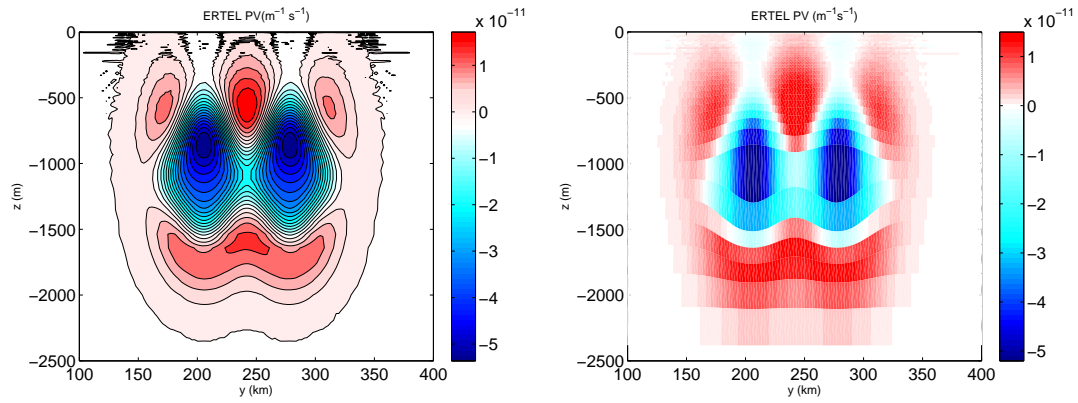


**Figure 4.22:** Vertical sections of Ertel Potential Vorticity (PVa) in cartesian (left) and isopycnal coordinates (right). Initial states for experiments on the merger of subsurface anticyclones are shown.

# Chapter 5

## Surface Signature of Mediterranean Water Eddies in a long-term high resolution simulation

This chapter is inspired by the paper

*Surface Signature of Mediterranean Water Eddies in a long-term high resolution simulation*, by

Daniele Ciani<sup>1</sup>, Xavier Carton<sup>1</sup>, Ana Claudia Barbosa Aguiar<sup>2</sup>, Álvaro Peliz<sup>3</sup>, Igor Bashmachnikov<sup>4,5</sup>, Federico Ienna<sup>3</sup> & Bertrand Chapron<sup>1</sup>

(1) Univ. Brest, CNRS, IRD, Ifremer, *Laboratoire d'Océanographie Physique et Spatiale* (LOPS), IUEM, 29280, Brest, France

(2) Met Office, Fitzroy Road, Exeter EX1 3PB, United Kingdom

(3) Instituto Dom Luiz, Faculdade de Ciências da Universidade de Lisboa, Lisbon, Portugal

(4) Institute of Earth Sciences, St. Petersburg State University (SPbSU), St. Petersburg, Russia

(5) NIERSC - Nansen International Environmental and Remote Sensing Centre, St. Petersburg, Russia

to be submitted to Deep Sea Research

## 5.1 Introduction

Mediterranean Water eddies (Meddies) are mesoscale subsurface-intensified anticyclones generated by the outflow of Mediterranean water into the Atlantic Ocean. The first documented evidence of Meddies dates back to the late 60s, when rotating and anomalously high salinity structures were found in the proximity of the Strait of Gibraltar [Swallow (1969)]. Later on, a hydrological survey allowed the detection of a similar structure in the Hatteras abyssal plain (25°N, 70°W) [McDowell and Rossby (1978)]. Though the observation site was several thousands miles away from Gibraltar Strait, the eddy seemed to show thermohaline properties typical of the Mediterranean water (although some years later it was proved that the origin of this eddy laid in the north-western Atlantic ocean [Prater and Rossby (1999)]).

Meddy formation and propagation mechanisms, as well as their three-dimensional structure have been extensively investigated up to recent years. Baroclinic instability of the Mediterranean outflow (MO hereinafter), in addition to the interaction with topographic irregularities along the Iberian coasts, have proved to be the main mechanisms responsible for Meddy shedding [Käse et al. (1989), Chérubin et al. (1996), Bower et al. (1997), Serra et al. (2002), Serra et al. (2005) and Chérubin et al. (2007)].

Käse et al. (1989) and Chérubin et al. (2007), via a numerical approach, studied the instability of a northward jet and of a westward boundary current, respectively. These features are idealizations of the meridional and zonal branches of the MO, along the western and southern Iberian coasts. In both cases, meddy shedding clearly resulted from meandering of the initial baroclinically unstable jets. Aiki and Yamagata (2004) and Chérubin et al. (1996) pointed out that interactions with capes and canyons are also important in eddy shedding from a slope current. In the real ocean, it has been proven that the aforementioned conditions are all satisfied, the MO being a baroclinic jet interacting with canyons and capes along the Iberian coasts (e.g. Portimão Canyon, Cape São Vicente, Estremadura Promontory and Cape Ortegal) [Bower et al. (1997), Chérubin (2000)].

The detailed three-dimensional structure of Meddies has been investigated via direct hydrological observation and numerical modeling [McDowell and Rossby (1978), Armi and Zenk (1984), Prater and Sanford (1994), Armi et al. (1989), Käse

et al. (1989), Richardson et al. (1989), Pingree and Le Cann (1993b), Richardson et al. (2000a), Barbosa Aguiar et al. (2013), Bashmachnikov et al. (2015)]. Dynamically, such eddies have velocities mostly in the horizontal plane and their swirling velocities can exceed 30 cm/s. Their radii range from 10 to around 100 km and their thicknesses range between 200 and 1200 m, with a resulting aspect ratio  $\mathcal{O}(10^{-2})$  and Rossby numbers that can reach 0.3 [Aubert et al. (2012), Bashmachnikov et al. (2015)]. Hydrological observations confirmed that Meddy cores (if defined with respect to salinity) are mostly intensified at depths around 1000 m, even though occurrences of cores at 700 m depth are possible [Pingree and Le Cann (1993a)].

The use of both observational and numerical approaches revealed that the Meddy generation rate is roughly 20/yr [Bower et al. (1997), Barbosa Aguiar et al. (2013)] and that their lifetime can easily exceed one year. Most Meddies are characterized by sharp vorticity gradients at their peripheries, whose main effect is to shield the core from the surrounding ocean [Tokos and Rossby (1991), Ménesguen et al. (2012)]. Furthermore, self-propagation, in addition to coupling with other eddies and/or regional currents makes Meddies non-stationary features, hence, able to propagate up to the Mid-Atlantic Ridge and even further. [Käse and Zenk (1987), Colin de Verdière (1992), Morel (1995), Morel and McWilliams (1997), Carton et al. (2002), Carton et al. (2010)]. On average, a single Meddy can carry up to  $10^{11}$  tons of salt [Bashmachnikov et al. (2015)], demonstrating the importance of Meddies for the redistribution of tracers (heat and salt) in the North Atlantic (see e.g. Shapiro et al. (1995), Stephens and Marshall (1999), Richardson et al. (2000a)). Thus, tracking Meddies is essential to evaluate heat and salt fluxes and distribution at thermocline level off the Iberian coast (up to 40-45°W, western limit of the Mediterranean salinity tongue [Joyce (1981)]).

One of the most efficient Meddy-tracking strategies relies on the use of neutral buoyancy floats directly deployed at typical depths of MO (or inside Meddy cores). Using this technique, Bower et al. (1997) detected ten Meddy-formation events, as well as the trajectory of several Meddies formed at Cape São Vicente and Estremadura Promontory. Similarly, the use of research vessels allows the detailed description of Meddy structures via CTD surveys, deployment of XBT, profilers, etc. [McDowell and Rossby (1978), Pingree and Le Cann (1993b), Richardson and Tychensky (1998), Tychensky and Carton (1998), Carton et al. (2002)]. The only

disadvantage of these strategies is the lack of synopticity, allowing the analysis of only a few meddies at a time. A rough calculation based on Meddy formation rate and mean lifetime, states that a snapshot of the North Atlantic would reveal around 30 Meddies in the basin [Richardson et al. (2000b)]. For these reasons, many attempts at detecting Meddies have relied on the synoptic information provided by satellite sensors.

Käse and Zenk (1987) hypothesized that Meddies should have surface anti-cyclonic vorticity signals, and they confirmed this using satellite-tracked drifters, whose trajectories were clearly driven by an underlying meddy. Stammer et al. (1991), using Geosat altimetry data found that, in the presence of Meddies, local bumps in sea-surface height (SSH hereinafter) fields are highly correlated with Meddies found in dynamic topography at Mediterranean water depths. Meddies appeared as local bumps in the sea-surface elevation. This result was also confirmed by Bashmachnikov et al. (2009), who showed that the Meddy induced sea-level anomalies are rather stable features in time and by Ienna et al. (2014), who tracked Meddies using satellite altimetric signals (AVISO gridded data) filtered at timescales larger than 6 months. Oliveira et al. (2000), combining fine-resolution sea-surface temperature (SST hereinafter) and SSH measurements, confirmed that Meddies induce local positive anomalies in the elevation of the sea-surface. On the other hand, as corroborated by Bashmachnikov et al. (2013), Meddy signatures in SST strongly depend on the local thermal conditions at the sea-surface and are only detectable when SST gradients exist near an underlying Meddy. Occurrences of Meddy "mushroom-like" signatures in SST fields are also possible, and are observed when a Meddy is coupled with a cyclonic companion at depth [Serra et al. (2010)].

All the works cited here were successful at tracking Meddies from space, though, at least in the initial stages of tracking, they relied on hydrological informations confirming the presence of a Meddy at depth.

The factors that can influence the surface expression of a Meddy in SSH are both due to the surrounding ocean and to the Meddy itself. Bashmachnikov and Carton (2012) and Ciani et al. (2015) state that an increase in Meddy radius, swirl velocity and thickness generate larger sea-surface elevations. On the other hand, a larger depth of the Meddy core can diminish the eddy surface signal. Surface turbulent features, like surface eddies shedded by fronts (e.g, the Azores Front

[Bashmachnikov et al. (2013), Bashmachnikov et al. (2014)]) can also perturb the anticyclonic signature of a Meddy and enhance the signal or make it disappear. Bashmachnikov and Carton (2012) found that stronger upper ocean stratifications can also reduce the SSH bumps related to an underlying Meddy. Most of the limitations in Meddy detectability via altimetry (an all-weather-available satellite technique) are due to interpolation, necessary to get two-dimensional maps from along-track data; 2 cm is the uncertainty for along-track data, while this value raises up to 4 cm for interpolated data far from the satellite swath [Fu and Cazenave (2000)]. Larger Meddies can generate local SSH bumps around 10 to 15 cm [Bashmachnikov and Carton (2012)], though smaller eddies (even in idealized contexts) can have signatures below the 2 cm threshold [Ciani et al. (2015)]. The future SWOT satellite mission [Fu et al. (2009)], will directly provide global submesoscale-resolving and two-dimensional maps with uncertainties around 2 cm. Moreover, the combination with present-day remotely sensed salinity (e.g. SMOS satellite) and temperature data could help Meddy detection from space.

All these considerations lead us to look for surface signatures of Mediterranean water eddies in a high-resolution realistic model, thoroughly described in Barbosa Aguiar et al. (2013). Using the model outputs, we colocated the surface signatures of a Meddy to its structure and displacement at depth. This was done for the SSH, SST and sea-surface salinity (SSS hereinafter) fields. The aim is to understand to which extent the combination of these informations can help us track a Meddy and isolate its signature from that of surface features.

This chapter is structured as follows: in section 5.2, the materials and methods of our investigations are presented, while section 5.3 contains the detailed analysis of the surface signature of three long lived Meddies in the model, each of them exhibiting a different pathway off the Strait of Gibraltar. We go on determining the typical timescales over which a Meddy surface signature varies due to a change in the Meddy structure at depth, in section 5.4. Section 5.5 deals with the overall behavior of the surface signatures for the 90 longest lived Meddies in the model, with lifetimes ranging from 1 to more than 2 years. Finally, the main conclusions of our work are given in section 5.6.

## 5.2 Methods

### 5.2.1 The model

The main characteristics of the model settings and outputs [Barbosa Aguiar et al. (2013)], are described here. The model is the primitive equations Regional Oceanic Modeling System (ROMS [Shchepetkin and McWilliams (2005)]). The modeled oceanic basin extends from  $4.5^{\circ}\text{W}$  to  $20^{\circ}\text{W}$  and from  $32^{\circ}\text{N}$  to  $41^{\circ}\text{N}$  in the zonal and meridional directions, respectively (see e.g. figure 5.2). The grid horizontal spacing is around 3 km and the vertical discretization is given by 32 levels. Integration in time is performed every 300 s and the outputs are averaged every 3 days. The model was run for 24 years (year zero is arbitrarily renamed as 2000) and a climatological atmospheric forcing was applied (COADS monthly climatologies [Da Silva et al. (1994)]). Though the model time will be used for convenience, one must remember the climatological nature of the forcing as well as the arbitrariness in the choice of the initial year.

Finally, we point out that in Barbosa Aguiar et al. (2013), Meddies' trajectories have been determined via an automatic eddy tracking software (ETS hereinafter [Nencioli et al. (2010)]) at the nominal depths of 600 and 1000 m. In the results that follow, taking advantage of the *a-priori* known Meddies trajectories, we were able to collocate the eddy instantaneous position to that of its surface expression (when present). This allowed us to describe the properties of the sea-surface anomalies induced by such eddies on oceanic surface elevation, temperature and salinity fields.

### 5.2.2 Definition of the Meddy surface signature

We identify the Meddy dynamical surface signature via the Okubo-Weiss pattern (OW hereinafter) in the model surface layer. For a given Meddy trajectory, we search for a minimum OW value spatially correlated with the position of the Meddy at depth, i.e., such point must lie within one Meddy radius from the Meddy center (the latest being independently detected at depth). Then, we take zonal and meridional sections of the OW surface field crossing the OW minimum. For every section, the horizontal extent of the signature is defined by the width of the U-shaped profile of the surface OW (see e.g. figure 5.1). As long as OW exhibits

a negative sign, we assume it is associated to the Meddy anticyclonic vorticity. In figure 5.1, the center and horizontal extent of the Meddy surface signature are indicated by the red dots.

Finally, the Meddy signature is evaluated in SSH, SSS and SST linearly detrended fields. In particular, for every instant of the Meddy lifetime, the corresponding anomaly in sea-surface height will be defined using the information provided by the OW pattern. The anomaly is evaluated across the width of the OW profile and is given by the averaged SSH-differences between the center and the boundary of the Meddy dynamical signature. This is done for both the meridional and the zonal directions (see e.g. the blue radials in figure 5.1-top panel). On the other hand, the Meddy-induced anomalies in SSS-SST fields are computed as the difference between the mean SSS-SST values in a "central" and a "peripheral region", respectively. Such regions are indicated in figure 5.1 (bottom panel): the central one (yellow circle) is the area extending from the center up to 0.25 radii of the Meddy dynamical signature, while, the peripheral one (blue annulus) extends from the edge of the central area up to 1.5 radii of the Meddy dynamical signature. This choice allows a better estimation of the anomalies when a flow convergence takes place in correspondence of the Meddy dynamical signature. Indeed, in those cases, a four points evaluation would not be suitable to evaluate the Meddy-induced anomaly with respect to the center of the signature.

### 5.2.3 Meddy metrics and oceanic background parameters

In order to characterize the behavior of the Meddies' surface signature, some properties of the Meddy, as well as of the surrounding ocean are derived along the eddy trajectory. We want to evaluate to what extent the seasonal and/or geographical variability of oceanic and Meddy parameters can affect the surface signature of such eddies.

This will be done for both the subsets of Meddies tracked (via the ETS) at 600 m and 1000 m depths. The along-trajectory properties are given in table 5.1.

The Meddy parameters are derived from the model in combination with the ETS. The Meddy **Depth (D)** is computed from vertical salinity profiles through the position of the Meddy center, the latest being an output of the ETS. The depth of the eddy core is given by the position of the maximum salinity along the vertical

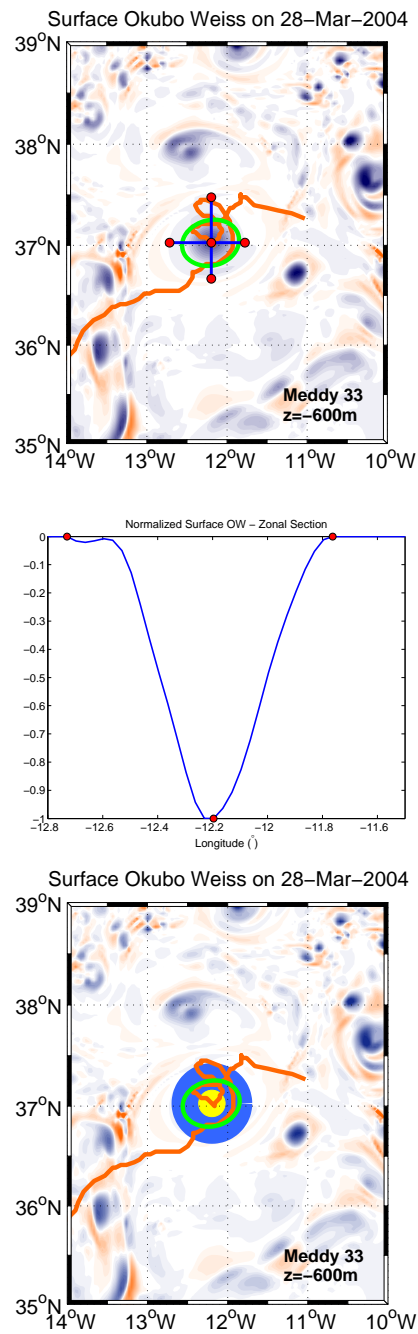


**Figure 5.1:** Surface signature associated to a Meddy. Top: surface Okubo-Weiss field for a specific position of Meddy 33 (tracked at a depth of 600 m, see also figure 5.3). The Meddy trajectory and its dynamical radius are indicated in orange and green, respectively (ETS output, Nencioli et al. (2010)). The zonal and meridional sections of the surface OW fields are given by the blue radials. The red dots indicate the center and limits of the radials. Middle: zonal section of the OW surface fields generated by the Meddy 33 on March, 28th 2004 (model time). Bottom: surface Okubo-Weiss fields with tracking method for SST and SSS anomalies. The central and peripheral areas of the Meddy signature are given by the yellow and blue regions, respectively.

**Table 5.1:** *Along-trajectory Meddy and background parameters. MLD: Mixed Layer Depth,  $N$ : Brunt-Väisälä frequency,  $\nabla h_B^e$ : bottom oceanic topography,  $U_{clim}$ : climatological zonal surface currents,  $SV$ : Swirl Velocity,  $R$ : Radius,  $Th$ : Thickness,  $D$ : Depth,  $i$ -EPVa: volume integrated potential vorticity anomaly,  $i$ -Sa: volume integrated salinity anomaly,  $i$ -Ta: volume integrated temperature anomaly.*

BACKGROUND	MLD	$N$	$\nabla h_B^e$	$U_{clim}$			
MEDDY	SV	R	Th	D	i-EPVa	i-Ta	i-Sa

within the 500-1500 m depth-range. This choice is justified by most of the earlier works based on hydrological data [McDowell and Rossby (1978), Käse and Zenk (1987), Pingree and Le Cann (1993a), Pingree and Le Cann (1993b), Richardson et al. (2000a), Bashmachnikov et al. (2015)] stating that Meddies are mostly intensified in the aforementioned depth-range. The **Swirl Velocities (SV)** and **Radii (R)** are both evaluated at the depth of the salinity core. Firstly, we compute the quantity  $U = \sqrt{u^2 + v^2}$ , where  $u$  and  $v$  are the zonal and meridional components of the currents, respectively. Then, we average the four maximum values of  $U$  ( $U_{max}$ ) observed along two radial sections passing through the Meddy center and oriented meridionally and zonally. The four  $U_{max}$  values are identified by the region where the  $U$  gradient, evaluated along the radial sections from the Meddy center towards its periphery, becomes zero for the first time. Hence, such radial sections also provide an information on the dynamical radius, which is defined here as the average distance between the Meddy center and the four positions of  $U_{max}$ . The Meddy **Thickness (Th)** is also evaluated using vertical salinity profiles passing through the eddy center. The vertical boundaries of the eddy are searched in the 200 to 2000 m depth-range. This choice allows one to neglect the salinity values associated to the oceanic surface layers, i.e., not related to the Mediterranean outflow. Such boundaries are defined as the uppermost point in which the vertical salinity gradient is positive and the lowermost in which such gradient is negative ( $z$  increasing downward for the computation of the vertical gradient). In addition, such points must be characterized by a salinity anomaly  $\Delta S \geq 0.1$  PSU. Notice that the salinity anomaly is defined with respect to a model-derived climatological salinity. Finally, the **i-EPVa**, **i-Sa** and **i-Ta** are the three-dimensional integrals of the Ertel potential vorticity (EPV hereinafter), salinity and temperature anoma-

lies, respectively. Such integrals are computed within the Meddy volume, whose vertical bounds are given by the aforementioned salinity criterion. The Meddy lateral bounds, for each vertical level, are considered in the integral computation algorithm: only values exhibiting EPV, salinity and temperature anomalies (with respect to the surrounding ocean) larger than  $0.1 \cdot (10^{11}) \text{ m}^{-1}\text{s}^{-1}$ , 0.1 PSU and 0.1 °C within two Meddy radii are taken into account, respectively. Notice that, although anticyclones generally have negative EPV cores, in this study we integrate the  $(-1) \cdot \text{EPV}$  quantity by convention.

Regarding the oceanic background parameters, the depth of the **Mixed Layer (MLD)** is computed from vertical temperature profiles as described in Lorbacher et al. (2006).

$\mathbf{N}$  is the average **Brunt-Väisälä** frequency above the Meddy upper limit (i.e., from the Meddy top to the ocean surface). Hence,  $\mathbf{N}$  will exhibit both a geographical and a seasonal variability, due to combined effect of the Meddy displacement and to the seasonal oscillations of the oceanic mixed layer depth.

The role of the **oceanic bottom topography** ( $\nabla h_B^e$ ) is also investigated. The superscript  $e$  indicates that such gradient is aware of the  $e$ -decay scale of the eddy properties with depth  $H_m$  [Bashmachnikov et al. (2014)]. In particular, we compute the gradient of the along-trajectory bottom features, using (5.1) and (5.2):

$$\nabla h_B^e(t) = \frac{h_{t+1} - h_t}{s_{t+1} - s_t} \cdot e^{-\frac{|z-z_0|}{H_m}} \quad (5.1)$$

$$H_m = \frac{\sqrt{2}Rf}{1.53N_b} \quad (5.2)$$

In (5.1) and (5.2),  $h$  is the local elevation of the bottom topography,  $s_{t+1} - s_t$  is the curvilinear distance between two Meddy successive positions,  $z$  is the depth of the oceanic bottom,  $z_0$  the depth of the Meddy core,  $f$  is the local Coriolis parameter and  $N_b$  is the mean Brunt-Väisälä frequency averaged between the Meddy lower limit and the oceanic bottom. This allow us to verify whether or not a bump or a depression in the ocean bottom can correlate with the eddy surface signature.

Finally, the model-derived **climatology of the zonal surface currents**

( $U_{\text{clim}}$ ) is also computed. This information gives an indication of the position of the Azores front in the model (see e.g. figure 5.2), allowing to evaluate whether the interaction between the Meddy surface signature and the front is destructive or not. The position of the Azores front will be also used to separate the region of study on the Atlantic Ocean into the "Northern Basin" and the "Southern Basin", north and south of the front, respectively.

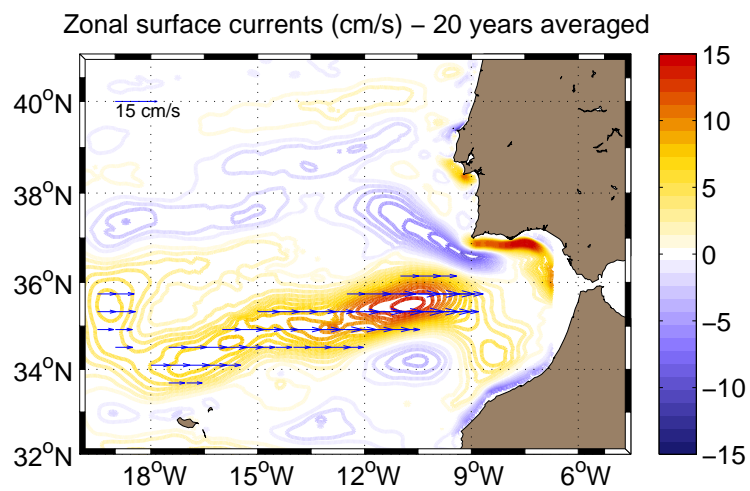


**Figure 5.2:** Climatological zonal surface currents (model-derived). The zonal band located between  $34^{\circ}\text{N}$  and  $36^{\circ}\text{N}$  is the footprint of the Azores front (also evidenced by the blue arrows). The intensities of the surface currents are given in cm/s.

## 5.3 Results

In a first step, Meddies were classified into three groups, according to their lifetime (Group 1: Lifetime exceeding 2 years, Group 2: Lifetime comprised between 1 and 2 years, Group 3: Lifetime less than 1 year). In our work, we will focus on the Meddies of Group 1 and 2. This choice, though reducing the number of eddies that can be analyzed, allows us to investigate Meddies which travel over long distances in the Atlantic Ocean, hence, whose evolution is more likely to be influenced by geographical factors, seasonal effects or Meddy intrinsic variations, if compared to shorter-lived structures (lifetime  $\mathcal{O}(\text{month})$ ). Indeed, the eddy parameters can significantly vary as the eddy drifts away from the Iberian coast [Armi et al. (1989), Barbosa Aguiar et al. (2013), Bashmachnikov et al. (2015)]. Moreover, environmental parameters (e.g, stratification, Mixed Layer Depth, etc.) also vary due to a combination of seasonal and geographical effects (since most Meddies drift southwestward). Such a choice proves useful if one wants to evaluate the capability of satellite sensors to track Meddies over several months.

### 5.3.1 Along-trajectory Meddy surface signature

The trajectories of the eight longest-lived Meddies in the model (lifetimes between 1.5 and 2.5 years) are given in figure 5.3. In this figure, each eddy is labeled after the ETS outputs and its initial and final positions are respectively indicated by a circle and a cross. Note that Meddies 68, 139 and 169 can be classified as "Westward Moving Meddies", since 98%, 66% and 100% of their trajectory respectively lies north of the Azores Front (see e.g. figure 5.2 and 5.3). The other Meddies remain in the Northern Basin for less than 50% of their trajectory.

In what follows, we present a comparative study of Meddies 33, 169 and 120. While Meddy 33 and 169 show pathways typical of most Meddies in the Atlantic Ocean [Barbosa Aguiar et al. (2013), Bower et al. (1997)], Meddy 120 exhibits a mostly southward and unusually looping trajectory. The implications of these different behaviors on the Meddies' expression at the sea-surface will be discussed in detail.

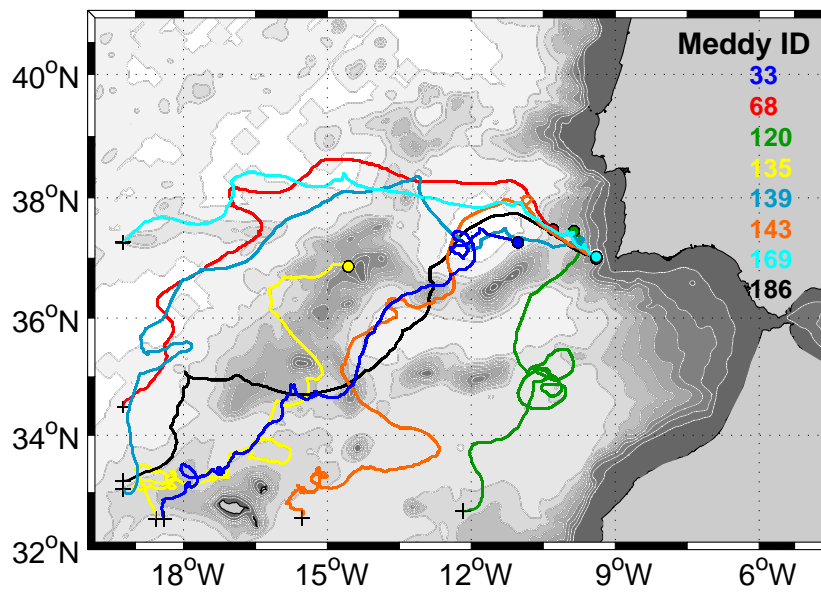


**Figure 5.3:** Trajectories of the longest-living Meddies in the model, detected at both 600 m and 1000 m depth. Their lifetime exceeds 2 years. Meddies are labeled after the automatic detection algorithm [Nencioli et al. (2010)].

### Meddy 33

Meddy 33 is the longest-living Meddy of Group 1 (lifetime  $\simeq 2.5$  years). This eddy, like most of the subsurface-intensified anticyclones in the  $\beta$ -plane approximation, exhibits an equatorward trajectory [see e.g. Morel and McWilliams (1997)].

Firstly detected on January, 1st 2004 (model time) in the proximity of Gorringe Bank ( $11^\circ W$ ,  $37^\circ N$ ), it makes its way through the Horseshoe Seamounts and, after crossing the Azores front on October, 30th 2004 it reaches the edge of the modeled domain (the sponge layer) on June 9th, 2006. The along-trajectory properties of the Meddy and background ocean are illustrated in figure 5.4 and 5.5.

During the 2.5 years of evolution, the Meddy constantly generates a surface signature (in the OW fields) that extends between 0.2 and 2 eddy radii. The induced **SSH anomaly** is always positive and has an overall decreasing linear trend of 2 cm/year. Its maximum value is around 7 cm, as observed during April 2004. The SSH anomaly abruptly decreases around October 2004 and then keeps a fairly constant value ( $\simeq 1.5$  cm) up to the last Meddy tracked position. Several physical processes contributed to the evolution of this anomaly; they can be understood with figures 5.4, 5.5, 5.6 and table 5.2.

From January to April 2004, the SSH anomaly grows by about 1.7 cm/month; afterwards, the signal is fairly constant and exhibits a peak during June 2004. The initial positive trend in SSH anomaly, as well as the peak observed in June 2004 are also associated to increases in Meddy radius and swirl velocity. This was mainly due to the merger of Meddy 33 with nearby Meddies (see e.g. figure 5.6). Such merger events are schematically indicated with yellow dots in the SSH anomaly time series of figures 5.4 and 5.5. The merger events are corroborated by the corresponding positive trends in the integrated EPVa, temperature and salinity anomaly. This mechanism is confirmed by theoretical studies in the framework of the quasi-geostrophic theory, dealing with isolated subsurface anticyclones in idealized oceans [Bashmachnikov and Carton (2012), Ciani et al. (2015)]. These studies point out that, if a subsurface vortex does not interact with topography or advection currents, one can directly relate its integrated EPVa, radius and thickness to the induced stream-function at the sea-surface (the latest being directly proportional to the sea-surface elevation in the quasi-geostrophic theory). Moreover, Ciani et al. (2016) state that, if two identical Meddies merge, the integrated

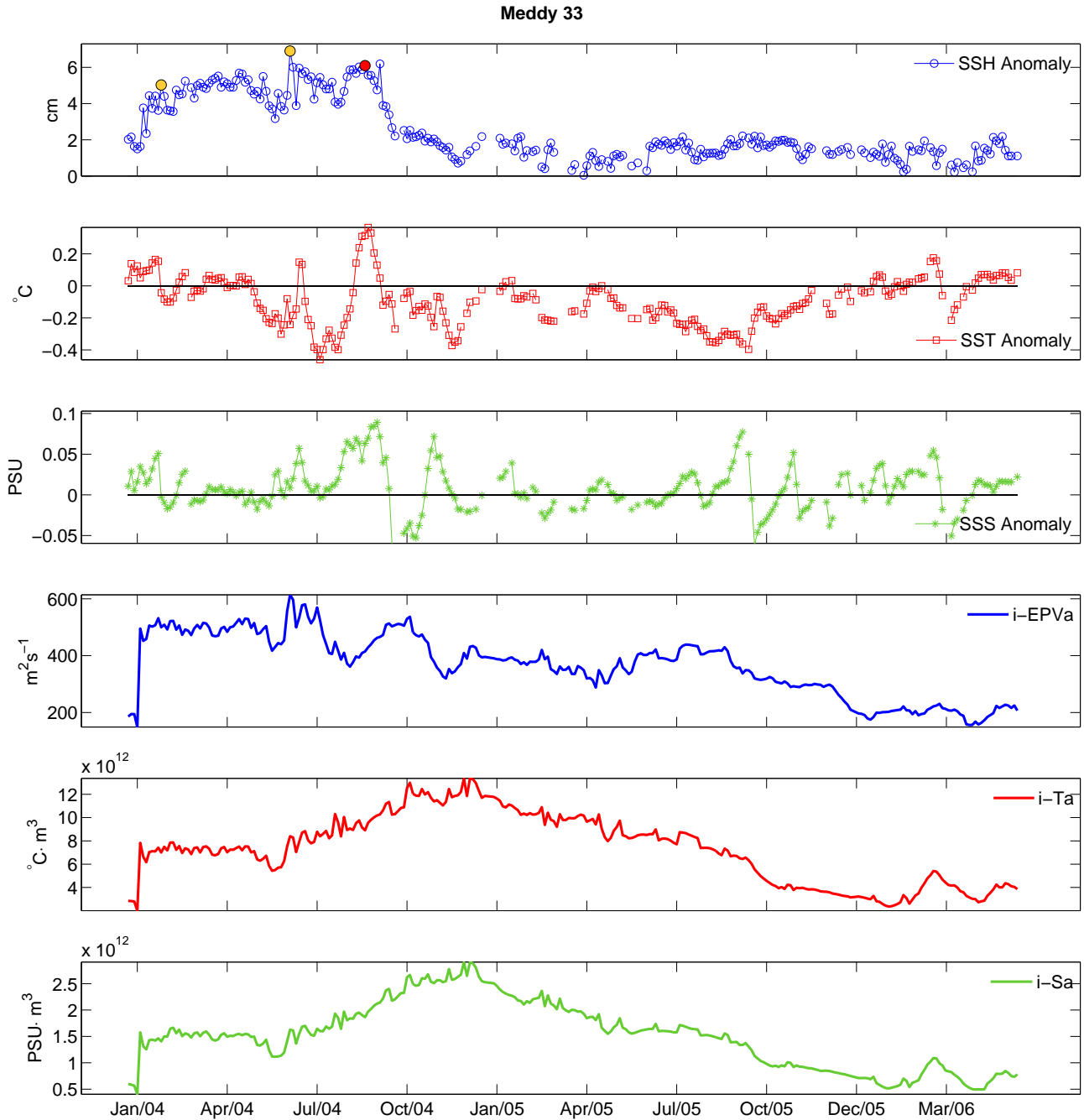


**Figure 5.4:** Surface signature and volume-integrated eddy parameters along the trajectory of Meddy 33 (see also Figure 5.3). SSH anomaly (blue circles. The colored dots are commented in section 5.3.1-Meddy 33), SST anomaly (red squares), SSS anomaly (green stars), *i-EPVa* (integrated Ertel potential vorticity anomaly, blue), *i-Ta* (integrated temperature anomaly, red), *i-Sa* (integrated salinity anomaly, green).

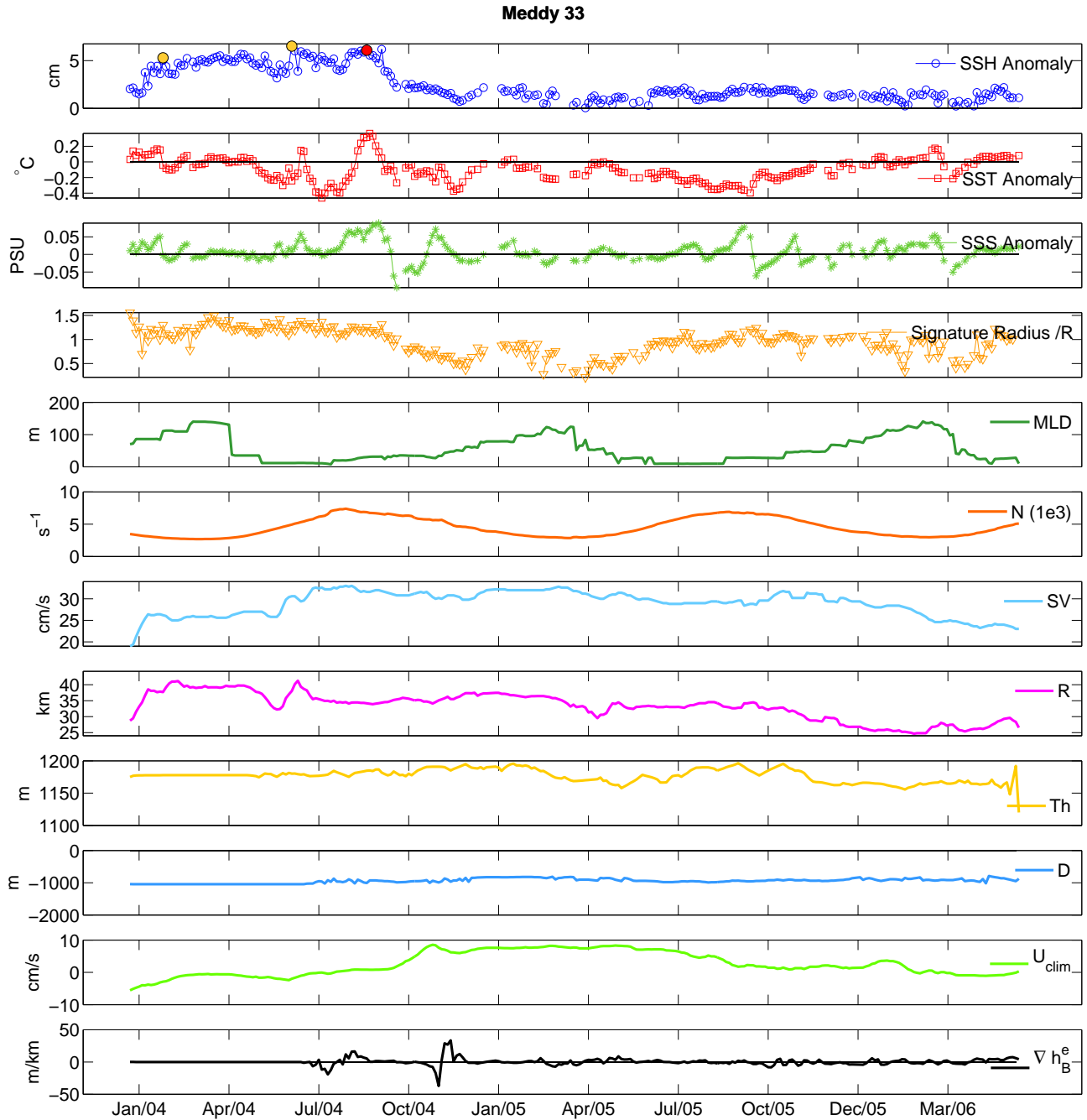


**Figure 5.5:** Surface signatures and Meddy/background properties along the trajectory of Meddy 33 (see also Figure 5.3). SSH anomaly (blue circles. The colored dots are commented in section 5.3.1-Meddy 33), SST anomaly (red squares), SSS anomaly (dark red stars) Signature Horizontal Extent (dark yellow triangles), Mixed Layer Depth (green), Brunt-Vaisala frequency (orange), Meddy Swirl Velocity (cyan), Meddy Radius (magenta), Meddy thickness (yellow), Meddy Depth (light blue), Intensity of climatological zonal surface currents (light green) and gradient of oceanic bottom topography (black).

EPVa and radius of the resulting Meddy respectively increase by 40% and 30%, while the Meddy is only slightly shallower (if compared to the initial Meddies). Here the variations were different as Meddy 33 firstly merged with a much larger Meddy and afterwards with a smaller one (see e.g. figure 5.6).

A third peak in SSH anomaly is observed between July and October 2014 (the peak is schematically highlighted by a red dot in the SSH anomaly time series of figures 5.4 and 5.5). No merger events can be associated to this SSH anomaly. Indeed, the integrated EPVa shows a local minimum in correspondence to the SSH anomaly peak. This minimum is due to lateral friction with the Goringe Bank seamount, as confirmed by the decrease in swirl velocity during the Meddy/Seamount interaction. Instead, this peak was a case of indirect signature. Meddy 33 vertically aligned with a surface anticyclone shedded by a meander of the Azores front (not shown). This surface anticyclone had a dynamical radius around 35 km, a swirl velocity around 30 cm/s and extended vertically over 400 m. According to Polvani (1991), given the characteristics of both the surface-anticyclone and the Meddy, vertical alignment is possible in this case, as both of the eddies have radii comparable with the Rossby deformation radius in the north-eastern Atlantic (i.e., where the alignment took place) [Chelton et al. (1998)].

Just afterwards, the Meddy crossed the Azores front and started interacting with the Horseshoe seamounts chain, experiencing a series of lateral and bottom collisions. The combination of these two effects, plus the Meddy erosion itself (evidenced by the decreasing radius, thickness, and swirl velocity in the second half of its lifetime) makes the SSH anomaly decrease abruptly and maintain a fairly constant value up to the end of its trajectory (i.e. when it reached the sponge layer of the region of study in the model).

It is worth noticing that, among the eddy/seamounts collisions, the one which mostly eroded Meddy 33 is the bottom one (with the Unicorn Seamount in early November 2004), as evidenced by the EPVa field, the meridional section of the zonal swirl velocity across the Meddy (shown in figure 5.7), the large value of the  $\nabla h_B^e$  time series and by the corresponding decreasing swirl velocity. Moreover, observing the i-Ta, i-Sa and i-EPVa behaviors in figure 5.4, one can clearly see how the overall decreasing trend of these quantities becomes evident in correspondence of the Meddy bottom collision, consistently with Shapiro et al. (1995). In general, the behavior of the i-Ta and i-Sa (for Meddy 33) can be explained as a combination

of merger, hydrological properties of the surrounding ocean and the interaction of Meddy 33 with seamounts. Indeed, temperature and salinity of the surrounding ocean (at the Meddy depth) decrease all along the Meddy trajectory, as also confirmed by model-derived temperature and salinity climatologies (not shown). Hence, the  $i$ -Ta and  $i$ -Sa, initially growing because of merger, subsequently increase because the Meddy encounters fresher and cooler waters. Afterwards, when the Meddy starts interacting with seamounts, the  $i$ -Ta and  $i$ -Sa gradients become negative, most likely because the water mass losses due to collisions, as well as the Meddy erosion due to diffusion.

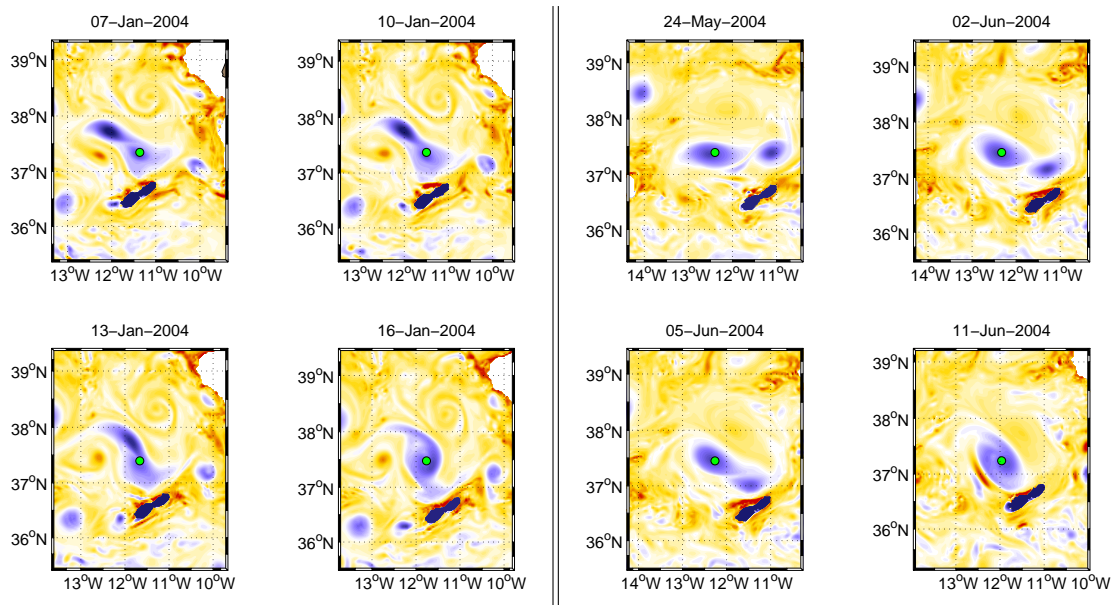


**Figure 5.6:** *Merger of Meddy 33 with nearby Meddies. Left: first merger event, January 2004. Right: second merger event: May/June 2004. In both panels, merger is shown via horizontal sections of EPVa at the Meddy instantaneous depth ( $z \simeq -1000$  m). The green dot indicates the instantaneous position of the Meddy center (ETS output).*

Differently from SSH anomaly, a trend for the behavior of the **SST anomaly** and **SSS anomaly** cannot be defined. As the Meddy makes its way into the Atlantic, such anomalies can assume either positive or negative values around zero, as also shown by the percentage of positive and negative SST and SSS anomalies listed in table 5.3 (for Meddy 33, the negative SST anomalies slightly dominate on the

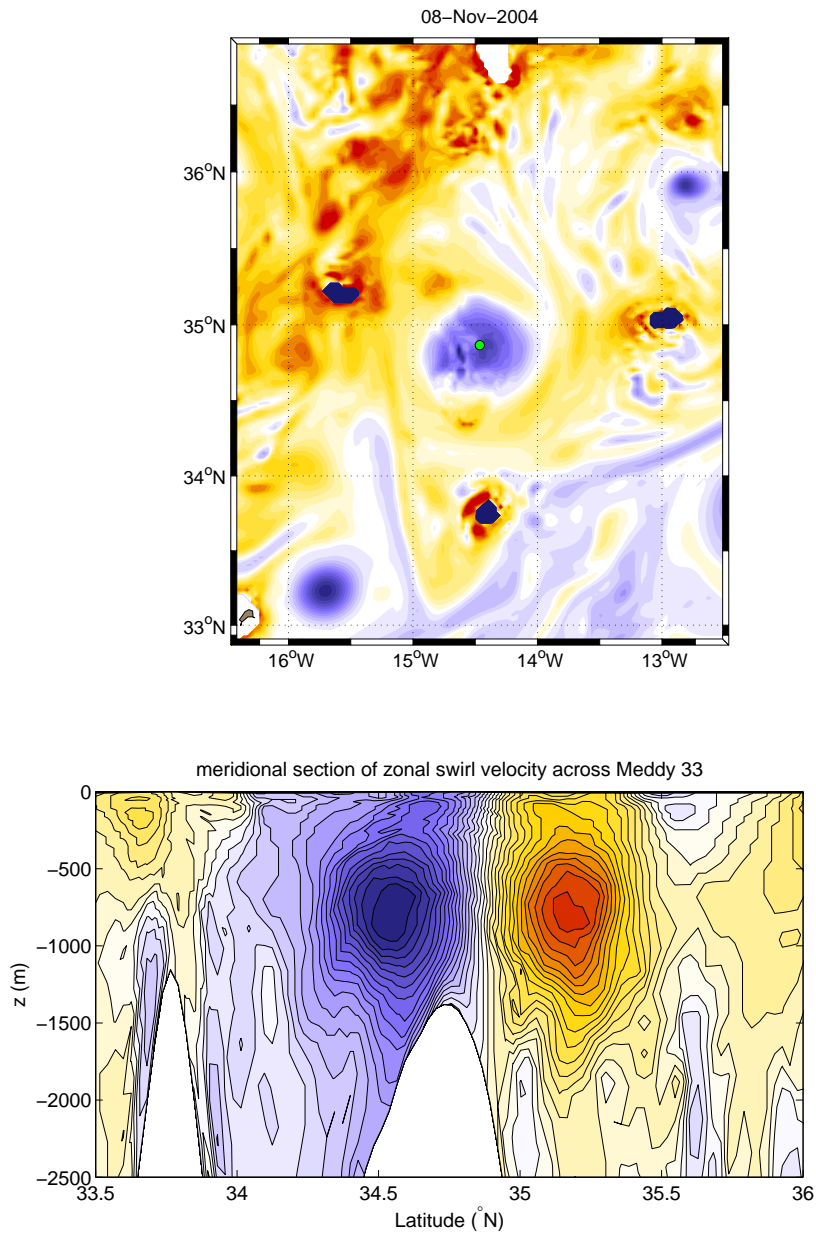


**Figure 5.7:** Bottom collision of Meddy 33 with the Unicorn seamount. Top panel: horizontal section of EPVa at a depth of 1000 m (the green dot indicates the instantaneous center of the Meddy, which is an ETS output). Bottom panel: vertical cross section of the Meddy swirl velocity (zonal component), the darkest red and blue areas indicate a velocity field of  $\pm 30$  cm/s, respectively.

**Table 5.2:** Pearson’s correlation coefficients ( $R_P$ ) between the Meddy 33 (M33) surface-signatures and the along-trajectory Meddy/background ocean characteristics. The largest values are highlighted in red.

<b>M33-<math>R_P</math></b>	<b>SV</b>	<b>R</b>	<b>Th</b>	<b>MLD</b>	<b>N</b>	<b>U clim</b>	$\nabla h_B^e$	<b>i-EPVa</b>	<b>i-Ta</b>	<b>i-Sa</b>
SSH <sub>anom</sub>	<b>0.69</b>	0.55	0.59	0.04	0.13	-0.53	-0.02	<b>0.71</b>	0.15	0.15
<b>M33-<math>R_P</math></b>	<b>SV</b>	<b>R</b>	<b>Th</b>	<b>MLD</b>	<b>N</b>	<b>U clim</b>	$\nabla h_B^e$	<b>i-EPVa</b>	<b>i-Ta</b>	<b>i-Sa</b>
SST <sub>anom</sub>	-0.14	-0.15	0.14	-0.24	0.31	0.04	0.10	-0.08	0.14	0.15
<b>M33-<math>R_P</math></b>	<b>SV</b>	<b>R</b>	<b>Th</b>	<b>MLD</b>	<b>N</b>	<b>U clim</b>	$\nabla h_B^e$	<b>i-EPVa</b>	<b>i-Ta</b>	<b>i-Sa</b>
SSS <sub>anom</sub>	0.14	-0.02	0.31	0.11	0.22	-0.18	0.13	0.15	0.21	0.20

positive ones, being observed during 65% of the Meddy lifetime). The positive and negative peaks in the SST and SSS anomalies are seldom correlated with the evolution of the i-Ta and i-Sa. This suggests that the evolution of such anomalies is mostly driven by local surface conditions rather than from an internal dynamics (i.e. from the presence of an underlying Meddy).

**Table 5.3:** Mean properties of Meddy 33 surface signatures.

<b>MEDDY 33</b>	SSH <sub>anom</sub>	SST <sub>anom</sub>	SSS <sub>anom</sub>
Max	7.2 cm	0.34°C	0.10 PSU
Min	0.10 cm	-0.45°C	-0.06 PSU
% $\geq 0$	100	35	64
% $< 0$	0	65	36

The general surface expression of Meddy 33 can also be summarized by means of table 5.2, showing the Pearson’s correlation coefficients [Fisher et al. (1946)] between each of the aforementioned anomalies and the time series of the Meddy/background characteristics. SSH anomalies are very highly correlated with the variability of the Meddy swirl velocity and i-EPVa (the coefficients are around 0.7 in both cases). As stated previously, the Meddy radius and thickness are also correlated with the Meddy-induced SSH anomaly, showing coefficients larger than 0.5. A moderate anticorrelation is observed with respect to the along-trajectory time series of the surface climatological zonal currents  $U_{clim}$  ( $R_P=-0.53$ ). Recall-

ing that the climatological surface currents allow us to evaluate the proximity of a Meddy with respect to the climatological imprint of the Azores front (see also figure 5.2), we can conclude that the SSH anomaly can be significantly degraded by the interaction with surface fronts. Indeed, as  $U_{clim}$  reaches its maximum value of about 10 cm/s (maintained for several months of the Meddy evolution, as shown by figure 5.5), the SSH anomaly is damped by about 4 cm. It is worth noticing that this happened 9 days before the Meddy went through the bottom collision with a seamount (shown in figure 5.7). Note that, in table 5.2, all the correlation coefficients exhibit a significance level higher than 85% (except for the correlations between SSH-SSS-SST anom and  $\nabla h_B^e$ , where it goes down to 60%). The significance reaches 95% for the correlation between SSH anom and i-EPVa. The along-trajectory depth of the oceanic mixed layer, and consequently, the average Brunt-Väisälä frequency above the Meddy have an oscillatory character. This is mostly due to their intrinsic seasonal variation during the 2.5 years of the Meddy evolution. Though Bashmachnikov and Carton (2012) pointed out that more stratified environments can degrade the surface signature of Meddies (in terms of the induced SSH anomaly, see their figures 8, 9 and equation 12) here, the surface expression is not highly correlated with the upper oceanic stratification; although it is worth noticing that the maximum SSH anomaly has been observed in correspondence of the first maximum of MLD (i.e., for a less stratified ocean, around April 2004). A possible explanation for this is related to the environment of Meddy 33. In fact, Bashmachnikov and Carton (2012), in order to determine theoretical dependence of the Meddy surface signature with respect to the oceanic stratification, dealt with isolated features, neglecting Meddy/Meddy and Meddy/topography interaction, which is not true for Meddy 33. The role of the along-trajectory gradient of oceanic bottom topography  $\nabla h_B^e$  has already been commented previously. Even though it is not correlated with the overall SSH anomaly, we saw that local topographic features can interact with the Meddy and modify its three-dimensional structure, as well as its surface expression. Finally, the time series of i-Ta and i-Sa are not correlated with the Meddy-induced SSH anomaly, exhibiting  $R_p$  values never exceeding 0.2. Also the correlation between the eddy-induced SST/SSS anomalies and the Meddy/background parameters never show values exceeding 0.3. This result reinforces our previous statements on the role of local surface oceanic conditions in driving the Meddy thermohaline surface signature. A similar result

is also found in Oliveira et al. (2000).

### **Comparison with the longest-lived "Westward moving Meddy": Meddy 169**

In this section, we compare the results obtained for Meddy 33 to the ones of the longest-lived-westward-traveling Meddy: Meddy 169 (lifetime  $\simeq 1.5$  years, see also figure 5.3). Not only had Meddy 169 the peculiarity of an almost straightforward and westward trajectory, but it also traveled far away from topographic features (except for the first days of its evolution, being firstly detected in proximity of Cape São Vicente, hence, close to continental shelf). This property, excluding interaction with other Meddies, makes Meddy 169 an isolated subsurface anticyclone (unlike Meddy 33, which underwent interaction with other Meddies, seamounts and the Azores front). The along-trajectory Meddy and background oceanic properties are given in figures 5.8 and 5.9. The time series shown in these figures clearly evidence that the SSH anomaly is a monotonically increasing function of time for more than half of the Meddy's lifetime (from July 2019 to April 2020), and so it is for its radius, swirl velocity, signature horizontal extent and  $i$ -EPVa. On the other hand, the  $i$ -Sa and  $i$ -Ta monotonically increase up to the end of the Meddy trajectory, in November 2020. Meddy 169 was born in a highly turbulent region, rich in mesoscale and submesoscale cyclonic and anticyclonic features (see e.g. figure 5.10). Its initial radius and swirl velocity are around 20 km and 10 cm/s, respectively. Afterwards, the Meddy started growing in size, to rotate faster, and its integrated EPV, salt and temperature anomalies also increased. This was due to a long series of merger events which fed the recently-formed Meddy (Bower et al. (1997) also identified Cape São Vicente as a Meddy generation site), modifying its initial structure and letting its surface signature grow both in size and intensity. In figure 5.10, the horizontal sections of EPVa catch two merger events of Meddy 169 with nearby small-scale anticyclonic eddies in less than two weeks. The month of April 2020 is the approximate date when the  $i$ -EPVa and the Meddy radius reach a plateau and stabilize around a constant value (see figure 5.8 and 5.9). A rough computation showed that by that date, Meddy 169 had drifted for 615 km off the Iberian coast. Bashmachnikov et al. (2015) studied the mean properties of Meddies as a function of distance from the Iberian coast. They found that within

a distance of 600 km, the mean radii of Mediterranean water eddies monotonically increase, and that this is principally due to merger. Indeed, Meddies are abundant in that distance range and the probability of merger events is high. The case of Meddy 169 is in agreement with this result, also because no evidence of merger was found after April 2020, making the Meddy an isolated feature (see also figure 5.10).

Once the series of merger events finished, the Meddy swirl velocity stopped growing and maintained a fairly constant value. The radius and thickness, after a "plateau-phase", only slightly increased and decreased, respectively. Such behavior is consistent with the results of Colin de Verdière (1992), who showed that the southward motion of Meddies can be due to their vertical shrinking and horizontal relaxation. Indeed, Meddy 169, while approaching the western boundary of the region of study, started exhibiting a southward displacement, switching from a latitude of 38.5°N to 37.3°N during the last 5 months of evolution (i.e. with a net southward velocity of around 0.65 cm/s). The SSH anomaly (as well as the horizontal extent of the Meddy signature in the OW fields) shows a decreasing trend of -0.5 cm/month in the last months of evolution. In this context, where the eddy did not interact with topography (the  $\nabla h_B^e$  values are only significant in the early stages of the Meddy evolution) nor with other Meddies, the role of the oceanic upper stratification can become more significant in driving the surface expression. Indeed, as shown by figure 5.9, the SSH anomaly (whose maximum value is observed when the MLD is deepest) starts decreasing when the oceanic mixed layer becomes shallower, indicating the occurrence of a higher stratification. Moreover, as shown by table 5.4, the anticorrelations between SSH and the Brunt-Väisälä frequencies (or MLD) are significantly higher than for Meddy 33, being both around -0.5.

The  $i$ -Ta and  $i$ -Sa show an overall increasing trend throughout the Meddy 169 lifetime, though they both reach a plateau when merger events stop feeding the initial Meddy (around April 2020). We attributed this behavior to the fact that the Meddy 169 (whose structure is not significantly perturbed during its westward displacement), reaching the westernmost areas of the studied region, encountered fresher and cooler waters. This was also confirmed by model-derived salinity and temperature climatologies at typical Meddy depths (not shown). Hence, even though the Meddy itself kept its overall structure almost unchanged, its thermo-haline anomalies (at depth) became larger.

Similarly to the previous case, the overall characteristics of Meddy signatures can be summarized with tables 5.4 and 5.5. As for Meddy 33, the quantity which is best correlated with the evolution of the SSH anomaly is the integrated EPVa (with a value around 0.9). In the case of Meddy 169, the whole set of Meddy parameters (swirl velocities, radius and thickness) shows a significant correlation with the Meddy-induced SSH anomalies, with values exceeding 0.7 (the significance of the correlations is analogous to the one discussed in the case of Meddy 33). This behavior is the expected one for isolated subsurface anticyclones, in idealized contexts [Bashmachnikov and Carton (2012), Ciani et al. (2015)]. Indeed, Ciani et al. (2015) showed that the SSH anomaly induced by isolated subsurface quasi-geostrophic anticyclones is proportional to  $\Xi = i\text{-EPVa} \cdot D^{-2}$  (see also table 5.1 for a description of the variables). A further proof that Meddy 169 can be seen as an isolated feature is illustrated in figure 5.11. The scatter plot of the normalized time series of SSH anomaly (SSH anom\*) and the quantity  $\Xi^*$  is shown for both Meddy 33 and Meddy 169. The results of the scatter plot show that the proportionality between SSH anomalies and  $\Xi$  is best verified for Meddy 169, as also indicated by the linear fit of the data (SSH anom\* = 1.12 $\Xi^*$  - 0.32). The existence of a negative intercept for the linear plot, though physically unacceptable, may be due to two facts: first, the theory dealt with uniformly stratified oceans, hence, did not account for geographical and/or seasonal variations of the Brunt-Väisälä frequency (which had an impact on the evolution of Meddy 169); moreover, the possibility of a threshold effect must be taken into account, indicating that a minimum  $i\text{-EPVa}$  content is required for a Meddy to have an observable surface signature (especially in presence of surface-turbulence).

The possibility of a quadratic relation between  $\Xi^*$  and SSH anom\* is also excluded. Indeed, changing the linear fit for a quadratic fit does not improve the  $R^2$ ; therefore a linear relation between SSH anom\* and  $\Xi^*$  is reasonable, and is supported by the regional model results. On the other hand, for Meddy 33 no linear relation can be established. Instead, the scatter plot evidenced the coexistence of two classes of values, schematically indicated as  $\Omega_1$  and  $\Omega_2$  in figure 5.11. The  $\Omega_1$  group of values is related to the earlier stages of the Meddy 33 evolution, i.e., before it crossed the Azores front and experienced the bottom collision with a seamount.

As previously stated, the high correlation between SSH anomaly and  $i\text{-Ta}$  and  $i\text{-Sa}$  for Meddy 169 is due to the combination of merger and the displacement of

the Meddy towards fresher and cooler areas. The evolution of the Meddy surface thermohaline expressions is not correlated with the Meddy intrinsic/background oceanic properties (the  $R_P$  coefficients never exceed 0.4 in both cases). The physical reasons for these low correlations are those indicated for the study of Meddy 33.

The maximum SSH anomaly induced by Meddy 169 is comparable with the one of Meddy 33. Indeed, the two eddies have comparable mean structures and their maximum surface expressions in SSH took place under similar background oceanic conditions (lower oceanic stratification above the eddy). Occurrences of positive and negative thermohaline anomalies at the surface are possible throughout the Meddy lifetime, hence, differently from SSH anomaly, they cannot uniquely be associated to the Meddy properties at depth [Oliveira et al. (2000), Bashmachnikov et al. (2013)].

**Table 5.4:** *Pearson's correlation coefficients ( $R_P$ ) between the Meddy 169 (M169) surface-signatures and the along-trajectory Meddy/background ocean characteristics. The largest values are highlighted in red.*

<b>M169-<math>R_P</math></b>	<b>SV</b>	<b>R</b>	<b>Th</b>	<b>MLD</b>	<b>N</b>	<b>U clim</b>	$\nabla h_B^e$	<b>i-EPVa</b>	<b>i-Ta</b>	<b>i-Sa</b>
$SSH_{anom}$	0.78	0.82	0.72	-0.47	-0.52	0.23	-0.27	0.91	0.6	0.6
<b>M169-<math>R_P</math></b>	<b>SV</b>	<b>R</b>	<b>Th</b>	<b>MLD</b>	<b>N</b>	<b>U clim</b>	$\nabla h_B^e$	<b>i-EPVa</b>	<b>i-Ta</b>	<b>i-Sa</b>
$SST_{anom}$	-0.09	0.12	0.04	0.30	0.34	-0.40	-0.04	-0.02	0.22	0.23
<b>M169-<math>R_P</math></b>	<b>SV</b>	<b>R</b>	<b>Th</b>	<b>MLD</b>	<b>N</b>	<b>U clim</b>	$\nabla h_B^e$	<b>i-EPVa</b>	<b>i-Ta</b>	<b>i-Sa</b>
$SSS_{anom}$	-0.31	-0.30	-0.35	0.15	0.20	-0.27	0.23	-0.28	-0.42	-0.39

**Table 5.5:** *Mean properties of Meddy 169 surface signatures.*

<b>MEDDY 169</b>	$SSH_{anom}$	$SST_{anom}$	$SSS_{anom}$
Max	6.1 cm	0.29°C	0.13 PSU
Min	0.01 cm	-0.21°C	-0.06 PSU
% $\geq 0$	100	57	79
% $< 0$	0	43	21

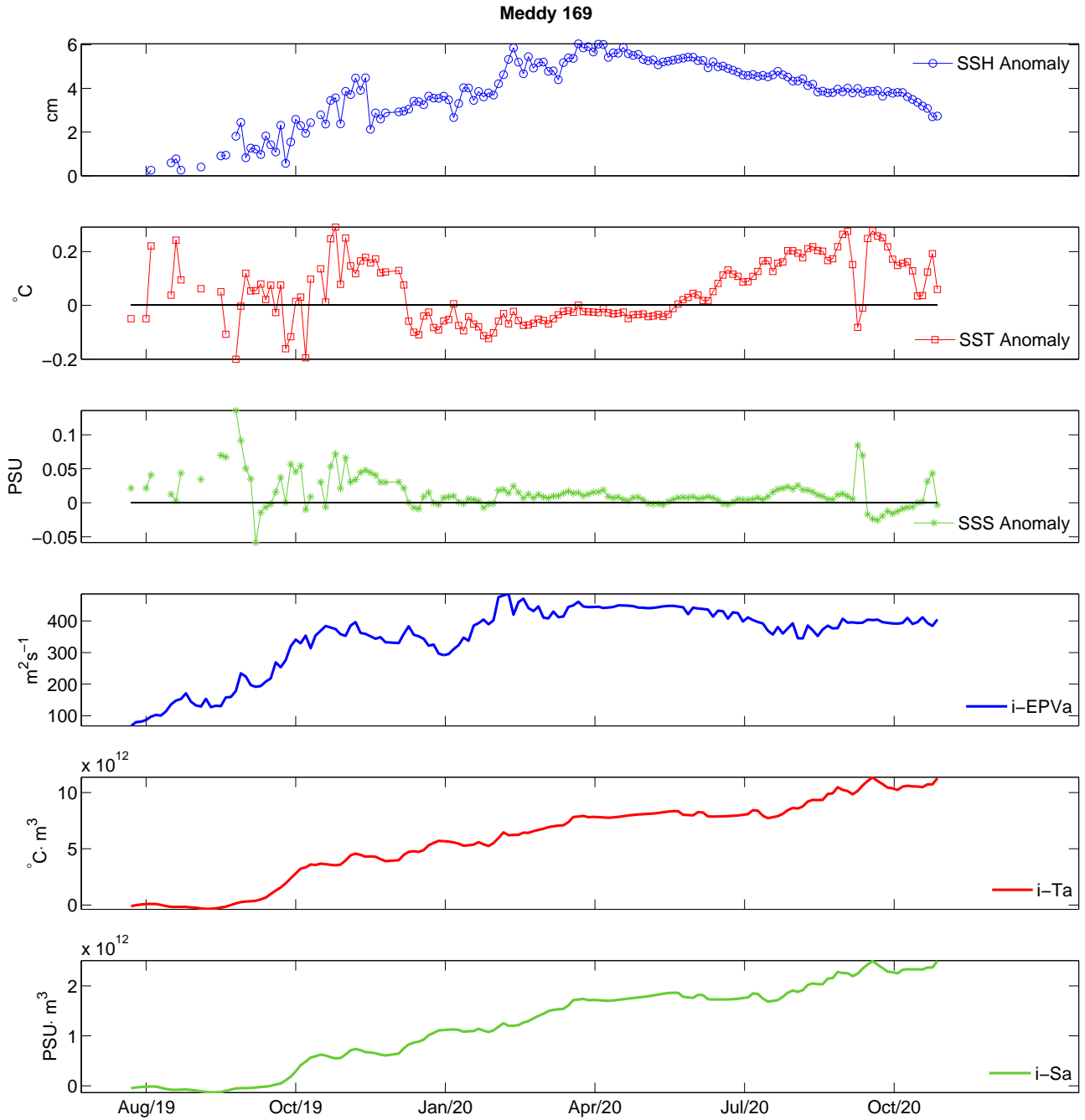


**Figure 5.8:** Surface signature and volume-integrated eddy parameters along the trajectory of Meddy 169 (see also Figure 5.3). SSH anomaly (blue circles), SST anomaly (red squares), SSS anomaly (green stars), *i-EPVa* (integrated Ertel potential vorticity anomaly, blue), *i-Ta* (integrated temperature anomaly, red), *i-Sa* (integrated salinity anomaly, green).

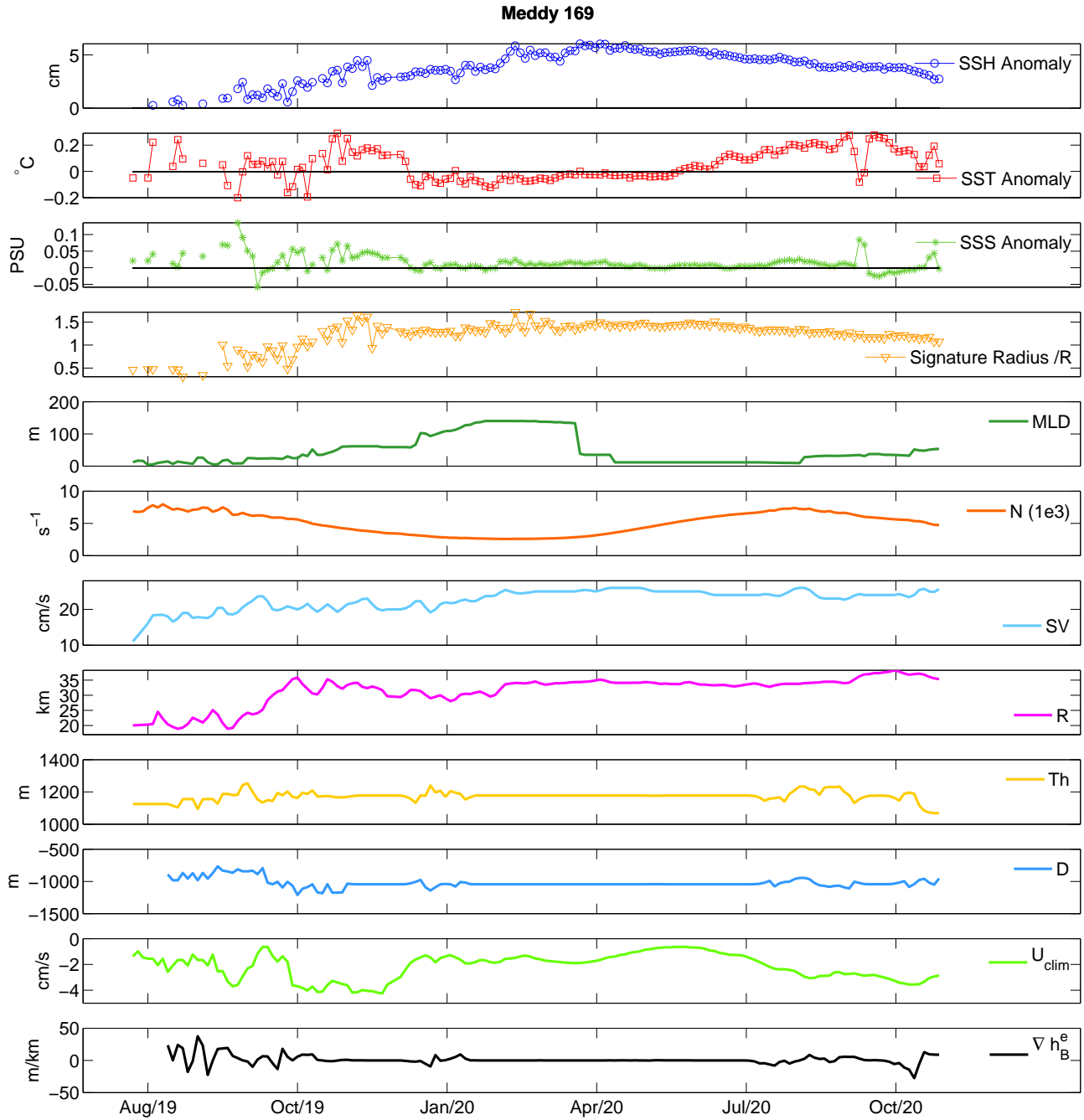


**Figure 5.9:** Surface signatures and Meddy/background properties along the trajectory of Meddy 169 (see also Figure 5.3). SSH anomaly (blue circles), SST anomaly (red squares), SSS anomaly (dark red stars) Signature Horizontal Extent (dark yellow triangles), Mixed Layer Depth (green), Brunt-Vaisala frequency (orange), Meddy Swirl Velocity (cyan), Meddy Radius (magenta), Meddy thickness (yellow), Meddy Depth (light blue), Intensity of climatological zonal surface currents (light green) and gradient of oceanic bottom topography (black).

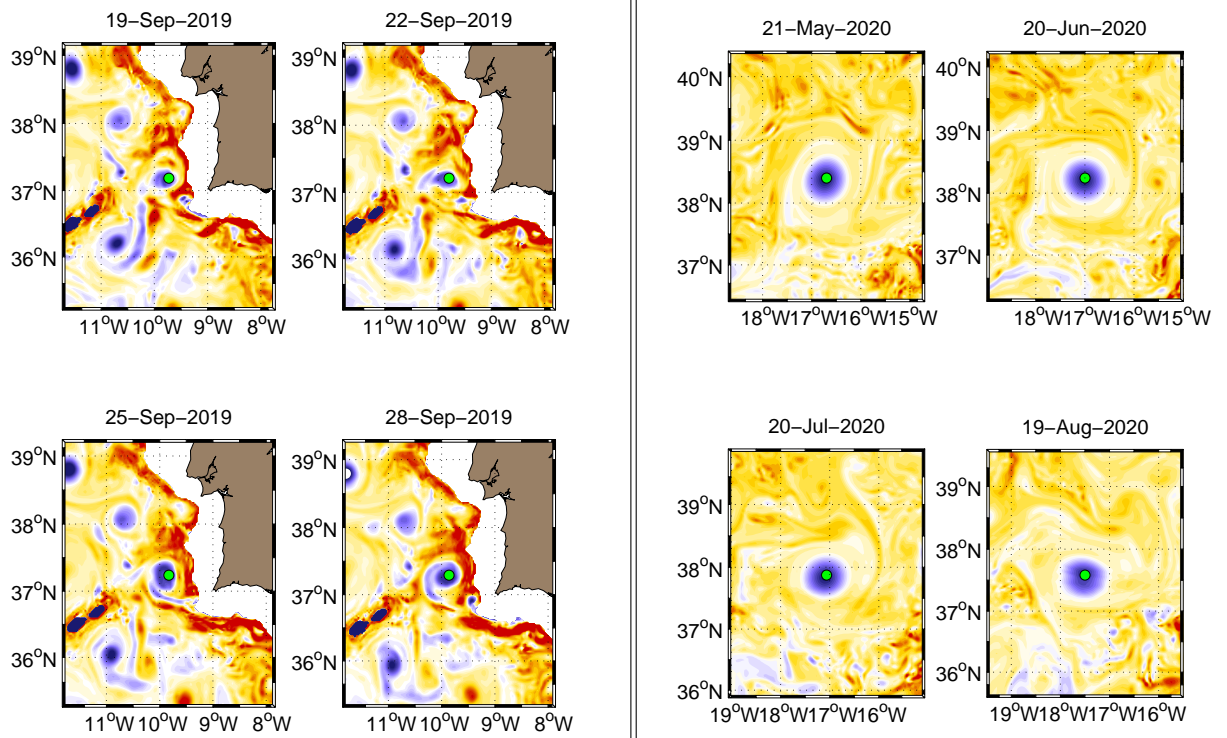


**Figure 5.10:** *Left: merger of Meddy 169 with nearby anticyclonic features off Cape São Vicente. Right: instantaneous positions of Meddy 169 in May, June, July and August 2020 indicating the absence of merger events. Here the eddy can be considered as an isolated feature. In both panels, Meddy 169 is observed via horizontal sections of EPVa at the Meddy instantaneous depth ( $z \simeq -1000$  m). The green dot indicates the instantaneous position of the Meddy center (ETS output).*

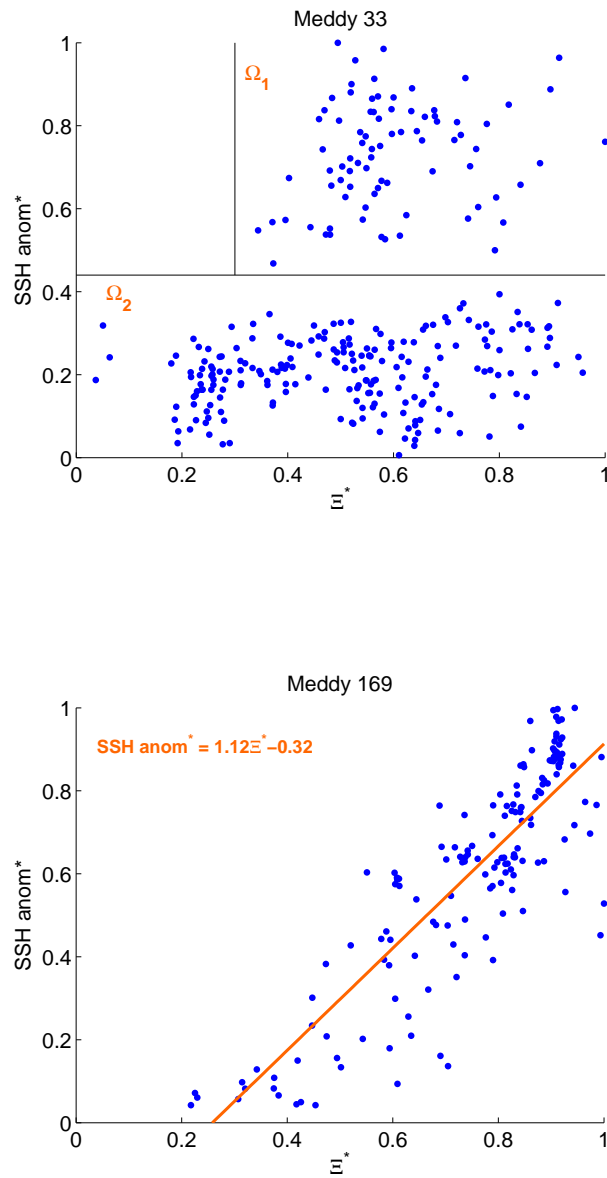


**Figure 5.11:** Scatter plot for the time series of SSH anomaly vs  $\Xi = i-EPVa \cdot D^{-2}$  (see table 5.1 for a description of the variables). The superscript "\*" indicates that normalized quantities have been used. Top panel: Meddy 33, Bottom panel: Meddy 169.

### **The case of a south-southwestward Meddy: Meddy 120**

We conclude the comparative study of the longest-lived Meddies in the model by analyzing the case of Meddy 120. Similarly to Meddy 169, it originated near Cape São Vicente, its initial coordinates being  $37^{\circ}\text{N}$  and  $9^{\circ}\text{W}$ . This eddy, whose lifetime is around 1.7 years, is characterized by a mostly south-southwestward drift (see e.g. figure 5.3). A looping trajectory is observed between November 2013 and October 2014. Visual inspection of the Meddy evolution at 1000 m depth, evidenced the two main causes of this behavior, namely, a series of Meddy/eddy and Meddy/-topography interactions. In particular, Meddy 120 coupled with several cyclonic features that, during each interaction, drastically modified its original trajectory. Indeed, between November 2013 and October 2014, Meddy 120 occupied a region where subsurface cyclones are abundant [Serra et al. (2010)]. Some of these subsurface cyclones were generated by stirring of positive EPVa from the Moroccan continental shelf (east of Meddy 120) and nearby seamounts (west of Meddy 120), caused by the action of other Meddies (see e.g. the Meddy located at  $34.5^{\circ}\text{N} - 9^{\circ}\text{W}$  on 21-Dec-2013 shown in figure 5.12). As a result, Meddy 120 underwent a series of couplings with subsurface cyclones, that, via dipolar and tripolar effects, spatially bounded the Meddy forcing him to loop (figure 5.12 shows a case of dipolar drift). Another point that makes Meddy 120 a particular case study is that it spent 70% of its lifetime in a highly turbulent region, where eddy activity is also very intense at the sea-surface. Indeed, the Meddy initially drifted and looped close to the area where the imprint of the Azores front is more intense (see e.g. figure 5.2 and 5.14), hence, where surface-intensified cyclones and anticyclones are abundantly ejected by meandering of the Azores front [Barbosa Aguiar et al. (2011)]. This had consequences on the surface expression of the Meddy, which exhibited an oscillatory signal seldom correlated with the behavior of the i-EPVa, if compared to Meddy 33 and 169 (see e.g. figure 5.13 and 5.14). Indeed, despite the initial evolution of the i-EPVa and the visual inspection of EPVa maps at the depth of Meddy 120 indicate the occurrence of merger (not shown), the SSH anomaly was soon affected by the repeated interaction with surface cyclones and anticyclones.

It is also worth noticing that, in this case, the Meddy surface expression is very intermittent, if compared to the the previous cases. Indeed, the Meddy surface signature detection algorithm, described in section 5.2, automatically discards all

cases in which the surface OW fields do not comply with the structure shown in figure 5.1 (i.e. an OW minimum within 1 Meddy radius distance from the surface projection of the Meddy center). In other words, the highly intermittent surface-signature is a further (although indirect) proof of the turbulent surface activity above Meddy 120. When the Meddy stopped looping and eventually drifted south of the turbulent region (in October 2014), its surface-signature clearly reappeared at the sea-surface. The corresponding SSH anomaly (from October 2014 onward) exhibited values never exceeding 2 cm until the end of the Meddy lifetime, i.e., when it reached the model sponge layer. Such low values are explained by the degradation of Meddy 120, evidenced by the decreasing trend in the *i*-Sa, *i*-Ta and *i*-EPVa, as well as by the decreasing swirl velocity. Also, in the last months of the Meddy lifetime, its almost straightforward-southward trajectory is also evidenced by its increasing radius and decreasing thickness, as proved by Colin de Verdière (1992).

Regarding the Meddy-induced surface salinity and temperature anomalies, their evolution is completely analogous to the case of Meddies 33 and 169. Furthermore, differently from the previous cases, we do not show the table containing the Pearson's correlation coefficients between the Meddy surface expression and the Meddy/background oceanic parameters. Indeed, as one could expect from observation of figures 5.13 and 5.14, none of the coefficients exceeds 0.4, indicating that correlations are not strong. Once again, we attribute this to the highly turbulent region (both at depth and in proximity of the sea-surface) in which Meddy 120 spent most of its lifetime.

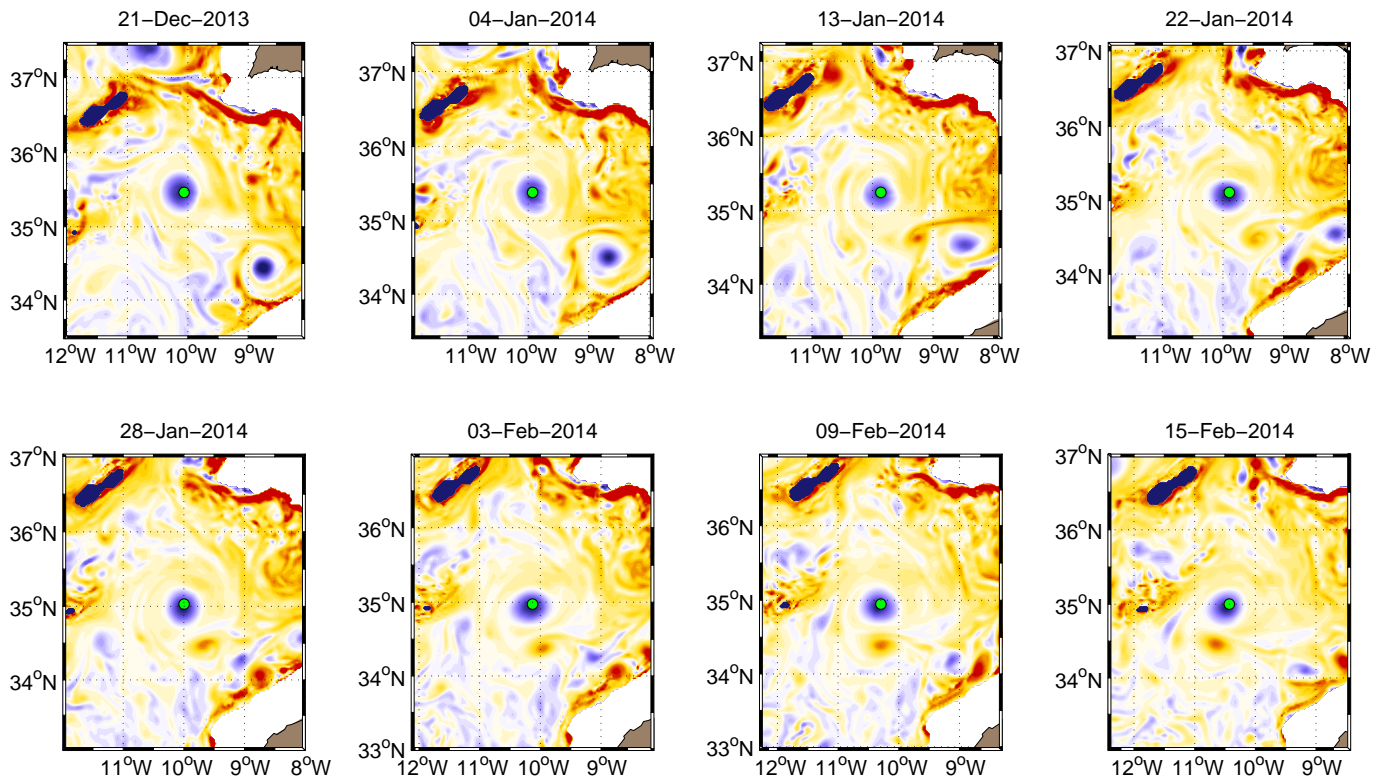


**Figure 5.12:** *Coupling of Meddy 120 with a subsurface cyclone. The cyclone is generated by stirring of positive EPVa along the Moroccan continental slope due to another Meddy (see e.g the Meddy located at 34.5°N-9°W on 21-Dec-2013). The Meddy evolution is studied via horizontal sections of EPVa at the Meddy depth ( $z \approx 1000$  m). The instantaneous position of Meddy 120 is given by the green dot (ETS output).*

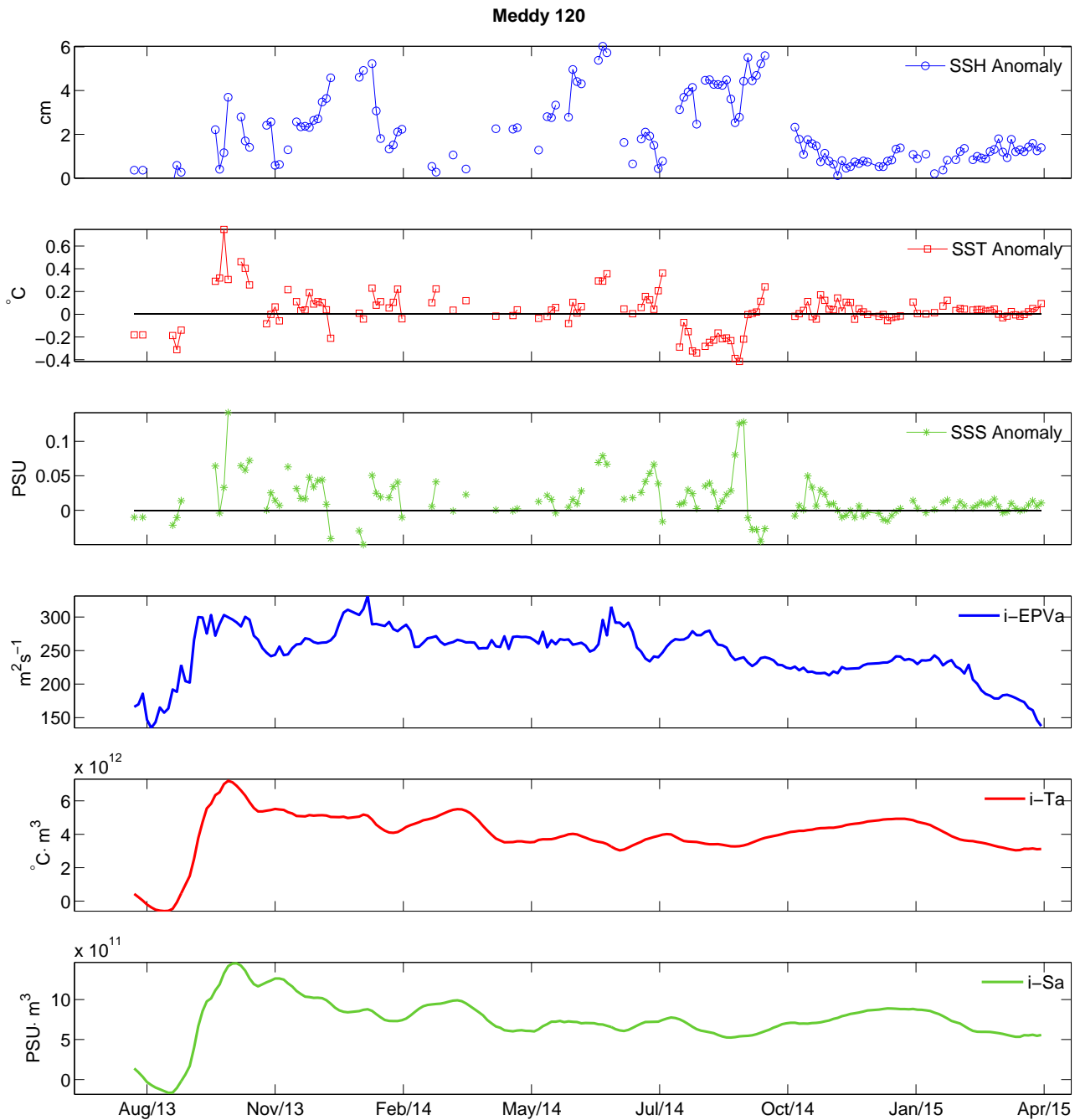


**Figure 5.13:** Surface signature and volume-integrated eddy parameters along the trajectory of Meddy 120 (see also Figure 5.3). SSH anomaly (blue circles), SST anomaly (red squares), SSS anomaly (green stars), *i-EPVa* (integrated potential vorticity anomaly, blue), *i-Ta* (integrated temperature anomaly, red), *i-Sa* (integrated salinity anomaly, green).

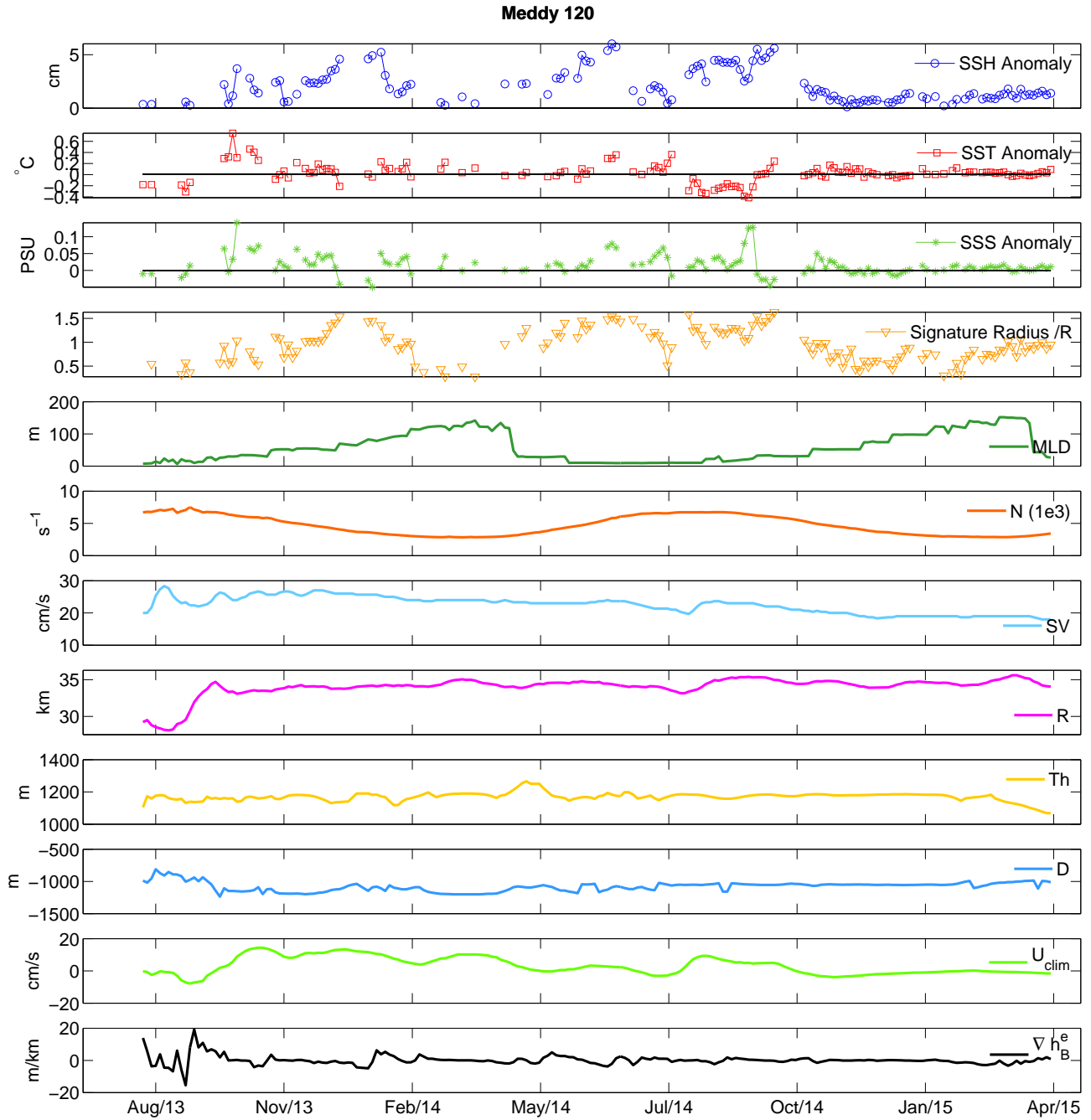


**Figure 5.14:** Surface signatures and Meddy/background properties along the trajectory of Meddy 120 (see also Figure 5.3). SSH anomaly (blue circles), SST anomaly (red squares), SSS anomaly (dark red stars) Signature Horizontal Extent (dark yellow triangles), Mixed Layer Depth (green), Brunt-Vaisala frequency (orange), Meddy Swirl Velocity (cyan), Meddy Radius (magenta), Meddy thickness (yellow), Meddy Depth (light blue), Intensity of climatological zonal surface currents (light green) and gradient of oceanic bottom topography (black).

## 5.4 SSH response to i-EPVa changes

In section 5.3.1, we showed the leading role of EPV in driving the surface expressions of two long-lived Meddies in SSH fields. The linear relation between a Meddy's core i-EPVa and its SSH anomaly is best verified when the Meddy evolves far from surface or bottom oceanic features, e.g., surface-intensified eddies, fronts and seamounts. Nevertheless, these two quantities can be significantly correlated (with coefficients exceeding 0.7) even when the Meddy structure is perturbed by external factors. Taking advantage of this information, one might wonder how long it takes for a Meddy to communicate with the sea-surface. In other words, given a change of the Meddy i-EPVa, we determine the time lag after which this change will impact the Meddy surface signature. In order to show this, we computed lagged cross correlations between the Meddy i-EPVa and SSH anom for the set of Meddies shown in figure 5.3 (except for Meddy 120).

**Table 5.6:** *Lags of maximum cross-correlation between the i-EPVa and SSH anom for the longest-lived Meddies in the model. Colors refer to figure 5.3.*

MEDDY <b>33</b>	Lag of Max Correlation ( $\Delta t$ )
MEDDY <b>68</b>	0
MEDDY <b>135</b>	0
MEDDY <b>139</b>	1
MEDDY <b>143</b>	0
MEDDY <b>169</b>	0
MEDDY <b>186</b>	0

The results of this analysis are shown in table 5.6. All Meddies show the highest correlations within a time lag going from 0 to 1  $\Delta t$ ,  $\Delta t$  being the time interval between two model outputs. Recalling that, in the model, the outputs are available every 3 days (see also section 5.2.1), we conclude that, given a change in the Meddy i-EPVa, the corresponding surface signature is affected within a maximum delay going from 3 to 6 days (at least for the longest-lived Meddies in the model).

## 5.5 Statistics of SSH anomalies over modelled meddies

In section 5.3.1 (analyzing the life cycle of Meddy 33, 68 and 120) we showed that, among the Meddy-induced sea-surface signatures, the SSH anomalies are the ones exhibiting the most significant correlations with the Meddy and the background oceanic parameters (unless Meddies spend most of their lifetime in highly turbulent regions). These results motivated us to investigate a larger set of Meddies, i.e., all the Meddies of Group 1 and 2 (see also section 4.3 for further details). In this case, since we dealt with a large number of Meddies (total number = 86), we provide an overall description of the SSH anomaly evolution. In particular, we will determine which are the most significant Pearson's correlation coefficients between the Meddy surface signature (in SSH fields) and the Meddy/background oceanic parameters. For this purpose, the Meddies were divided in two main groups, according to the nature of their trajectories. The two groups are schematically represented in figure 5.15, where blue and red trajectories refer to "westward moving Meddies" and "southwestward moving Meddies". These groups respectively indicate Meddies whose trajectories entirely lie north of the climatological imprint of the Azores front (27 Meddies) and Meddies that could cross it, eventually reaching the southernmost areas of the region of study (59 Meddies).

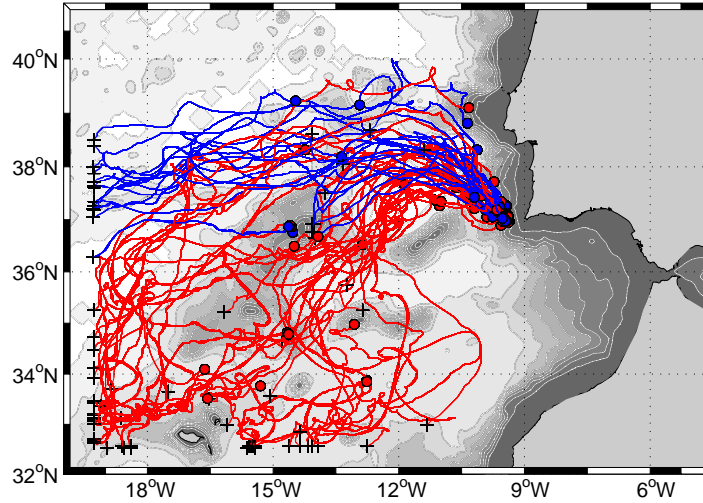


**Figure 5.15:** Trajectories of Meddies belonging to Group 1 and 2 (see also section 4.3 for further details). Blue and red trajectories are for "Westward moving Meddies" and "Southwestward moving Meddies", respectively.

**Table 5.7:** Averaged Pearson's correlation coefficients ( $R_P$ ), for the "westward moving" and the "southwestward moving" Meddies. See also table 5.1

Westward Moving (n=27)		
Meddy Parameter	SV	i-EPVa
$R_P$ (SSH anomaly)	0.45	0.50
Southwestward Moving (n=59)		
Meddy Parameter	SV	i-EPVa
$R_P$ (SSH anomaly)	0.42	0.45

A first look at table 5.7 indicates that the averaged Pearson's correlation coefficients are lower, if compared to what shown for Meddies 33 and 169. Indeed, in this case, a thorough check of the Meddy evolution and of the corresponding background oceanic conditions (including the sea-surface) was not possible. Hence,

any possible deviation from what we expect from theory, or from the analysis we showed in the previous sections, is inevitable. Nevertheless, table 5.7 indicates that the dominating factors in driving the surface expression of Meddies in SSH fields are essentially the Meddy integrated potential vorticity and its rotation rate (notice that this latest variable is actually contained in the Meddy potential vorticity via the relative vorticity, [Vallis (2006)]). All the other correlations are not shown as they never exceed the value of  $\pm 0.2$  (except for the Meddy radius for the westward-moving Meddies, where  $R_P=0.33$ ). Surprisingly, this result does not change if one makes a distinction between the "westward moving" and the "southwestward moving" Meddies. Indeed one expects that, in the second case, significant anticorrelations between the Meddy surface signature and bottom oceanic topography or surface currents could arise. Nevertheless, in section 5.3.1, we proved that these features can only locally generate strong changes in the intensity of the Meddy surface signature. Hence, excluding specific cases, like the one of Meddy 120, we can state that, once again, the Meddy i-EPVa proves to be the key factor in determining the surface expression of Meddies in terms of SSH anomaly all along the Meddy trajectory. Moreover, considering the size of our dataset (constituted by around 90 Meddies), we assume our sample to be statistically significant and that no other simulations are needed to confirm these results.

## 5.6 Discussion and Conclusions

In this chapter, we have investigated the surface expression of Mediterranean Water eddies (Meddies) in a realistic numerical model simulation (using the Regional Oceanic Modeling System, ROMS [Shchepetkin and McWilliams (2005)]). For this purpose, we took advantage of a model initially built to determine a census of Meddies' characteristics (mainly generation sites, radii, vertical extents, propagation patterns and rotation rates) via a numerical approach. These results are thoroughly described in Barbosa Aguiar et al. (2013) and showed a very good agreement with previous studies based on hydrological surveys [Bower et al. (1997), Richardson et al. (2000a)]. Our aim was to evaluate the possibility of tracking Meddies, generally found at depths around 1000 m, from observations of the sea-surface. The work consisted in studying the surface signature of a large

number of Meddies (around 90) in the model. The novelty, as well as the main advantage of this approach was the simultaneous availability of the informations on the three-dimensional Meddy structure, the oceanic background conditions and of the sea-surface (in terms of sea-surface height, temperature and salinity).

Firstly, we studied the evolution of the longest-lived Meddies in the model, selecting three Meddies exhibiting different types of trajectories: purely westward, southwestward and southward. All of these Meddies had mean radii, swirl velocities and depths around 30 km, 20 cm/s and 1000 m, respectively.

In the first two cases, the integrated potential vorticity anomaly (i-EPVa) proved to be the main factor in driving the Meddy surface signature in terms of SSH anomaly (with Pearson's correlation coefficients between i-EPVa and SSH anomalies up to 0.9). The Meddies always exhibited positive SSH anomalies and the maximum values were around 7 cm; the corresponding maximum horizontal extent of the surface-signature was around 1.5 Meddy radii and this is in the range of values predicted in Bashmachnikov et al. (2014). The estimated time delay between a change in the Meddy i-EPVa structure and a change between its surface signature never exceeded 6 days. Recently, Bashmachnikov and Carton (2012) reviewed the characteristics of several real oceanic Meddies detected via *in-situ* observations (see their table 1). They showed that Meddies with structures comparable to our Meddy 33 and 169 can generate sea-level anomalies whose intensities range from 5 to 13 cm, indicating a very good agreement with our results.

On the other hand, as also stated by Oliveira et al. (2000), the Meddy thermohaline surface signatures assumed positive and negative values all along the Meddy trajectory and never showed correlations with the Meddy integrated salt and heat content. Such behavior confirmed that the oceanic surface conditions dominate on any existent Meddy-induced thermohaline surface expression.

In the third case, the Meddy (Meddy 120) spent most of its lifetime in a highly turbulent region, i.e., where surface and subsurface eddies are abundant. At the sea-surface, such eddies are mostly generated by the instability of the Azores Front, while the Mediterranean outflow and the stirring of vorticity in meddy/topography interactions mostly produce vortical structures at typical Meddy depths. The combined effect of these surface and subsurface-intensified eddies gave Meddy 120 a very unusual looping trajectory; this happened in proximity of the most intense climatological imprint of the Azores front. Hence, its surface signature exhibited

a very noisy behavior and often was not detectable in the surface OW fields.

Excluding cases like the one of Meddy 120, the link between the Meddy i-EPVa and its surface expression in SSH fields is also verified for all the Meddies that lived more than one year in the model.

Significative changes in the evolution of Meddies' surface signature in SSH fields are mainly caused by the following factors (mostly given to changes in the Meddy i-EPVa structure):

- vertical alignment of the Meddy with surface anticyclones and interaction with cyclonic features, respectively resulting in an increase and a decrease of the intensity in the SSH anomaly;
- merger of a Meddy with surrounding Meddies, mostly in the first 600 km from the Iberian coast (see also Bashmachnikov et al. (2015)), causing an increase in the SSH intensity;
- lateral/bottom collision of a Meddy with seamounts, both causing a degradation of the Meddy SSH anomaly;

In particular, the role of merger proved to be crucial for the detectability of Meddies in SSH fields. Newly formed Meddies, though younger and less eroded by interaction with bottom topography or by lateral and vertical diffusion [Armi et al. (1989), Shapiro et al. (1995)] are often too small in size and their potential vorticity content is too poor for their surface signature to exceed the threshold of 1 cm. Merger feeds the original Meddy structure with potential vorticity and progressively allows the Meddy to develop in size, also enhancing its surface signature. Indeed, the highest increases in Meddy-induced SSH anomalies were always registered after a series of coalescence events; the increase was around 600% for the case of Meddy 169.

This work also indicates that a synergy between SSH, SST and SSS fields, that proved to be useful to study surface and near-surface-intensified motions (see e.g. Lapeyre and Klein (2006), Isern-Fontanet et al. (2008b), González-Haro and Isern-Fontanet (2014)), is not helpful to track Meddies along their whole trajectories. Instead, the SSH anomalies proved to be the most reliable feature to follow these subsurface anticyclones from observations of the sea-surface. Lapeyre and Klein (2006) and Isern-Fontanet et al. (2008b) pointed out that, given the

horizontal distribution of the meridional large scale oceanic potential vorticity, the oceanic subsurface dynamics can be reconstructed from sea-surface density (SSD hereinafter) and temperature, respectively. Indeed, in the framework of the surface quasi-geostrophic theory, the SSD can be seen as a source of potential vorticity for the ocean interior. In that context, it was shown that the reconstruction was only possible in the first 500 m of the water column. Hence, it is not surprising to ascertain that, in our study, surface patterns of temperature (and salinity) are not correlated with the Meddy motions, i.e., at depths that can even exceed 1000 m. More recently, Ponte and Klein (2013), via a numerical approach, tried to infer the oceanic subsurface dynamics from high resolution SSH. This approach, relying on SSH fields only, makes the reconstruction possible even when SSD anomalies are weak, confirming that a relation between SSH and internal potential vorticity anomalies can be established. In our study, despite the depth of the Meddies (1000 m), the SSH anomalies were constantly detectable and were supported by the Meddy potential vorticity structure at depth (i-EPVa). Even when abrupt changes in the Meddy structure took place, the Meddy-induced SSH anomalies could still exhibit intensities not far from 2 cm.

Hence, this study confirms that the role of the incoming SWOT satellite mission will be a leading one for inferring subsurface dynamics from oceanic surface informations. Indeed, combining the knowledge of the mean Meddies pathways and generation sites, hydrological data (e.g. ARGO floats) to identify an initial position for the Meddy, an automatic tracking is possible via satellite altimetry. A natural follow-up of this study could rely on primitive equations models with a high frequency atmospheric forcing, as a monthly climatology was used in our case. Indeed, a climatological forcing can give smoother evolutions of SST and SSS fields, if compared to remotely sensed data. With a higher-frequency forcing, a comparison with observations, e.g., a match-up between satellite-derived SST/SSS and Meddies positions identified via ARGO profiles, would acquire more significance.

## 5.7 Further Studies: Meddies' aspect ratio in the numerical simulation

In this appendix, we describe further details about the Meddies' metrics in the numerical model. We will focus on the Meddies' aspect ratio, expressing the ratio between the Meddy horizontal and vertical extent. We will compare our estimation to the theoretical law derived by Aubert et al. (2012), expressed by the following equation,

$$\alpha = \left( \frac{Ro(1 + Ro)}{N_c^2 - \bar{N}^2} \right)^{1/2} \quad (5.3)$$

For an eddy living in a rotating stratified environment, the terms of this equation are the following:

- $\alpha = H/L$ : the eddy aspect ratio, with  $H$  and  $L$  the eddy half-width and radius, respectively;
- $Ro = \omega_c/2f$ : the eddy Rossby number, with  $\omega_c$  the relative vorticity at the eddy center and  $f$  the Coriolis' parameter;
- $N_c$ : the Brunt-Väisälä frequency at the eddy center;
- $\bar{N}$  the Brunt-Väisälä frequency of the oceanic background, supposed at rest.

Aubert et al. (2012) showed that their law could successfully predict the aspect ratios of laboratory vortices (whose evolution was studied in rotating tanks) Jovian Vortices and Meddies. We recall that for Meddies, in general,  $\alpha$  is  $\mathcal{O}(10^{-2})$ .

In our work, the Meddies' horizontal and vertical extents were respectively derived from dynamical and salinity-based criteria, as described in detail in section 5.2.3; making the computation of the Meddies' aspect ratio a straightforward task. Nevertheless, given the use of a realistic model, we could rely on the knowledge of the three-dimensional Meddy structure and of the background ocean, which encouraged us to compare our results with the prescriptions of equation 5.3. In particular, we defined:

- $\alpha = H/L$ : the ratio between the Meddy half-width (i.e. the distance between the Meddy upper boundary and the Meddy core) and its radius;

- $\omega_c$ : the value of the maximum relative vorticity observed within the Meddy vertical boundaries (along a vertical profile across the Meddy center). This value was used to define the Meddy Rossby number;
- $N_c$ : the Brunt-Väisälä frequency inside the Meddy, at the same position of  $\omega_c$ ;
- $\bar{N}$ : the Brunt-Väisälä frequency outside the Meddy. This value was computed as the mean of four values of  $N(x, y, z)$  at the depth of the Meddy core and 2 radii away from the Meddy center (along a meridional and a zonal radial across the Meddy center).

These quantities allowed us to evaluate equation 5.3 throughout the Meddy's lifetime. We performed this computation for the eight longest-lived Meddies in the simulation, whose trajectories are shown in figure 5.3. On average, the ratio between  $H/L$  and  $\alpha$  is very close to unity for all the analyzed Meddies, indicating that our estimation of the eddy half-width and horizontal extent (based on salinity and dynamical criteria) are compatible with an independent estimation of the Meddy aspect ratio (see e.g. figure 5.16). Despite this, figure 5.16 also indicates that there are cases, like the one of Meddy 68, 120 and 169, in which the match between the two methods is particularly good throughout most of the Meddies' lifetime. Indeed, these Meddies traveled far away from the most prominent topographic features in the region of study, as shown by figure 5.3. On the contrary, when the Meddies lower boundaries ( $M_{bot}$ ) hit the oceanic bottom ( $h_B$ ), i.e., when  $M_{bot}-h_B < 0$  (like during the very early lifecycles of Meddy 143, 169 and 186) the  $(H/L)/\alpha$  ratio diverged from unity. In those cases, the main sources of error was mainly due to abrupt changes in the Meddy Brunt-Väisälä frequency  $N_c$ , affecting the determination of  $\alpha$  via equation 5.3.

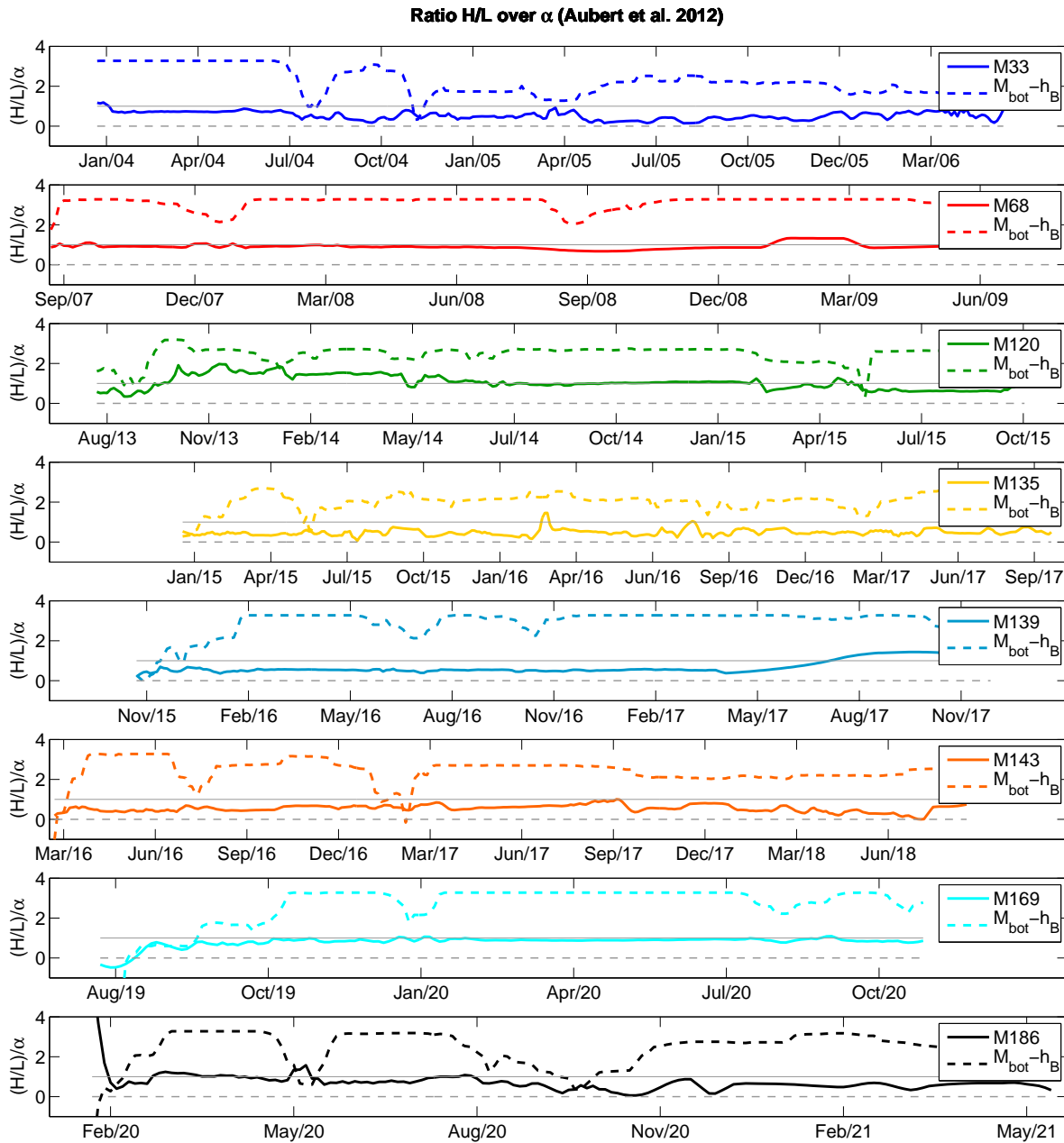


**Figure 5.16:** Continuous lines: Meddy aspect ratio ( $H/L$ ) over the theoretical estimation of Aubert et al. (2012) ( $\alpha$ ). Dashed lines: difference between the Meddy bottom boundary ( $M_{bot}$ ) and the bottom oceanic topography ( $h_B$ ). The lines colors are coherent with the ones of figure 5.3. The continuous and dashed thin grey lines respectively indicate the 1 and 0 values.

# Chapter 6

## Conclusions and Perspectives

In this final chapter, we will draw the main conclusions of the studies we have presented throughout the manuscript. Moreover, we will go through the main unanswered questions, which constitute the source for future investigations based on our work.

Firstly, we pointed out that the study of the subsurface ocean is crucial for the understanding of the average oceanic behavior at global scale. Indeed, there is a class of oceanic motions, among which we have subsurface currents and subsurface-intensified eddies, that are able to modify significantly the three-dimensional distribution of tracers, like e.g. heat, salt and nutrients at global scale. This context clarifies the need for determining the mean positions and pathways of the major subsurface oceanic motions. In the specific case of our work, we focused on structures that are able to propagate several thousands of miles in the ocean: the class of subsurface-intensified eddies.

We reviewed the present-day techniques for the investigation of the oceanic subsurface motions, considering the advantages and limitations of two main approaches: *in-situ* observations and the satellite-derived three-dimensional reconstructions of the subsurface dynamics. The first represent the most straightforward way to study the subsurface ocean, as they can describe in detail the oceanic motion up to submesoscale resolutions. Nevertheless, they only provide pointwise informations, which is not satisfying in the perspective of a global-scale study. Recently, it was proved that the combined use of theoretical arguments (like the SQG theory, [Lapeyre and Klein (2006)]) and satellite observations (mainly SST and SSH) al-

lows the reconstruction of the ocean three-dimensional dynamics from observations of the sea-surface [Isern-Fontanet et al. (2008a), Ponte and Klein (2013), Ponte et al. (2013a)]. This could actually make up for the lack of synopticity of *in-situ* observations, but the results of such a method mostly proved to be satisfactory in the first 500 m of the water column, while several subsurface-intensified eddies can be found at depths exceeding 1000 m. For all these reasons, we decided to study how subsurface vortices, with *a-priori* known structure, can influence the sea-surface. Our goal was to determine how, and under which conditions, subsurface eddies are able to generate a signature at the sea-surface that can be used to track their displacement at depth.

## 6.1 Main results

### 6.1.1 Surface signatures of subsurface anticyclones in idealized oceanic basins

We started investigating the surface expression of subsurface anticyclones (mainly in SSH) via analytical models in the context of the quasi-geostrophic (QG) theory and numerical simulations based on QG and primitive equations (PE) models. In these initial studies, we chose the idealized approximation of a surrounding ocean at rest. This choice allowed us to better characterize the eddies' surface signature as a function of their in-depth characteristics, avoiding any destructive interaction with nearby surface eddies or fronts.

The main reason for focusing only on SSH fields is to evaluate the contribution of a high-resolution and high-precision future satellite mission (like SWOT, [Fu et al. (2009)]) for the study of subsurface ocean dynamics from observations of the sea-surface. Indeed, the SWOT mission will provide global-scale observations of the sea-surface with precisions around 2 cm (this is only achieved for along-track data by present-day satellite altimetry [Fu and Cazenave (2000)]).

The analytical models were developed with the aim of studying the surface signature of subsurface shielded anticyclones (whose potential vorticity anomaly can change in sign horizontally and vertically, see e.g. Morel and McWilliams (1997)) reduced to equivalent point-vortex structures. We found that, for steady vortices, the surface signature is given by positive and monopolar anomalies in SSH fields.

The intensity of such anomalies depends mostly quadratically on the eddy's radius and linearly on its vertical extent and potential vorticity. Moreover, our study indicated that the introduction of a shield around the central eddy's core modifies the dependence of the eddy's signature with respect to the eddy's depth, if compared to the unshielded case. In particular, the intensity of the eddy-induced sea-level anomaly can decrease quadratically or cubically with the eddy's depth, due to the screening effect of the eddy peripheral shields. Hence, this study generalized the results of Bashmachnikov and Carton (2012), who modeled the surface-expression of Meddies (Mediterranean Water eddies) via simple point-vortex structures, yielding a linear decrease of the vortex surface signature as a function of its depth.

The numerical experiments with the ROMS model (PE model), in idealized configuration (and in absence of bottom density fluctuations), confirmed the theoretical predictions (except for the dependence on the vortex radius). Furthermore, they suggested that only subsurface eddies in the mesoscale range have chances to be detected by present-day and future satellite altimetry. Indeed, only mesoscale eddies can generate signatures  $\mathcal{O}(\text{cm})$ , even in very idealized oceanic basins (with flat bottom, in absence of atmospheric forcing and of nearby surface turbulence). In a further study, we also wondered if subsurface anticyclones with no initial signature in SSH (and in absence of bottom density fluctuations) are able to develop one as a result of their displacement, the latest being a consequence of the planetary  $\beta$ -effect or of the interaction with an advection current. In other words, we determined the "dynamical component" of the eddy surface-signature. Qualitative analytical models, based on the conservation of potential vorticity in a layered ocean (still neglecting interactions with the oceanic bottom), allowed to predict that the displacement of a subsurface anticyclone first causes a compression and then a release of the water columns above it (along the direction of its displacement). The consequence of this mechanism is the generation of a dipolar signature in SSH, where the positive pole is vertically aligned with the leading half of the vortex and the negative one with the trailing half. This prediction was confirmed by numerical simulations with a QG model, as well as with the ROMS model. If, in the ROMS model, the vortex drifts only due to planetary  $\beta$ -effect, the analytical prediction is only true in the limit of short times ( $\mathcal{O}(\simeq 1 \text{ month})$ ).

### 6.1.2 Merger of subsurface anticyclones

We focused on a specific aspect of the subsurface eddies' life cycle: the merger with nearby eddies. The motivation for such an investigation comes from several past and recent studies indicating that merger is very frequent among oceanic and atmospheric vortices [Masina and Pinardi (1991), Kieu and Zhang (2008), Barbosa Aguiar et al. (2013), L'Hégaret et al. (2014), Molemaker et al. (2014), Delbende et al. (2015)]. In particular, we treated the case of subsurface anticyclones, with the aim of providing a description for the merger of Peddy and Meddy-like vortices (respectively Persian Water Eddies and Mediterranean Water Eddies) found in the Arabian and Mediterranean Sea. This study allowed us to evaluate the critical conditions for merger to occur as well as the effects of merger on the three-dimensional structure of the subsurface anticyclones. Furthermore, our previous analytical and numerical studies pointed out that the surface signature of subsurface-intensified anticyclones depends on the in-depth vortex characteristics. Hence, merger is among the processes that can drive the impact of subsurface eddies on the ocean surface.

We studied this problem via a numerical and idealized approach, using the PE model ROMS and considering couples of identical subsurface eddies lying at the same depth. The potential vorticity structure of the modeled eddies indicated that, even in these experiments, we were dealing with shielded subsurface anticyclones. We found that, if typical Peddy and Meddy-like vortices are considered, the critical relative distances allowing merger are respectively  $2.6 R$  and  $2.5 R$ , where  $R$  is the vortex radius. The simulations also indicated that the merging process started with a co-rotation phase (during which the initial eddies are deformed elliptically) and eventually yielded a single-core structure after about 20 days of interaction (which is in agreement with observations [Schultz Tokos et al. (1994)]). If the relative distances were increased by about  $0.1 R$ , the vortices, after the initial co-rotation phase, moved away from each other via dipolar interactions (due to the effect of the eddies' peripheral shields). High-resolution simulations on merging Peddy and Meddy-like vortices (M and P-Vortices) indicated that, once the merging process was completed, the merged vortex was characterized by an enhanced potential vorticity content (+ 40% for both M and P-vortices), an enhanced radius (+30% for M-vortices, +20% for P-vortices) and a reduced vertical extent (-20% for M vortices

and -10% for P-vortices), if compared to a single initial eddy. Hence, merger is keen to yield slightly shallower, larger and more energetic vortices. Furthermore, during the merging process, several submesoscale features were generated by the instabilities of the vortex central and peripheral areas (e.g. fragmentation of the peripheral shields and roll-up of filaments ejected by the eddies' cores). This means that merger, at the same time, can yield larger and smaller-scale structures, if compared to the single initial eddy. Hence, we could also conclude that merger is involved in a double energy cascade in the oceans.

### 6.1.3 Surface signature of Mediterranean Water Eddies (Meddies) in a realistic simulation

The last chapter of this thesis can be thought as a validation of the results we showed throughout the manuscript. In this chapter, we described the surface signature of Mediterranean Water Eddies in a realistic long-term simulation ( $\simeq 20$  years) based on the PE model ROMS [Barbosa Aguiar et al. (2013)]. Meddies are subsurface eddies (mostly anticyclones) found in the north-eastern Atlantic at mean depths of 1000 m.

We searched for the surface signatures of Meddies in sea-surface height fields, trying to relate their behavior to the Meddies' structure at depth. Moreover, taking advantage of a realistic simulation, we could go even further. We evaluated whether the synergy between sea-surface height (SSH), temperature (SST) and salinity (SSS) fields can help tracking the displacement of Meddies from observations of the sea-surface. We focused on the evolution of Meddies that, since the beginning of their lifetime (i.e., when first detected by an automatic tracking software), exhibited a dynamical signature in sea-surface Okubo-Weiss fields. Their dynamical imprint on the sea-surface allowed us to define the Meddy-induced sea-surface anomalies in terms of SSH, SST and SSS.

We found that the realistic model was able to correctly reproduce the Meddies-induced anomalies in SSH fields, if compared to observations. Indeed, in the simulation, mesoscale Meddies (Radius  $\geq 30$  km) could generate local monopolar anomalies up to 7 cm. Furthermore, such anomalies also exhibited positive values throughout the whole Meddies' life cycle. This is in agreement with the results of Bashmachnikov and Carton (2012), who, using observations, found anomalies

$\mathcal{O}(10\text{ cm})$  for real Meddies. Notice that in the idealized studies presented in chapter 3, the subsurface eddies were generating smaller signatures in SSH fields. This is most likely due to the vertical extent of the modeled subsurface anticyclones ( $\simeq 400\text{ m}$ ), which is below the typical Meddies values (800 to 1200 m).

Moreover, when Meddies could be considered as isolated (i.e., when they did not interact with surface-intensified dynamical structures or bottom oceanic topography) the behavior of their surface expression was in agreement with the theoretical predictions we derived in the context of the quasi-geostrophic theory. In those cases, the Meddy-induced anomalies in SSH fields depended mostly linearly on the Meddy integrated potential vorticity content and decreased quadratically with the Meddy's depth.

The simulation also evidenced several occurrences of merger between Meddies. This mostly happened in the first 600 km west of the Iberian Coast and positively influenced the Meddy's expression in SSH fields. Indeed, in one case, a merger event let the Meddy's SSH-anomaly increase by about 600%.

In general, the correlations between the intensity of the Meddies' surface signature (in SSH fields) and its in-depth characteristics indicated that the parameter that mainly drives the Meddy surface signature is the potential vorticity integrated content. This was also confirmed by statistics over a large number of Meddies ( $\simeq 90$ ).

The Meddies' thermohaline signatures at the sea-surface behaved differently, compared to the ones in SSH. Indeed, the SST and SSS anomalies, in correspondence of an underlying Meddy, could assume positive and negative values throughout the Meddy's lifetime and their evolutions did not seem to be correlated with the Meddy in-depth characteristics. This behavior principally suggested that the thermohaline sea-surface anomalies were mostly dominated by the local surface dynamics rather than the Meddy evolution at depth.

Considering these results, we concluded that the detection of Meddies from observations of the sea-surface should mostly rely on satellite altimetry (in combinations with *in-situ* observations that could occasionally be provided by ARGO floats or other hydrological surveys). Although the combination of SST and SSH observations proved satisfactory to reconstruct surface and near-surface-intensified motions, [Isern-Fontanet et al. (2008a), González-Haro and Isern-Fontanet (2014), Assassi et al. (2016)], this is not suitable to detect eddies found at 1000 m (or

more) below the sea-surface and with horizontal extents seldom exceeding 100 km.

## 6.2 The main perspectives

The main unanswered questions of this work will be listed below. We believe they represent topics that, if investigated, could give new hints on the study of the subsurface oceanic motions from space.

- The surface signature of subsurface eddies (in SSH) should be further investigated in terms of its shape, both in numerical simulations and observations. Similarly to Chelton et al. (2011) (see e.g. their figure 15), one should try to derive the mean shape of the SSH anomalies induced by subsurface eddies as a function of their radii. In this case, the questions to be answered will be: do subsurface eddies locally deform the sea-surface differently from surface-intensified ones? If so, under which conditions can we use this information to detect intrathermocline eddies from observations of the sea-surface? Moreover, being aware of the repetitiveness of the future SWOT mission ( $\simeq 21$  days) one should determine the time scales over which the shapes of the signatures vary significantly in time. This could be achieved via numerical approaches, for example, simulating the life-cycle of a subsurface vortex and studying its surface signature using a SWOT simulator [Gaultier et al. (2016)];
- The study of merger between intrathermocline cyclones and anticyclones can also be significantly improved, if compared to the study we presented in chapter 4. Recalling that we studied the merger of identical anticyclones (and cyclones) swirling at equal depths, one could investigate the effects of changing the eddies' structure on the possibility of merger. What would happen if the eddies were unequal or if we added a vertical offset between them? And what if their rotational axes were tilted, similarly to Reinaud and Dritschel (2005)? Moreover, the presence of the bottom oceanic topography was neglected in our experiments. Introducing seamounts or abyssal plains in the numerical simulations could give a more realistic description for the merger of both surface and subsurface-intensified eddies. For example, in the case of Meddies, merger mostly occurs in a region where seamounts and

canyons are abundant [Bashmachnikov et al. (2015), Barbosa Aguiar et al. (2013)];

- Finally, the study of the Meddies' expression at the sea-surface (via realistic numerical approaches) could probably benefit from the introduction of a high-frequency atmospheric forcing in the simulation. In our case, a monthly climatology was used and, as we stated at the end of chapter 5, this could give smoother time evolutions of the SST and SSS fields (if compared to satellite-derived observations). We also wonder to which extent, switching to a realistic forcing could change the results on the Meddies-induced SST and SSS anomalies. Indeed, at the end of our study, we excluded the use of these informations to track Meddies from observations of the sea-surface. Increasing the degree of realism of the simulation will certainly help understanding the limits of our conclusions.

# Acknowledgements

Dans cette section finale, je souhaite remercier tous ceux qui ont rendu possible ce travail de thèse et qui m'ont aidé à garder des très beaux souvenirs de mon séjour brestois. D'abord, ce travail a bénéficié du soutien financier de l'Université de Bretagne Occidentale, de la Région Bretagne et du Labex MER, que je remercie pour avoir eu confiance en moi en tant que personne et étudiant. Je tiens également à remercier Xavier Carton et Bertrand Chapron, mes directeurs de thèse.

Xavier, avec son regard attentif et son investissement quotidien, a su me guider avec patience et respect dans une domaine qui était complètement inconnue pour moi. En outre, il m'a permis d'apprendre beaucoup sur l'océanographie et sur moi-même, comme le sens de responsabilité et de liberté qu'on ressent quand on aborde un sujet de recherche de façon autonome.

Bertrand a toujours représenté une source d'idées très intéressantes et m'a souvent aidé à comprendre quelle était la bonne direction pour avancer dans mes recherches. En outre, je tiens à le remercier pour l'originalité et la beauté de nos échanges informelles, pendant lesquelles je me permettait d'exprimer mes pensées très librement, tout en me sentant à l'aise et en sécurité.

Merci à tous les membres de mon jury de thèse: Igor Bashmachnikov, Xavier Carton, Bertrand Chapron, Alain Colin de Verdière, Yves Morel, Álvaro Júdice Peliz, Gilles Reverdin et Jacques Verron. J'ai été très content de présenter mon travail de thèse devant eux et j'ai vraiment apprécié leurs questions et suggestions pendant la soutenance.

Ma vie quotidienne au travail a bénéficié de la présence de tous les composants du LOPS, à partir de mes collègues plus proches jusqu'à ceux que j'ai le moins côtoyé. Je voudrais les remercier tous pour avoir accepté et compris (j'espère!) mon caractère souvent très réservé et silencieux, qui n'est que le résultat de mon histoire personnelle. Certains composants du laboratoire sont devenus des amis

très proches pour moi et, même s'ils sont partis loin pendant ma thèse, j'ai pu sentir leur soutien et sympathie pendant la phase plus critique de mon travail: la finalisation du manuscrit et la préparation de la soutenance. Souvent, leur mots et attentions m'ont agréablement surpris et ont rendu mes journées vraiment plus colorées. Merci à vous Séverine, Antoine, Pierre, Clémence, Clément, José-Luis, Gildas, Tonia, Emanuela, Katherine, Natalie Moagabo, Jérémy, Laurie, Rui, Nicolas et Claire!

Je voudrais aussi remercier tous mes collaborateurs extérieurs: Ana Claudia Barbosa Aguiar, Álvaro Júdice Peliz, Igor Bashmachnikov, Jacques Verron et Federico Ienna. Interagir avec eux a été source de satisfaction et a représenté une activité très nourrissante pour mon esprit.

C'è un insieme di persone che, durante la mia permanenza a Brest, è stato capace di accompagnarmi quotidianamente con ironia, coraggio e pazienza. Si tratta della mia famiglia, attualmente composta da Giovanni, Naida, Elisa, Davide, Paoletto, Annamaria, Virgilio e Maria. Sono rimasto stupito dalla loro capacità di attendere e di incoraggiarmi. Questo ha rappresentato l'arma migliore contro tutti i dubbi e le incertezze che mi accompagnano costantemente. Tutti loro sono stati il mio faro.

Ho trovato molto emozionante il rapporto con i miei amici di sempre, i quali mi hanno regalato il ritmo giusto per scacciare la noia e la paura. Grazie carissimi Pepa, Giulia, Francesca, Paolo, Simona P, Simona G, Tea, Lela, Argia, Massimo, Frenklev, Monica, Davide, Giordano, Sara, Benedetta, Alice, Barthélémy, Mario e Tiziano.

Después de agradecer a mi familia y mis amigos de origen, sigo con la familia que el destino me dio en Brest. Esa familia es más pequeña que la otra, pero ha funcionado de la misma manera, porque sus ingredientes eran respecto, intimidad, solidaridad y comida siempre buena y lista cuando llegaba a casa por la noche. Gracias Cristina, y gracias a todos los que decidieron unirse durante el camino: Nico (además de los cangrejos, las vieras, las lubinas...), Lucía, Manuel, Laura González García, Claudio, Laura Ifremer, Laura Dialogues, Pat Star\*, Tania y Carolina.

Un merci très sincère aux Choeurs en Cavale du Patronat Laïque de la Cavale Blanche. Je n'oublierai jamais le premier accord que nous avons chanté ensemble. En particulier, je tiens à citer Hervé, Yann, Lydiane, Cecilia, Luc, Merwen, Em-

manuel, Marie-Noëlle, Babeth, Michelle et Annie. Merci, car vous m'avez ouvert vos maisons et vous m'avez présenté vos familles et amis. Ce n'est pas donné d'atterrir à Brest et de pouvoir côtoyer des bretons pur beurre comme vous (et de goûter un kig ha farz du Haut-Léon fait maison, n'est-ce pas Cathy?).

Merci à Luce, Maria, Phaco et la magnifique coloc de Locquilloc. Vous avez représenté une touche d'originalité pendant mon séjour brestois, car vous êtes tellement différents de moi que je me sentais très riche de pouvoir être à côté de vous de temps en temps.

Pour revenir au LOPS, merci à tous ceux qui ont partagé le bureau avec moi: Dhouha Ferjani, Jérémy Collin et Nicolas Ducousso. Ce n'est pas évident de rentrer dans son bureau le matin en sachant que la journée ira bien se passer, avec plein d'ironie, de fou rire et de complicité. Merci à tous ceux qui m'ont aidé à préparer ma soutenance de thèse et à rendre ma présentation plus efficace: Xavier, Bertrand, toute l'équipe SIAM, Quentin, Pat Star\*, Bernard, Camille, Claire et Mathieu. En outre, un grand merci à Camille qui, un peu par hasard, s'est retrouvée à me soutenir dans un des moments plus durs de l'année. Merci à toi pour m'avoir aidé, avec plein de sympathie et discrétion, à relier et envoyer mes manuscrit de thèse aux rapporteurs...

Merci à quatre personnes qui aimaient débarquer (certains d'entre eux en dansant) dans mon bureau au bâtiment G de l'UBO: Laura, Mathieu, Nicolas et Pauline. Merci pour votre ironie très drôle et mature, j'ai toujours aimé discuter et rigoler avec vous.

Je voudrais aussi remercier tout le personnel administratif de l'UBO et de l'EDSM, ainsi que le président de l'EDSM: Gilberte, Françoise, Elisabeth et Fred. J'étais toujours très content de venir vous embêter avec mes questions, car vous avez toujours été sympathiques, bienveillants et disponibles avec moi.

Merci enfin à Giulia, qui m'a ramené à Roma avec sa conduite attentive et sportive et à Pepa, pour le beau séjour à *La Casa dei Guaglioni*, pendant lequel j'ai pu rédiger ces remerciements en souriant, soutenu par l'ironie, la tolérance, les couleurs et les rythmes de la ville de Napoli.

Tourbillons Océaniques intensifiés en subsurface :  
signature en surface et interactions mutuelles

Daniele Ciani

3 décembre 2016

# Table des matières

1	Introduction Générale	1
2	Signature de surface des anticyclones de subsurface	3
3	Interactions entre anticyclones de subsurface : fusion	8
4	Tourbillons d'eau Méditerranéenne : signatures à la surface de la mer dans une simulation réaliste à haute résolution	13
5	Conclusions	18

# Chapitre 1

## Introduction Générale

La Mer d'Arabie est caractérisée par d'importantes variations spatiales et temporelles de température, salinité et courants à différentes échelles. Dans cette région, il est possible d'observer des variations de ces paramètres physiques de l'échelle régionale (300-500 km) à l'échelle des tourbillons (30-50 km). Ce contexte géophysique est le résultat de l'action des forçages atmosphériques sur la Mer d'Arabie et sur les mers adjacentes (Golfe Persique et Mer Rouge) [Lee et al. (2000)]. En particulier, le Golfe Persique et la Mer Rouge sont des bassins caractérisés par une forte évaporation, ce qui cause la formation d'eaux denses (avec une anomalie positive en salinité et température) qui plongent et coulent vers la Mer d'Arabie. Ce mécanisme crée des sous-courants qui, en interagissant avec des structures dynamiques préexistantes en Mer d'Arabie, peuvent générer des filaments et des tourbillons intensifiés en subsurface [Senjyu et al. (1998), Carton et al. (2012)]. De la même façon, les échanges de masses d'eau entre la Mer Méditerranée et l'Océan Atlantique génèrent un sous-courant en correspondance de l'étroit de Gibraltar, avec des veines principales intensifiées entre 700 et 1000 m de profondeur [Pingree and Morrison (1973)]. Ce courant (aussi caractérisé par une anomalie positive en température et salinité par rapport à son environnement) peut générer des tourbillons intensifiés à environ 1000 m de profondeur via des instabilités baroclines ou des interactions avec la topographie [Swallow (1969), Bower et al. (1997), Richardson et al. (2000a), Barbosa Aguiar et al. (2013)]. Ce cadre prouve l'existence de structures tourbillonnaires (plutôt anticycloniques) de subsurface dans la mer d'Arabie et l'Océan Atlantique nord-oriental.

---

En général, les tourbillons sont des structures cohérentes avec des temps de vie qui peuvent excéder un an. En outre, en étant des structures non-stationnaires, ils sont capables de transporter les traceurs océaniques (chaleur, salinité et nutriments) pour des très longues distances (jusqu'à plusieurs milliers de km du site de génération, [Chelton et al. (2011)]). La détection de ces structures est donc fondamentale pour évaluer le bilan tridimensionnel des traceurs océaniques à échelle globale.

L'approche idéale pour l'identification et la caractérisation des tourbillons profonds est représentée par les mesures *in-situ*. Cette approche permet de décrire des structures avec des tailles horizontales typiques de la sous-mésoéchelle océanique ( $\simeq 10$  to  $20$  km) [L'Hégaret (2015)] mais peut seulement fournir des informations ponctuelles et ne donne pas une description synoptique de l'océan globale. En revanche, une étude basée sur des mesures satellitaires résoudrait les limites de couverture spatiale et temporelle imposées par les mesures *in-situ*. Cela signifie que le suivi des tourbillons se ferait à travers leur signature à la surface de l'océan (si présente). Le travail de cette thèse consiste en l'optimisation de plusieurs études théoriques et numériques pour déterminer de quelle façon les tourbillons océaniques (anticycloniques) influencent la surface de la mer. Le but de ces études sera d'évaluer l'apport des missions satellitaires à haute résolution (par exemple la mission conjointe de CNES et NASA "SWOT" [Fu et al. (2009)]) pour étudier la dynamique profonde de l'océan à travers des observations de surface. La mission satellitaire SWOT, prévue pour l'année 2020, permettra d'avoir des observations altimétriques à échelle globale avec des précisions de mesure de moins de 2 cm, ce qui est actuellement possible seulement pour une fraction des observations globales [Fu and Cazenave (2000)].

Le travail a été organisé selon la hiérarchie suivante : dans un premier temps nous avons déterminé la signature de surface des anticyclones profonds avec des approches analytiques dans le cadre de l'approximation quasi-géostrophique (QG) ainsi que avec des modèles numériques QG et aux équations primitives (PE) idéalisés. Ensuite, nous avons évalué les effets de l'interaction entre anticyclones de subsurface. Le but était de déterminer sous quelles conditions ce type d'interaction pouvait déclencher des processus de fusion et quelle était l'influence de ces mécanismes sur la structure tridimensionnel du tourbillon finale. Enfin, nous avons étudié les mécanismes physiques décrits précédemment dans un cadre plus réaliste.

En utilisant une simulation numérique initialement conçue pour décrire le cycle de vie des Meddies (Tourbillons d'eau Méditerranéenne) dans l'océan Atlantique nord-orientale, nous avons étudié leur signatures à la surface de la mer durant leur évolution.

## Chapitre 2

# Signature de surface des anticyclones de subsurface

Dans ce chapitre nous étudierons la signature de surface des anticyclones de subsurface à travers des modèles analytiques QG ainsi que des expériences numériques QG et PE. Nous nous concentrerons sur la signature en termes d'élévation de la surface libre de la mer (généralement indiquée comme sea-surface height ou SSH), en présence d'un tourbillon intensifié en profondeur dans la colonne d'eau. Ce choix est principalement due à l'évaluation d'une mission altimétrique pour la détection des tourbillons de subsurface depuis l'espace, comme par exemple la mission SWOT [Fu et al. (2009)]. Des travaux antérieurs [Bashmachnikov and Carton (2012), Bashmachnikov et al. (2013)] ont permis de dire que, dans un cas anticyclonique, les tourbillons de subsurface sont associés à des anomalies SSH monopolaires positives à la surface de la mer (et une anomalie négative en température). Cette signature dépend linéairement de la vorticité potentielle du tourbillon, de l'inverse de sa profondeur et du cube de son rayon dynamique. Ceci est résumé par la relation 2.1

$$SSH_{anom} \propto \frac{|q|R^3}{NH} \quad (2.1)$$

où  $q$  est la vorticité potentielle du tourbillon,  $R$  son Rayon,  $N$  est la fréquence de Brunt-Väisälä des couches océaniques près de la surface et  $H$  est la profondeur du tourbillon.

Des calculs analytiques dans le cadre de l'approximation géostrophique, schématisant le tourbillon de manière mathématique sous forme de "point-vortex" statique, ont permis de mieux comprendre cela. En particulier, ces calculs analytiques constituent une amélioration des modèles proposés précédemment car ils considèrent le tourbillon comme une structure de vorticit  potentielle totale nulle. Ceci  vite de se poser dans une situation dans laquelle le tourbillon g n re une  nergie cin tique infinie dans le bassin oc anique consid r . En particulier, les sch mas propos s sont montr s en figure 2.1.

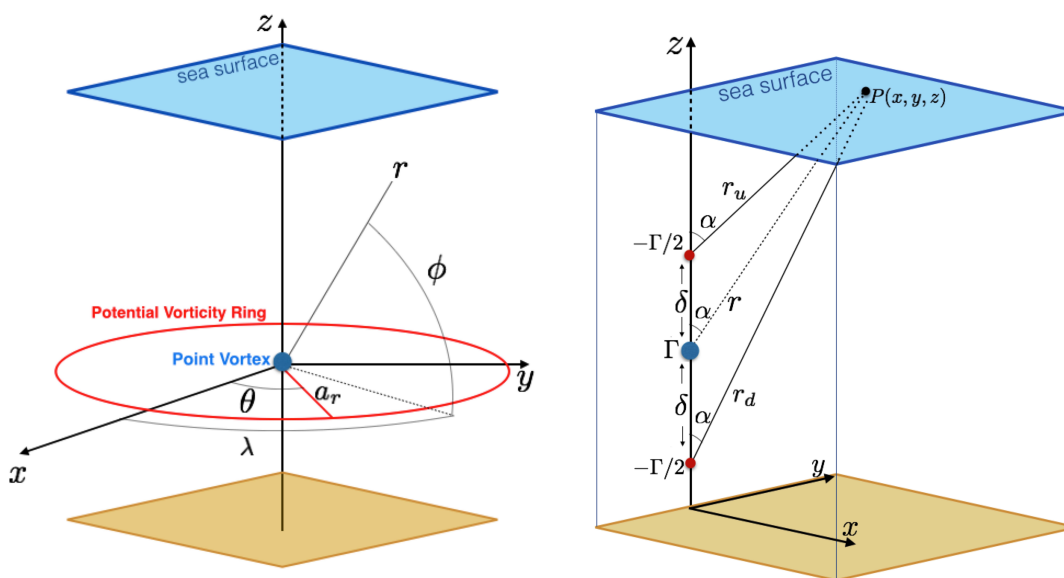


**FIG. 2.1:** *A gauche : "point-vortex" entour  d'un anneau de vorticit  potentielle (R-vortex). A droite : Tripole vertical de vorticit  potentielle (S-vortex).*

Ces deux mod les, en outre, consid rent une structure en vorticit  potentielle qui est conforme aux configurations de type "S-vortex" ou "R-vortex", d j  utilis es par Morel and McWilliams (1997) pour mod liser l' volution des tourbillons de subsurface dans l'oc an. En outre, ces mod les sont en accord avec la structure des anticyclones de subsurface observ s dans l'oc an reel et avec les tourbillons  tudi s dans les experiments num riques, dont un exemple est montr  en figure 2.2.

Dans ce cas sp cifique, la structure en vorticit  potentielle du tourbillon montre des caract ristiques appartenantes aux tourbillons de type "S" et "R" en m me temps. Les expressions pour la signature de surface (proportionnelle   la fonction

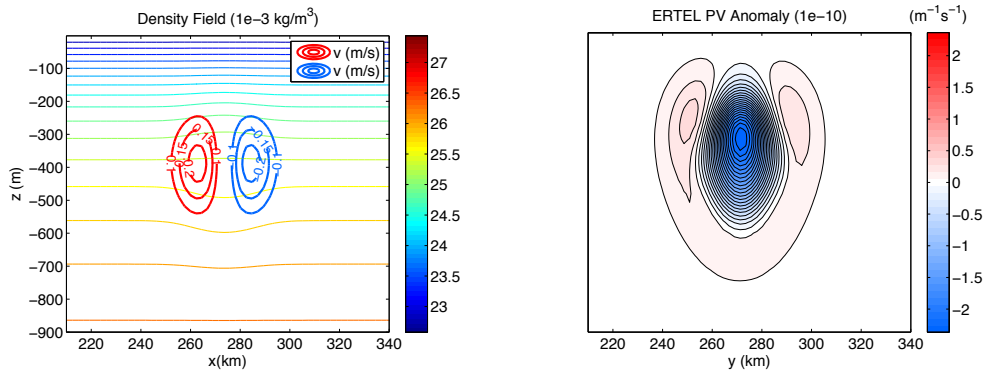


**FIG. 2.2:** Champs de vitesse (gauche) et structure verticale de la vorticité potentielle de ERTTEL (droite) pour un anticyclone de subsurface. Rayon du tourbillon=15 km, Profondeur=350 m, Extension verticale = 300 m, Vitesse de rotation = 0.2 m/s.

de courant générée par le tourbillon) de ces types de tourbillons sont les suivantes :

$$\psi_S \propto \frac{\Gamma}{4\pi} \left( \frac{\delta^2 r^2 \cos^2 \alpha}{r^5 - \delta^2 r (r \cos \alpha)^2} \right) \quad (2.2)$$

$$\psi_R \propto -\frac{\Gamma}{4\pi r} + \frac{\Gamma}{4(r^2 + a_r^2)^{1/2}} \left[ 1 + \frac{3a_r^2 r^2}{8(r^2 + a_r^2)^2} \right] \quad (2.3)$$

où  $r = (x^2 + y^2 + Z^2)^{1/2}$ ,  $Z = (N/f)z$  et  $f$  le paramètre de Coriolis. Ceci montre que l'estimation analytique de la signature SSH du tourbillon est linéaire par rapport à la vorticité potentielle " $\Gamma$ ". De toute façon, on obtient une décroissance par rapport à la profondeur du tourbillon qui n'est pas linéaire, comme le confirment aussi des simulations numériques avec le modèle ROMS [Shchepetkin and McWilliams (2005)] en configuration idéalisée de type plan- $f$  (voir aussi figure 2.3).

En outre, en utilisant le modèle numérique aux équations primitives (ROMS, plan- $\beta$ ), ainsi qu'un modèle quasi-géostrophique, on a pu caractériser le comportement de la signature altimétrique dans un cas dynamique. Dans ce cas, nous avons pris en compte les effets de déplacement du tourbillon (sans signature de surface,  $SSH_{anom}=0$  au début de la simulation) dans un bassin océanique idéalisé au repos.

Les résultats numériques montrent que l'intensité de la signature de surface

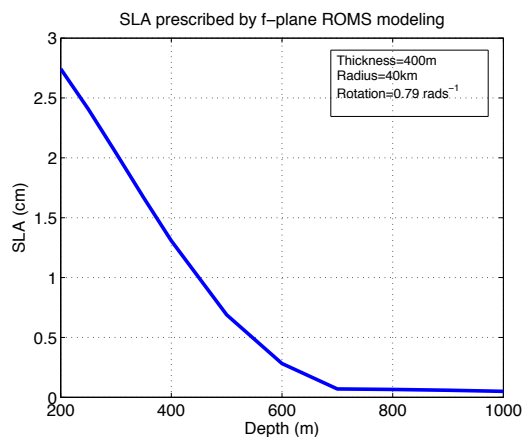


**FIG. 2.3:** Anomalie de hauteur de la mer (Sea-Level Anomaly, SLA) générée par un tourbillon anticyclonique profond en fonction de sa profondeur. (Les paramètres du tourbillon sont : Rayon = 40 km, Extension verticale = 400 m et Vitesse de Rotation = 0.3 m/s. Cas Statique.

augmente avec le rayon du tourbillon, son extension verticale et sa vorticité potentielle, alors qu'elle est inversement proportionnelle à sa profondeur. En outre, la signature dominante à la surface est toujours dipolaire (comme montré en figure 2.4) et, si on considère les sorties du modèle ROMS, on trouve que l'on atteint des intensités de l'ordre de 2 cm (seuil de l'erreur de mesure SWOT) seulement si on choisit des tourbillons de mésoéchelle océanique (avec un rayon d'environ 40 km). Une première conclusion de ce travail est que, dans un cas idéalisé, la détection systématique des tourbillons profonds à travers SWOT (ou plus en général avec une approche altimétrique) n'est possible que pour des structures de mésoéchelle d'une durée de vie de plusieurs mois.

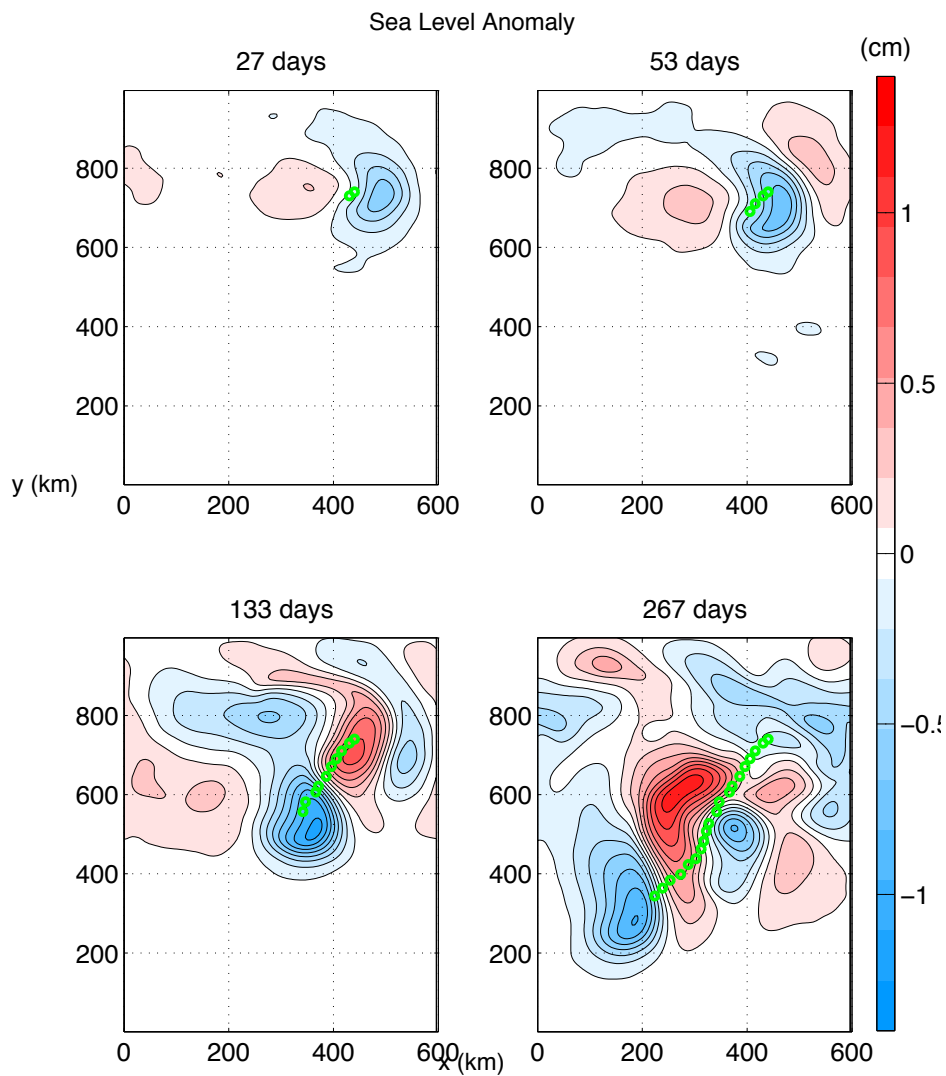


**FIG. 2.4:** Evolution de la signature altimétrique pour un tourbillon profond (en vert, on indique la projection superficielle de la position du tourbillon profond). Rayon du tourbillon = 40 km, Profondeur = 700m, Extension verticale = 400m, Vitesse de rotation = 0.4 m/s.

## Chapitre 3

# Interactions entre anticyclones de subsurface : fusion

Ce chapitre est dédié à l'étude des interactions entre anticyclones de subsurface. La motivation principale pour ce type d'investigation vient de la preuve que ces tourbillons sont capables de fusionner, ainsi modifiant leur structure initiale. Ceci a été montré pour les tourbillons d'eau Méditerranéenne (Meddies) à travers des observations *in-situ* [Schultz Tokos et al. (1994), Richardson et al. (2000b), L'Hégaret et al. (2014), Bashmachnikov et al. (2015)] ainsi que à travers des experiments numériques [Barbosa Aguiar et al. (2013)]. Les processus de fusion peuvent générer des tourbillons de rayon et vorticité potentielle accrus par rapport à la structure de départ. Ceci, selon les résultats présentés dans le Chapitre 2, élige la fusion comme un des mécanismes qui favorisent la détection des tourbillons profonds à travers l'observation de la surface de la mer.

Nous avons étudié ce phénomène via des experiments numériques avec le modèle ROMS, dans un bassin idéalisé au repos, à fond plat et en négligeant toutes interactions avec l'atmosphère. Les tourbillons ont été modélisés avec une structure typiques des Meddies, comme montré dans la figure 3.1. Leur structure en vorticité potentielle (toujours montrée en figure 3.1) indique que ces tourbillons mélangent les propriétés des tourbillons "R" et "S" (vues dans le Chapitre 2). Effectivement, leur anomalies de vorticité potentielle changent de signe verticalement et horizontalement, ainsi générant des écrans de vorticité tout autour du coeur centrale.

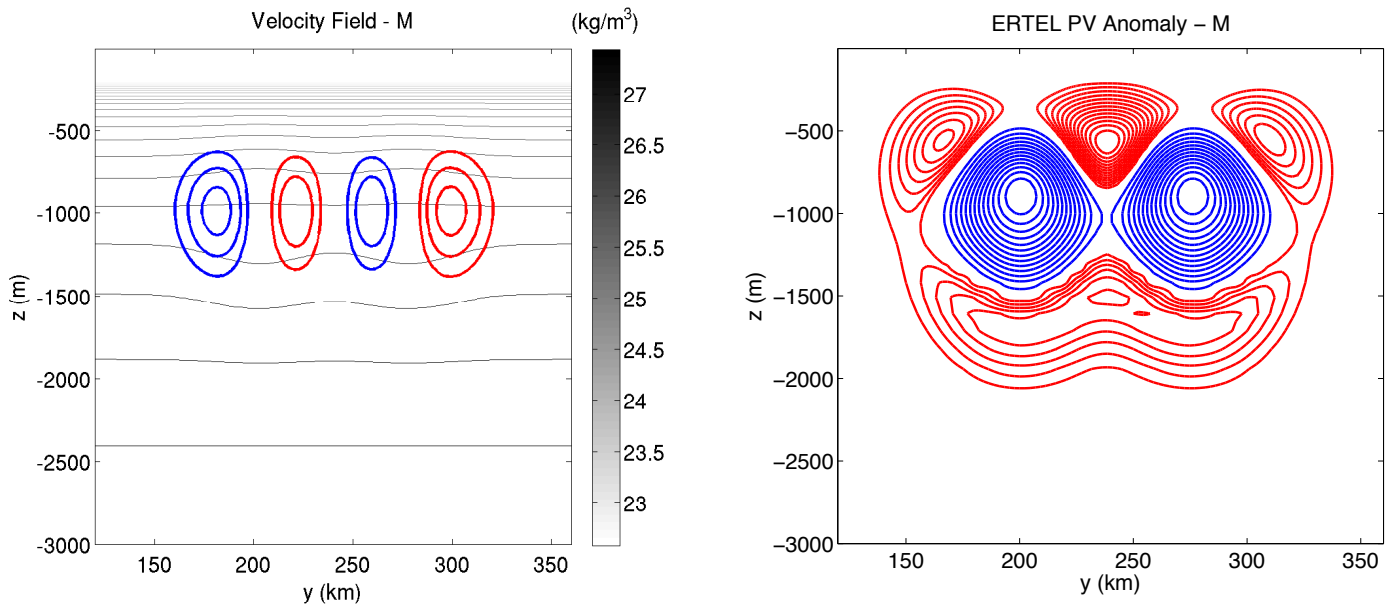


**FIG. 3.1:** *Etat initiale des simulations numériques sur l'interaction entre anticyclones de subsurface. Gauche : sections verticales de densité et champs de vitesse. Les contours colorés indiquent la composante zonale de la vitesse de rotation (de 0.1 m/s jusqu'à 0.2 m/s par pas de 0.05 m/s). Les lignes en bleu (rouge) indiquent un écoulement vers le (ou sortant du) plan  $y$ - $z$ , respectivement. Droite : sections verticales d'anomalie de vorticité potentielle. Les écrans de vorticité potentielle sont indiqués en rouge.*

D'abord, nous avons déterminé les conditions critiques pour lesquelles la fusion entre anticyclones de subsurface était possible. Nous avons trouvé que, pour deux tourbillons identiques, intensifiés à la même profondeur et dans un océan au repos, la distance critique pour le déclenchement de la fusion est de  $2.5 R$ , où  $R = 30$  km est le rayon du tourbillon. Les deux tourbillons, après une phase initiale de corotation, fusionnent et génèrent un nouveau tourbillon après environ 20 jours d'interactions (voir figure 3.2). Lorsque cette distance critique est augmentée de  $0.1 R$ , les deux tourbillons, après une phase initiale de corotation, s'éloignent l'un de l'autre via un effet dipolaire due à la redistribution de la vorticité potentielle périphérique (celle associée aux écrans).

Si on compare la structure des tourbillons avant et après la fusion (par rapport à un seul tourbillon initial) on trouve que, une fois le processus de fusion achevé :

- le rayon du tourbillon finale augmente d'environ 30% ;

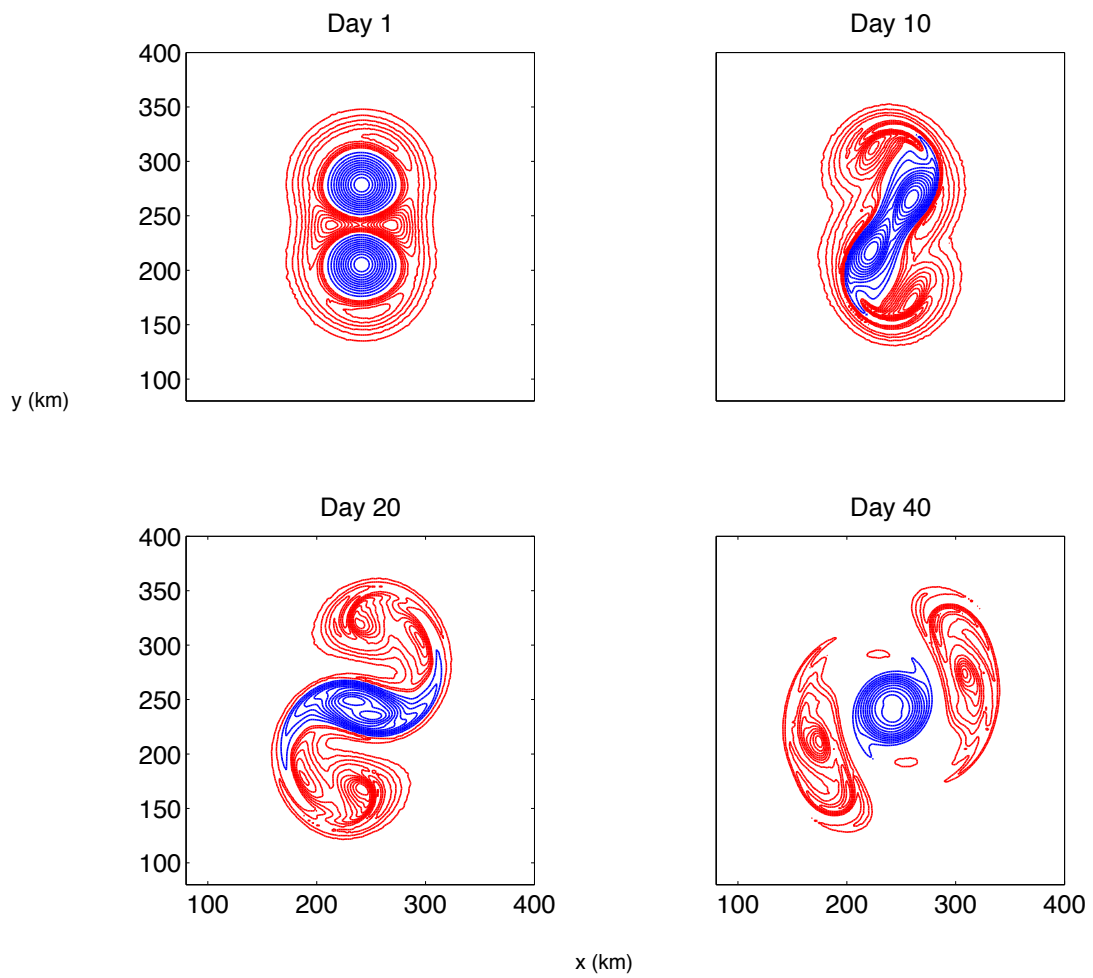


**FIG. 3.2:** *Anomalie de vorticité potentielle montrant la fusion de deux anticyclones de subsurface (section horizontale à 1000 m de profondeur).*

- l'intégrale volumique de la vorticité potentielle augmente de 40% ;
- l'extension verticale du tourbillon diminue de 20%
- le processus de fusion génère des structures de sous-mésoéchelle (filaments et tourbillons) due aux instabilités de la vorticité potentielle périphériques et à l'éjection de masses d'eau depuis le centre du tourbillon fusionné.

La figure 3.3 montre en détail la structure initiale et finale des tourbillons suite à un événement de fusion.

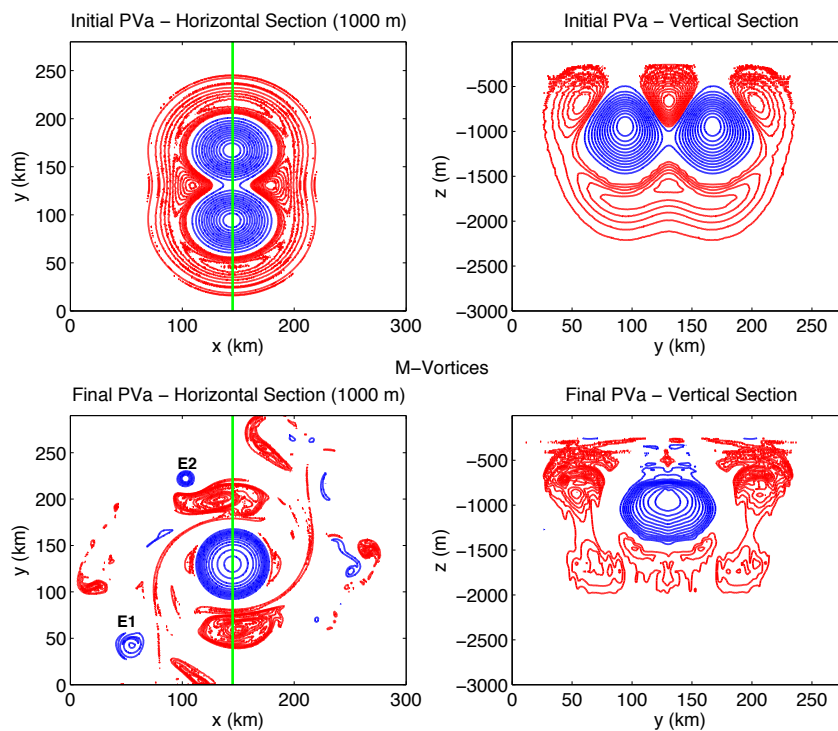


**FIG. 3.3:** Sections d'anomalie de vorticité potentielle avant et après le processus de fusion. Les sections verticales ont été obtenues le long des radiales indiquées en vert. Les tourbillons périphériques de sous-mésoéchelle sont indiqués avec E1 and E2.

En conclusion, le processus de fusion entre anticyclones de subsurface est capable de générer des tourbillons avec une extension horizontale et un integrale volumique de vorticité potentielle accrus par rapport à un seul tourbillon initiale. Ceci, en considérant les resultats du Chapitre 2 prouve que la fusion peut effectivement faciliter l'expression en surface des tourbillons intensifiés en profondeurs. En outre,

nous avons aussi trouvé que les processus de fusion sont impliqués dans une double cascade d'énergie dans l'océan. Si d'un côté la fusion génère des tourbillons de taille horizontale accrue, de l'autre côté elle génère aussi des structures de fine échelle ( $\simeq 5-10$  km d'extension horizontale).

## Chapitre 4

# Tourbillons d'eau Méditerranéenne : signatures à la surface de la mer dans une simulation réaliste à haute résolution

Dans cette étude finale, en utilisant une simulation à haute résolution spatiale ( $\simeq 3$  km) en configuration réaliste (avec le modèle ROMS), nous caractérisons la signature de surface des tourbillons d'eau Méditerranéenne (Meddies) pendant leur cycle de vie. Les sorties de ce modèle ont été initialement utilisées pour étudier l'évolution des Meddies dans l'Atlantique nord-orientale, au large de l'étréit de Gibraltar. La mise en place du modèle, ainsi que l'analyse de l'évolution des Meddies sont decries dans Barbosa Aguiar et al. (2013). Le choix d'une configuration réaliste nous a permis d'étudier la signature de surface des Meddies non seulement en termes de SSH mais aussi dans les champs de temperature (SST) et salinité de surface (SSS), en tenant compte des interactions entre les tourbillons et avec la topographie, ainsi que d'autres structures dynamiques (courants et/ou tourbillons de surface). En outre, les informations combinées de SSH, SSS et SST permettent d'évaluer la possibilité d'une synergie entre différentes mesures satellitaires pour la détection des Meddies depuis l'espace. Notre étude se base principalement sur l'analyse des Meddies qui ont vécu plus longtemps dans la simulation (temps de vie entre 1 et 2 ans), dont les trajectoires sont représentées en figure 4.1.

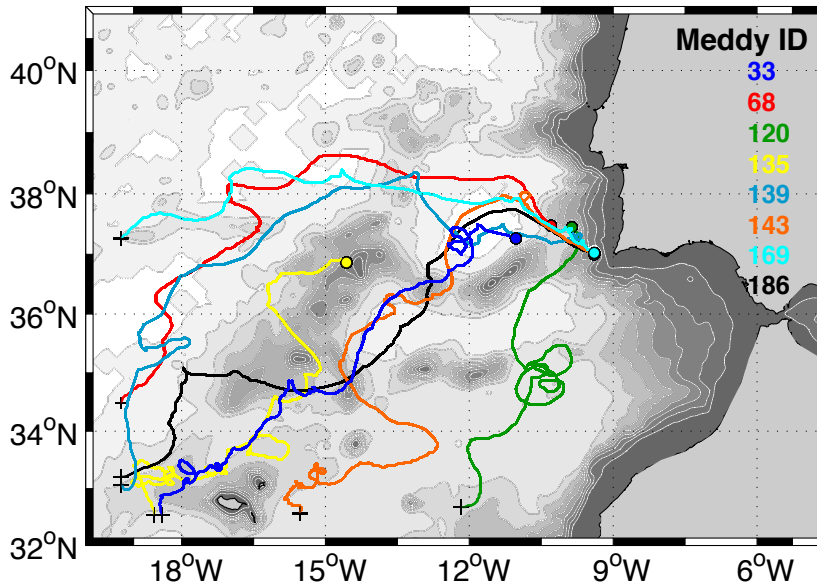


**FIG. 4.1:** *Trajectoires des Meddies qui vivent plus longtemps dans la simulation.*

Nous décrivons ici l'évolution de la signature de surface du Meddy 33, étant celui de plus grande longévité (temps de vie  $> 2$  ans), sachant que tous les autres Meddies montrent un comportement similaire, si comparé à celui du Meddy 33. Il est généré à proximité de Gorrings Bank ( $11^{\circ}W$ ,  $37^{\circ}N$ ) en Janvier 2004 (noter que la date est donnée en fonction du temps du modèle, il ne s'agit pas d'une date réelle). Il poursuit son chemin à travers les Monts du Fer à Cheval et, après avoir dépassé le front des Azores en Octobre 2004, il rejoint le bord de la region modelisée en Juin 2006.

La détermination des signatures de surface est basée sur un critère dynamique. Nous identifions d'abord des régions surfaciques en régime de rotation (paramètre d'Okubo-Weiss  $< 0$ ) spatialement corrélées avec la position du Meddy en profondeur et nous supposons que cette signature dynamique soit associée à l'existence du Meddy. Ensuite, nous évaluons les intensités des signatures en SSH, SSS et SST comme la différence de ces champs entre les bords et le centre de la signature dynamique. L'évolution des signatures a été étudiée en fonction du temps et a été mis en relation avec les paramètres océaniques suivants (déterminés le long des tra-

jectoires des Meddies) : le contenu intégré de sel/température/vorticité potentielle du Meddy (i-Ta/i-Sa/i-EPVa), la profondeur de la couche de mélange océanique (MLD), la fréquence de Brunt-Väisälä (N), la vitesse de rotation du Meddy (SV), son rayon dynamique (R), son extension verticale (Th), sa profondeur (D), la valeur climatologique des courants des surface ( $U_{clim}$ , un indicateur de la position du front des Azores), et le gradient de la topographie ( $\nabla h_B^e$ ), comme montré en figure 4.2 et 4.3.

En termes de SSH, le Meddy 33 génère des anomalies positives pendant tout son cycle de vie. La valeur maximale est de 7 cm, en correspondance de deux événements de fusion avec d'autres Meddies (en Janvier et en Mai 2004). En Octobre 2004 l'anomalie subit une diminution suite à des interactions destructives avec le front des Azores et avec des monts sous-marins. De toute façon, la valeur de l'anomalie SSH associée au Meddy prend une valeur d'environ 2 cm jusqu'à la fin de son cycle de vie. Des analyses statistiques sur le comportement de cette anomalie, montrent qu'elle est majoritairement corrélée avec l'évolution du contenu intégré de vorticité potentielle (avec un coefficient de corrélation de Pearson autour de 0.7 [Fisher et al. (1946)]).

Contrairement à la SSH, les anomalies de SSS et SST prennent des valeurs positives et négatives pendant le cycle de vie du Meddy et ne montrent pas des corrélations significatives avec les paramètres du Meddy ainsi que de l'environnement océanique. Ceci indique que les signatures thermohalines sont plutôt déterminées par la dynamique locale de surface que par la présence du Meddy en profondeur.

Le comportement de ce Meddy (ainsi que celui des autres Meddies qui ont été analysés) montre que les anomalies de SSH représentent la signature plus fiable pour le suivi des Meddies depuis l'espace. Même en présence d'obstacles topographiques ou suite à des interactions destructives avec des courants de surface, les Meddies sont capables de générer des signatures avec des intensités (autour de 2 cm) compatibles avec les données altimétriques actuels et ceux qui seront fournis par la mission satellitaire SWOT.

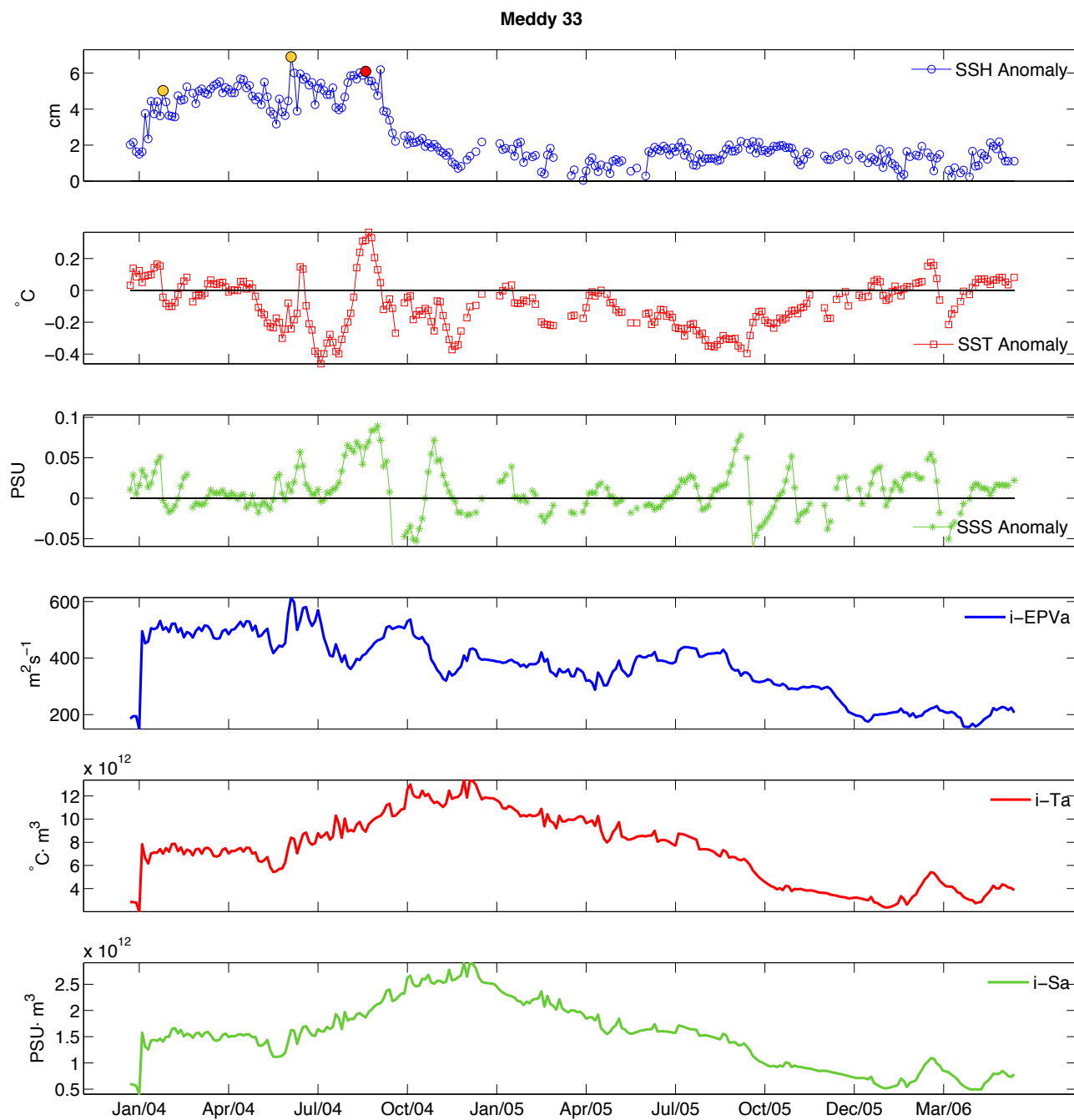


**FIG. 4.2:** Signatures de surface du Meddy 33 (voir aussi la figure 4.1). SSH (cercles bleu), SST (carrés rouges), SSS (étoiles vertes), *i-EPVa* (anomalie de vorticité potentielle intégrée), *i-Ta* (anomalie de température intégrée, rouge), *i-Sa* (anomalie de salinité intégrée, vert).

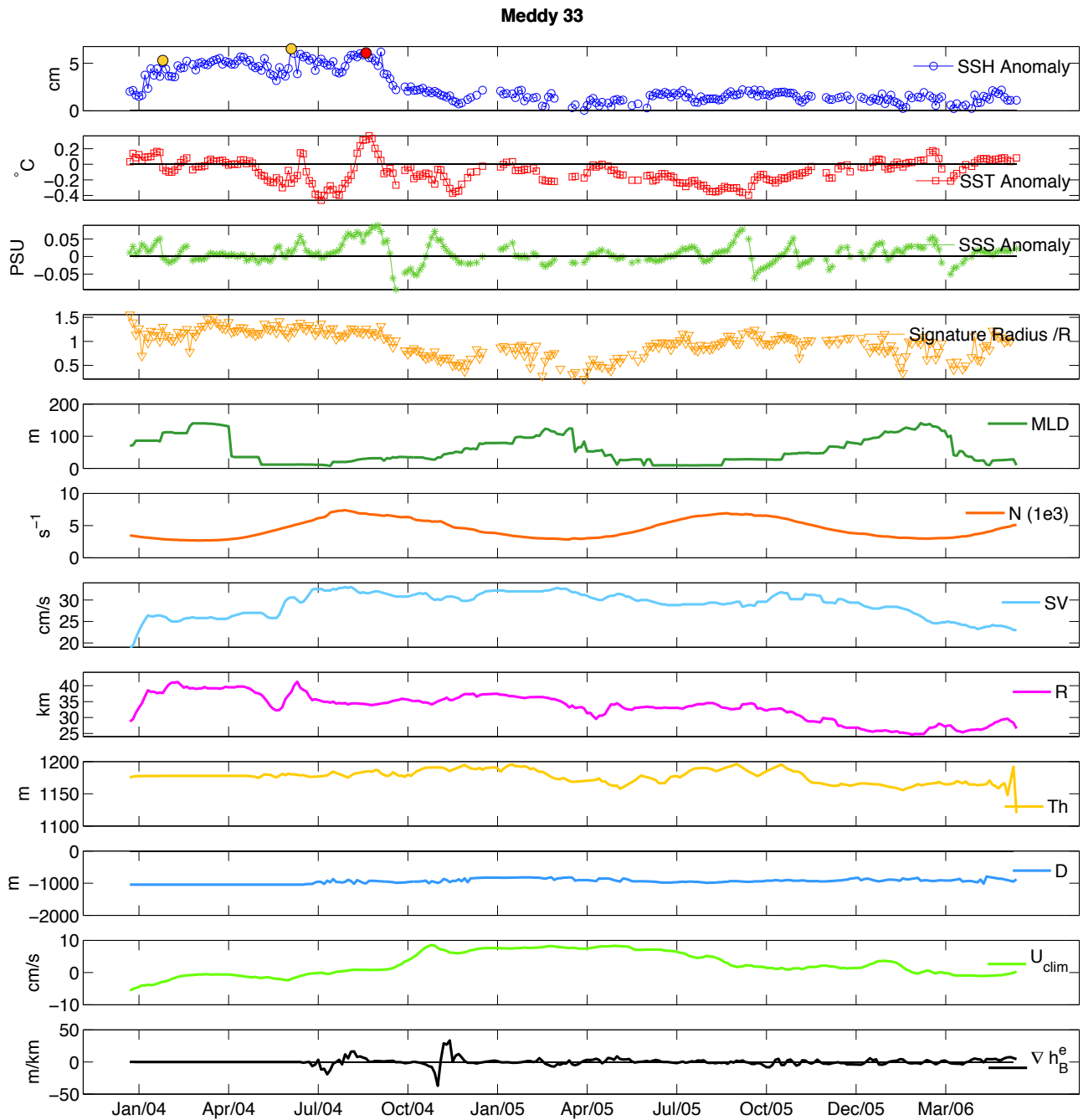


**FIG. 4.3:** Signatures de surface du Meddy 33 (voir aussi la figure 4.1). SSH (cercles bleus), SST (carrés rouges), SSS (étoiles vertes), Extension horizontale de la signature (triangles jaunes), Profondeur de la couche de mélange (vert), fréquence de Brunt-Väisälä (orange), Vitesse de rotation du Meddy (bleu ciel), Rayon du Meddy (magenta), Extension verticale du Meddy (jaune), Profondeur du Meddy (bleu clair), Intensité des courants de surface climatologiques (vert clair), gradient de la topographie (noir).

# Chapitre 5

## Conclusions

Cette thèse a porté sur l'étude des tourbillons de subsurface (de type anticyclonique) au but de déterminer la possibilité de les détecter à travers des capteurs satellitaires. L'intérêt de ce type d'investigation est lié aux propriétés des tourbillons océaniques, étant des structures qui vivent longtemps et qui sont capables de transporter les traceurs océaniques pour plusieurs milliers de kilomètres de leur région d'origine. Le suivi des tourbillons par satellite permettrait d'évaluer le bilan des traceurs océaniques de façon globale et synoptique.

Les résultats des travaux théoriques et numériques ont permis de déterminer que l'intensité de l'expression de surface (en SSH) des anticyclones de subsurface dépend linéairement du contenu intégré de vorticité potentielle du tourbillon, de son extension verticale, quadratiquement de son rayon et non-linéairement par rapport à l'invers de sa profondeur dans la colonne d'eau. Nous avons trouvé que, même dans un contexte idéalisé (dans un environnement au repos), seulement les tourbillons de subsurface de mésoéchelle sont capables de générer des signatures (en termes d'anomalie de SSH) détectables par l'altimétrie satellitaire actuelle et future (mission SWOT).

En outre, nous avons déterminé un des facteurs principales qui peuvent favoriser l'expression de surface des tourbillons intensifiés en profondeur. Il s'agit de la fusion entre tourbillons. Ce processus est capable de modifier la structure tridimensionnelle originale du tourbillon en augmentant son rayon et son contenu intégré en vorticité potentielle. Le processus de fusion est également capable de générer des structures de sous-mésoéchelle océanique, comme des filaments et des

---

tourbillons de petite échelle ( $\simeq 10$  km).

Enfin, nous avons pu étudier la signature de surface des Meddies (des anticyclones de subsurface d'eau Méditerranéenne) dans une simulation réaliste, en évaluant aussi la possibilité de combiner des observations de SSH, SST et SSS pour leur suivi automatique. Les résultats de cette étude indiquent que la SSH est la quantité plus fiable pour la détection des tourbillons de subsurface. En effet, même quand les Meddies rencontrent des obstacles topographiques ou interagissent avec des courants de surface, sont toujours capables de générer une signature en SSH spatialement corrélée avec leur position en profondeur. Le rôle de la fusion entre tourbillons a été confirmé dans le cas des Meddies. Les événements de fusion entre Meddies sont toujours associés à des augmentations de la signature de surface en SSH. En revanche, les signatures en SST et SSS ne semblent pas avoir une dynamique liée aux déplacements des Meddies en profondeur.

Ces travaux excluent la possibilité d'une synergie entre mesures différentes pour le suivi des tourbillons de subsurface (aux profondeurs typiques des Meddies). De toute façon ils confirment l'importance de l'altimétrie satellitaire, et aussi la contribution d'une mission satellitaire à haute résolution comme SWOT, pour étudier la dynamique océanique de subsurface depuis l'espace.

# References

- Aiki, H. and Yamagata, T. (2004). A numerical study on the successive formation of Meddy-like lenses. *Journal of Geophysical Research: Oceans*, 109(C6).
- Ambar, I. (1983). A shallow core of Mediterranean water off western Portugal. *Deep Sea Research Part A. Oceanographic Research Papers*, 30(6):677–680.
- Arhan, M., Colin De Verdière, A., Gascard, J., Jeannin, P., and Harvey, J. (1983). The tourbillon experiment: a study of a mesoscale eddy in the Eastern North Atlantic. *Deep-sea research. Part A. Oceanographic research papers*, 30(5A):475–511.
- Arhan, M. and De Verdière, A. C. (1985). Dynamics of eddy motions in the eastern North Atlantic. *Journal of Physical Oceanography*, 15(2):153–170.
- Armi, L., Hebert, D., Oakey, N., Price, J. F., Richardson, P. L., Rossby, H. T., and Ruddick, B. (1989). Two years in the life of a Mediterranean salt lens. *Journal of Physical Oceanography*, 19(3):354–370.
- Armi, L. and Zenk, W. (1984). Large lenses of highly saline Mediterranean water. *Journal of Physical Oceanography*, 14:1560–1576.
- Assassi, C., Morel, Y., Vandermeirsch, F., Chaigneau, A., Pegliasco, C., Morrow, R., Colas, F., Fleury, S., Carton, X., Klein, P., and Cambra, R. (2016). An index to distinguish surface and subsurface intensified vortices from surface observations. *Journal of Physical Oceanography*, In press.
- Aubert, O., Le Bars, M., Le Gal, P., and Marcus, P. S. (2012). The universal aspect ratio of vortices in rotating stratified flows: experiments and observations. *Journal of Fluid Mechanics*, 706:34–45.

- Bambrey, R. R., Reinaud, J. N., and Dritschel, D. G. (2007). Strong interactions between two corotating quasi-geostrophic vortices. *Journal of Fluid Mechanics*, 592:117–133.
- Barbosa Aguiar, A., Peliz, A., Cordeiro Pires, A., and Le Cann, B. (2011). Zonal structure of the mean flow and eddies in the Azores Current system. *Journal of Geophysical Research: Oceans*, 116(C2).
- Barbosa Aguiar, A. C., Peliz, Á., and Carton, X. (2013). A census of Meddies in a long-term high-resolution simulation. *Progress in Oceanography*, 116:80–94.
- Bashmachnikov, I., Boutov, D., and Dias, J. (2013). Manifestation of two Meddies in altimetry and sea-surface temperature. *Ocean Science*, 9:249–259.
- Bashmachnikov, I. and Carton, X. (2012). Surface signature of Mediterranean water eddies in the Northeastern Atlantic: effect of the upper ocean stratification. *Ocean Science*, 8(6):931–943.
- Bashmachnikov, I., Carton, X., and Belonenko, T. (2014). Characteristics of surface signatures of Mediterranean water eddies. *Journal of Geophysical Research: Oceans*, 119(10):7245–7266.
- Bashmachnikov, I., Machín, F., Mendonça, A., and Martins, A. (2009). In situ and remote sensing signature of Meddies east of the mid-atlantic ridge. *Journal of Geophysical Research: Oceans*, 114(C5).
- Bashmachnikov, I., Neves, F., Calheiros, T., and Carton, X. (2015). Properties and pathways of Mediterranean water eddies in the Atlantic. *Progress in Oceanography*, 137:149–172.
- Bishop, C. and Thorpe, A. (1994). Potential vorticity and the electrostatics analogy. *Quart. J. roy. Meteor. Soc.*, (120):713–731.
- Bosse, A., Testor, P., Mortier, L., Prieur, L., Taillandier, V., d’Ortenzio, F., and Coppola, L. (2015). Spreading of levantine intermediate waters by submesoscale coherent vortices in the northwestern Mediterranean Sea as observed with gliders. *Journal of Geophysical Research: Oceans*, 120(3):1599–1622.

- Bower, A. S., Armi, L., and Ambar, I. (1997). Lagrangian observations of meddy formation during A Mediterranean Undercurrent Seeding Experiment. *Journal of Physical Oceanography*, 27(12):2545–2575.
- Bretherton, F. (1966). Critical layer instability in baroclinic flows. *Quart. J. Roy. Meteor. Soc.*, (393):325–334.
- Brundage, W. and Dugan, J. (1986). Observations of an anticyclonic eddy of 18 C water in the Sargasso Sea. *Journal of Physical Oceanography*, 16(4):717–727.
- Capet, X., McWilliams, J. C., Molemaker, M. J., and Shchepetkin, A. (2008). Mesoscale to submesoscale transition in the California Current System. part i: Flow structure, eddy flux, and observational tests. *Journal of Physical Oceanography*, 38(1):29–43.
- Carton, X. (1992). On the merger of shielded vortices. *EPL (Europhysics Letters)*, 18(8):697.
- Carton, X. (2001). Hydrodynamical Modeling of Oceanic Vortices. *Surveys in Geophysics*, 22:179–263.
- Carton, X., Chérubin, L., Paillet, J., Morel, Y., Serpette, A., and Le Cann, B. (2002). Meddy coupling with a deep cyclone in the Gulf of Cadiz. *Journal of Marine Systems*, 32(1):13–42.
- Carton, X., Daniault, N., Alves, J., Cherubin, L., and Ambar, I. (2010). Meddy dynamics and interaction with neighboring eddies southwest of Portugal: observations and modeling. *Journal of Geophysical Research: Oceans*, 115(C6).
- Carton, X., L’Hegaret, P., and Baraille, R. (2012). Mesoscale variability of water masses in the Arabian Sea as revealed by argo floats. *Ocean Science*, 8:227–248.
- Cenedese, C., Adduce, C., and Fratantoni, D. M. (2005). Laboratory experiments on mesoscale vortices interacting with two islands. *Journal of Geophysical Research: Oceans (1978–2012)*, 110(C9).
- Chelton, D., De Szoeke, R., Schlax, M., El Naggar, K., and Siwertz, N. (1998). Geographical Variability of the First Baroclinic Rossby Radius of Deformation. *Journal of Physical Oceanography*, 28:433–459.

- Chelton, D. B., Schlax, M. G., and Samelson, R. M. (2011). Global observations of nonlinear mesoscale eddies. *Progress in Oceanography*, 91(2):167 – 216.
- Chérubin, L., Carton, X., and Dritschel, D. (2007). Vortex dipole formation by baroclinic instability of boundary currents. *Journal of Physical Oceanography*, 37(6):1661.
- Chérubin, L. M., Carton, X. J., and Dritschel, D. G. (1996). Vortex expulsion by a zonal coastal jet on a transverse canyon. In *ESAIM: Proceedings*, volume 1, pages 481–501. EDP Sciences.
- Chérubin, L. (2000). Descriptive analysis of the hydrology and mixing of the Mediterranean outflow; effects of topography on its stability. *Ph.D. thesis, Université Aix-Marseille*.
- Ciani, D., Carton, X., Bashmachnikov, I., Chapron, B., and Perrot, X. (2015). Influence of deep vortices on the ocean surface. *Interdisciplinary Journal of Discontinuity, Nonlinearity and Complexity*, 4(3):281–311.
- Ciani, D., Carton, X., and Verron, J. (2016). On the merger of subsurface isolated vortices. *Geophysical & Astrophysical Fluid Dynamics*, 110(1):23–49.
- Colin de Verdière, A. (1992). On the southward motion of Mediterranean salt lenses. *Journal of Physical Oceanography*, 22(4):413–420.
- Collins, C. A., Margolina, T., Rago, T. A., and Ivanov, L. (2013). Looping rafof floats in the California Current System. *Deep Sea Research Part II: Topical Studies in Oceanography*, 85:42–61.
- Colton, M. T. and Chase, R. R. P. (1983). Interaction of the Antarctic Circumpolar Current with bottom topography: An investigation using satellite altimetry. *Journal of Geophysical Research: Oceans*, 88(C3):1825–1843.
- Cushman-Roisin, B. and Beckers, J.-M. (2011). *Introduction to geophysical fluid dynamics: physical and numerical aspects*, volume 101. Academic Press.
- Da Silva, A., Young, C., and Levitus, S. (1994). Algorithms and procedures. vol. 1, atlas of surface marine data 1994. *NOAA Atlas NESDIS*, 6:83.

- Delbende, I., Piton, B., and Rossi, M. (2015). Merging of two helical vortices. *European Journal of Mechanics-B/Fluids*, 49:363–372.
- Drillet, Y., Bourdallé-Badie, R., Siefridt, L., and Le Provost, C. (2005). Meddies in the Mercator north Atlantic and Mediterranean Sea eddy-resolving model. *Journal of Geophysical Research: Oceans*, 110(C3).
- Dritschel, D. G. (1985). The stability and energetics of corotating uniform vortices. *Journal of Fluid Mechanics*, 157:95–134.
- Dritschel, D. G. (1995). A general theory for two-dimensional vortex interactions. *Journal of Fluid Mechanics*, 293:269–303.
- Dritschel, D. G. and Legras, B. (1991). The elliptical model of two-dimensional vortex dynamics. ii: Disturbance equations. *Physics of Fluids A: Fluid Dynamics (1989-1993)*, 3(5):855–869.
- Ebbesmeyer, C. C., Taft, B. A., McWilliams, J. C., Shen, C. Y., Riser, S. C., Rossby, H. T., Biscaye, P. E., and Östlund, H. G. (1986). Detection, structure, and origin of extreme anomalies in a western Atlantic oceanographic section. *Journal of Physical Oceanography*, 16(3):591–612.
- Ebuchi, N. and Hanawa, K. (2001). Trajectory of mesoscale eddies in the Kuroshio Recirculation Region. *Journal of Oceanography*, 57(4):471–480.
- Fedorov, K. and Meschanov, S. (1988). Structure and propagation of Red Sea waters in the Gulf of Aden. *Okeanologia*, 28:357–363.
- Filyushkin, B. and Sokolovskiy, M. (2011). Modeling the evolution of intrathermocline lenses in the Atlantic Ocean. *Journal of Marine Research*, 69(2-3):191–220.
- Filyushkin, B., Sokolovskiy, M., Kozhelupova, N., and Vagina, I. (2011). Evolution of intrathermocline eddies moving over a submarine hill. In *Doklady Earth Sciences*, volume 441, pages 1757–1760. Springer.
- Fisher, R. A. et al. (1946). Statistical methods for research workers. *Statistical methods for research workers.*, (10th. ed.).

- Frenger, I., Gruber, N., Knutti, R., and Munnich, M. (2013). Imprint of southern ocean eddies on winds, clouds and rainfall. *Nature Geoscience*, 6(8):608–612.
- Fu, L., Alsdorf, D., E., R., Morrow, R., Mognard, N., Lambin, J. ana Vaze, P., and Lafon, T. (2009). The SWOT (Surface Water and Ocean Topography) mission: Spaceborne Radar Interferometry for Oceanographic and Hhydrological Applications.
- Fu, L.-L. and Cazenave, A. (2000). *Satellite altimetry and earth sciences: a handbook of techniques and applications*, volume 69. Academic Press.
- Gaultier, L., Ubelmann, C., and Fu, L.-L. (2016). The challenge of using future swot data for oceanic field reconstruction. *Journal of Atmospheric and Oceanic Technology*, 33(1):119–126.
- González-Haro, C. and Isern-Fontanet, J. (2014). Global ocean current reconstruction from altimetric and microwave SST measurements. *Journal of Geophysical Research*, 119(6):3378–3391.
- Gordon, A. L., Giulivi, C. F., Lee, C. M., Furey, H. H., Bower, A., and Talley, L. (2002). Japan/East Sea intrathermocline eddies. *Journal of Physical Oceanography*, 32(6):1960–1974.
- Held, I., Pierrehumbert, R., Gardner, s., and Swanson, K. (1995). Surface quasi-geostrophic dynamics. *Journal of Fluid Mechanics*, 282:1–20.
- Hoskins, B., M.E., M., and Robertson, A. (1985). On the use and significance of isentropic potential vorticity maps. *Quart. J. roy. Meteor. Soc.*, (111):877–946.
- Ienna, F., Jo, Y.-H., and Yan, X.-H. (2014). A new method for tracking Meddies by satellite altimetry. *Journal of Atmospheric and Oceanic Technology*, 31(6):1434–1445.
- Isern-Fontanet, J., Lapeyre, G., Klein, P., Chapron, B., and Hecht, M. (2008a). Three-dimensional reconstruction of oceanic mesoscale currents from surface information. *Journal of Geophysical Research: Oceans*, 113(C9):153–169.

- Isern-Fontanet, J., Lapeyre, G., Klein, P., Chapron, B., and Hecht, M. W. (2008b). Three-dimensional reconstruction of oceanic mesoscale currents from surface information. *Journal of Geophysical Research: Oceans*, 113(C9).
- Johns, W. E., Jacobs, G. A., Kindle, J. C., Murray, S. P., and Mike, C. (1999). Arabian Marginal Seas and Gulfs. Technical report.
- Joyce, T. M. (1981). The influence of the Mid-Atlantic Ridge upon the circulation and the properties of the mediterranean water southwest of the azores. Technical report, Woods Hole Oceanographic Institution.
- Kase, R. H., Beckmann, A., and Hinrichsen, H.-H. (1989). Observational evidence of salt lens formation in the Iberian Basin. *Journal of Geophysical Research: Oceans*, 94(C4):4905–4912.
- Käse, R. H., Beckmann, A., and Hinrichsen, H.-H. (1989). Observational evidence of salt lens formation in the Iberian Basin. *Journal of Geophysical Research: Oceans*, 94(C4):4905–4912.
- Käse, R. H. and Zenk, W. (1987). Reconstructed Mediterranean salt lens trajectories. *Journal of Physical Oceanography*, 17(1):158–163.
- Kieu, C. Q. and Zhang, D.-L. (2008). Genesis of tropical storm eugene (2005) from merging vortices associated with ITCZ breakdowns. part i: Observational and modeling analyses. *Journal of the Atmospheric Sciences*, 65(11):3419–3439.
- Klein, P., Isern-Fontanet, J., Lapeyre, G., Rouillet, G., Danioux, E., Chapron, B., Le Gentil, S., and Sasaki, H. (2009). Diagnosis of vertical velocities in the upper ocean from high resolution sea surface height. *Geophysical Research Letters*, 36(12).
- Lapeyre, G. and Klein, P. (2006). Dynamics of the upper oceanic layers in terms of surface quasigeostrophy theory. *Journal of Geophysical Research*, 36(2):165–176.
- Le Cann, B. and Serpette, A. (2009). Intense warm and saline upper ocean inflow in the southern Bay of Biscay in autumn–winter 2006–2007. *Continental Shelf Research*, 29(8):1014–1025.

- Lee, C., Burton, H., Brink, K., and Fischer, A. (2000). The upper-ocean response to monsoonal forcing in the Arabian Sea: seasonal and spatial variability. *Deep-Sea Research II*, 47:1177–1226.
- L'Hégaret, P., Carton, X., Ambar, I., Ménesguen, C., Hua, B. L., Chérubin, L., Aguiar, A., Cann, B., Daniault, N., and Serra, N. (2014). Evidence of Mediterranean Water dipole collision in the Gulf of Cadiz. *Journal of Geophysical Research: Oceans*, 119(8):5337–5359.
- L'Hégaret, P. (2015). Etude de la circulation de mésoéchelle et de sorties d'eaux du Golfe Persique dans l'Océan Indien Nord-Ouest. *PhD Manuscript, Université de Bretagne Occidentale*.
- Lorbacher, K., Dommenges, D., Niiler, P., and Köhl, A. (2006). Ocean mixed layer depth: A subsurface proxy of ocean-atmosphere variability. *Journal of Geophysical Research: Oceans (1978–2012)*, 111(C7).
- Lutjeharms, J. and Ballegooyen, R. (1988). The retroflection of the Agulhas Current. *Journal of Physical Oceanography*, 18:1570–1583.
- Masina, S. and Pinardi, N. (1991). Merging of barotropic symmetric vortices. A case study for gulf stream rings. *Il Nuovo Cimento C*, 14(6):539–553.
- McDowell, S. E. and Rossby, H. T. (1978). Mediterranean water: An intense mesoscale eddy off the Bahamas. *Science*, 202(4372):1085–1087.
- McGillicuddy, D., Johnson, R., Siegel, D., Michaels, A., Bates, N., and Knap, A. (1999). Mesoscale variations of biogeochemical properties in the Sargasso Sea. *Journal of Geophysical Research: Oceans (1978–2012)*, 104(C6):13381–13394.
- McWilliams, J. C. (1985). Submesoscale, coherent vortices in the ocean. *Reviews of Geophysics*, 23(2):165–182.
- Ménesguen, C., Hua, B.-L., Carton, X., Klingelhoefer, F., Schnürle, P., and Reichert, C. (2012). Arms winding around a Meddy seen in seismic reflection data close to the Morocco coastline. *Geophysical Research Letters*, 39(5).
- Meschanov, S. and Shapiro, G. (1998). A young lens of Red Sea water in the Arabian Sea. *Deep Sea Research*, 1(13).

- Millot, C. (1999). Circulation on the western Mediterranean Sea. *Journal of Marine Systems*, (20):423–442.
- Molemaker, M. J., McWilliams, J. C., and Dewar, W. K. (2014). Submesoscale instability and generation of mesoscale anticyclones near a separation of the California Undercurrent. *Journal of Physical Oceanography*, (2014).
- Morel, Y. (1995). The influence of an upper thermocline current on intrathermocline eddies. *Journal of Physical Oceanography*, 25(12):3247–3252.
- Morel, Y. and McWilliams, J. (1997). Evolution of isolated interior vortices in the ocean. *Journal of Physical Oceanography*, 27(5):727–748.
- Nencioli, F., Chang, D., Dickey, T., Washburn, L., and McWilliams, J. (2010). A Vector-Based Eddy Detection Algorithm and Its Application to a High-Resolution Numerical Model Product and High-Frequency Radar Surface Velocities in the Southern California Bight. *Journal of Atmospheric and Oceanic Technology*, 27:564–579.
- Niiler, P. P., Maximenko, N. A., Panteleev, G. G., Yamagata, T., and Olson, D. B. (2003). Near-surface dynamical structure of the Kuroshio Extension. *Journal of Geophysical Research: Oceans*, 108(C6).
- Nilsson, C. and Cresswell, G. (1980). The formation and evolution of East Australian Current warm-core eddies. *Progress in Oceanography*, 9(3):133 – 183.
- Oliveira, P. B., Serra, N., Fiúza, A. F., and Ambar, I. (2000). A study of Meddies using simultaneous in-situ and satellite observations. *Elsevier Oceanography Series*, 63:125–148.
- Olson, D. B. (1980). The physical oceanography of two rings observed by the cyclonic ring experiment. part ii: Dynamics. *Journal of Physical Oceanography*, 10(4):514–528.
- Overman, E. A., Zabusky, N. J., et al. (1981). Evolution and merger of isolated vortex structures. Technical report, DTIC Document.

- Paillet, J., Le Cann, B., Carton, X., Morel, Y., and Serpette, A. (2002). Dynamics and evolution of a northern Meddy. *Journal of Physical Oceanography*, 32(1):55–79.
- Pingree, R. and Le Cann, B. (1992). Three anticyclonic slope water oceanic eddies (SWODDIES) in the southern Bay of Biscay in 1990. *Deep Sea Research Part A. Oceanographic Research Papers*, 39(7/8):1147 – 1175.
- Pingree, R. and Le Cann, B. (1993a). A shallow meddy (a smeddy) from the secondary Mediterranean salinity maximum. *Journal of Geophysical Research: Oceans (1978–2012)*, 98(C11):20169–20185.
- Pingree, R. and Le Cann, B. (1993b). Structure of a meddy (Bobby 92) southeast of the Azores. *Deep Sea Research I*, 40(10):2077–2103.
- Pingree, R. and Morrison, G. (1973). The relationship between stability and source waters for a section in the northeast Atlantic. *Journal of Physical Oceanography*, 3(3):280–285.
- Polvani, L. (1991). Two-layer geostrophic vortex dynamics, 2, alignment and two-layer v-states. *Journal of Fluid Mechanics*, 225:241–270.
- Ponte, A. and Klein, P. (2013). Reconstruction of the upper ocean 3d dynamics from high-resolution sea surface height. *Ocean Dynamics*, 63:777–791.
- Ponte, A., Klein, P., Capet, X., Le Traon, P., Chapron, B., and Lherminier, P. (2013a). Diagnosing surface mixed layer dynamics from high-resolution satellite observations: numerical insights. *Journal of Physical Oceanography*, 43:1345–1355.
- Ponte, A. L., Klein, P., Capet, X., Le Traon, P.-Y., Chapron, B., and Lherminier, P. (2013b). Diagnosing surface mixed layer dynamics from high-resolution satellite observations: Numerical insights. *Journal of Physical Oceanography*, 43(7):1345–1355.
- Prater, M. D. and Rossby, T. (1999). An alternative hypothesis for the origin of the Mediterranean salt lens observed off the Bahamas in the fall of 1976. *Journal of Physical Oceanography*, 29(8):2103–2109.

- Prater, M. D. and Sanford, T. B. (1994). A Meddy off Cape St. Vincent. part i: Description. *Journal of Physical Oceanography*, 24(7):1572–1586.
- Qiu, B., Chen, S., Klein, P., Ubelmann, C., Fu, L.-L., and Sasaki, H. (2016). Reconstructability of three-dimensional upper-ocean circulation from SWOT sea surface height measurements. *Journal of Physical Oceanography*, 46(3):947–963.
- Quadfasel, D. and Baudner, H. (1993). Gyre-scale circulation cells in the Red-Sea. *Oceanologica Acta*, 16(3):221–229.
- Reinaud, J. N. and Dritschel, D. G. (2005). The critical merger distance between two co-rotating quasi-geostrophic vortices. *Journal of Fluid Mechanics*, 522:357–381.
- Richardson, P., Bower, A., and Zenk, W. (2000a). A census of Meddies tracked by floats. *Progress in Oceanography*, 45:209–250.
- Richardson, P., Bower, A., and Zenk, W. (2000b). A census of Meddies tracked by floats. *Progress in Oceanography*, 45(2):209–250.
- Richardson, P., Price, J., Walsh, D., Armi, L., and Schröder, M. (1989). Tracking three meddies with SOFAR floats. *Journal of Physical Oceanography*, 19(3):371–383.
- Richardson, P. L., Hufford, G. E., Limeburner, R., and Brown, W. S. (1994). North Brazil Current retroflection eddies. *Journal of Geophysical Research: Oceans*, 99(C3):5081–5093.
- Richardson, P. L. and Tychensky, A. (1998). Meddy trajectories in the Canary Basin measured during the SEMAPHORE experiment, 1993–1995. *Journal of Geophysical Research: Oceans*, 103(C11):25029–25045.
- Rubino, A., Falcini, F., Zanchettin, D., Bouche, V., Salusti, E., Bensi, M., Riccobene, G., De Bonis, G., Masullo, R., Simeone, F., et al. (2012). Abyssal undular vortices in the eastern Mediterranean basin. *Nature Communications*, 3:834.
- Schultz Tokos, K. L., Hinrichsen, H.-H., and Zenk, W. (1994). Merging and migration of two meddies. *Journal of Physical Oceanography*, 24(10):2129–2141.

- Senjyu, T., Ishimaru, T., Matsuyama, M., and Koike, Y. (1998). High salinity lens from the strait of hormuz. *Offshore Environment of the ROPME Sea Area after the War-Related Oil Spill*, Eds. A. Otsuki et al., pages 35–48.
- Serra, N., Ambar, I., and Boutov, D. (2010). Surface expression of Mediterranean Water dipoles and their contribution to the shelf/slope–open ocean exchange. *Ocean Science*, 6(1):191–209.
- Serra, N., Ambar, I., and Käse, R. H. (2005). Observations and numerical modelling of the Mediterranean outflow splitting and eddy generation. *Deep Sea Research Part II: Topical Studies in Oceanography*, 52(3):383–408.
- Serra, N., Sadoux, S., Ambar, I., and Renouard, D. (2002). Observations and laboratory modeling of meddy generation at Cape St. Vincent. *Journal of Physical Oceanography*, 32(1):3–25.
- Shapiro, G. and Meschanov, S. (1991). Distribution and spreading of Red Sea water and salt lens formation in the northwest indian ocean. *Deep Sea Research Part A. Oceanographic Research Papers*, 38(1):21 – 34.
- Shapiro, G., Meschanov, S., and Emelianov, M. (1995). Mediterranean lens Irving after its collision with seamounts. *Oceanologica Acta*, 18(3):309–318.
- Shchepetkin, A. F. and McWilliams, J. C. (2005). The regional oceanic modeling system (ROMS): a split-explicit, free-surface, topography-following-coordinate oceanic model. *Ocean Modelling*, 9(4):347–404.
- Sokolovskiy, M. A., Filyushkin, B. N., and Carton, X. J. (2013). Dynamics of intrathermocline vortices in a gyre flow over a seamount chain. *Ocean Dynamics*, 63(7):741–760.
- Stammer, D., Hinrichsen, H. H., and Käse, R. H. (1991). Can Meddies be detected by satellite altimetry? *Journal of Geophysical Research: Oceans*, 96(C4):7005–7014.
- Stephens, J. C. and Marshall, D. P. (1999). Dynamics of the Mediterranean salinity tongue. *Journal of Physical Oceanography*, 29(7):1425–1441.

- Swallow, J. (1969). A deep eddy off Cape St. Vincent. *Deep-Sea Research*, 16:285–295.
- Sweeney, E. N., Jr., D. J. M., and Buesseler, K. O. (2003a). Biogeochemical impacts due to mesoscale eddy activity in the Sargasso Sea as measured at the Bermuda Atlantic time-series study (bats). *Deep Sea Research Part II: Topical Studies in Oceanography*, 50(22/26):3017 – 3039. The {US} {JGOFS} Synthesis and Modeling Project: Phase {II}.
- Sweeney, E. N., McGillicuddy, D. J., and Buesseler, K. O. (2003b). Biogeochemical impacts due to mesoscale eddy activity in the Sargasso Sea as measured at the Bermuda Atlantic time-series study (bats). *Deep Sea Research Part II: Topical Studies in Oceanography*, 50(22):3017–3039.
- Testor, P. and Gascard, J.-C. (2003). Large-scale spreading of deep waters in the western Mediterranean Sea by submesoscale coherent eddies. *Journal of Physical Oceanography*, 33:75–87.
- Tokos, K. S. and Rossby, T. (1991). Kinematics and dynamics of a Mediterranean salt lens. *Journal of Physical Oceanography*, 21(6):879–892.
- Trieling, R., Fuentes, O. V., and van Heijst, G. (2005). Interaction of two unequal corotating vortices. *Physics of Fluids (1994-present)*, 17(8):87–103.
- Tychensky, A. and Carton, X. (1998). Hydrological and dynamical characterization of meddies in the Azores region: a paradigm for baroclinic vortex dynamics. *Journal of Geophysical Research: Oceans*, 103(C11):25061–25079.
- Valcke, S. and Verron, J. (1997). Interactions of baroclinic isolated vortices: The dominant effect of shielding. *Journal of Physical Oceanography*, 27(4):524–541.
- Vallis, G. K. (2006). *Atmospheric and Oceanic Fluid Dynamics*. Cambridge University Press, Cambridge, U.K.
- Verron, J., Hopfinger, E., and McWilliams, J. (1990). Sensitivity to initial conditions in the merging of two-layer baroclinic vortices. *Physics of Fluids A: Fluid Dynamics (1989-1993)*, 2(6):886–889.

- 
- Vic, C., Rouillet, G., Capet, X., Carton, X., Molemaker, M. J., and Gula, J. (2015). Eddy-topography interactions and the fate of the Persian Gulf outflow. *Journal of Geophysical Research: Oceans*, 120(10):6700–6717.
- Waugh, D. W. (1992). The efficiency of symmetric vortex merger. *Physics of Fluids A*, 4(8):1745–1758.